LINEAR SYSTEMS MODELLING OF TWO-DIMENSIONAL PIEZOELECTRIC STRUCTURES

VOL. II

Presented by

DEAN GILLIES

In the fulfilment of the requirement for the degree of Doctor of Philosophy of the University of Strathclyde

Department of Electronic and Electrical Engineering

September 1986 Glasgow

APPENDIX A

INVERSION OF THE BOUNDARY CONDITION MATRIX

APPENDIX A

This appendix presents a detailed mathematical solution to the boundary condition matrix given by equation 3.25, chapter III. The solution is obtained by performing a complex algebraic matrix inversion, which in turn provides expressions for $\bar{A}_1$, $\bar{B}_1$, $\bar{A}_3$ and $\bar{B}_3$.

Matrix equation 3.25 may be written in a simpler form if the first line is divided by $s(Zc_1+Z_R)$, the second line divided by $s(Zc_1+Z_L)$, the third line divided by $s(Zc_3+Z_B)$, and finally the fourth line is divided by $s(Zc_3+Z_F)$. This gives,

$$\begin{bmatrix} R_R e^{-sT_1} & -e^{sT_1} & T_R\bar{M}_{A1} & T_R\bar{M}_{B1} \\ 1 & -R_L & T_L\bar{M}_{A1} & T_L\bar{M}_{B1} \\ T_B\bar{M}_{A3} & T_B\bar{M}_{B3} & R_B e^{-sT_3} & -e^{sT_3} \\ T_F\bar{M}_{A3} & T_F\bar{M}_{B3} & 1 & -R_F \end{bmatrix} \begin{bmatrix} \bar{A}_1 \\ \bar{B}_1 \\ \bar{A}_3 \\ \bar{B}_3 \end{bmatrix} = \begin{bmatrix} \dfrac{-\phi\bar{V}_3}{s(Zc_1+Z_R)} \\ \dfrac{-\phi\bar{V}_3 + 2sZ_L\bar{A}_{11}}{s(Zc_1+Z_L)} \\ \dfrac{-h\bar{Q}}{s(Zc_3+Z_B)} \\ \dfrac{-h\bar{Q} + 2sZ_F\bar{A}_{33}}{s(Zc_3+Z_F)} \end{bmatrix} \qquad \text{A1.1}$$

where

$$\bar{M}_{A1} = \frac{-\psi_{31}\left[e^{-sT_3} - 1 \right]}{2sZc_1}$$

$$\bar{M}_{B1} = \frac{-\psi_{31}\left[e^{sT_3} - 1 \right]}{2sZc_1}$$

$$\bar{M}_{A2} = \frac{-\psi_{13}[\, e^{-sT_1} - 1 \,]}{2sZc_3}$$

and

$$\bar{M}_{B2} = \frac{-\psi_{13}[\, e^{sT_1} - 1 \,]}{2sZc_3}$$

It should be noted that,

$$\bar{M}_{A1}\bar{M}_{A3} = \bar{M}_{B1}\bar{M}_{B3}\, e^{-sT_1}\, e^{-sT_3}$$

and,

$$\bar{M}_{A1} = -\bar{M}_{B1}\, e^{-sT_3}$$

In order to solve the above matrix equation, it is first necessary to obtain an expression for the inverse of the four by four square matrix. The inverse of a non-singular complex matrix is given by,

$$[P]^{-1} = \frac{\text{adj } [P]}{\det [P]}$$

It is therefore necessary to obtain the adjoint matrix of [P] in addition to an expression for the determinant of [P].

CALCULATION OF THE DETERMINANT OF [P]

The determinant of the complex matrix [P] is calculated in the following manner,

$$
\det[p] = R_R e^{-sT_1}
\begin{vmatrix}
-R_L & T_L\bar{M}_{A1} & T_L\bar{M}_{B1} \\
T_B\bar{M}_{B3} & R_B e^{-sT_2} & -e^{sT_3} \\
T_F\bar{M}_{B3} & 1 & -R_F
\end{vmatrix}
$$

$$
-
\begin{vmatrix}
-e^{sT_1} & T_R\bar{M}_{A1} & T_R\bar{M}_{B1} \\
T_B\bar{M}_{B3} & R_B e^{-sT_2} & -e^{sT_3} \\
T_F\bar{M}_{B3} & 1 & -R_F
\end{vmatrix}
$$

$$
+ T_B\bar{M}_{A2}
\begin{vmatrix}
-e^{sT_1} & T_R\bar{M}_{A1} & T_R\bar{M}_{B1} \\
-R_L & T_L\bar{M}_{A1} & T_L\bar{M}_{B1} \\
T_F\bar{M}_{B3} & 1 & -R_F
\end{vmatrix}
$$

$$
+ T_F\bar{M}_{B3}
\begin{vmatrix}
-e^{sT_1} & T_R\bar{M}_{A1} & T_R\bar{M}_{B1} \\
-R_L & T_L\bar{M}_{A1} & T_L\bar{M}_{B1} \\
T_B\bar{M}_{B3} & R_B e^{-sT_2} & -e^{sT_3}
\end{vmatrix}
$$

which may be expanded to give,

$$
\begin{aligned}
\det[P] \;=\; & R_R e^{-sT_1}\Big[-R_L\,[\, -R_F R_B e^{-sT_3} + e^{sT_3}\,] \\
& - T_L\bar{M}_{A1}\,[\, -R_F T_B \bar{M}_{B3} + T_F \bar{M}_{B3}\, e^{sT_3}\,] \\
& + T_L\bar{M}_{B1}\,[\, T_B\bar{M}_{B3} - T_F R_B \bar{M}_{B3}\, e^{-sT_3}\,]\Big] \\
& - \Big[-e^{sT_1}\,[\, -R_F R_B e^{-sT_3} + e^{sT_3}\,] \\
& - T_R\bar{M}_{A1}\,[-R_F T_B \bar{M}_{B3} + T_F \bar{M}_{B3}\, e^{sT_3}\,] \\
& + T_R\bar{M}_{B1}\,[\, T_B\bar{M}_{B3} - T_F R_B \bar{M}_{B3}\, e^{-sT_3}\,]\Big] \\
& + T_B\bar{M}_{A3}\Big[-e^{sT_1}\,[\, -R_F T_L M_{A1} - T_L M_{B1}\,] \\
& - T_R\bar{M}_{A1}\,[\, R_L R_F - T_L T_F \bar{M}_{B1}\bar{M}_{B3}\,] \\
& + T_R\bar{M}_{B1}\,[\, -R_L - T_L T_F \bar{M}_{A1}\bar{M}_{B3}\,]\Big] \\
& - T_F\bar{M}_{B2}\Big[-e^{sT_1}\,[\, -T_L\bar{M}_{A1}\, e^{sT_3} - T_L\bar{M}_{B1}R_B\, e^{-sT_3}\,] \\
& - T_R\bar{M}_{A1}\,[\, R_L\, e^{sT_3} - T_L T_B \bar{M}_{B1}\bar{M}_{B3}\,] \\
& + T_R\bar{M}_{B1}\,[\, -R_L R_B\, e^{-sT_3} - T_L T_B \bar{M}_{B1}\bar{M}_{B3}\,]\Big]
\end{aligned}
$$

Giving,

$$\det[P] = e^{sT_1}\,e^{sT_3}\,[\,1 - R_L R_R\,e^{-2sT_1}\,][\,1 - R_F R_B\,e^{-2sT_3}\,]$$

$$+\ \bar{M}_{A1}\bar{M}_{A3}\Big[\ T_L T_B R_F\,e^{sT_1} + T_L T_B R_R\,e^{sT_3} - T_L T_F R_R R_B$$

$$+\ T_R T_F R_B\,e^{sT_1} + T_R T_F R_L\,e^{sT_3} - T_L T_B R_F R_R$$

$$+\ T_L T_F R_B\,e^{sT_1} + T_L T_F R_R\,e^{sT_3} - T_R T_B R_L R_F$$

$$+\ T_R T_B R_F\,e^{sT_1} + T_R T_B R_L\,e^{sT_3} - T_R T_F R_L R_B$$

$$-\ T_R T_F\,e^{sT_1}\,e^{sT_3} - T_L T_B\,e^{sT_1}\,e^{sT_3}$$

$$-\ T_R T_B\,e^{sT_1}\,e^{sT_3} - T_L T_F\,e^{sT_1}\,e^{sT_3}\ \Big]$$

Hence,

$$\det[P] = e^{sT_1}\,e^{sT_3}\Big[\,[\,1 - R_L R_R\,e^{-2sT_1}\,][\,1 - R_F R_B\,e^{-2sT_3}\,]$$

$$+\ \bar{M}_{A1}\bar{M}_{A3}\Big[\ T_L T_F\,[\,1 - R_R\,e^{-sT_1}\,][\,1 - R_B\,e^{-sT_3}\,]$$

$$+\ T_L T_B\,[\,1 - R_R\,e^{-sT_1}\,][\,1 - R_F\,e^{-sT_3}\,]$$

$$+\ T_R T_F\,[\,1 - R_L\,e^{-sT_1}\,][\,1 - R_B\,e^{-sT_3}\,]$$

$$+\ T_R T_B\,[\,1 - R_L\,e^{-sT_1}\,][\,1 - R_F\,e^{-sT_3}\,]\ \Big]\Big]$$

Finally,

$$\det [P] = e^{sT_1}\, e^{sT_3} \left[\bar{\beta}_1\, \bar{\beta}_3 \right] . \bar{M}$$

Where,

$$\bar{\beta}_1 = \left[1 - R_L R_R\, e^{-2sT_1} \right]$$

$$\bar{\beta}_3 = \left[1 - R_F R_B\, e^{-2sT_3} \right]$$

and

$$\bar{M} = \left[1 - \frac{\psi_{13}\, \psi_{31}\, \bar{K}_1\, \bar{K}_3}{s^2 Zc_1\, Zc_3} \right]$$

Also,

$$\bar{K}_1 = \left[T_L\, \bar{K}_L + T_R\, \bar{K}_R \right] / 2$$

$$\bar{K}_3 = \left[T_F\, \bar{K}_F + T_B\, \bar{K}_B \right] / 2$$

where,

$$\bar{K}_F = \left(1 - e^{-sT_3} \right) \left(1 - R_B\, e^{-sT_3} \right) / \bar{\beta}_3$$

$$\bar{K}_B = \left(1 - e^{-sT_3} \right) \left(1 - R_F\, e^{-sT_3} \right) / \bar{\beta}_3$$

$$\bar{K}_L = \left(1 - e^{-sT_1} \right) \left(1 - R_R\, e^{-sT_1} \right) / \bar{\beta}_1$$

$$\bar{K}_R = \left(1 - e^{-sT_1} \right) \left(1 - R_L\, e^{-sT_1} \right) / \bar{\beta}_1$$

$\bar{K}_1$ and $\bar{K}_3$ are as defined by Hayward [18], and the factor $\bar{M}$ is investigated in detail in chapter III.

FORMATION OF THE ADJOINT MATRIX

The adjoint matrix of [P] is obtained by firstly evaluating the cofactors α_{ij} of [P], and writing them in the correct transposed form. That is,

$$\text{adj } [P] = \begin{bmatrix} \alpha_{11} & -\alpha_{21} & \alpha_{31} & -\alpha_{41} \\ -\alpha_{12} & \alpha_{22} & -\alpha_{32} & \alpha_{42} \\ \alpha_{13} & -\alpha_{23} & \alpha_{33} & -\alpha_{43} \\ -\alpha_{14} & \alpha_{24} & -\alpha_{34} & \alpha_{44} \end{bmatrix}$$

The cofactors α_{ij} of the [P] matrix may be obtained as follows,

$$\alpha_{11} = \begin{vmatrix} -R_L & T_L\bar{M}_{A1} & T_L\bar{M}_{B1} \\ T_B\bar{M}_{B3} & R_B e^{-sT_3} & -e^{sT_3} \\ T_F\bar{M}_{B3} & 1 & -R_F \end{vmatrix}$$

$$= -R_L e^{sT_3} \bar{\beta}_3 \left[1 + \frac{T_L\bar{K}_3\bar{\psi}_{13}\bar{\psi}_{31} \left(1 - e^{sT_1} \right)}{2s^2 Zc_1 Zc_3 R_L} \right]$$

$$\alpha_{12} = \begin{vmatrix} 1 & T_L\bar{M}_{A1} & T_L\bar{M}_{B1} \\ T_B\bar{M}_{A2} & R_B e^{-sT_3} & -e^{sT_3} \\ T_F\bar{M}_{A3} & 1 & -R_F \end{vmatrix}$$

$$= e^{sT_3}\bar{\beta}_3\left[1 + \frac{T_L\bar{K}_3\psi_{13}\psi_{31}\left(e^{-sT_1} - 1\right)}{2s^2Zc_1Zc_3}\right]$$

$$\alpha_{13} = \begin{vmatrix} 1 & -R_L & T_L\bar{M}_{B1} \\ T_B\bar{M}_{A3} & T_B\bar{M}_{B3} & -e^{sT_3} \\ T_F\bar{M}_{A3} & T_F\bar{M}_{B3} & -R_F \end{vmatrix}$$

$$= \frac{\psi_{13}}{2sZc_3}\left[T_F e^{sT_3} - T_B R_F\right]\left[1 - R_L e^{-sT_1}\right]\left[1 - e^{sT_1}\right]$$

$$\alpha_{14} = \begin{vmatrix} 1 & -R_L & T_L\bar{M}_{A1} \\ T_B\bar{M}_{A3} & T_B\bar{M}_{B3} & R_B e^{-sT_3} \\ T_F\bar{M}_{A3} & T_F\bar{M}_{B3} & 1 \end{vmatrix}$$

$$= -\frac{\psi_{13}}{2sZc_3}\left[T_F R_B e^{-sT_3} - T_B\right]\left[1 - R_L e^{-sT_1}\right]\left[1 - e^{sT_1}\right]$$

$$\alpha_{21} = \begin{vmatrix} -e^{sT_1} & T_R\bar{M}_{A1} & T_R\bar{M}_{B1} \\ T_B\bar{M}_{B3} & R_B e^{-sT_3} & -e^{sT_3} \\ T_F\bar{M}_{B3} & 1 & -R_F \end{vmatrix}$$

$$= -e^{sT_1} e^{sT_3} \bar{\beta}_3 \left[1 + \frac{T_R\bar{K}_3\psi_{13}\psi_{31}\left(e^{-sT_1} - 1 \right)}{2s^2 Zc_1 Zc_3} \right]$$

$$\alpha_{22} = \begin{vmatrix} R_R e^{-sT_1} & T_R\bar{M}_{A1} & T_R\bar{M}_{B1} \\ T_B\bar{M}_{A3} & R_B e^{-sT_3} & -e^{sT_3} \\ T_F\bar{M}_{A3} & 1 & -R_F \end{vmatrix}$$

$$= R_R e^{-sT_1} e^{sT_3} \bar{\beta}_3 \left[1 + \frac{T_R\bar{K}_3\psi_{13}\psi_{31}\left(1 - e^{sT_1} \right)}{2s^2 Zc_1 Zc_3 R_R} \right]$$

$$\alpha_{23} = \begin{vmatrix} R_R e^{-sT_1} & -e^{sT_1} & T_R\bar{M}_{B1} \\ T_B\bar{M}_{A3} & T_B\bar{M}_{B3} & -e^{sT_3} \\ T_F\bar{M}_{A3} & T_F\bar{M}_{B3} & -R_F \end{vmatrix}$$

$$= -\frac{\psi_{13}}{2sZc_3} \left[T_F e^{sT_3} - T_B R_B \right] \left[1 - R_R e^{-sT_1} \right] \left[1 - e^{sT_1} \right]$$

$$\alpha_{24} = \begin{vmatrix} R_R\, e^{-sT_1} & -e^{sT_1} & T_R\bar{M}_{A1} \\ T_B\bar{M}_{A3} & T_B\bar{M}_{B3} & R_B\, e^{-sT_3} \\ T_F\bar{M}_{A3} & T_F\bar{M}_{B3} & 1 \end{vmatrix}$$

$$= \frac{\psi_{13}}{2sZc_3}\left[\, T_F\, R_B\, e^{-sT_3} - T_B\right]\left[\, 1 - R_R\, e^{-sT_1}\right]\left[\, 1 - e^{sT_1}\right]$$

$$\alpha_{31} = \begin{vmatrix} -e^{sT_1} & T_R\bar{M}_{A1} & T_R\bar{M}_{B1} \\ -R_L & T_L\bar{M}_{A1} & T_L\bar{M}_{B1} \\ T_F\bar{M}_{B3} & 1 & -R_F \end{vmatrix}$$

$$= \frac{\psi_{31}}{2sZc_1}\left[\, T_L\, e^{sT_1} - T_R R_L\right]\left[\, 1 - R_F\, e^{-sT_3}\right]\left[\, 1 - e^{sT_3}\right]$$

$$\alpha_{32} = \begin{vmatrix} R_R\, e^{-sT_1} & T_R\bar{M}_{A1} & T_R\bar{M}_{B1} \\ 1 & T_L\bar{M}_{A1} & T_L\bar{M}_{B1} \\ T_F\bar{M}_{A3} & 1 & -R_F \end{vmatrix}$$

$$= -\frac{\psi_{31}}{2sZc_1}\left[\, T_L\, R_R\, e^{-sT_1} - T_R\right]\left[\, 1 - R_F\, e^{-sT_3}\right]\left[\, 1 - e^{sT_3}\right]$$

$$\alpha_{33} = \begin{vmatrix} R_R\, e^{-sT_1} & -e^{sT_1} & T_R\bar{M}_{B1} \\ 1 & -R_L & T_L\bar{M}_{B1} \\ T_F\bar{M}_{A3} & T_F\bar{M}_{B3} & -R_F \end{vmatrix}$$

$$= -R_F\, e^{sT_1}\, \bar{\beta}_1 \left[1 + \frac{T_F\bar{K}_1\psi_{13}\psi_{31}\,(\,1 - e^{sT_3}\,)}{2s^2 Z_{c1} Z_{c3} R_F} \right]$$

$$\alpha_{34} = \begin{vmatrix} R_R\, e^{-sT_1} & -e^{sT_1} & T_R\bar{M}_{A1} \\ 1 & -R_L & T_L\bar{M}_{A1} \\ T_F\bar{M}_{A3} & T_F\bar{M}_{B3} & 1 \end{vmatrix}$$

$$= e^{sT_1}\, \bar{\beta}_1 \left[1 + \frac{T_F\bar{K}_1\psi_{13}\psi_{31}\,(\,e^{-sT_3} - 1\,)}{2s^2 Z_{c1} Z_{c3}} \right]$$

$$\alpha_{41} = \begin{vmatrix} -e^{sT_1} & T_R\bar{M}_{A1} & T_R\bar{M}_{B1} \\ -R_L & T_L\bar{M}_{A1} & T_L\bar{M}_{B1} \\ T_B\bar{M}_{B3} & R_B e^{-sT_3} & -e^{sT_3} \end{vmatrix}$$

$$= -\frac{\psi_{31}}{2sZ_{c1}} \left[T_L\, e^{sT_1} - T_R R_L \right] \left[1 - R_B\, e^{-sT_3} \right] \left[1 - e^{sT_3} \right]$$

$$\alpha_{42} = \begin{vmatrix} R_R\, e^{-sT_1} & T_R\bar{M}_{A1} & T_R\bar{M}_{B1} \\ 1 & T_L\bar{M}_{A1} & T_L\bar{M}_{B1} \\ T_B\bar{M}_{A3} & R_B e^{-sT_3} & -e^{sT_3} \end{vmatrix}$$

$$\alpha = \frac{\psi_{31}}{2sZc_1}\left[\, T_L R_R\, e^{-sT_1} - T_R\right]\left[\, 1 - R_B\, e^{-sT_3}\,\right]\left[\, 1 - e^{sT_3}\,\right]$$

$$\alpha_{43} = \begin{vmatrix} R_R\, e^{-sT_1} & -e^{sT_1} & T_R\bar{M}_{B1} \\ 1 & -R_L & T_L\bar{M}_{B1} \\ T_B\bar{M}_{A3} & T_B\bar{M}_{B3} & -e^{sT_3} \end{vmatrix}$$

$$= -\, e^{sT_1}\, e^{sT_3}\, \bar{\beta}_1\left[\, 1 + \frac{T_B\bar{K}_1\psi_{13}\psi_{31}\,\left(\, e^{-sT_3} - 1\,\right)}{2s^2Zc_1Zc_3}\,\right]$$

$$\alpha_{44} = \begin{vmatrix} R_R\, e^{-sT_1} & -e^{sT_1} & T_R\bar{M}_{A1} \\ 1 & -R_L & T_L\bar{M}_{A1} \\ T_B\bar{M}_{A3} & T_B\bar{M}_{B3} & R_B\, e^{-sT_3} \end{vmatrix}$$

$$= R_B\, e^{-sT_3}\, e^{sT_1}\, \bar{\beta}_1\left[\, 1 + \frac{T_B\bar{K}_1\psi_{13}\psi_{31}\,\left(\, 1 - e^{sT_3}\,\right)}{2s^2Zc_1Zc_3R_B}\,\right]$$

Having evaluated the cofactors in this manner, it is now possible to obtain Laplace transform expressions for the displacement functions $\bar{A}_1$, $\bar{B}_1$, $\bar{A}_3$ and $\bar{B}_3$ from equation A1.1. That is,

$$\begin{bmatrix} \bar{A}_1 \\ \bar{B}_1 \\ \bar{A}_3 \\ \bar{B}_3 \end{bmatrix} = \frac{\begin{bmatrix} \alpha_{11} & -\alpha_{21} & \alpha_{31} & -\alpha_{41} \\ -\alpha_{12} & \alpha_{22} & -\alpha_{32} & \alpha_{42} \\ \alpha_{13} & -\alpha_{23} & \alpha_{33} & -\alpha_{43} \\ -\alpha_{14} & \alpha_{24} & -\alpha_{34} & \alpha_{44} \end{bmatrix}}{\det [P]} \begin{bmatrix} \dfrac{-\phi\bar{V}_3}{s(Zc_1 + Z_R)} \\ \dfrac{-\phi\bar{V}_3 + 2sZ_L\bar{A}_{11}}{s(Zc_1 + Z_L)} \\ \dfrac{-h\bar{Q}}{s(Zc_3 + Z_R)} \\ \dfrac{-h\bar{Q} + 2sZ_F\bar{A}_{33}}{s(Zc_3 + Z_F)} \end{bmatrix} \qquad \text{A1.2}$$

The complete expressions for the four displacement functions are given in chapter III.

APPENDIX B

MATERIAL PARAMETERS AND EXPERIMENTAL PROCEDURES

APPENDIX B

This appendix firstly gives a detailed indication of the material parameters of the transducers and materials used in this thesis. Secondly, a list of the relevant experimental apparatus and procedures is presented.

(i) Properties of Lead-Zirconate-Titanate

Two different thickness mode PZT-5A transducers were used to provide the experimental results in chapter V. In each case 8 parameters are needed for the simulations. These parameters are given for the two transducers in tables B1 and B2 respectively, where the nominal, measured and simulation parameters are given.

The first transducer was 1.96mm thick, 50mm wide and 50mm long (1MHz). The second was 0.95mm thick, 20mm wide and 50mm long (2MHz).

(ii) Properties of Aluminium

The nominal and simulation data for the aluminium layers is presented in table B3. It should be noted that the value of Y_{13} was not available and is thus estimated only.

Due to a larger grain structure, the aluminium used exhibited more absorption loss than ceramic or steel.

This is reflected in the value of the relative loss factor used in the simulations.

(iii) Properties of steel

The nominal and simulation data for the steel layer is given in table B4. Again the value of Y_{13} is estimated.

(iv) Properties of Epoxy

The nominal and simulation data for the epoxy bondlines is given in table B5. Since the bondlines are all simulated for thickness mode operation, only only the relevant thickness mode parameters are shown.

(v) Properties of Natural Honey

Data was not available on the acoustic properties of natural honey. The relevant properties were measured by the author, and are given in table B6.

(vi) Properties of PVDF

The nominal and simulation properties of PVDF are given in table B7.

(vii) Impedance Measurement Set-up

All of the experimental impedance spectra presented in

this investigation, were measured in an automated procedure, based around the Hewlett Packard 4815A RF vector impedance meter. The complete set-up is illustrated in figure B1.

The frequency generator (Tektronix FG-504) produces a continuously variable frequency, taking 180 seconds to sweep through any selected range. In most cases this range was 400kHz - 4MHz, which corresponds to a sweep rate of 20Hz per second. The lower limit of 400kHz is determined by the lowest frequency at which the vector impedance meter will operate.

The magnitude and phase outputs of the impedance meter are subsequently digitised at a sampling rate of 10Hz, which corresponds to one sample for every 2kHz in the impedance spectra. The digitised data is subsequently transferred to an IBM PC-AT by GPIB link and finally to the University VAX by means of an RS-232 line. Spectral impedance plots are then produced on the VAX, and the data is archived for long term storage.

The measurement error on the vertical (magnitude/phase) axis in the impedance plots is due to quantisation error in the digitiser, and any inaccuracies in measurement by the vector impedance meter. Experimental error on the horizontal (frequency) axis is caused mainly by error in the timing of the sweep frequency generator. Although the frequency sweep time is nominally 180 seconds, this

was found to vary between 178 and 183 seconds. The maximum error on the freqency axis is estimated to be ± 20kHz, although this is clearly frequency dependant.

(viii) Voltage Measurement Set-up

Measurement of transducer voltges was performed using the set-up outlined in figure B2. The pulse generator (Thandar TG-105), produces a train of 15μs pulses at a pulse repetition frequency of 500Hz. This is applied to the relevant firing circuit in addition to the 30V supply (Coutant LQ100/30). The resultant voltage across the transducer is measured using a 250MHz X10 oscilloscope probe (P6106A), operating into either a Tektronix 466 or 7633 storage oscilloscope. Measurement error is due mainly to oscilloscope calibration accuracy, and again all lead lengths were kept to a minimum.

(ix) Force Profile Measurement Set-up

In order to measure the force output from a transducer the device must be coaxially aligned with the memrane hyrophone [60], as shown in figure B3. The hydrophone, illustrated in figure B4, was mounted on a three axis manipulator to permit accurate positioning in the sound field. Th transducer was fixed to the end of a length of stiff wire, and suspended securely in the tank. The standard firing circuit given in figure 5.13 was used with C_s equal to 2.2nF, and Rp equal to 100Ω. A very low

noise (2nV/√Hz) amplifier, was used to interface the hydrophone to the main amplifier. Additional desirable characteristics of a hydrophone amplifier, such as wide bandwidth and high input impedance are also offered by the AH0013 from OEI, which has a bandwidth of 30MHz and an input impedance of $10^{11}\Omega$. The main amplifier is constructed around the Plessey 560 operational amplifier.

The resulting force profile measurement was digitised at a sampling rate of 60Mhz, and subsequently transferred to the University VAX via an IBM PC-AT personal computer.

Due to scaling by the hydrophone, and absorption loss in the water column, the amplitude of the measured force profiles are ignored. Error in the time domain measurements is due mainly to the digitisation process.

(x) Transmit/Receive Measurement Set-up

Experimental measurement of transmit-receieve respnses comprise two different procedures. Transmission into water and reception via reflection from a glass block, and transmission directly into the glass block and reception via back wall reflection. The respective experimental set-ups are illustrated in figure B5 and B6.

In both cases the firing voltage was limited to 15V to avoid damage to the pre-amplifier, since no overvoltage protection circuitry was employed. Alignment of the

glass block in the water tank was also a critical factor, since small changes in position result in significant changes in the received waveform.

In the case of the transducer having no layers, and operating into the glass block, the device must overlap the edge of the glass to permit electrical connection to be made. This will clearly have some effect on the measured response, however, in spite of this the result presented in chapter V demonstrates reasonably good agreement.

The input impedance of the pre-amplifier is effectively swamped by the resistance of Rp (100Ω) in the firing circuit, this allows the input impedance of the pre-amplifier to be ignored in the simulations.

(xi) Beam Profile Measurement Set-up

All of the beam profile measurements in this thesis were performed using the apparatus outlined in figure B7.

The receiving transducer is a 5MHz, thickness mode PZT-5A element with a diameter of 2mm, which is coupled via Natural Honey to the steel test block. This device was fabricated and characterised by Stumpf. [66] The received signals are transferred to the VAX, where they are peak detected, and subsequently plotted as directivity functions.

This technique is however not ideal since the receiving transducer must be physically moved to a different point on the steel block for each angular reading. This movement may result in a different thickness of couplant layer and hence a slightly different response. However, since the directivity measurements constitute neither a major part of the investigation, nor are they used to verify any new theory, this was considered adequate.

APPENDIX C

DESCRIPTION OF COMPUTER PROGRAMS

APPENDIX C

The transducer modelling techniques presented in this thesis, have been implemented in software, to provide a fully interactive computer modelling package. The programs, written in FORTRAN 77, are resident on the VAX 11/782 cluster at Strathclyde University. Due to space constraints, listings are not included in the thesis. However, this appendix contains a description of the main operating features of the software.

The two-dimensional modelling package comprises three main programs. These are,

SYSMOD - This is the fundamental single transducer model based on the transfer function relationships derived in chapter III.

TMOD - This program simulates layered transducer structures which are stacked in the thickness dimension. The relevant equations are provided in chapter IV.

LMOD - This program describes the behaviour of structures which possess layers in the lateral dimension. Again, the relevant equations are given in chapter IV.

A number of subroutines are shared by the main programs. These will be described in addition to SYSMOD, TMOD and LMOD.

THE SHARED SUBROUTINES

The first common stage in each program is the specification of the transducer structure and the mechanical and piezoelectric properties. This is performed in a single subroutine (IPDAT), where the user submits the number of layers (for SYSMOD this is 1 by default); the mechanical and/or piezoelectric properties of the layer(s); the electrical load configuration; the mechanical load configuration; and all of the relevant dimensions. This data may be stored offline for future reference. For example, the properties of a PZT-5A layer may be stored and selected automatically.

The subroutine FREQIP is also shared by all three main programs. This subroutine permits the user to select the required excitation function, which may be either a voltage (transmitter) or a force (receiver). The routine provides a number of standard input functions, in addition to the option of accessing an offline datafile. Since the programs all operate in the frequency domain, all of the input functions are specified as frequency domain quantities.

The simulation outputs from the programs may be plotted, or stored offline in frequency domain datafiles, under the control of the subroutines PLOTWORK and PLOTSORT. These routines permit plotting and storage of frequency domain magnitude and phase information, in addition to time domain data which is generated using a standard inverse fast fourier transform algorithm (IFFT). The IFFT is a commercially available package supplied by the Numerical Analysis Group (NAG).

SYSMOD

Operation of the fundamental two-dimensional modelling program, outlined in the flowchart given in figure C1, may be described in the following manner.

Firstly, the program calls the subroutine IPDAT, which supply all the relevant information regarding the transducer and the electrical/mechanical configuration. The appropriate model may then be selected (transmitter, receiver or operational impedance). Depending on which model is selected, the relevant transfer function is evaluated. Having obtained the transfer function, the program then calls the subroutine FREQIP to supply the excitation function, which is subsequently multiplied by the transfer function, to provide the required output. The simulated output may then be plotted or stored in a datafile for further use. For example, to simulate a pulse-echo response, the force output of the transmitter

model is saved and subsequently applied to the receiver model.

TMOD

The second main program, TMOD, which simulates layers in the thickness dimension may be described by the flowchart depicted in figure C2. The first stage comprises a call to the subroutine IPDAT, in order to provide the relevant configuration and material parameters. The input excitation function is then selected via the subroutine FREQIP. It should be noted that force and voltage inputs may be applied simultaneously to this program. The next part of TMOD involves the formation of the relevant matrices as described in chapter IV. The system matrix is then evaluated, and the relevant outputs may be plotted or stored as required. The solution of the system matrix equation requires the inversion of a complex matrix for each frequency point of interest. Since the order of the matrix increases in relation to the number of layers, the CPU time required to run the program is increased accordingly. Extending the frequency range of interest also increases the required CPU time, although to a lesser extent. For example, a five layer structure, evaluated over a bandwidth of, say, 50MHz requires a little more than 10 minutes CPU time on the VAX 11/782. Under such conditions, the program must be operated in a batch mode to permit the use of more than 10 minutes CPU time.

LMOD

The program which evaluates layered structures in the lateral direction, LMOD, operates essentially in an identical manner to TMOD, apart from the formation of the matrix equation. The differences in the two matrix representations was illustrated in chapter IV.

To conclude, the description of the software, it should be noted that due to the process of continual development, the programs and subroutines relating to the two-dimensional model are not optimal in terms of efficiency. However, for the present application, to verify the new theory, and to characterise small numbers of transducers, they are considered adequate. Further information, and listings are available from the author or Dr. G. Hayward at Strathclyde University.

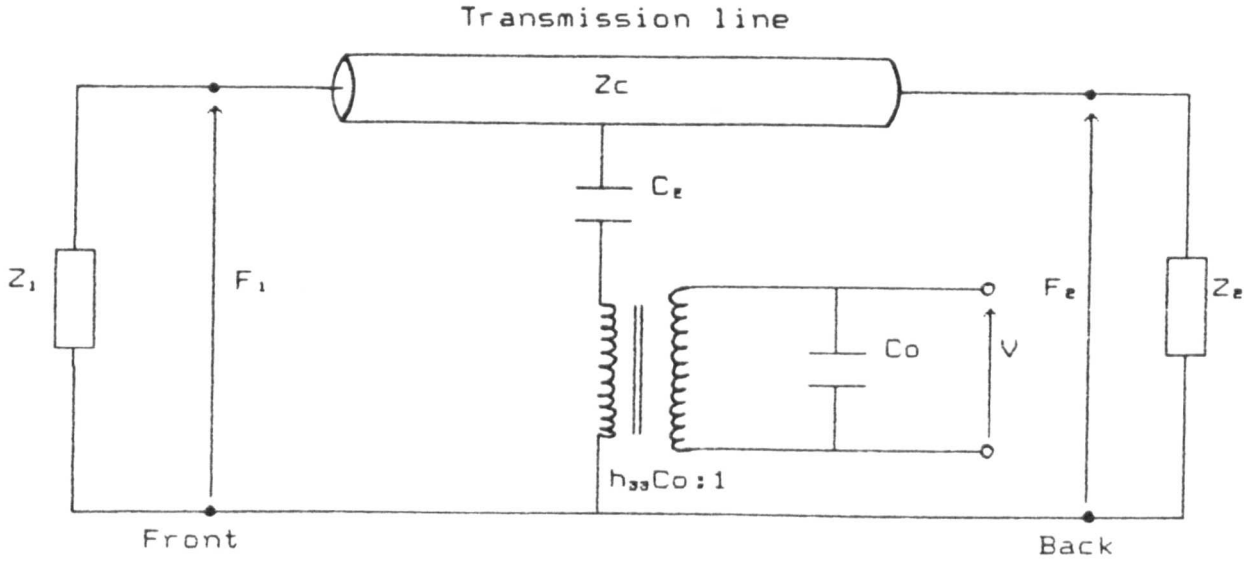

$$C_\varepsilon = -\frac{1}{h_{33}^2 Co}$$

Co = static or clamped capacitance

Figure 2.1 The electromechanical equivilent circuit model according to Mason.

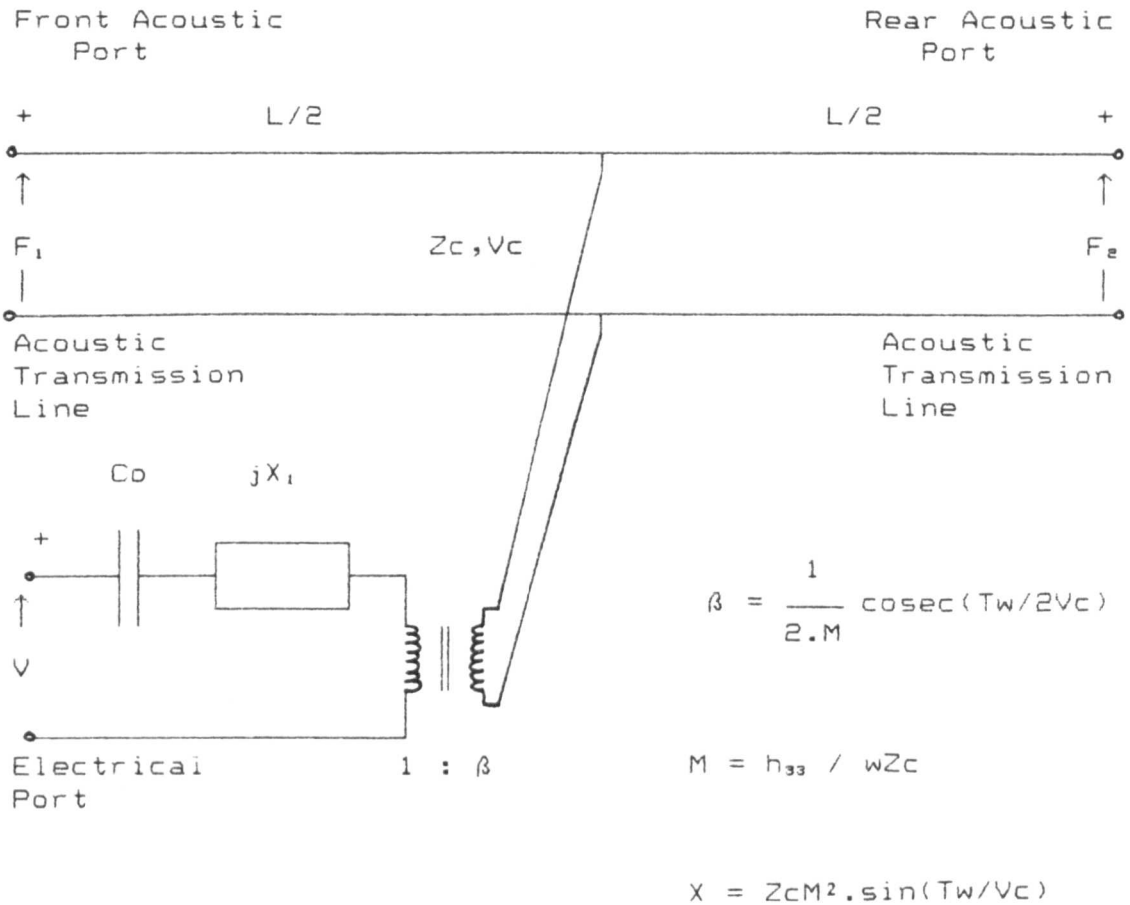

w is the angular frequency, and T is the transit time for longitudinal waves to traverse the thickness dimension.

Figure 2.2 The KLM model of a thickness mode transducer.

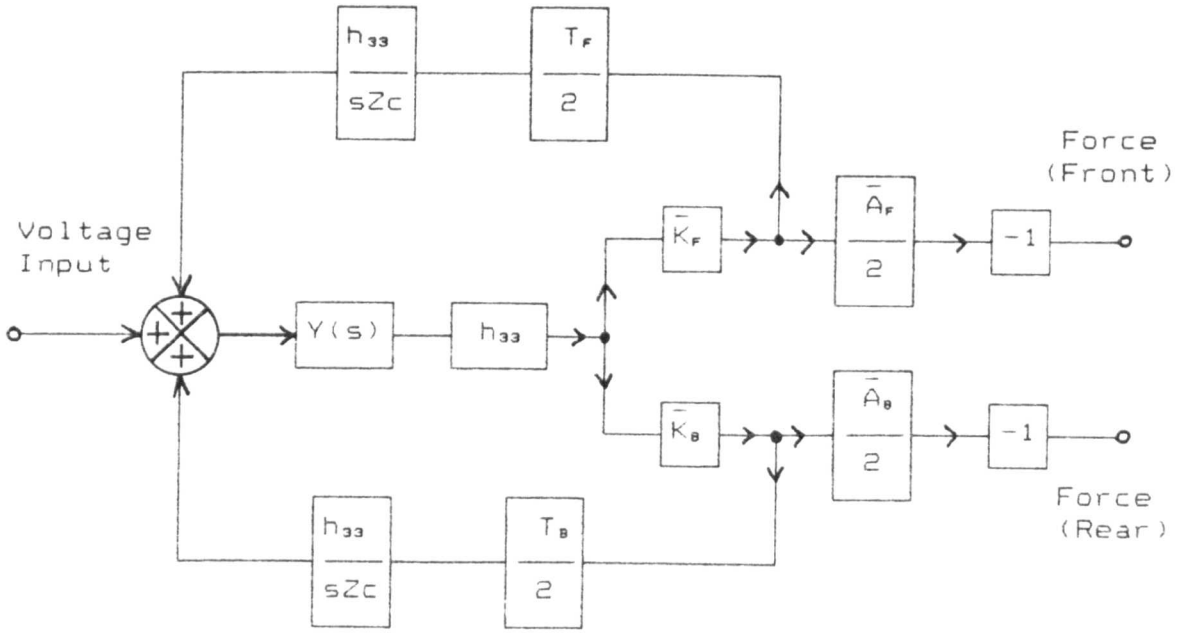

$$Y(s) = \frac{Co}{1 + sCoZo}$$

Zo = Thevenin equivilent electrical load impedance

Figure 2.3 Hayward's Block diagram model for a piezoelectric transmitter.

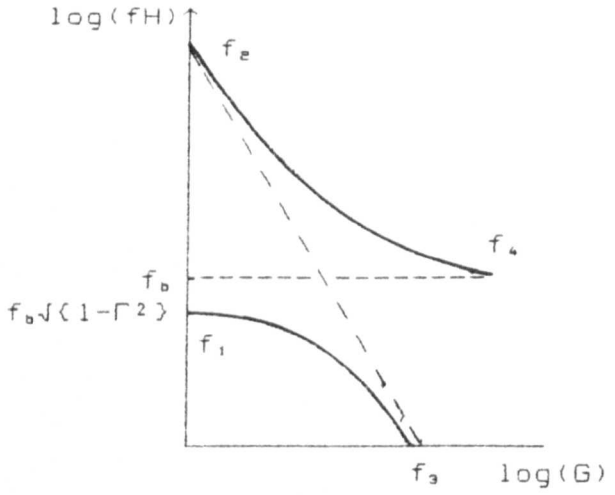

Figure 2.4 Log-Log plots of coupled resonant frequencies Vs configuration ratio. Broken lines show uncoupled frequencies.

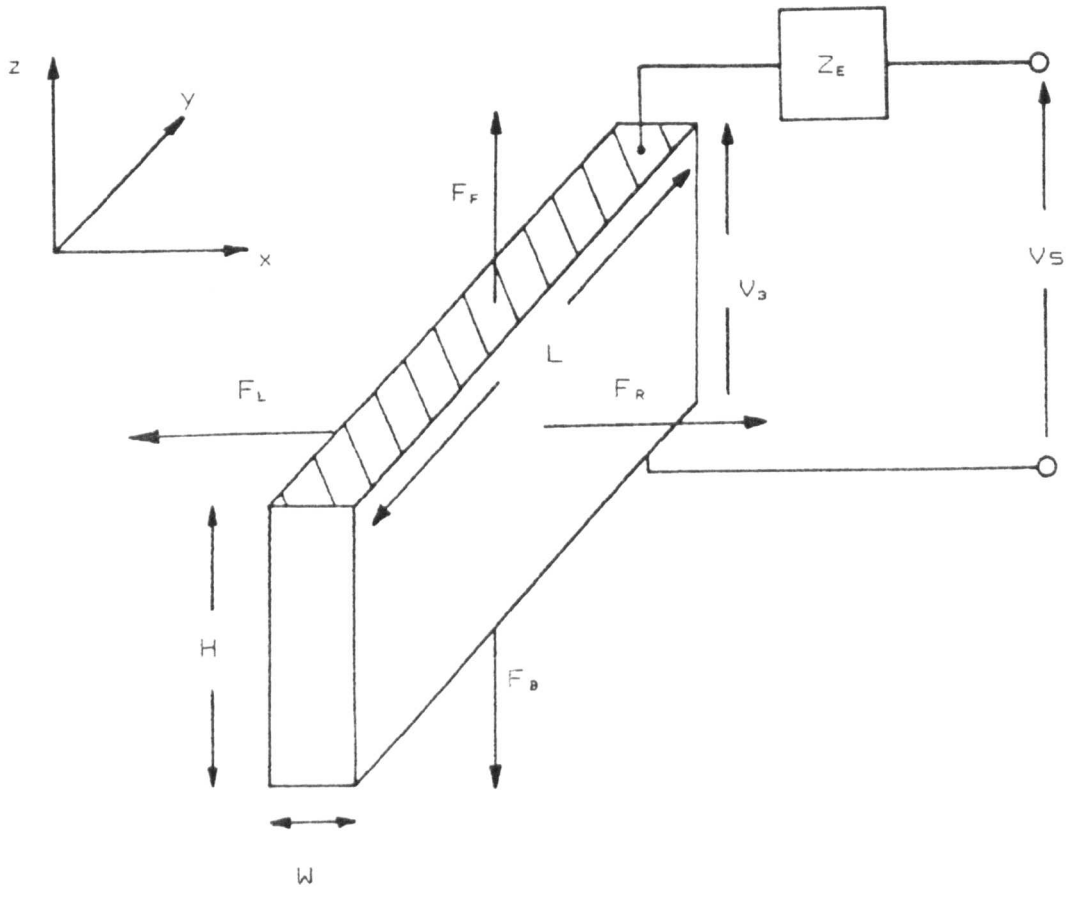

Figure 3.1 Transducer configuration.

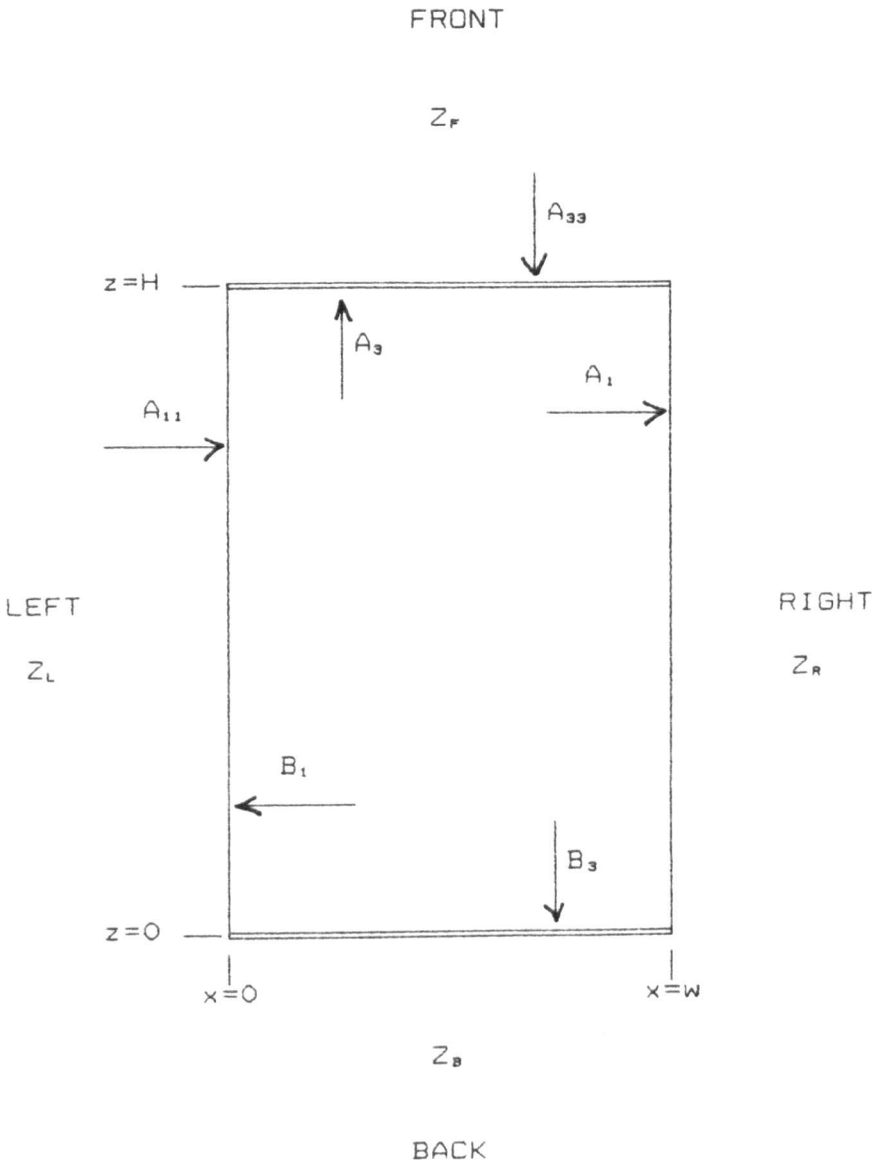

Figure 3.2 Transducer mechanical configuration

Loaded Face	Acoustic Impedance	Acoustic Velocity	Forward Displac--ement	Backward Displac--ement	Total Displa--cement	Total Force
Left	Z_L	v_L	A_{11}	B_{11}	ξ_{11}	F_{11}
Right	Z_R	v_R	A_{12}	B_{12}	ξ_{12}	F_{12}
Front	Z_F	v_F	A_{33}	B_{33}	ξ_{33}	F_{33}
Back	Z_B	v_B	A_{34}	B_{34}	ξ_{34}	F_{34}

Table 3.1

Table showing the force functions, displacement functions and the properties relating to the load media positioned at each of the four faces.

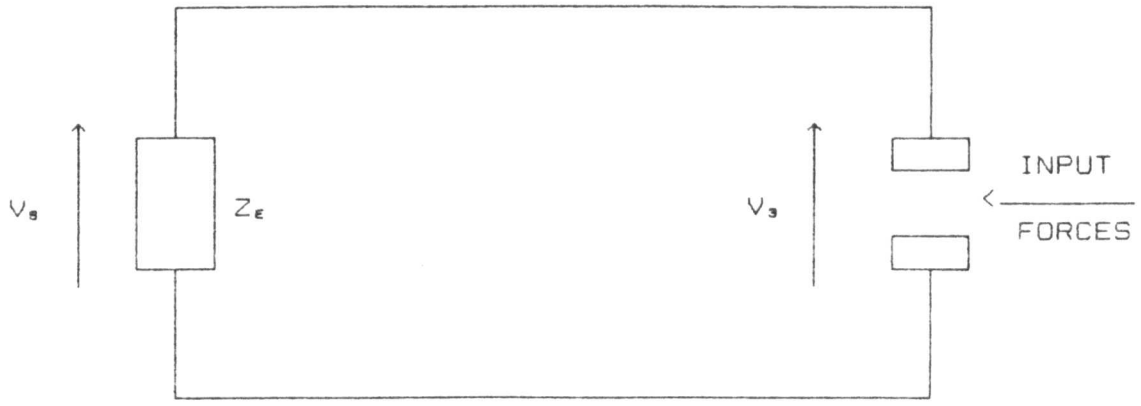

Figure 3.3 Receiver electrical configuration

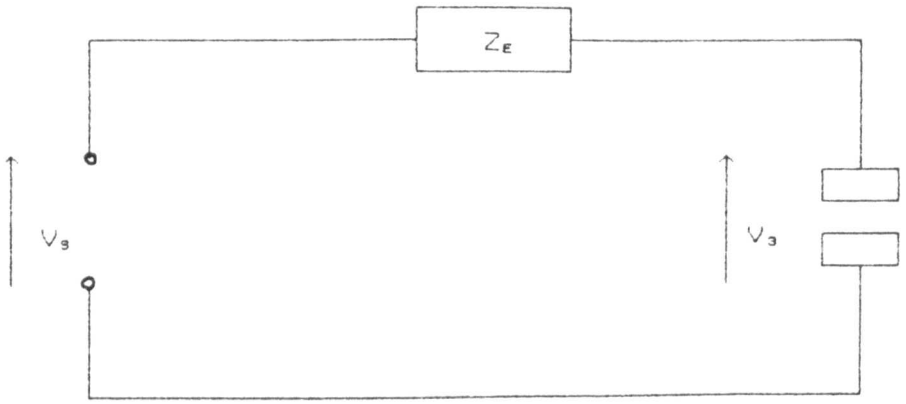

Figure 3.4 Transmitter electrical configuration

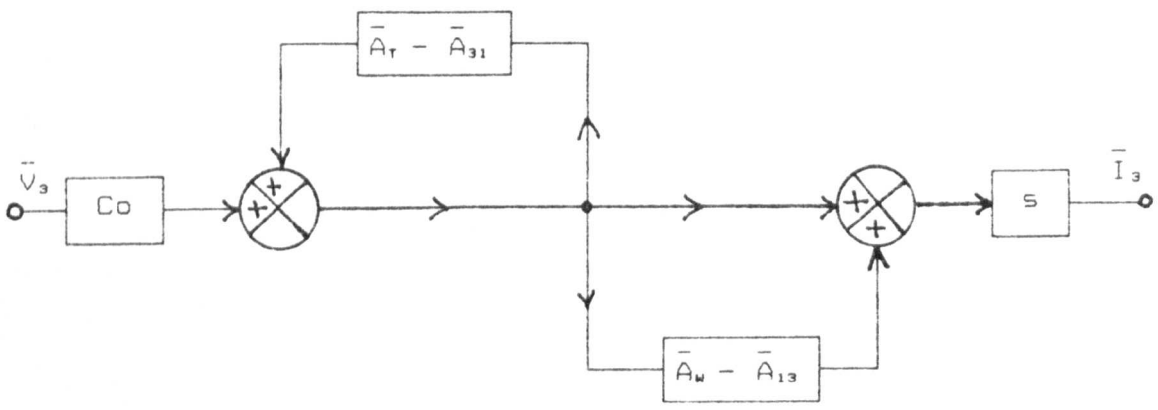

Figure 3.5 Block diagram representation of the transducer electrical admittance.

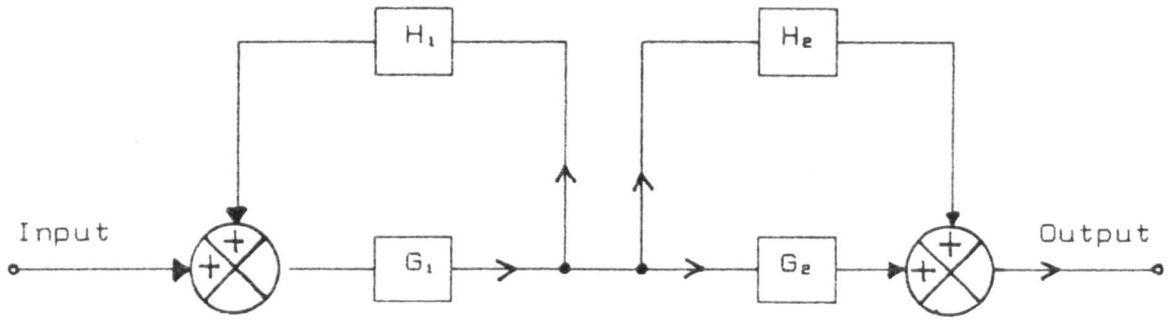

Figure 3.6 Block diagram representation of a cascaded feedback/forward system.

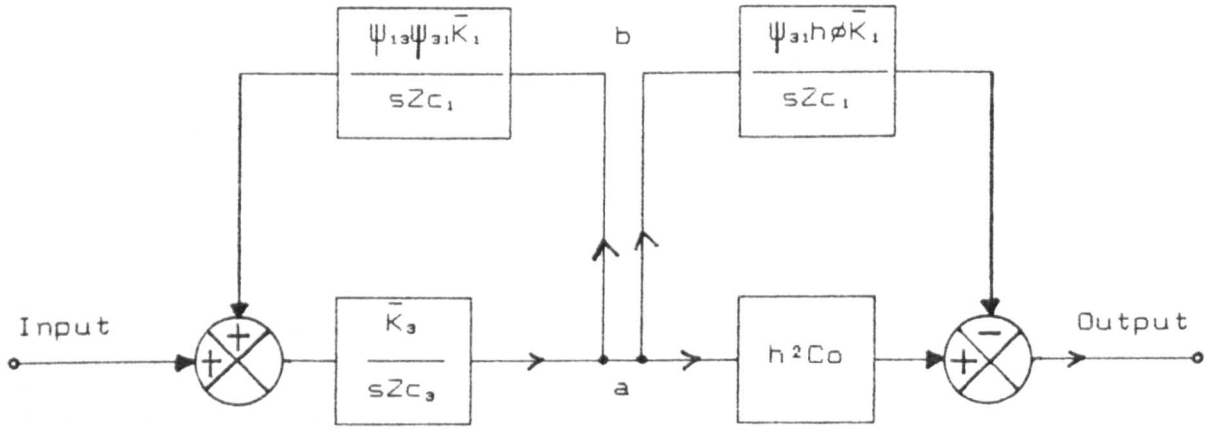

Figure 3.7 Block diagram describing the expression

$[\ \bar{A}_T - \bar{A}_{31}\ ]$.

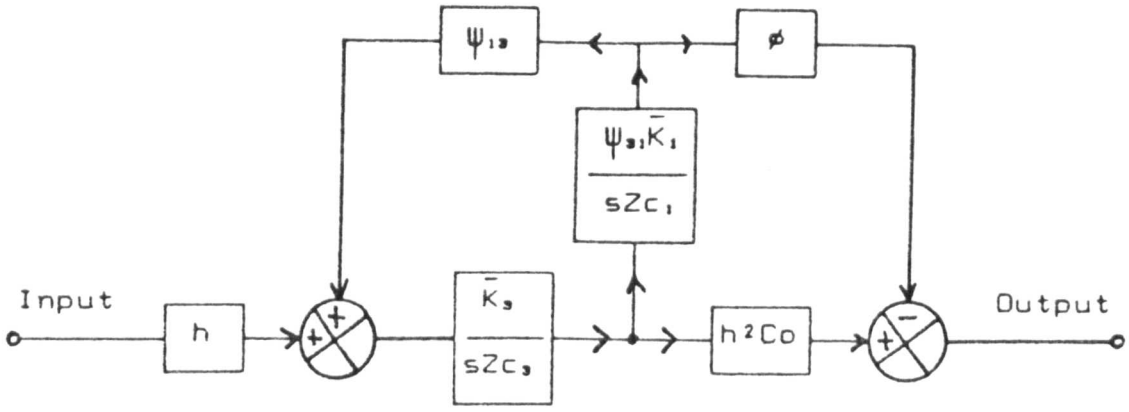

Figure 3.8 Restructured block diagram describing the expression [$\bar{A}_7 - \bar{A}_{31}$].

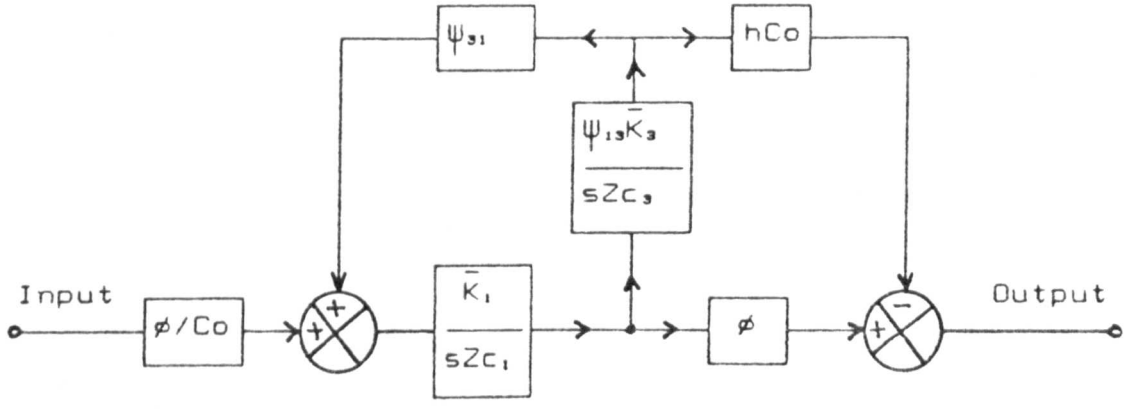

Figure 3.9 Block diagram describing the expression [$\bar{A}_{11} - \bar{A}_{13}$].

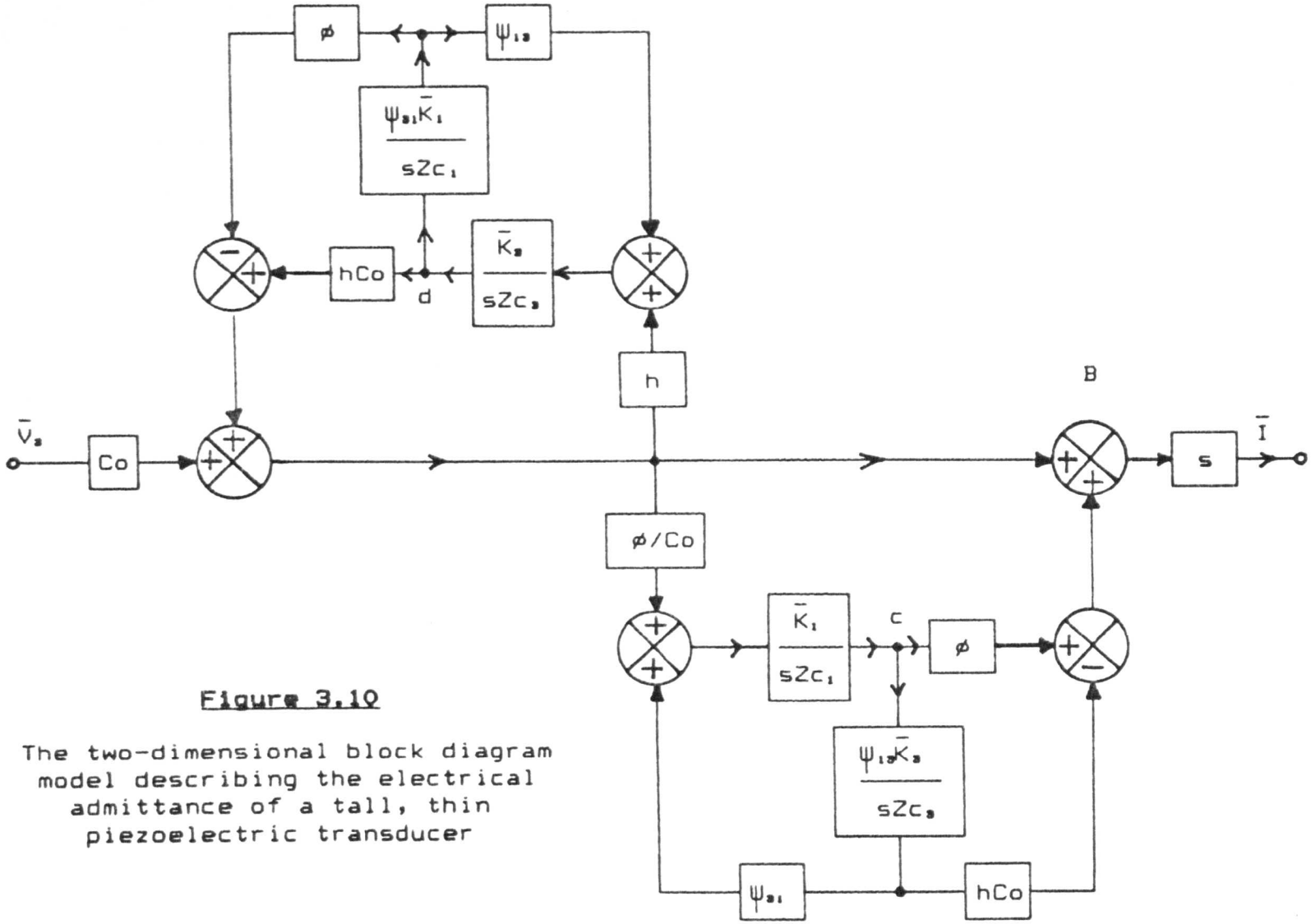

Figure 3.10

The two-dimensional block diagram model describing the electrical admittance of a tall, thin piezoelectric transducer

Property / Material	Density Kg/m^2	Y^D_{11} $*10^{10}$ N/m^2	Y^D_{13} $*10^{10}$ N/m^2	Y^D_{33} $*10^{10}$ N/m^2	h_{13} $*10^8$ N/C	h_{33} $*10^8$ N/C	ϵ^T_{33}
Lithium Niobate	4700	21.9	7.6	25.2	8	51	30
Lead Zirconate Titanate PZT-5A	7750	12.6	6.52	14.7	-7.3	21.5	800
PolyVinylidene--flouride PVDF	1780	*	*	0.86	*	16.5	8

* Not available

Table 3.2

A Comparison of the material and piezoelectric properties of a selection of different transducer materials.

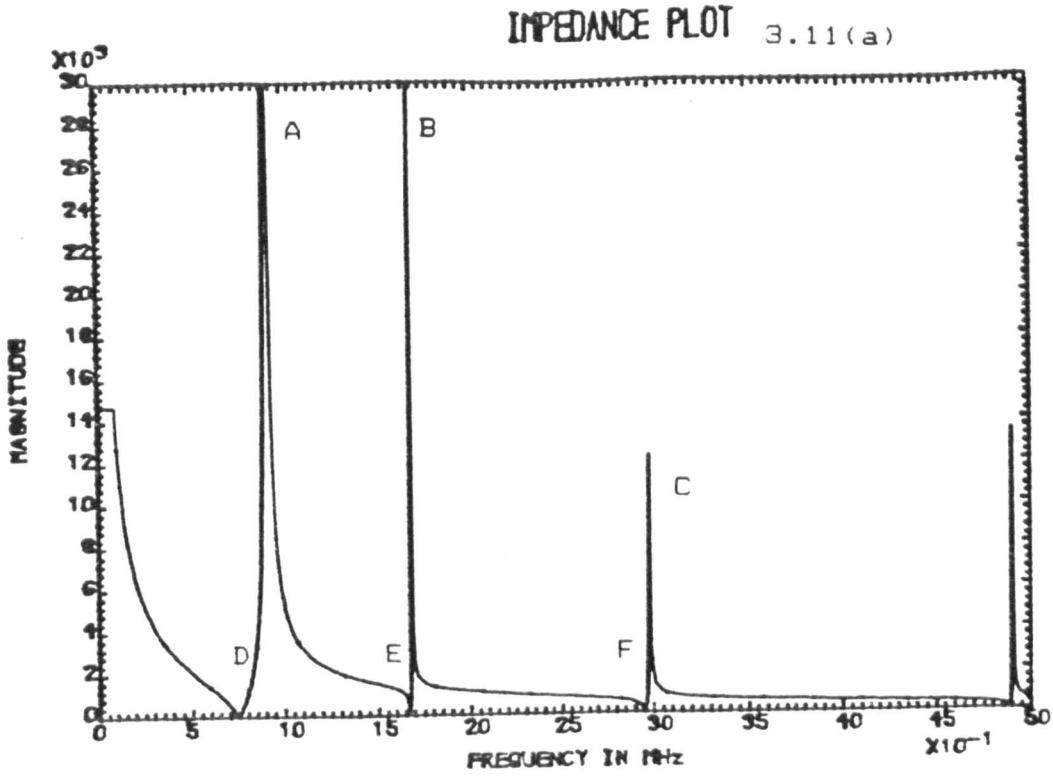

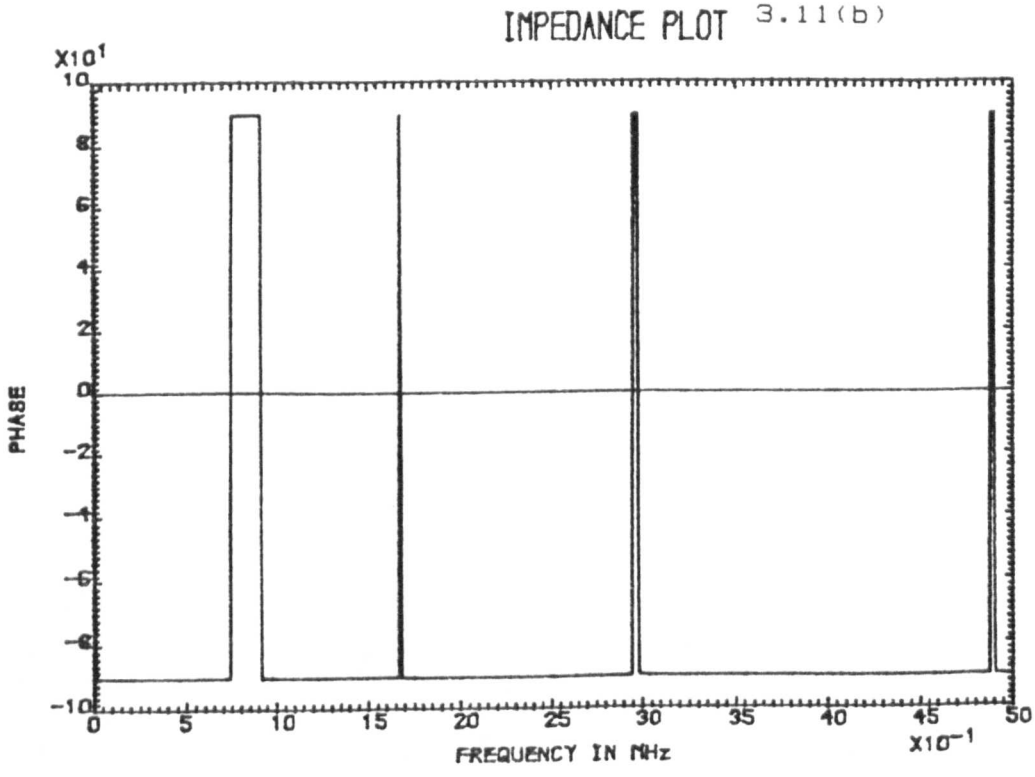

Figure 3.11 Spectral magnitude and phase characteristics of a typical electrical impedance function.

3.12(a)

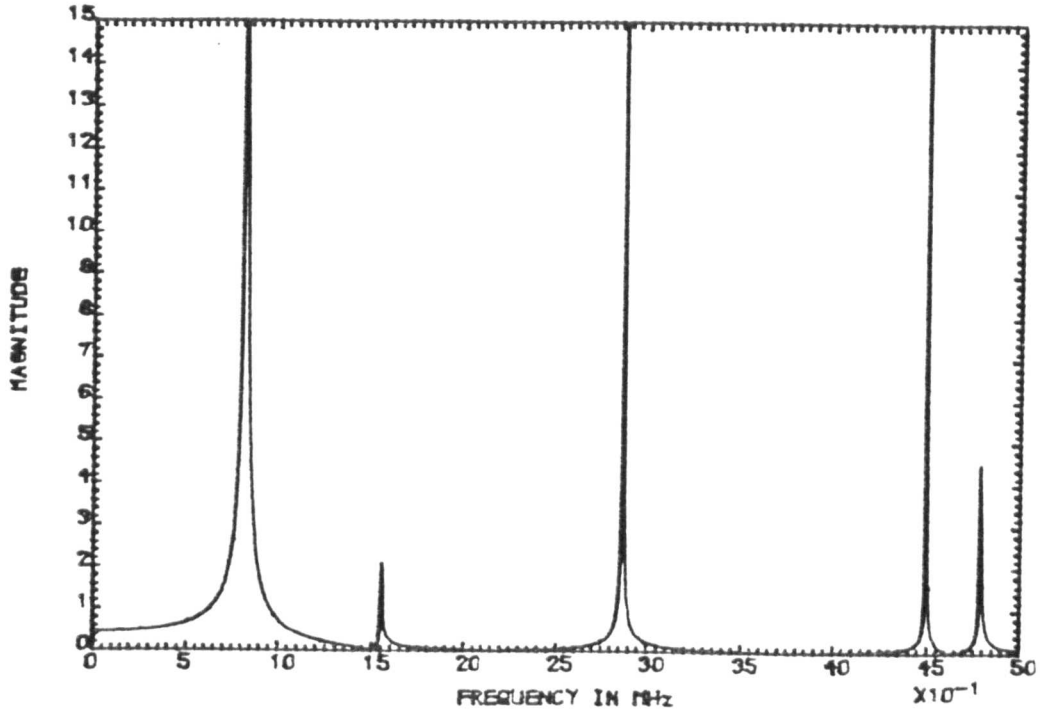

3.12(b)

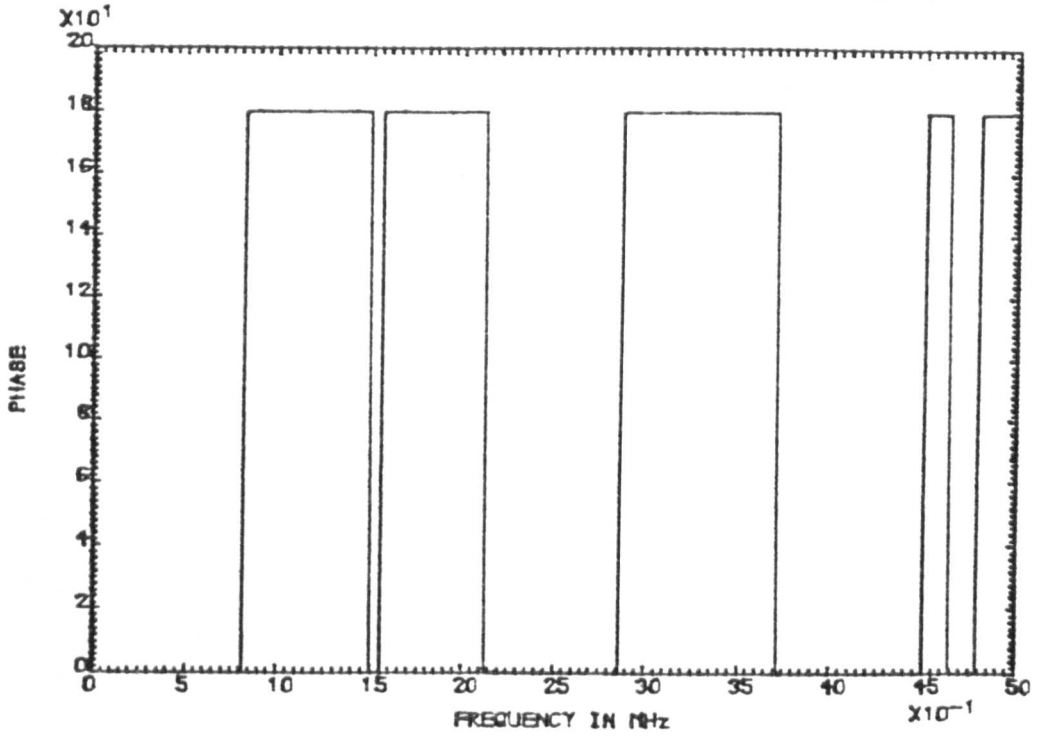

Figure 3.12 Spectral behaviour of the equivilent two-dimensional feedback factor under mechanically unloaded conditions.

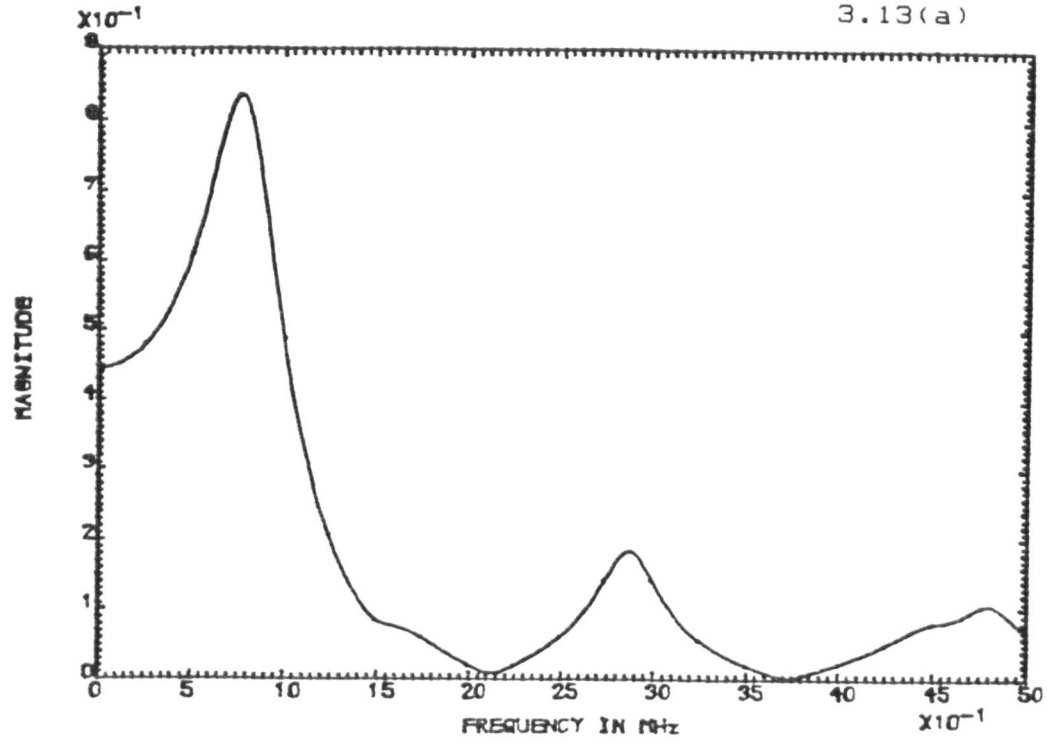

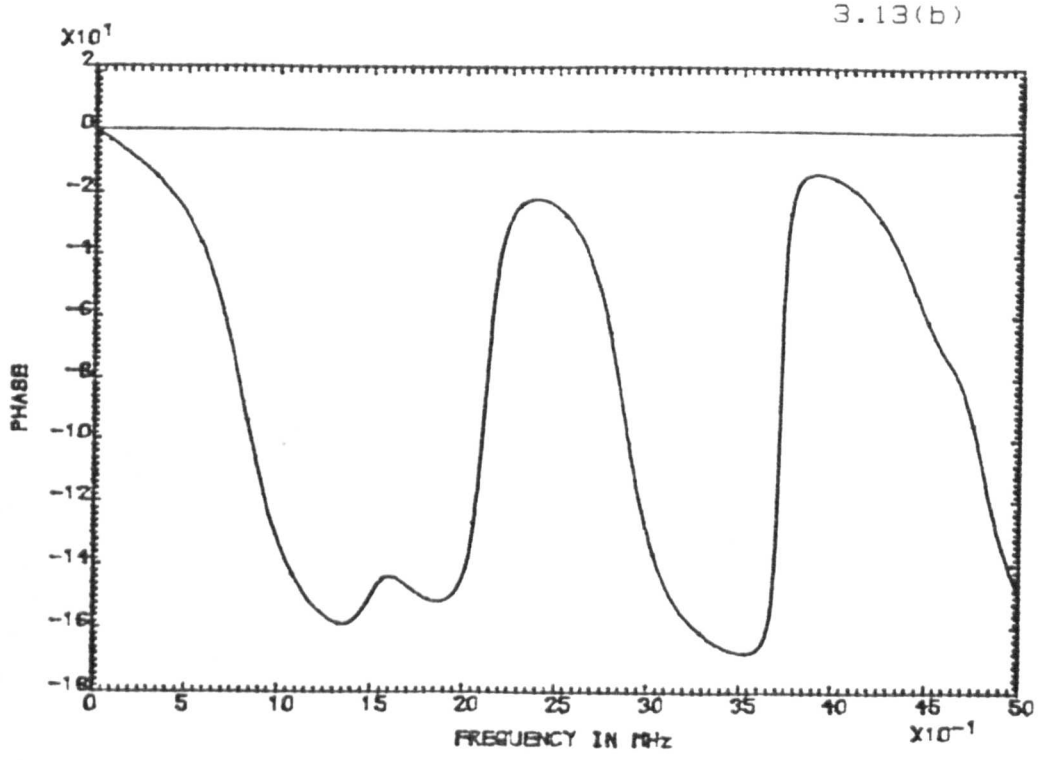

Figure 3.13 Spectral behaviour of the equivilent two-dimensional feedback factor under mechanically loaded conditions.

3.14(a)

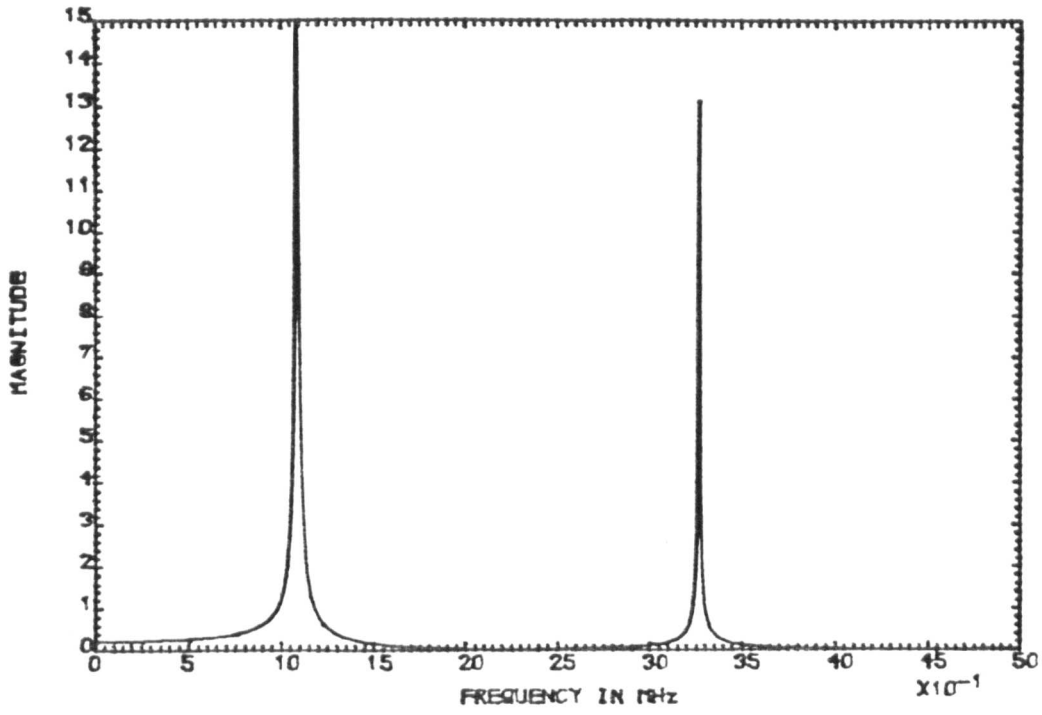

3.14(b)

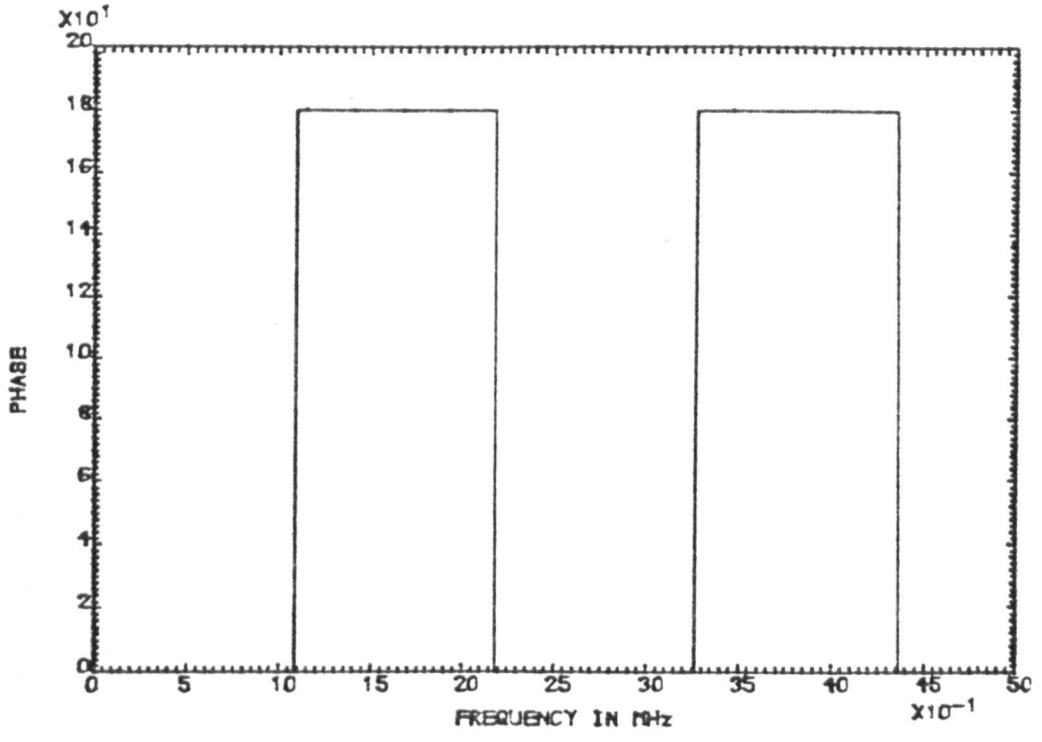

Figure 3.14 Spectral behaviour of the mechanically free unidimensional thickness mode feedback factor.

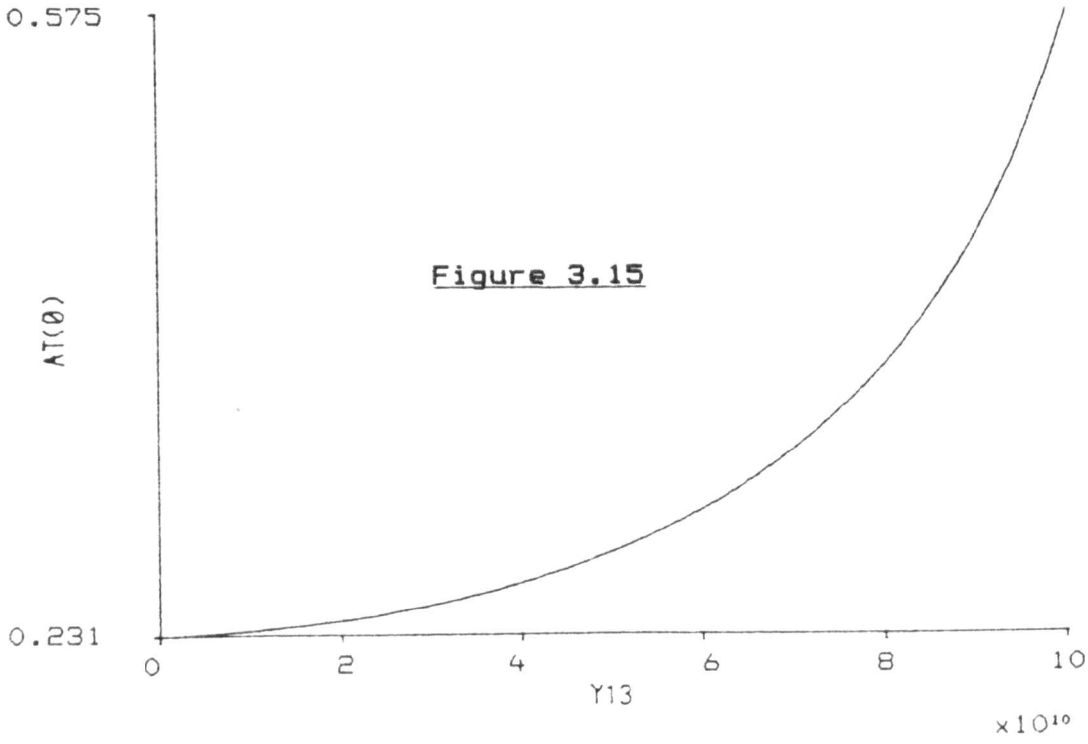

Figure 3.15

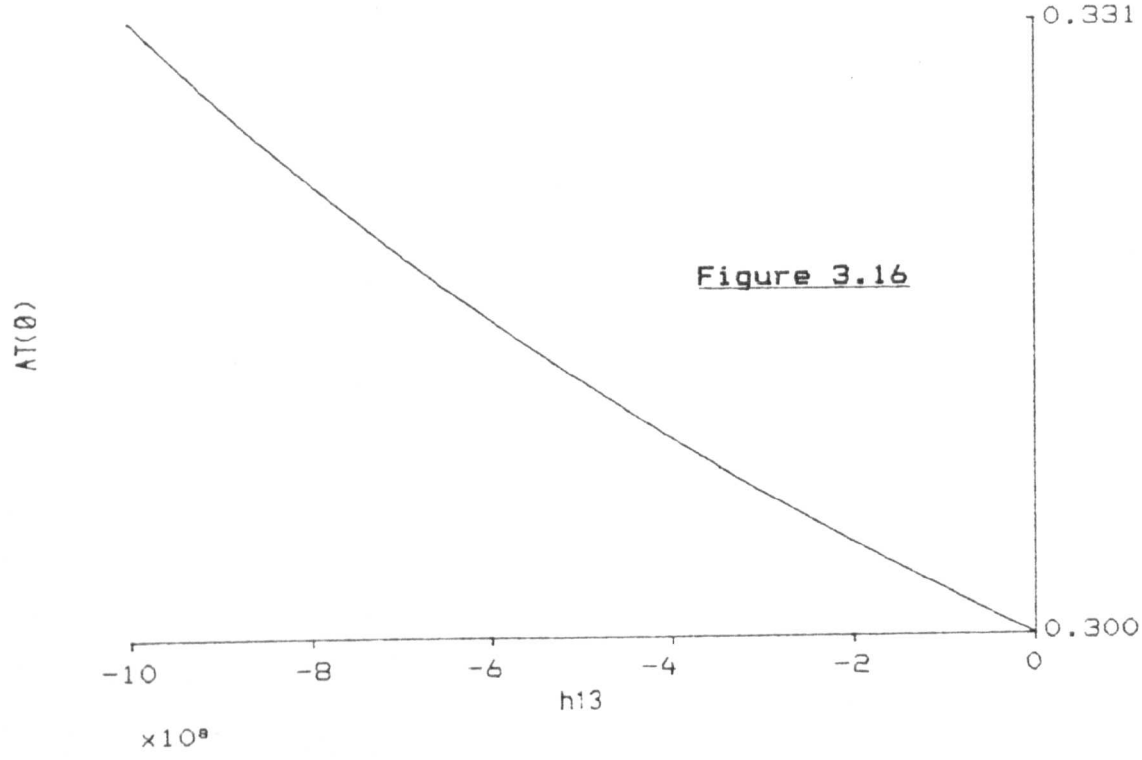

Figure 3.16

Variation of $\bar{A}_T(0)$ with the material parameters Y_{13} and h_{13}.

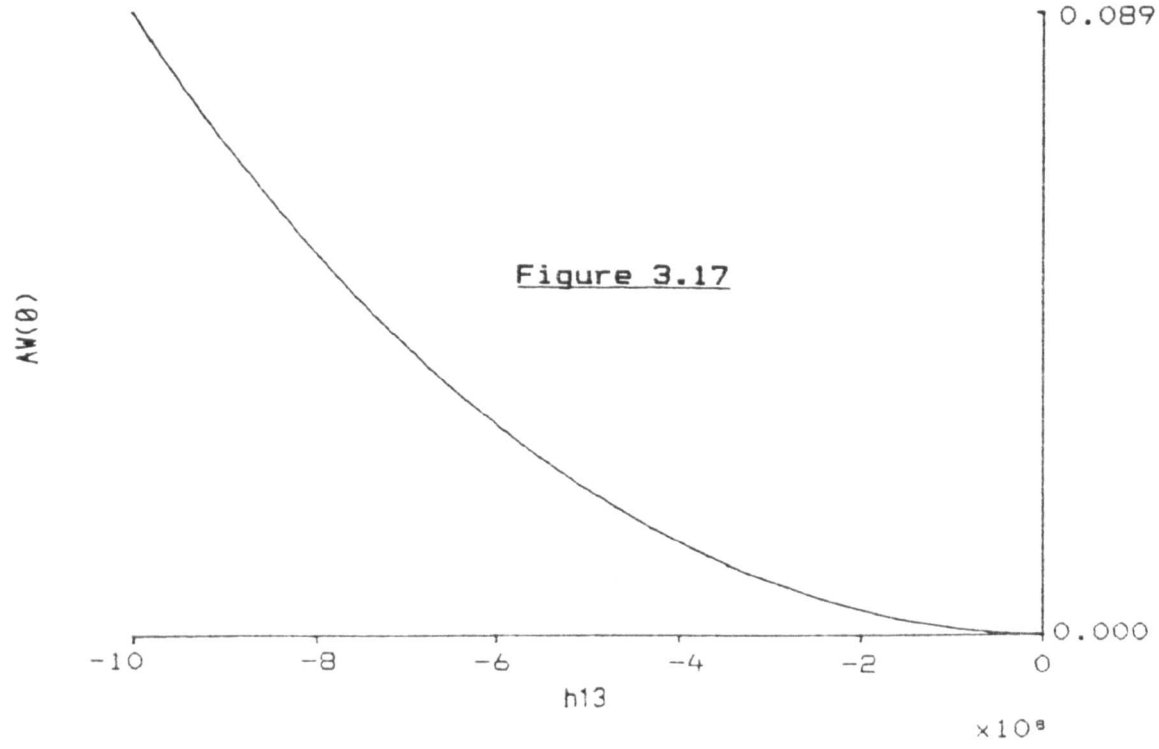

Figure 3.17

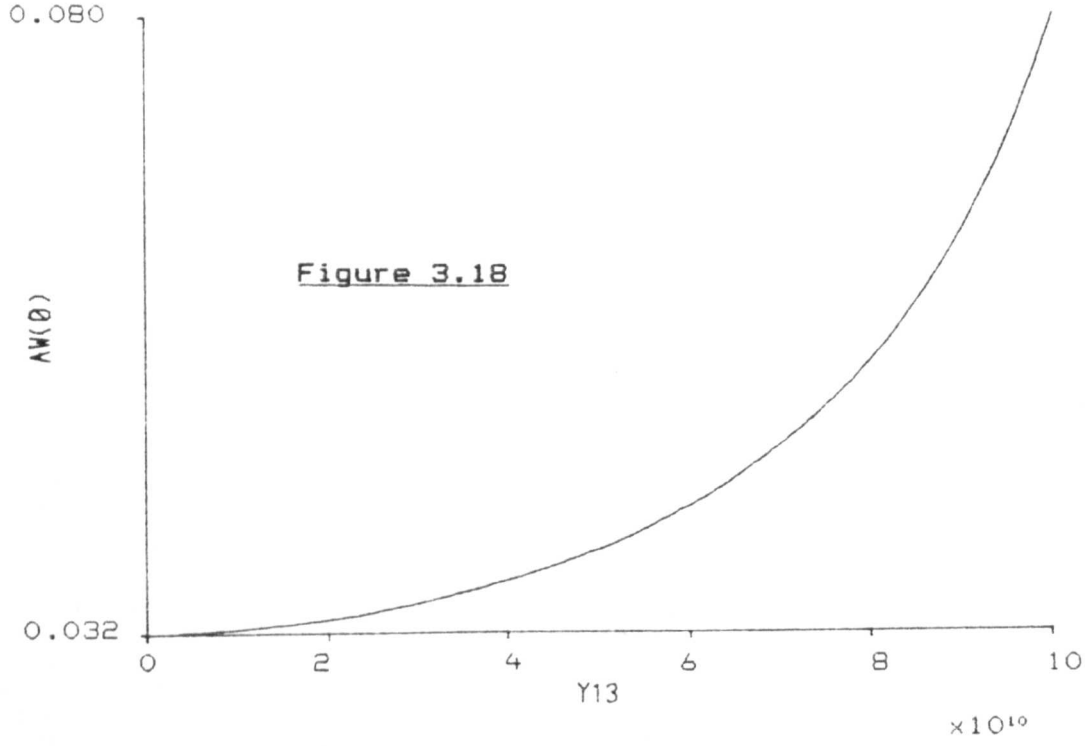

Figure 3.18

Variation of $\bar{A}_w(0)$ with the material parameters h_{13} and Y_{13}.

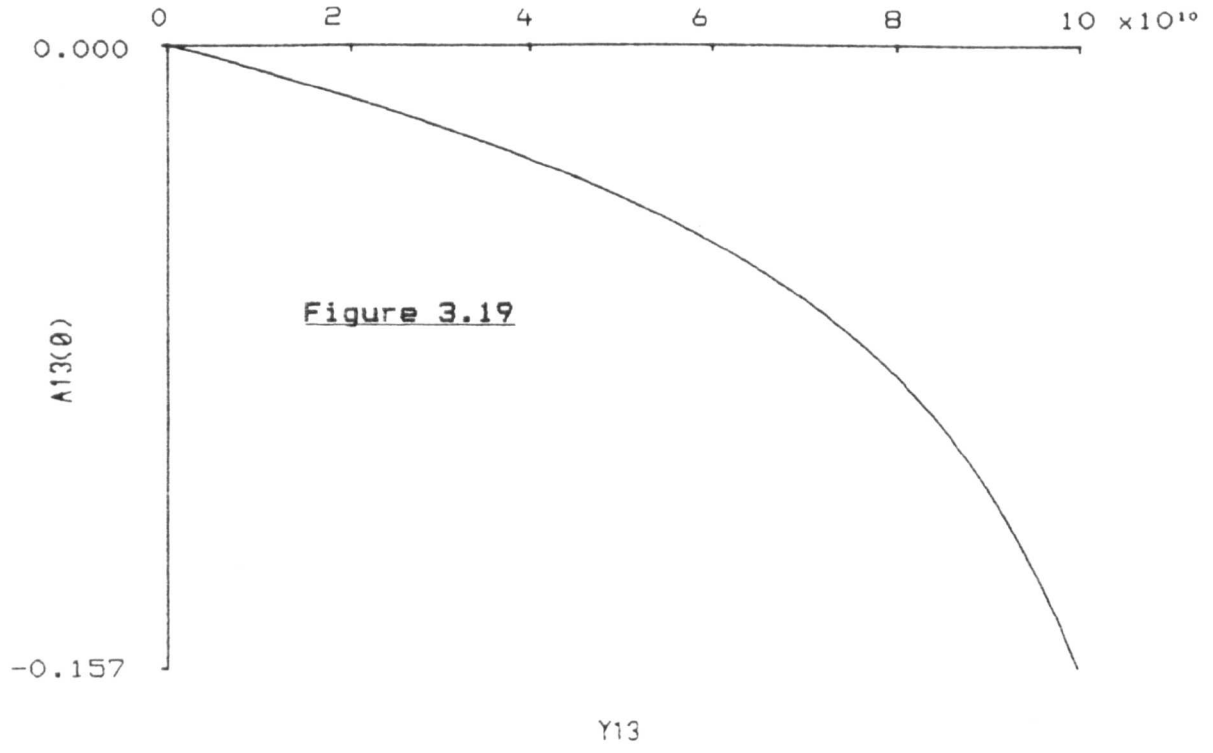

Figure 3.19

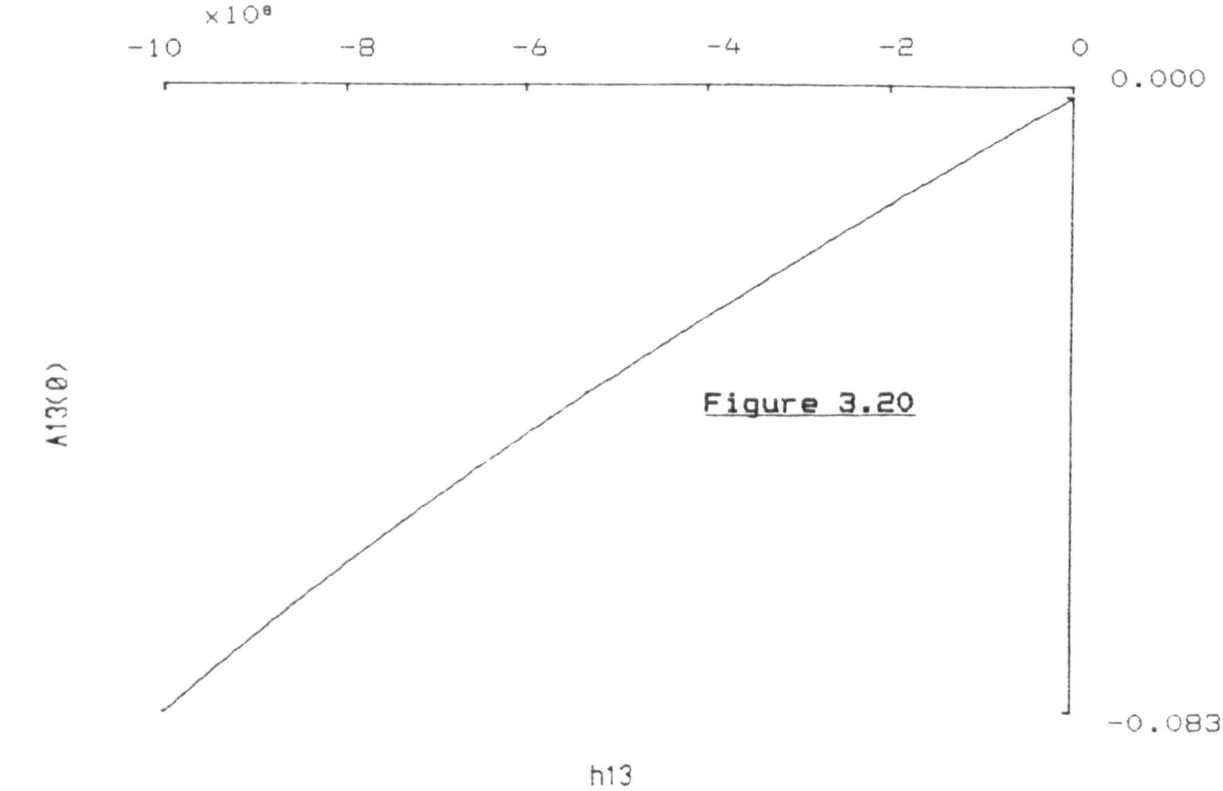

Figure 3.20

Variation of $\bar{A}_{13}(0)$ with the material parameters Y_{13} and h_{13}.

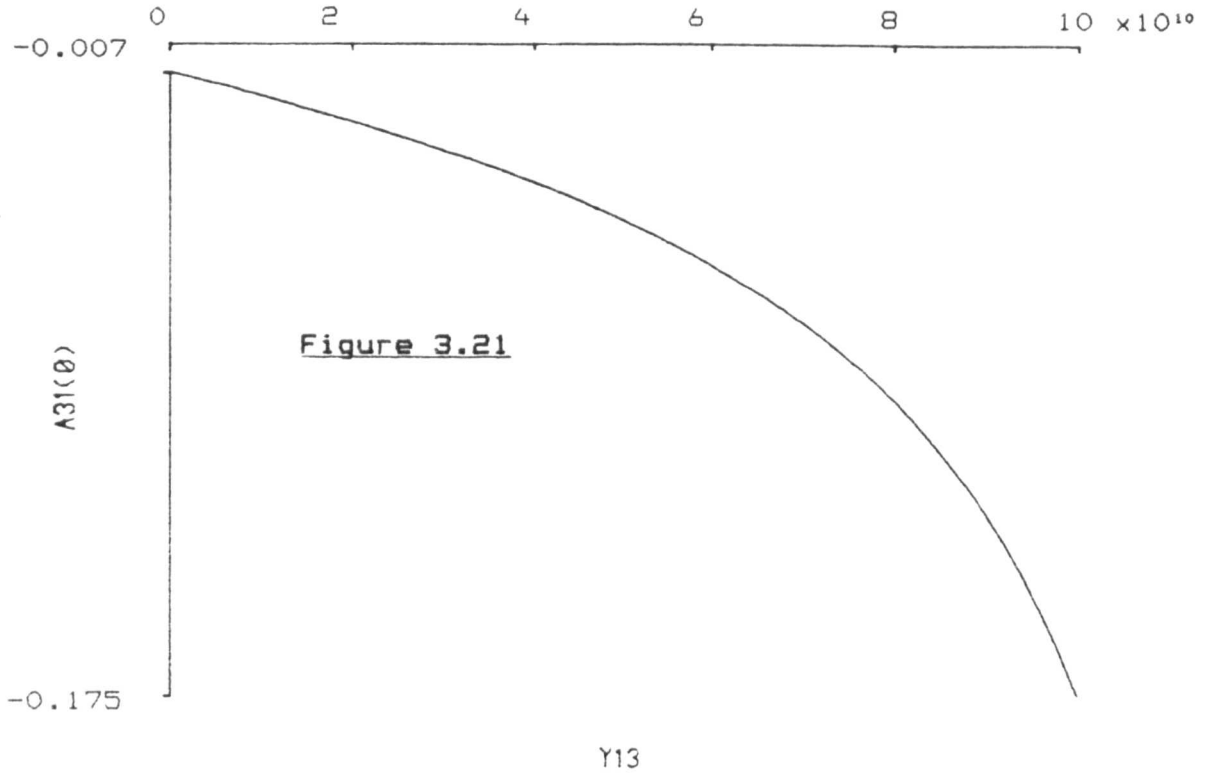

Figure 3.21

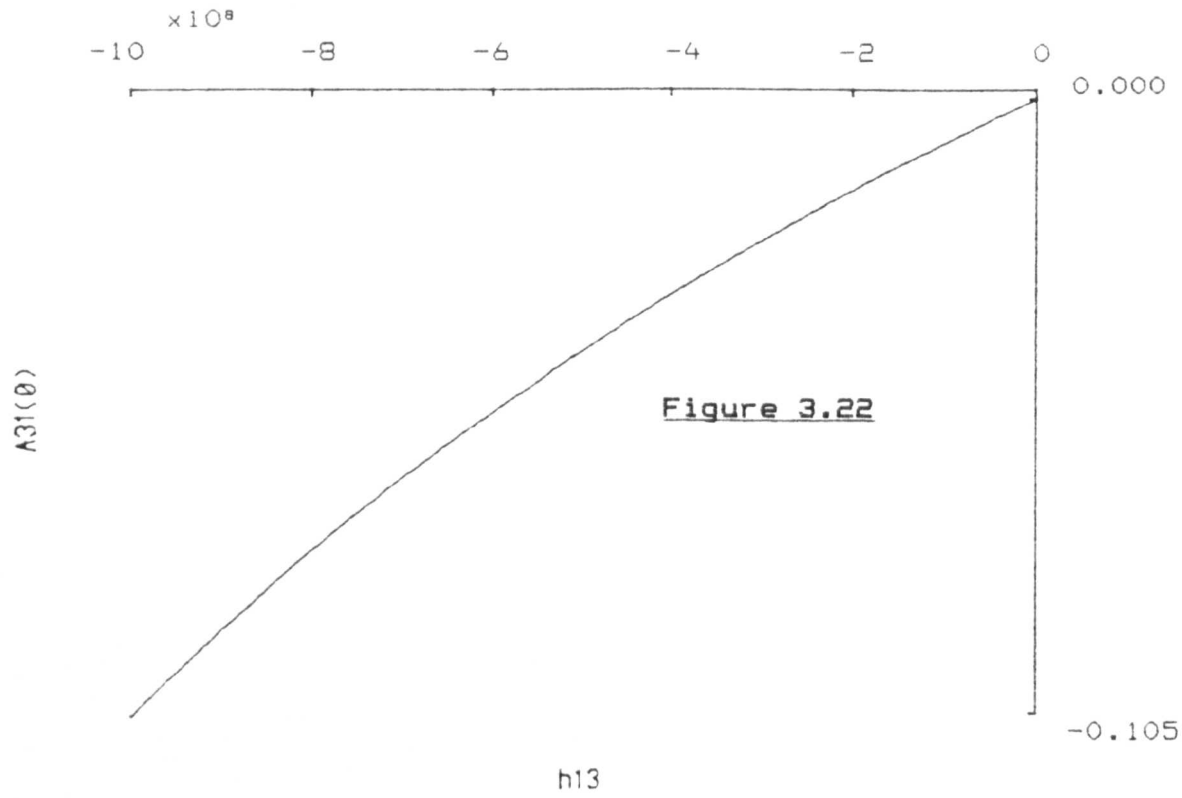

Figure 3.22

Variation of $\bar{A}_{31}(0)$ with the material parameters Y_{13} and h_{13}.

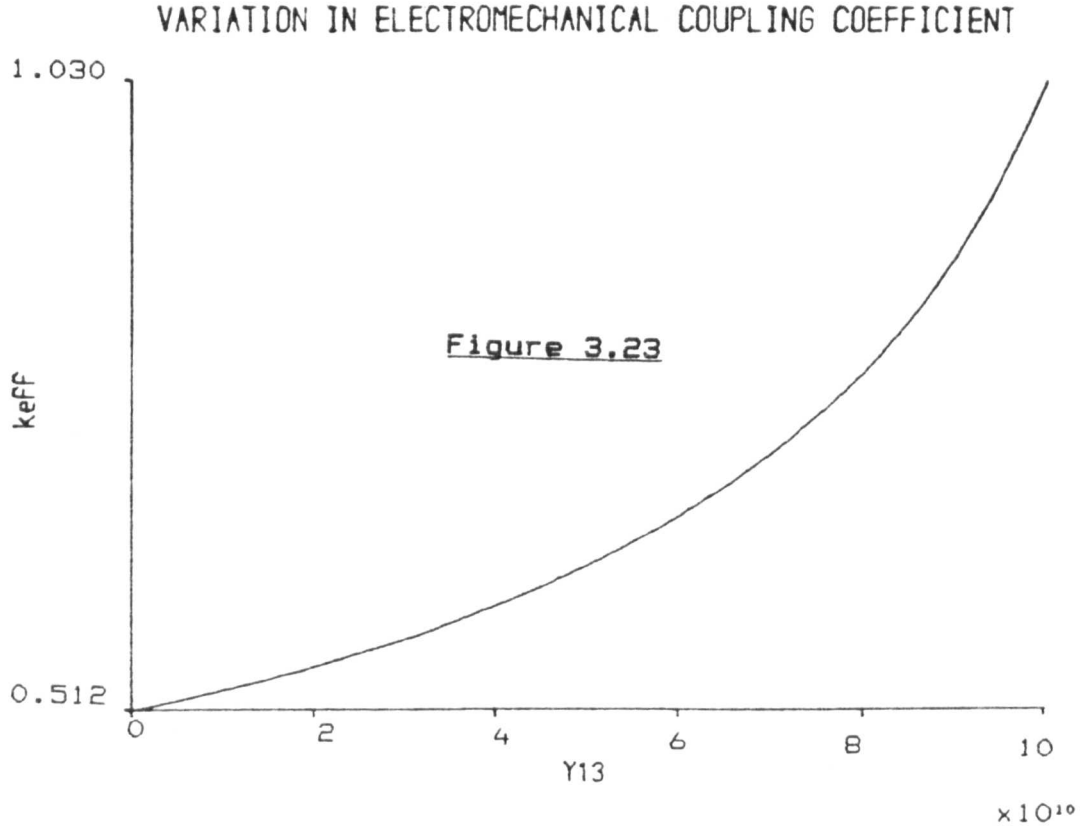

Figure 3.23

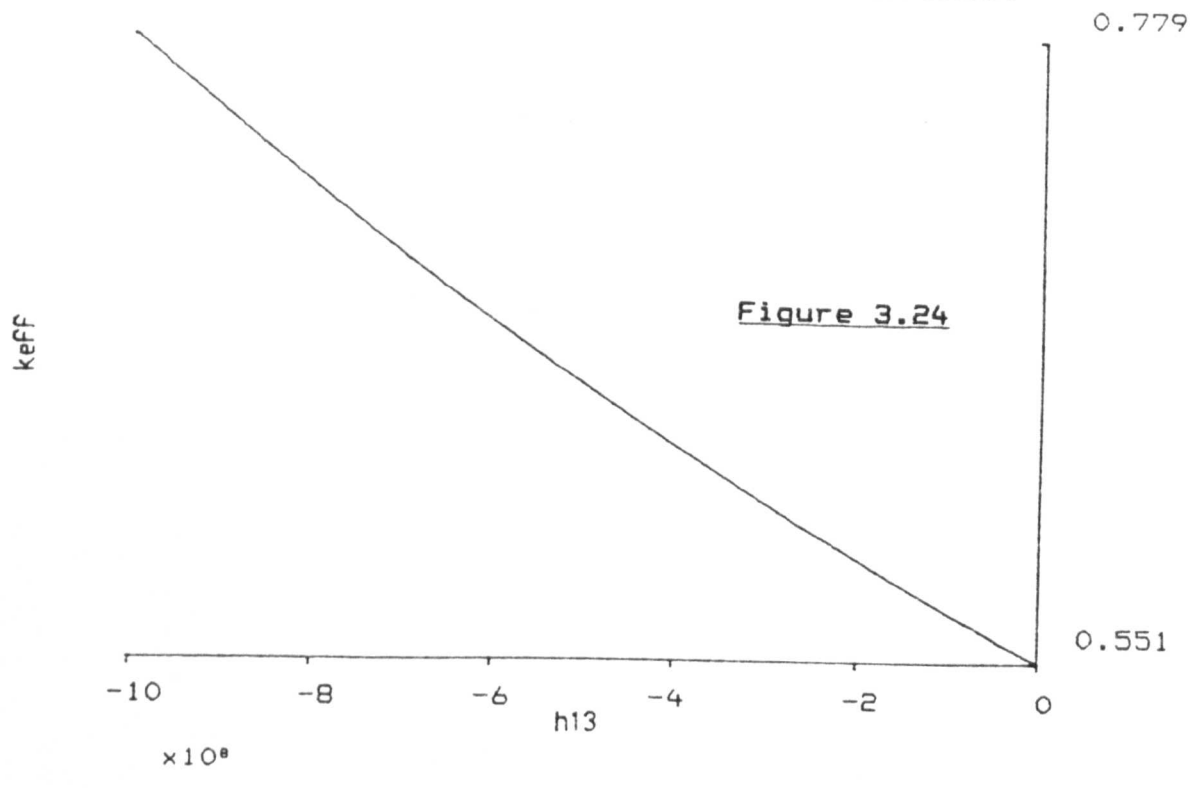

Figure 3.24

Variation of k_{EFF} with the material parameters Y_{13} and h_{13}.

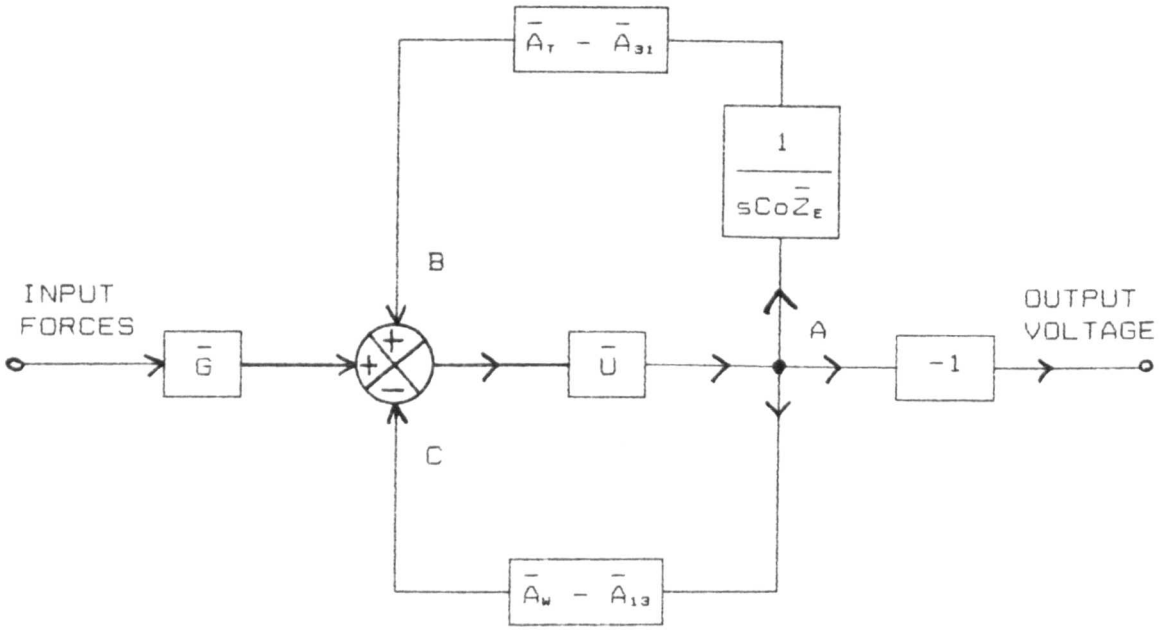

Figure 3.25 Block diagram representation of a two-dimensional piezoelectric receiver.

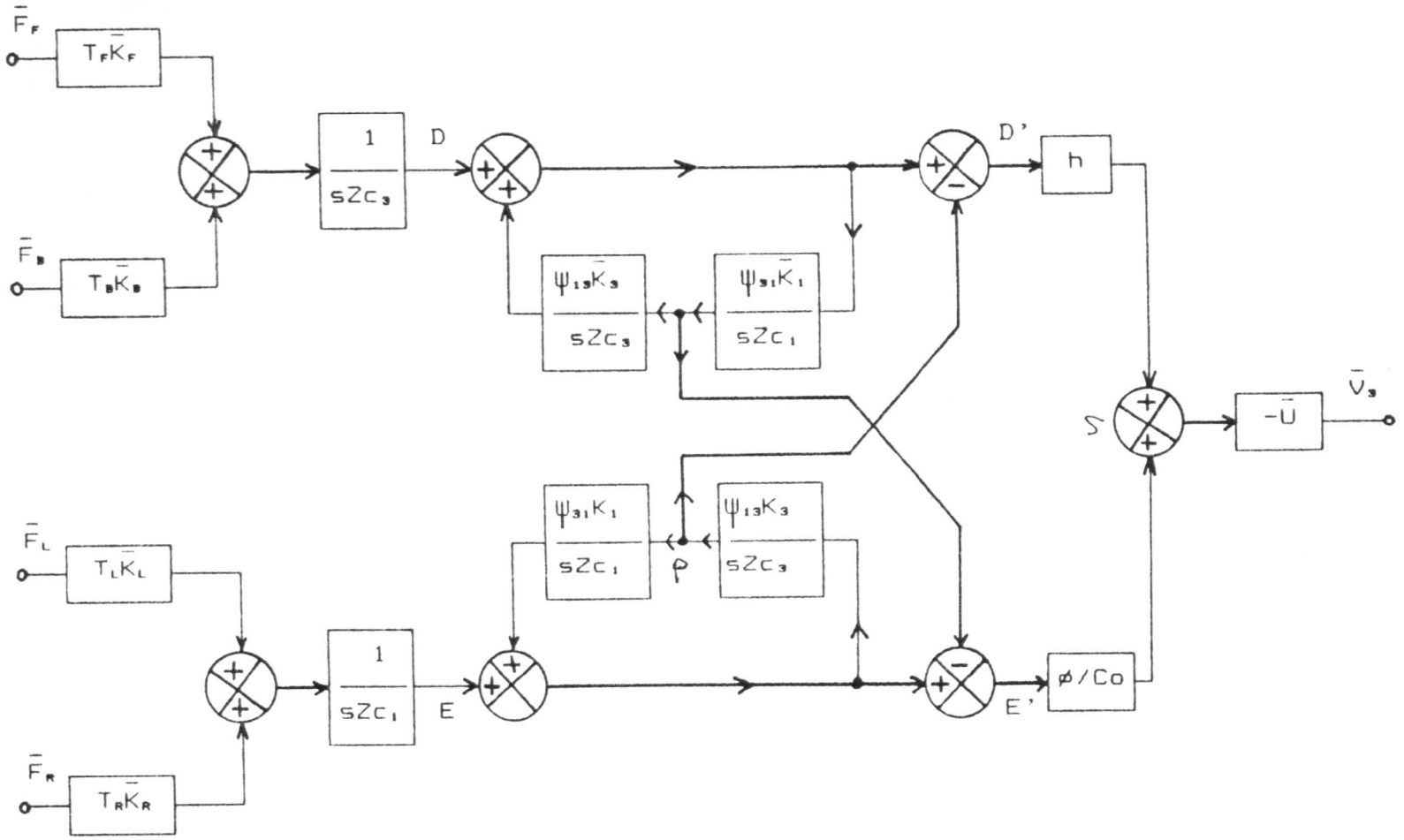

Figure 3.26 Block diagram representation of the forward path of a two-dimensional piezoelectric receiver.

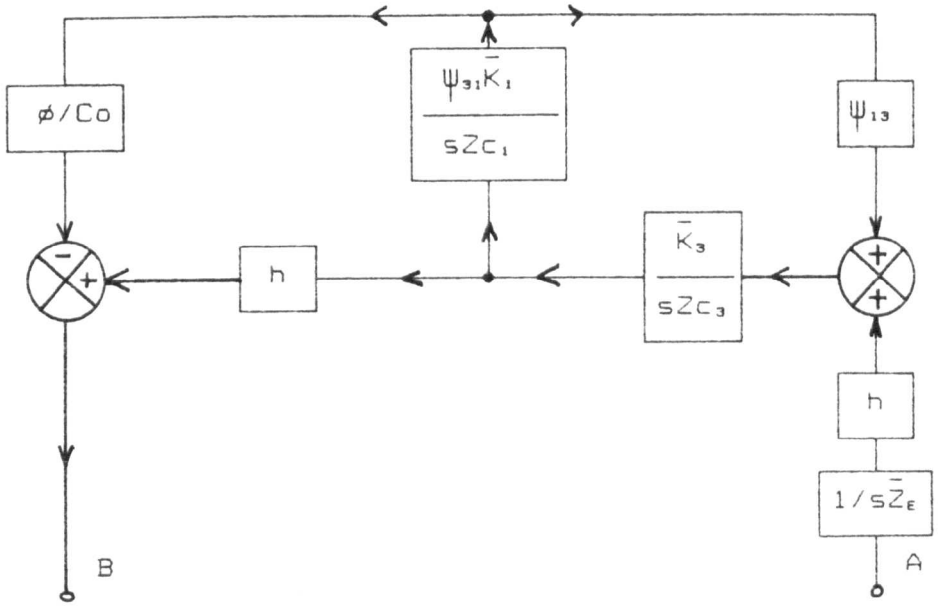

Figure 3.27 Feedback loop describing the function $[\bar{A}_T - \bar{A}_{31}]$

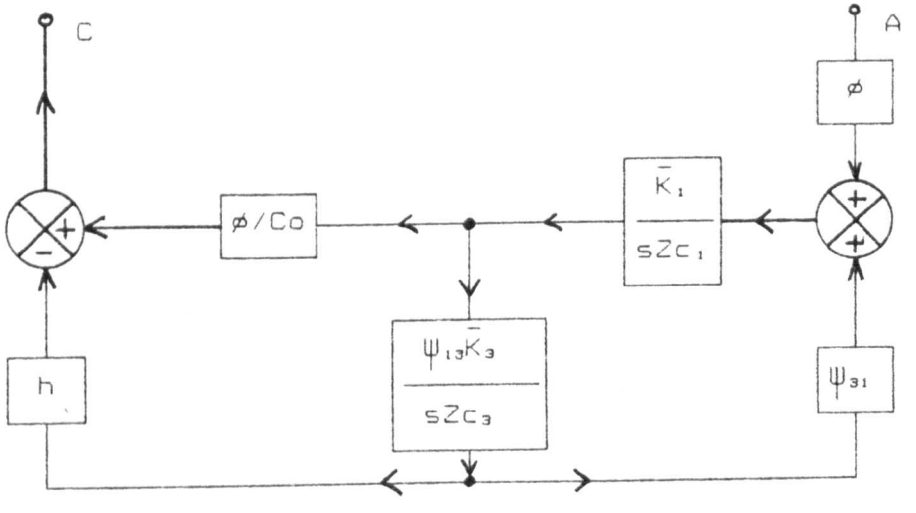

Figure 3.28 Feedback loop describing the function $[\bar{A}_W - \bar{A}_{13}]$

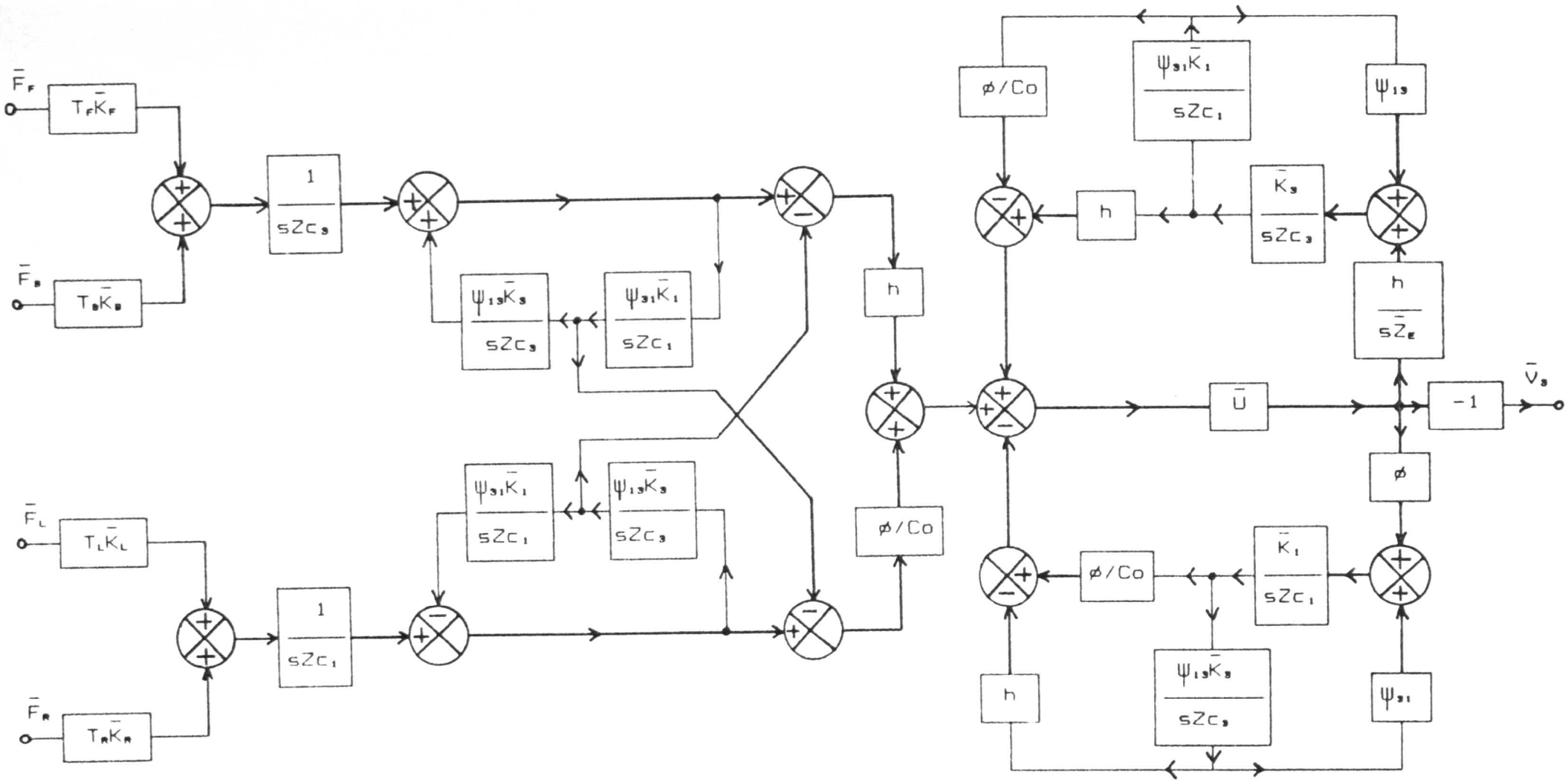

Figure 3.29 Block diagram model of a two-dimensional piezoelectric receiver.

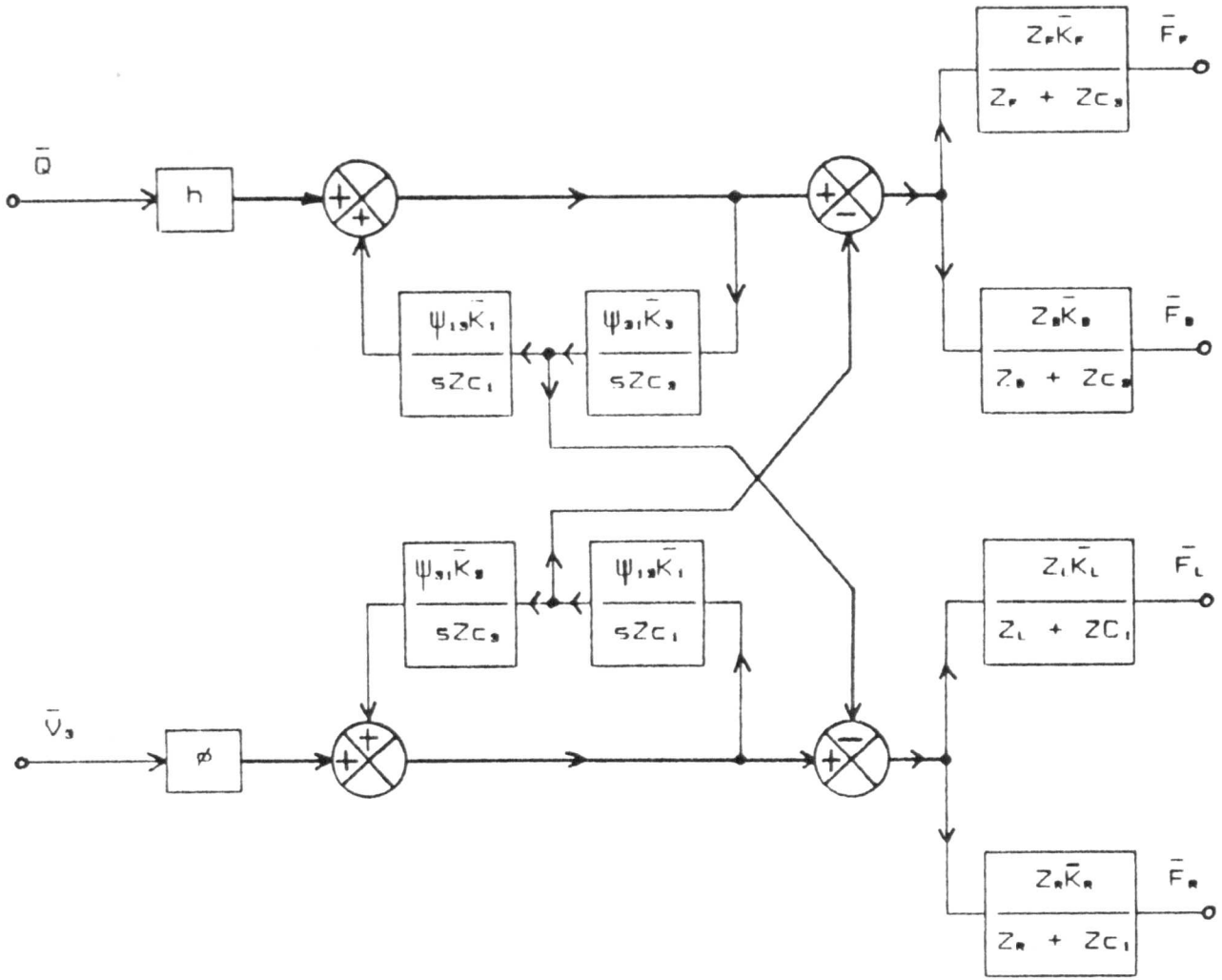

Figure 3.30 Block diagram model of a two-dimensional piezoelectric transmitter

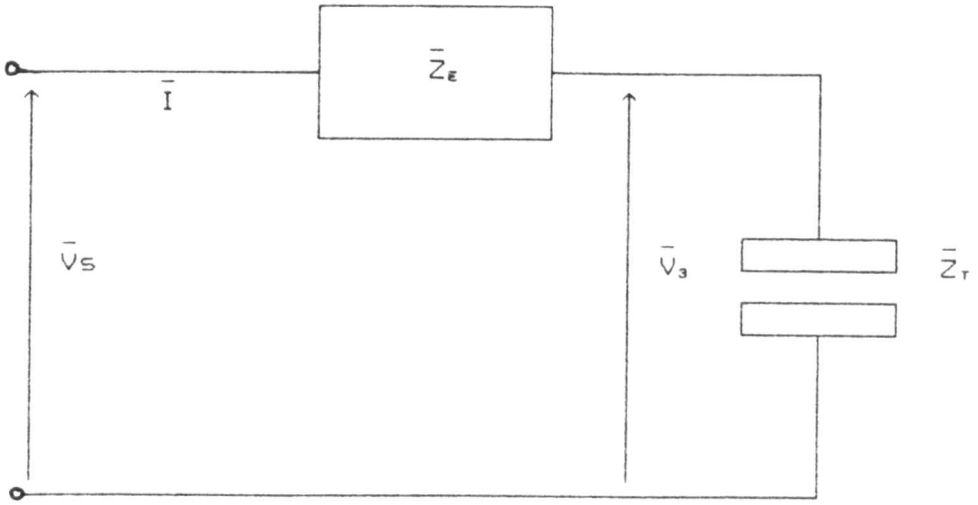

Figure 3.31 Transmitter electrical configuration

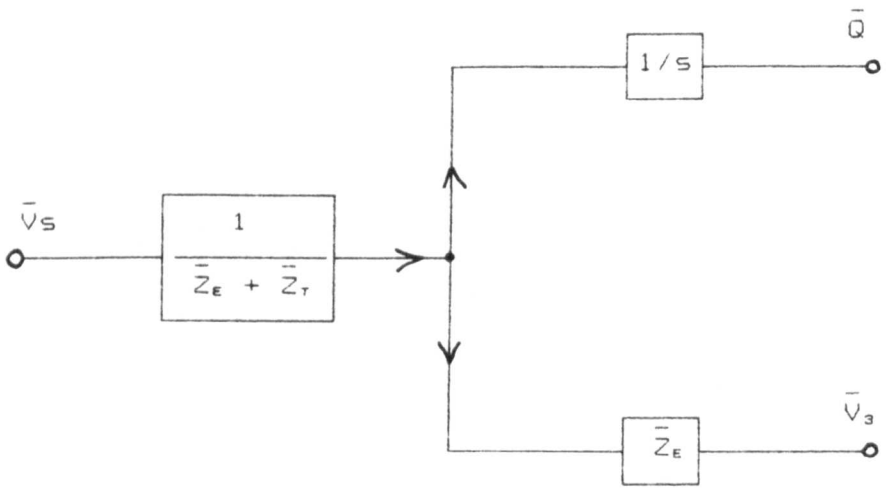

Figure 3.32 Block diagram representation of the electrical behaviour of a loaded piezoelectric transmitter.

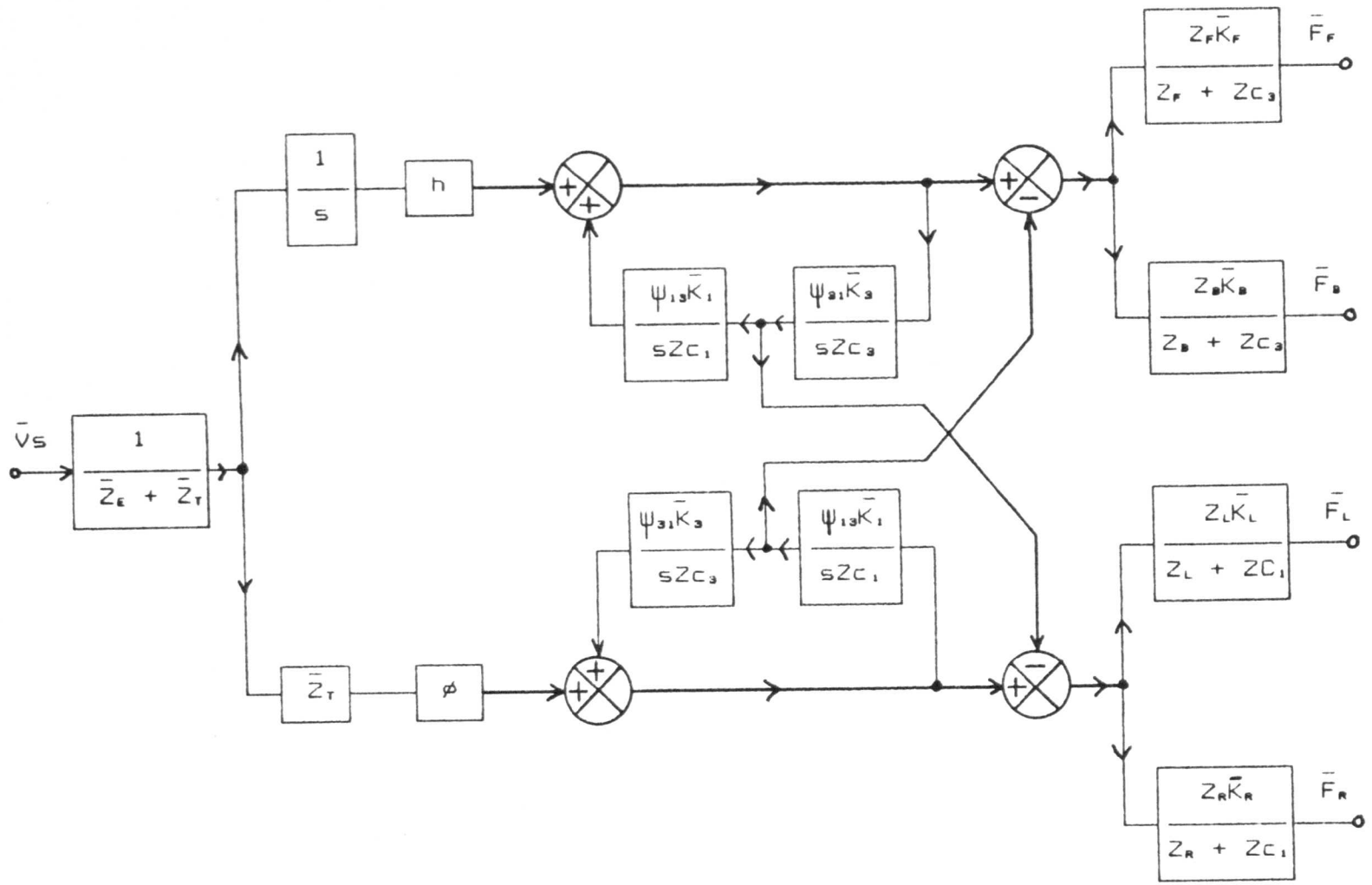

Figure 3.33 Block diagram model of a two-dimensional piezoelectric transmitter

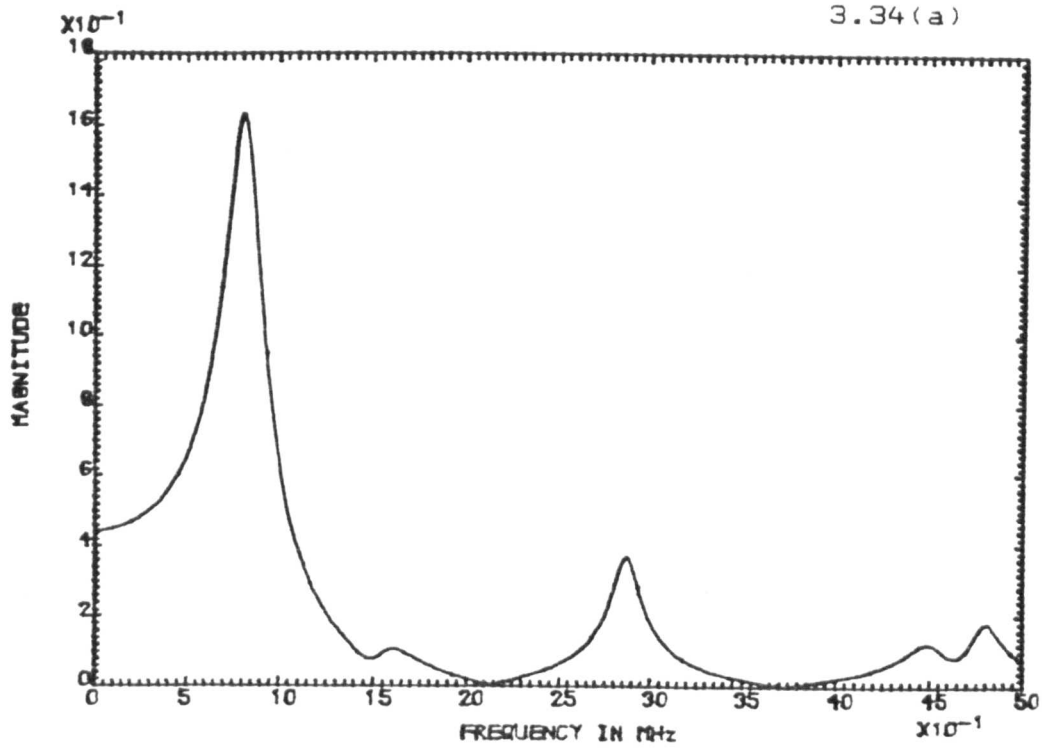

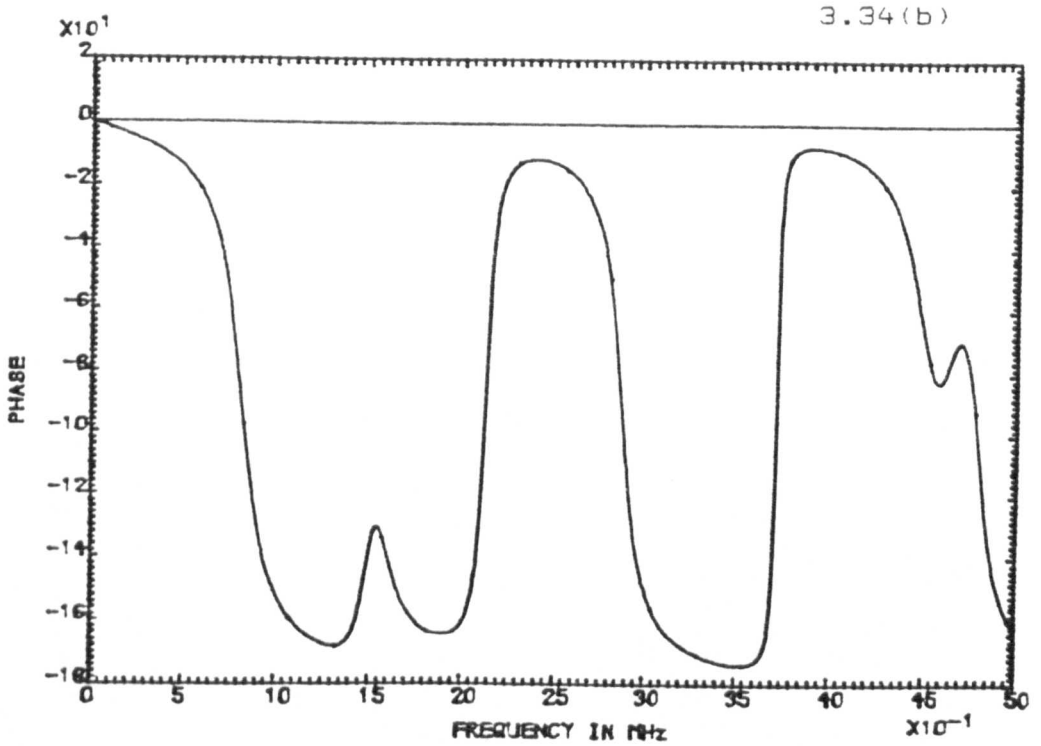

Figure 3.34 Spectral characteristics of the equivilent two-dimensional feedback factor under conditions of light mechanical damping.

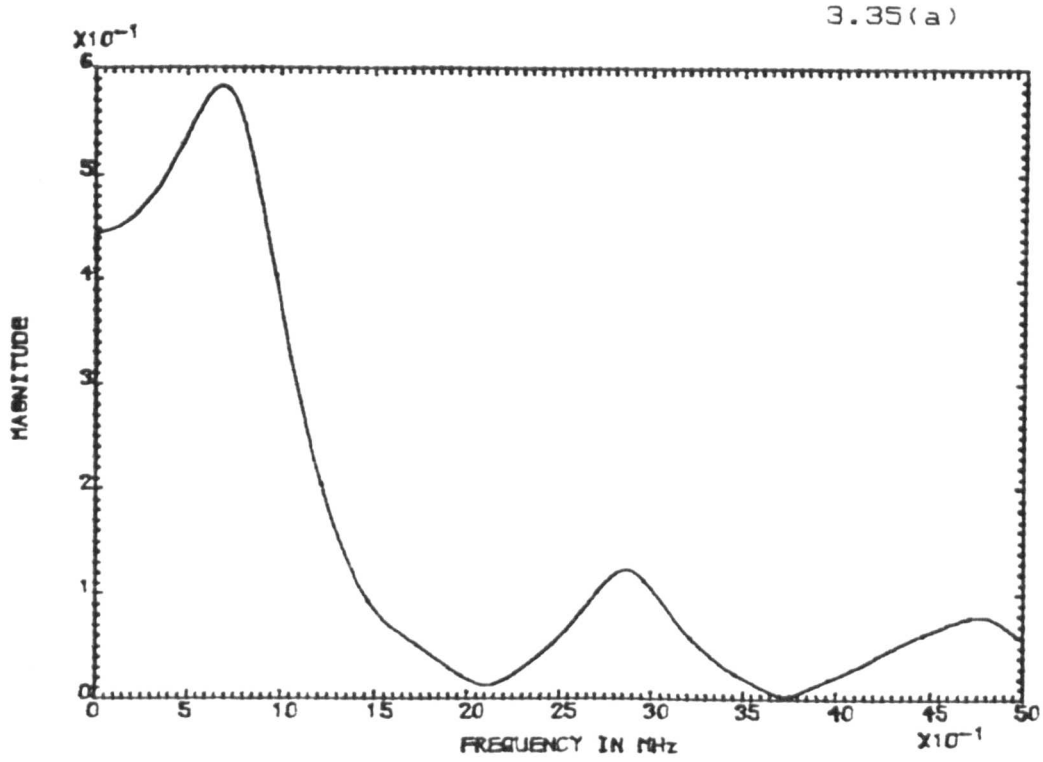

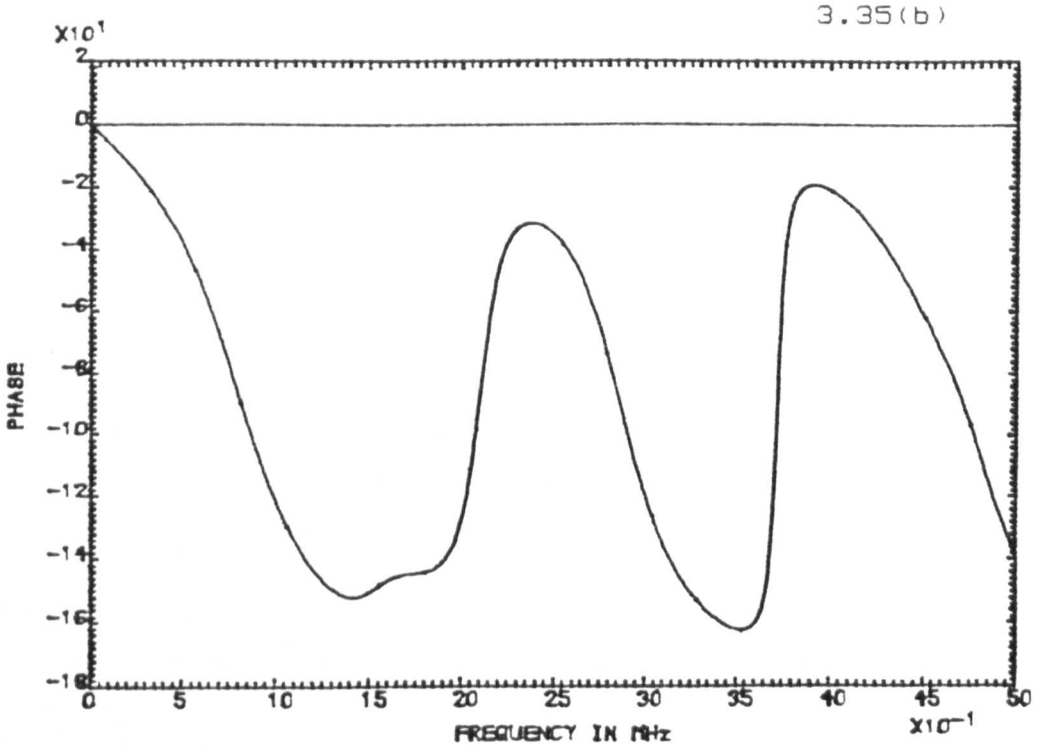

Figure 3.35 Spectral characteristics of the equivilent two-dimensional feedback factor under conditions of medium mechanical damping.

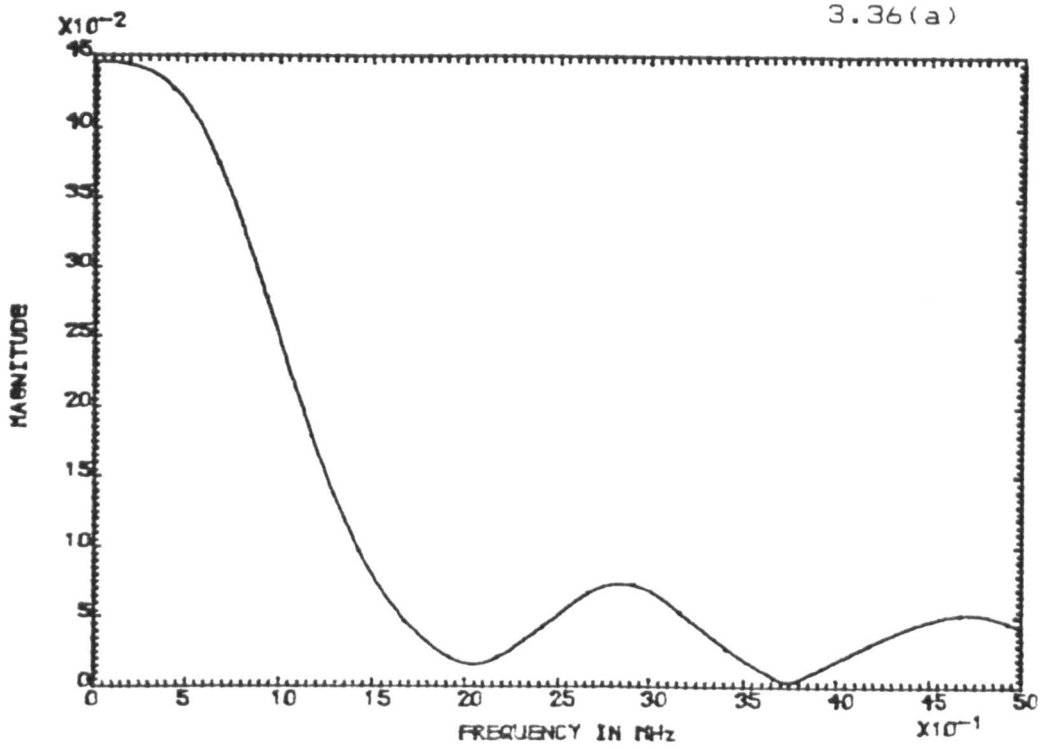

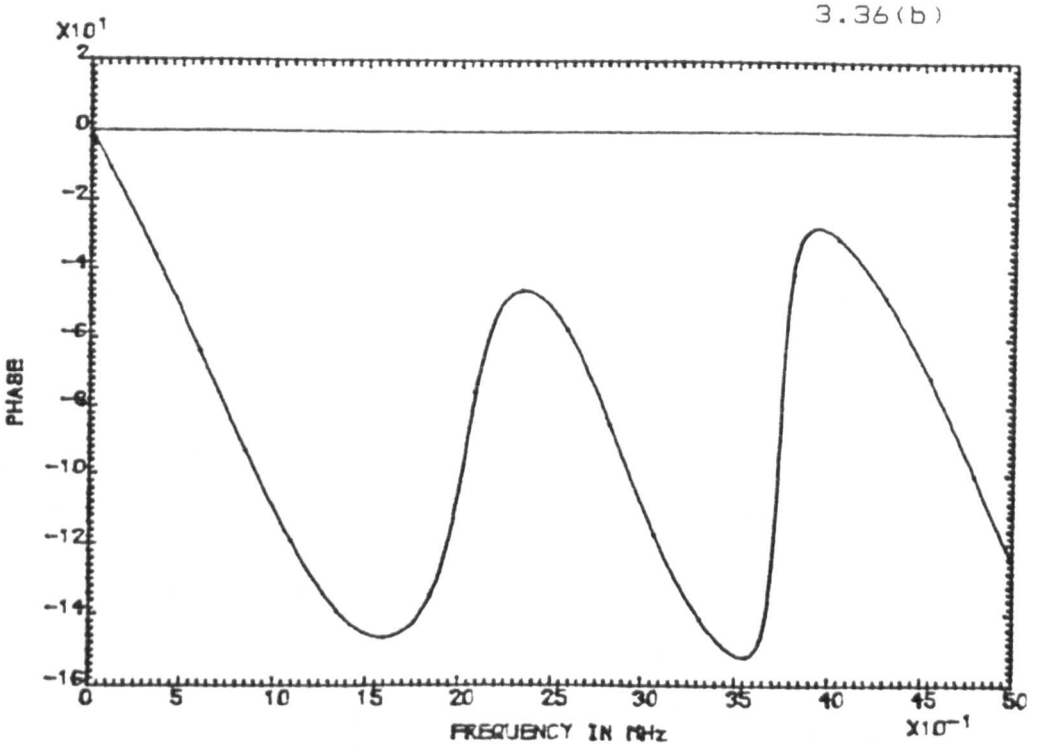

Figure 3.36 Spectral characteristics of the equivilent two-dimensional feedback factor under conditions of heavy mechanical damping.

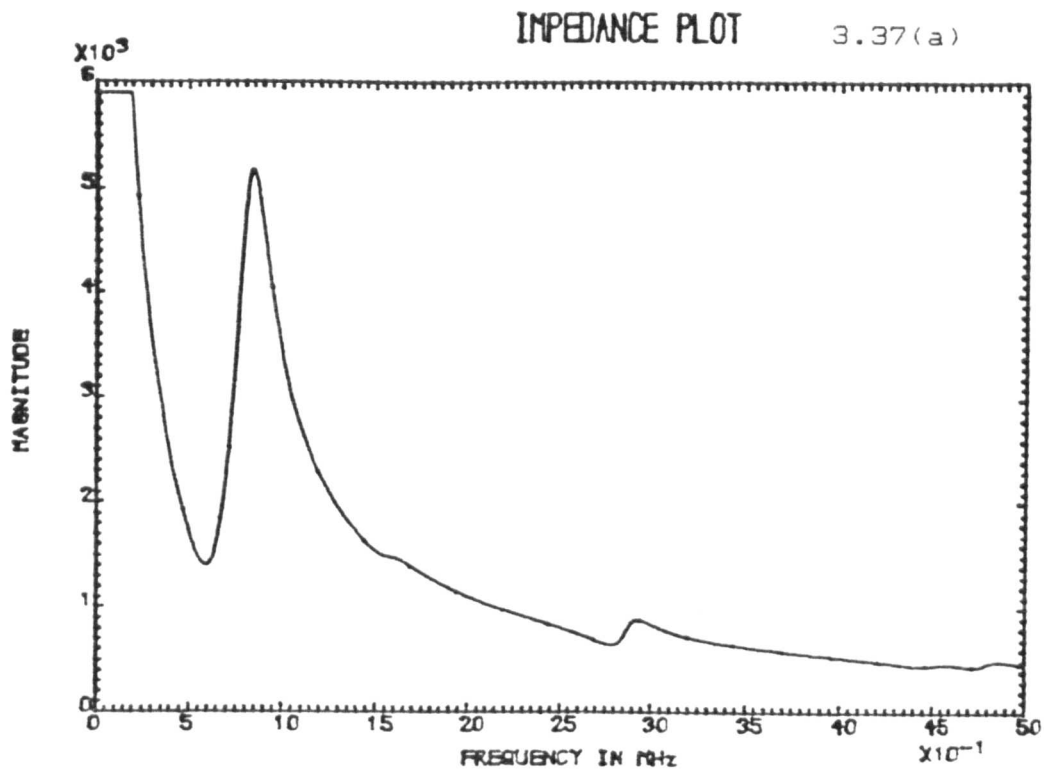

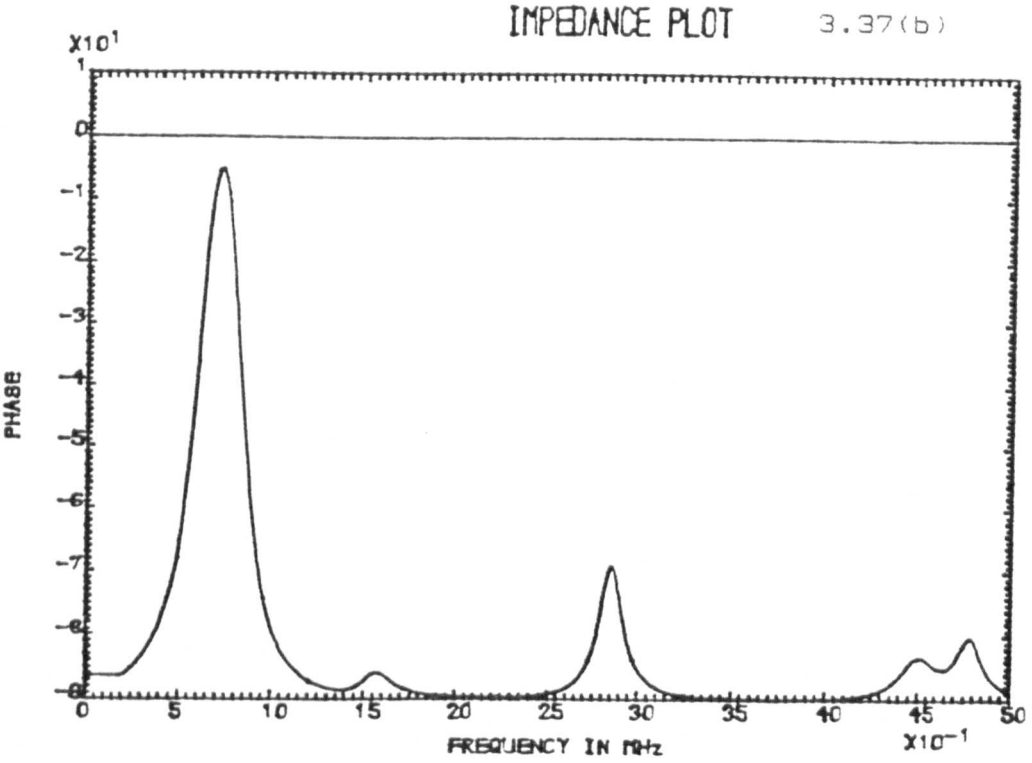

Figure 3.37 Spectral characteristics of the electrical impedance function under conditions of light mechanical damping.

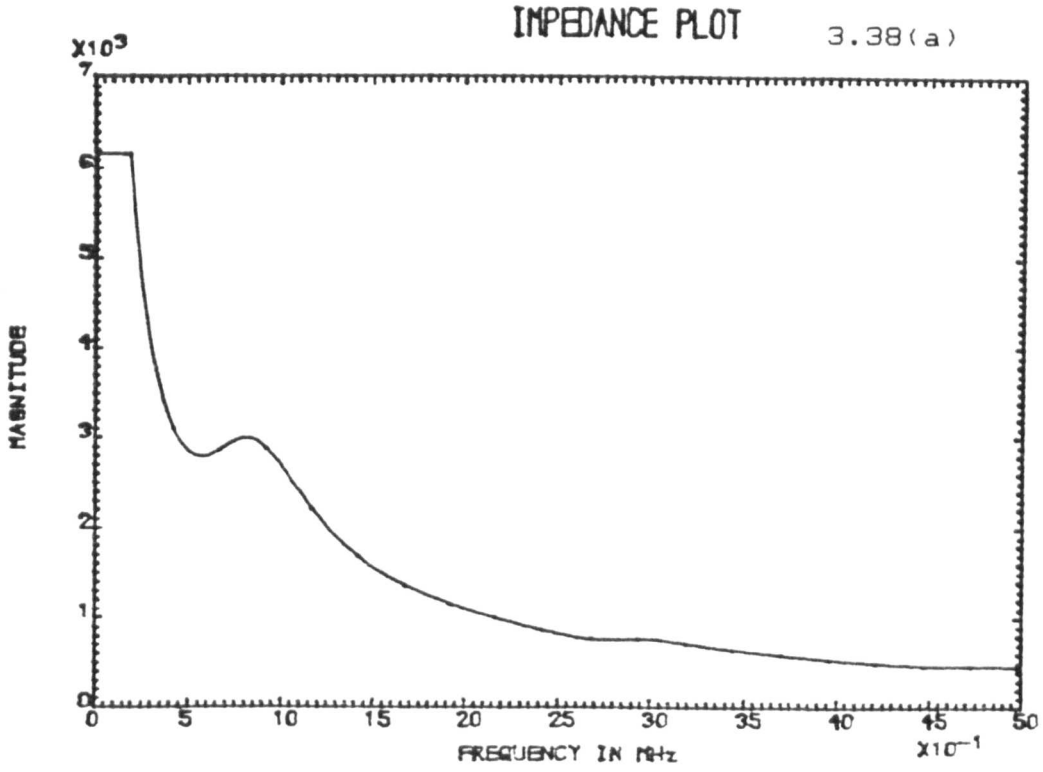

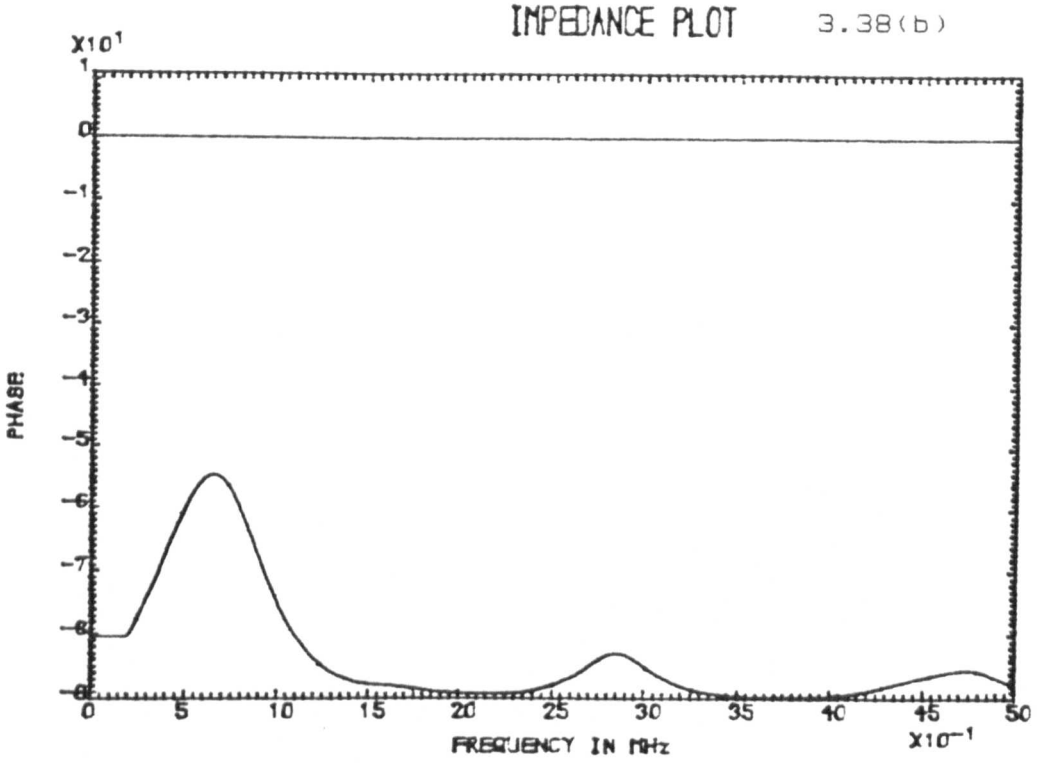

Figure 3.38 Spectral characteristics of the electrical impedance function under conditions of medium mechanical damping.

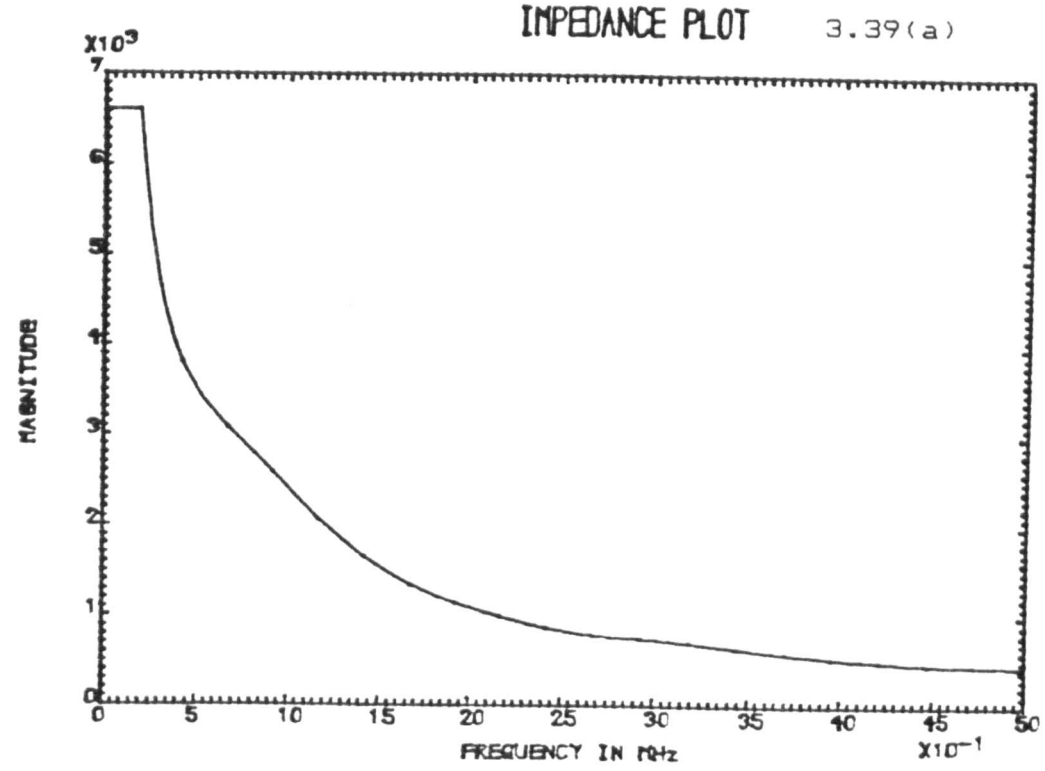

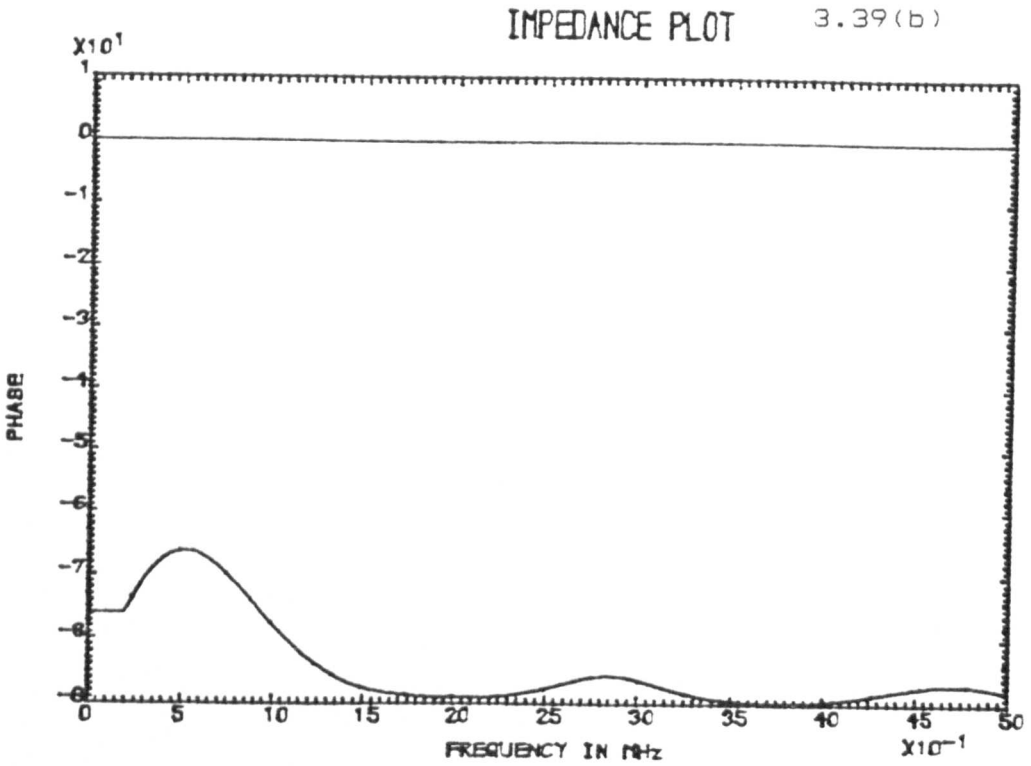

Figure 3.39 Spectral characteristics of the electrical impedance function under conditions of heavy mechanical damping.

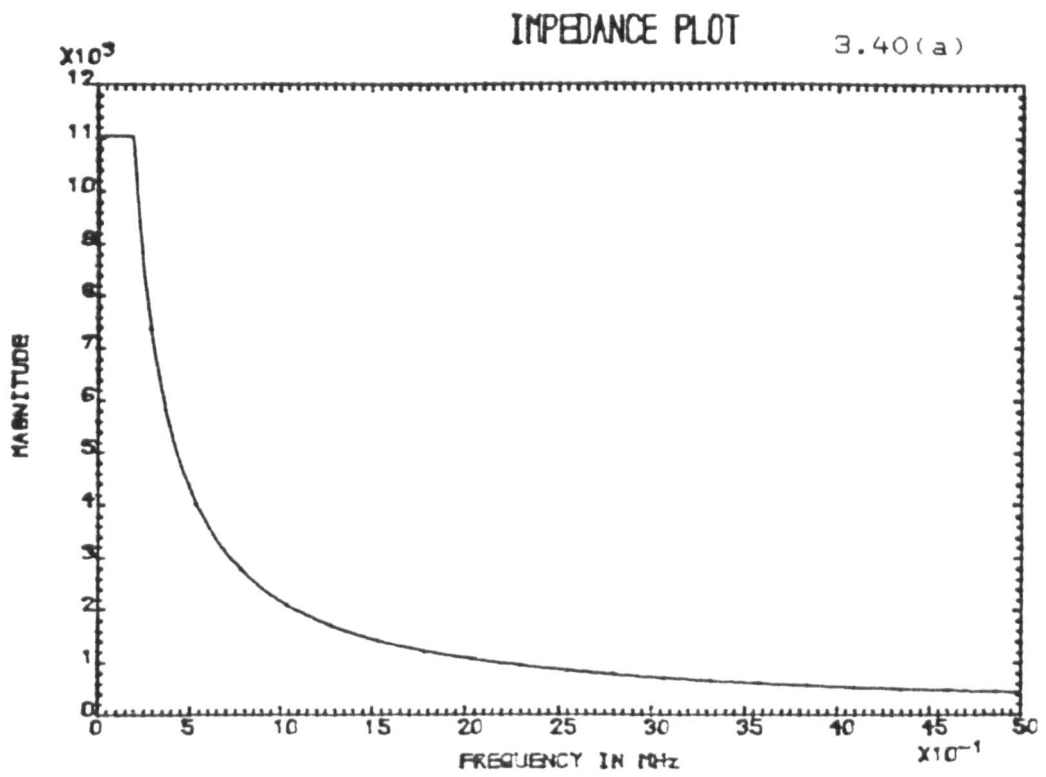

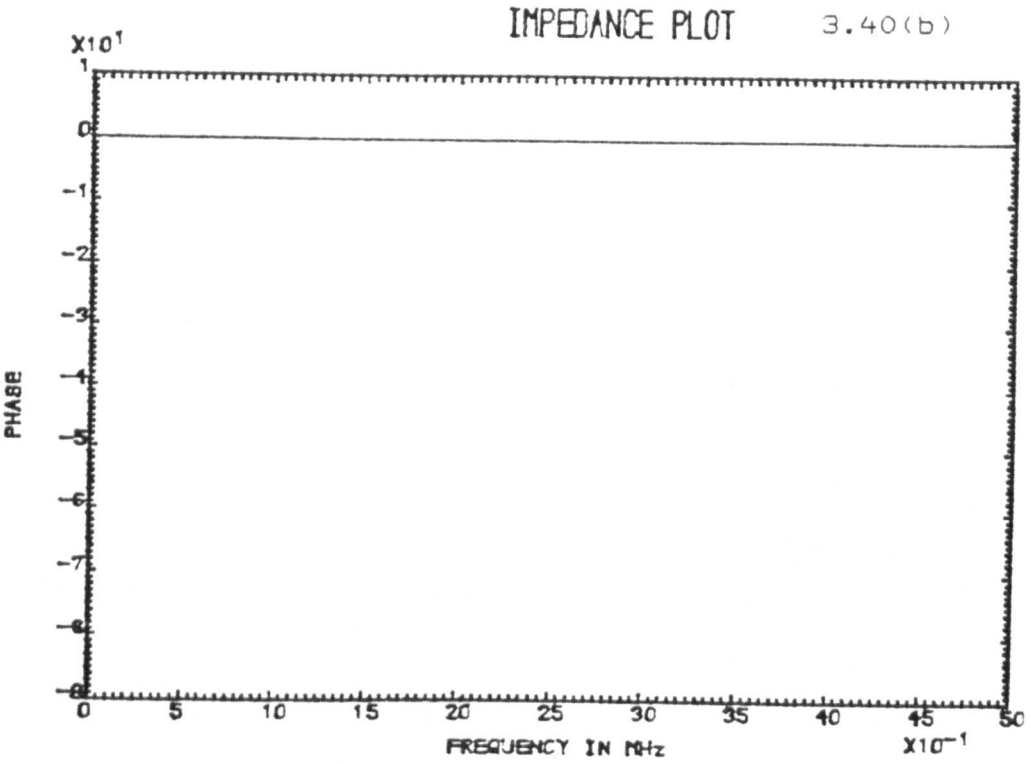

Figure 3.40 Spectral characteristics of the electrical impedance function under conditions of rigid mechanical damping on all faces.

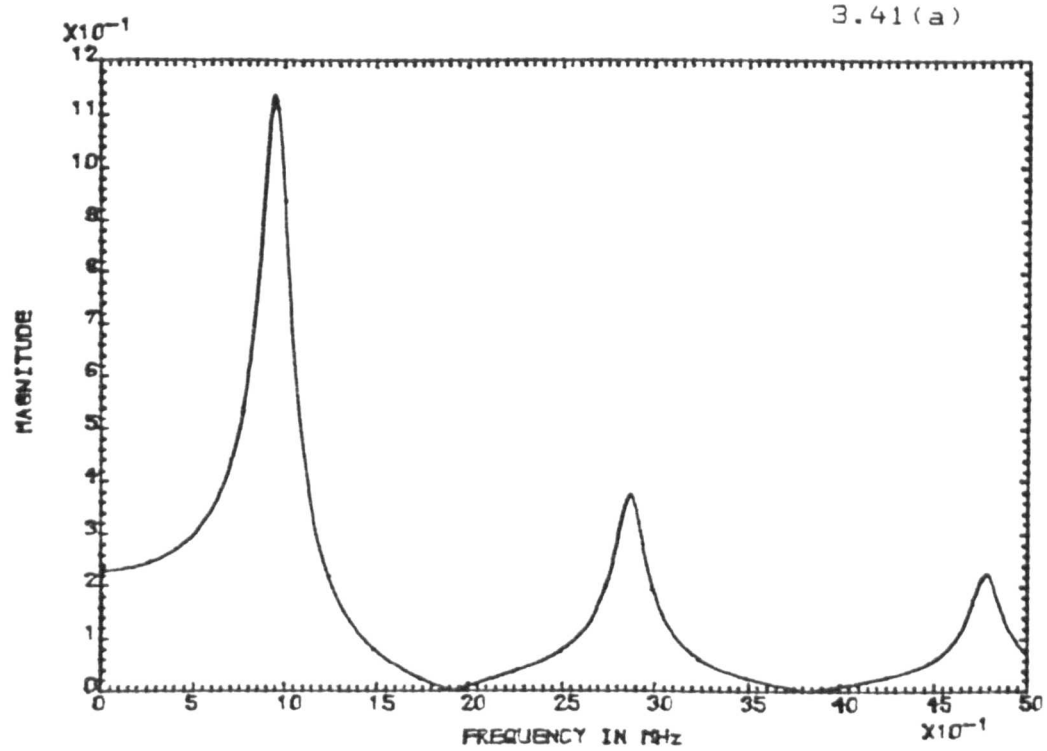

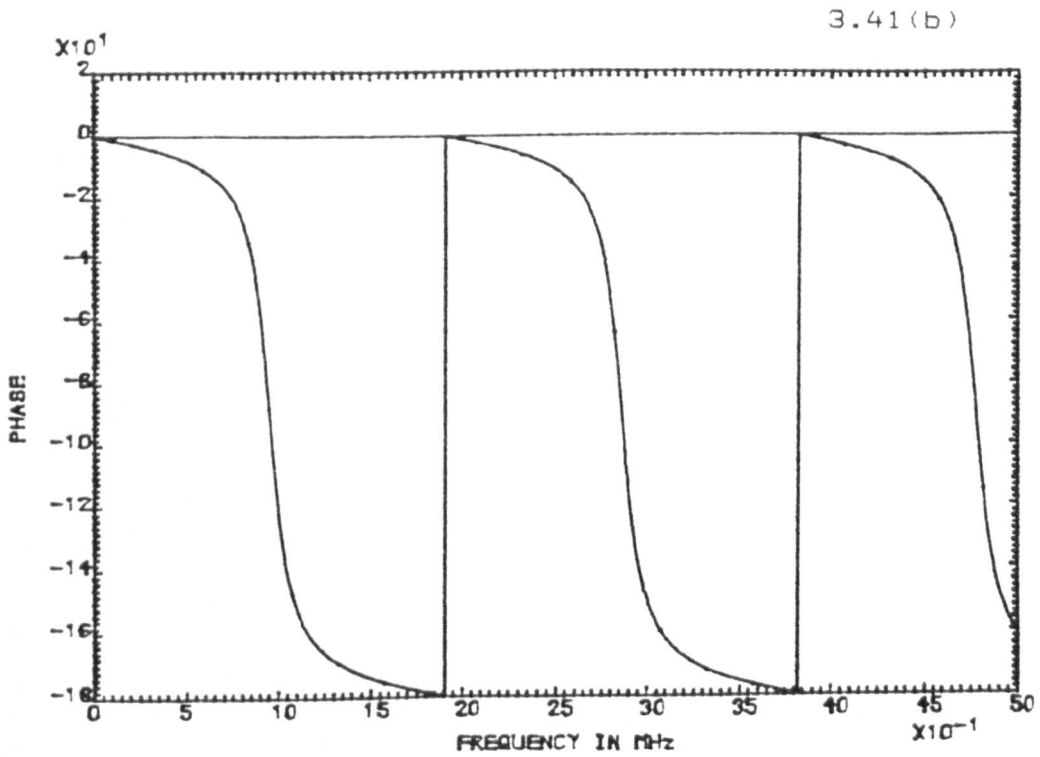

Figure 3.41 Spectral characteristics of the equivilent two-dimensional feedback factor under conditions of rigid lateral damping and light thickness damping.

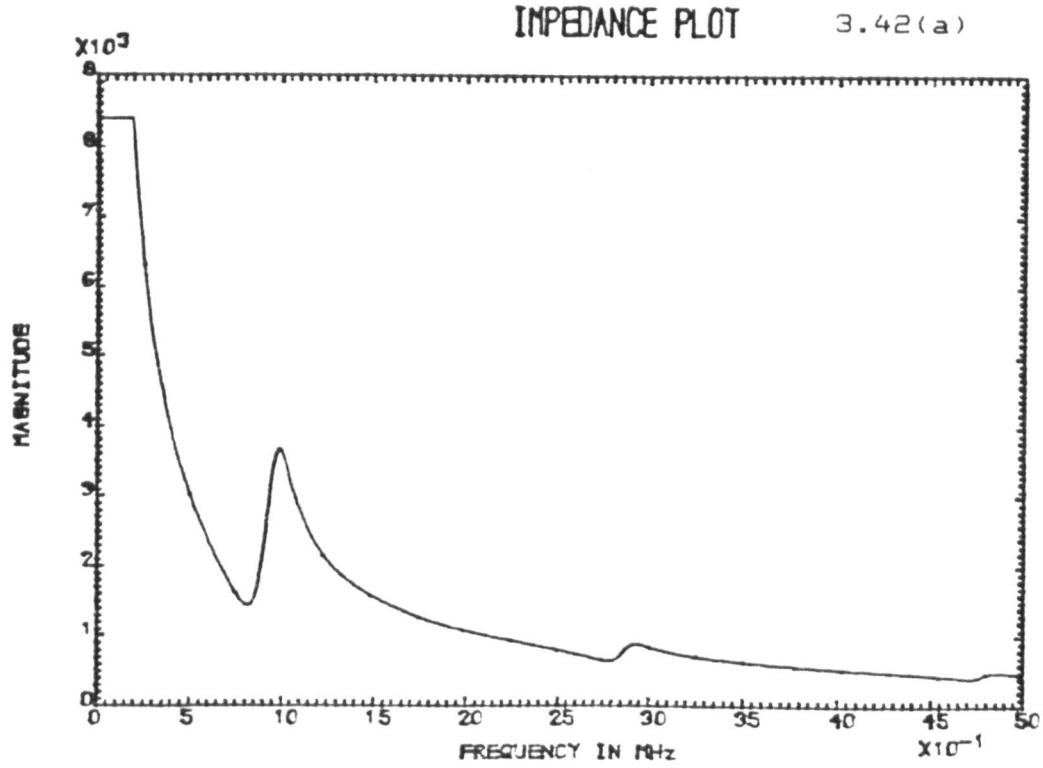

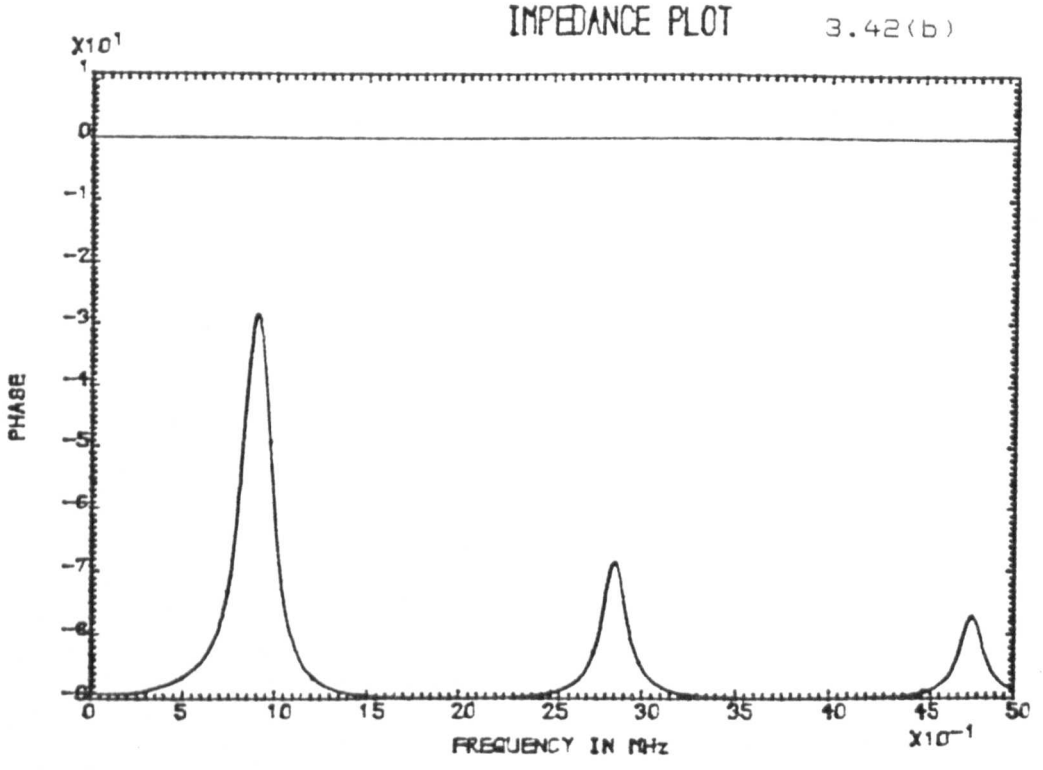

Figure 3.42 Spectral characteristics of the electrical impedance function under conditions of rigid lateral damping and light thickness damping.

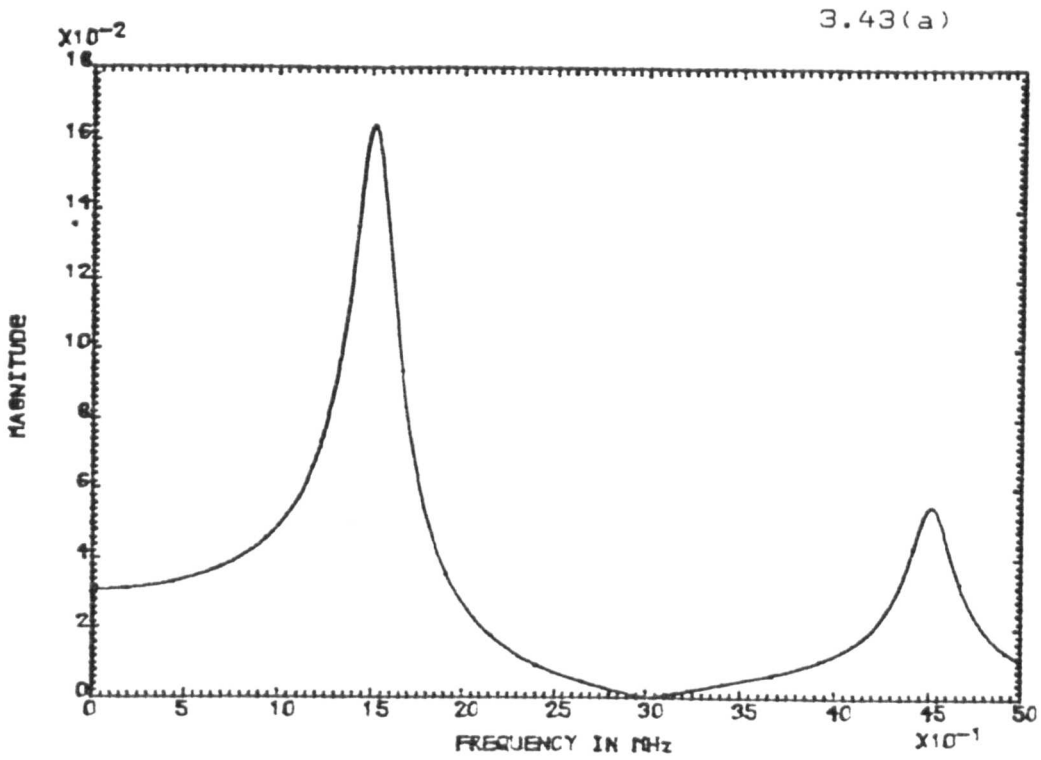

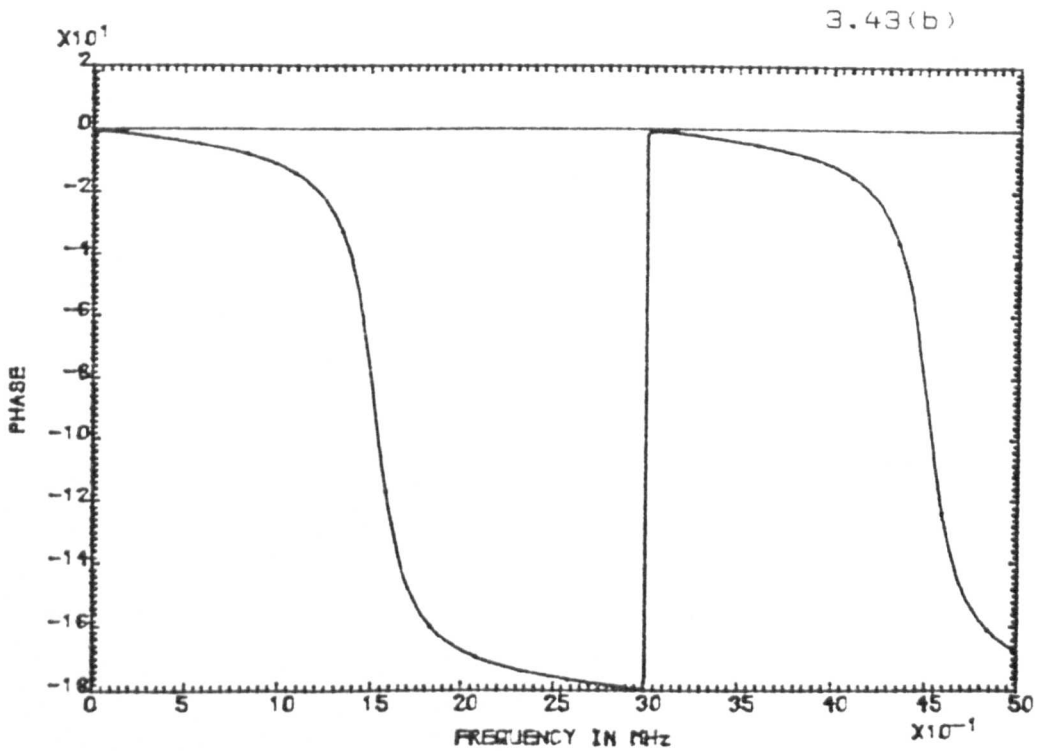

Figure 3.43 Spectral characteristics of the equivilent two-dimensional feedback factor under conditions of rigid thickness damping and light lateral damping.

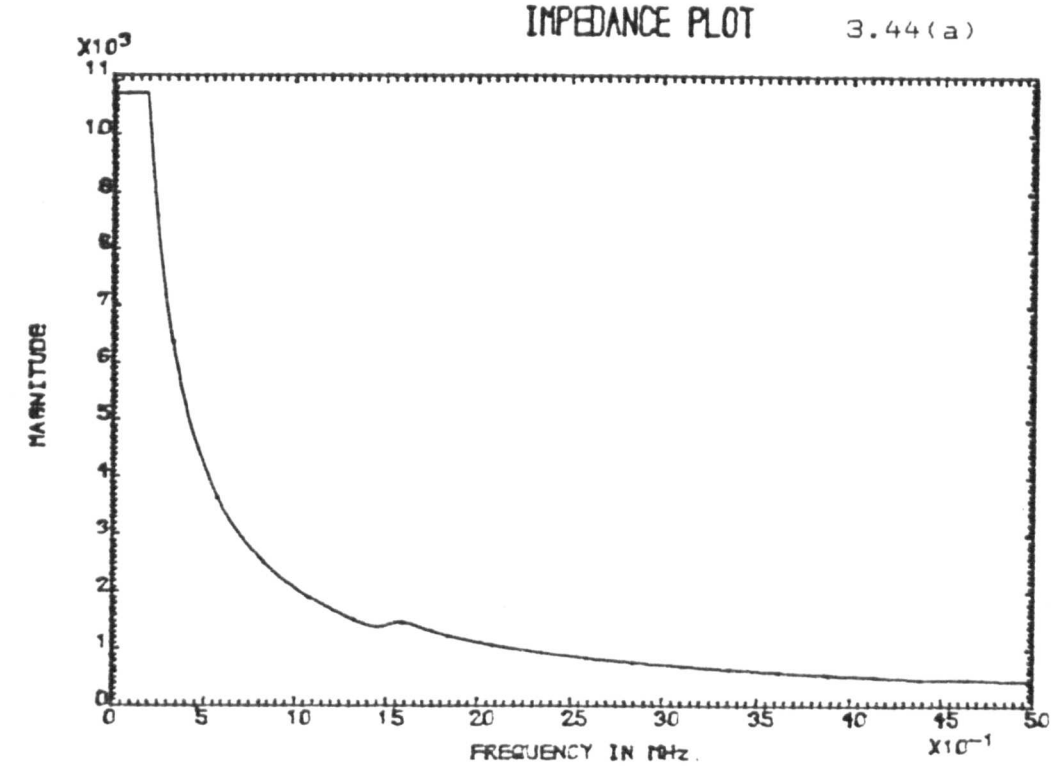

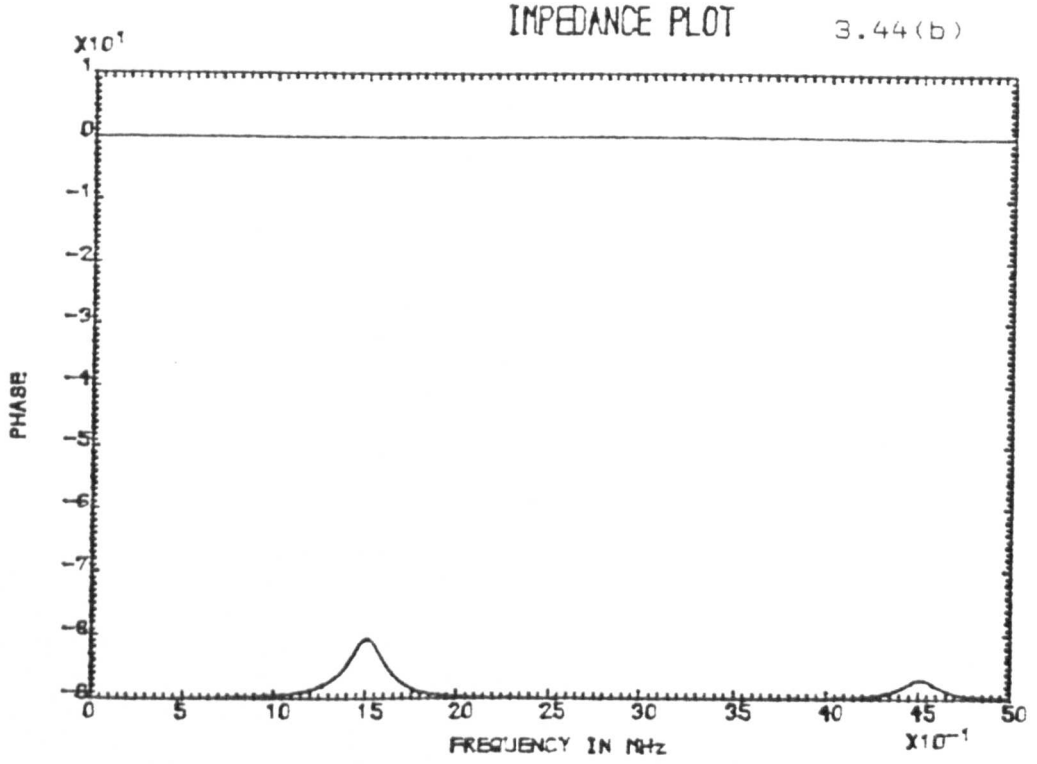

Figure 3.44 Spectral characteristics of the electrical impedance function under conditions of rigid thickness damping and light lateral damping.

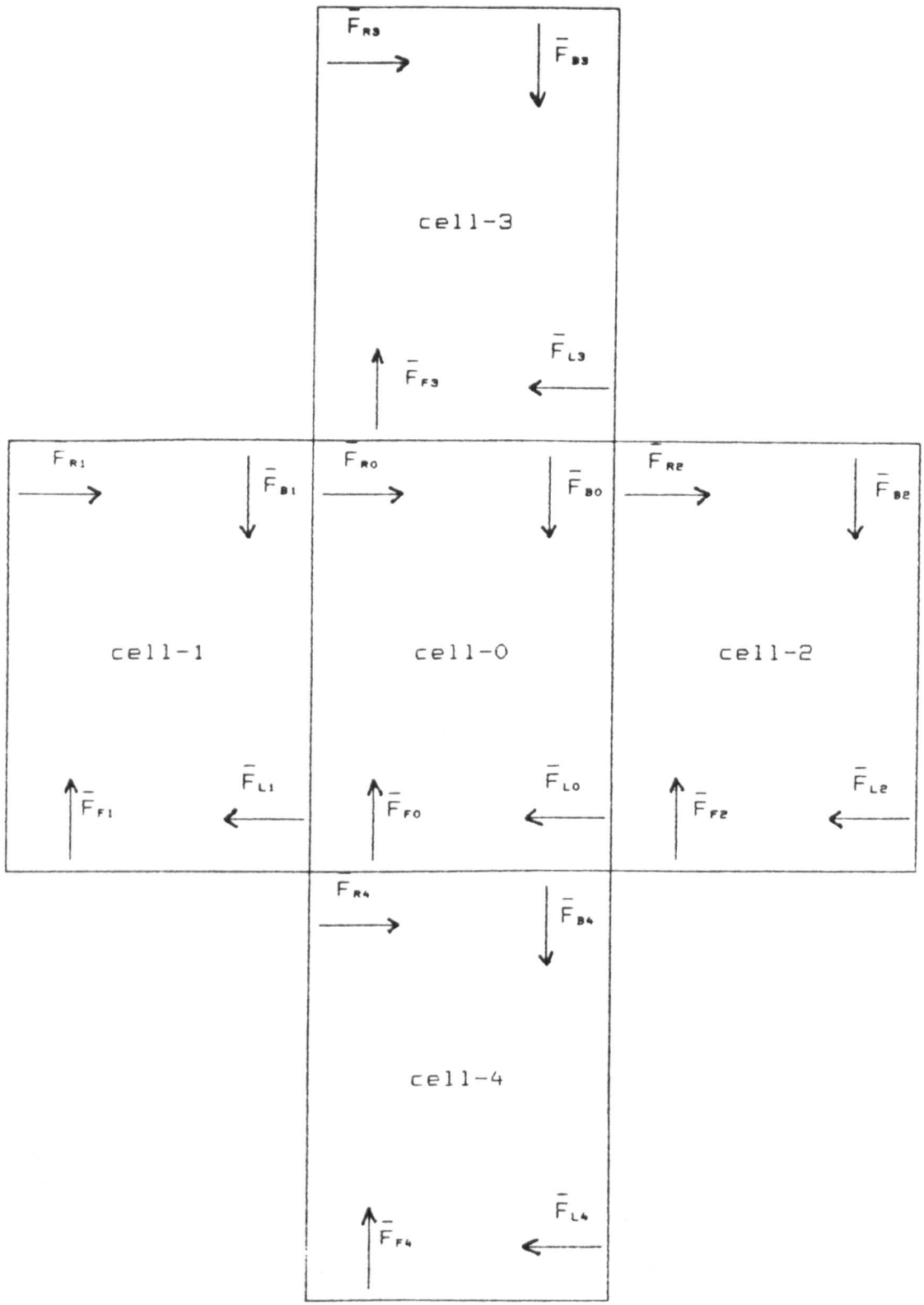

Figure 4.1

Cellular transducer configuration
representing layers in two dimensions.

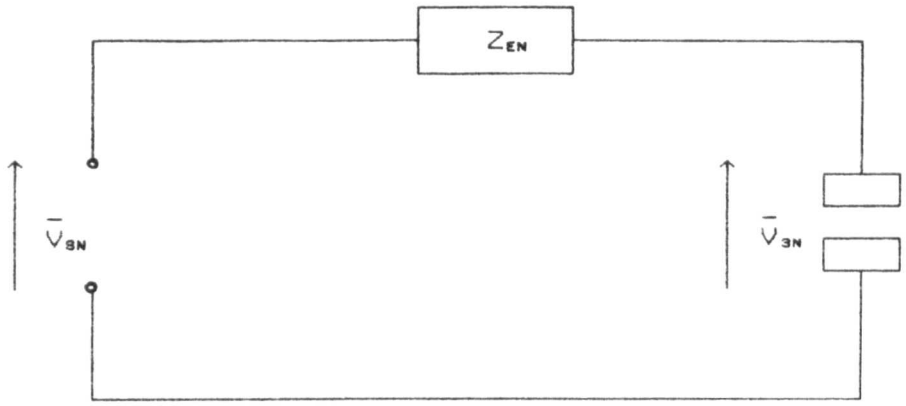

Figure 4.2 Transducer electrical configuration

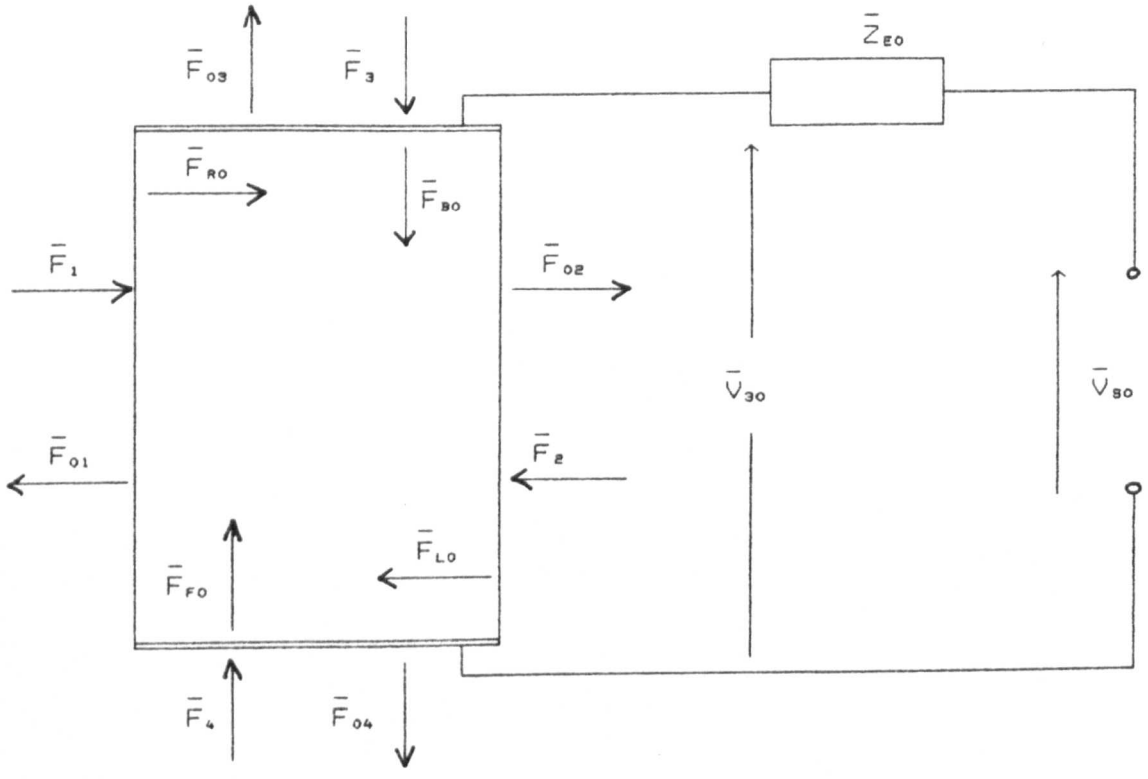

Figure 4.3

Transducer with no mechanical
or piezoelectric layers.

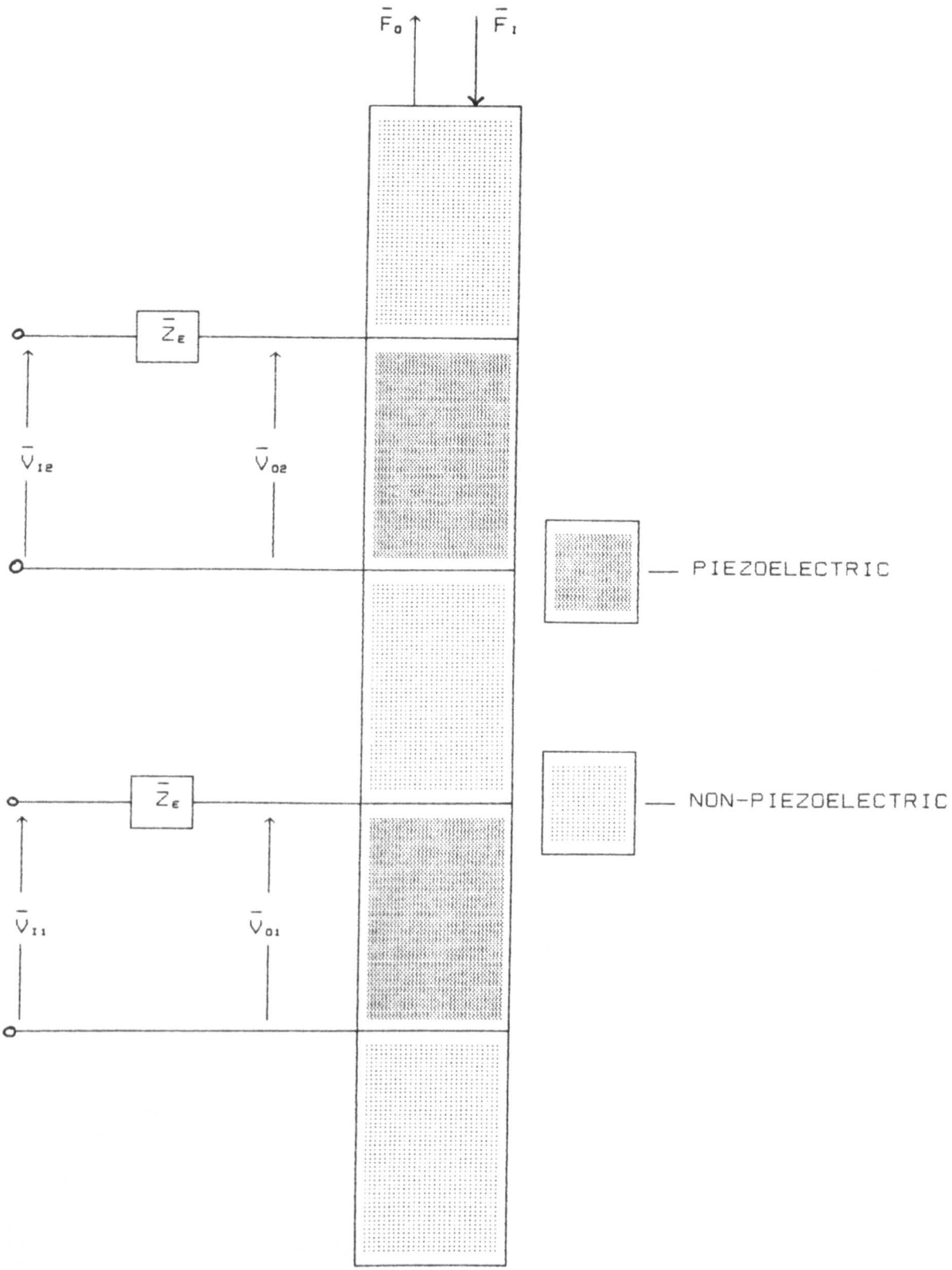

Figure 4.4 The configuration for thickness layers.

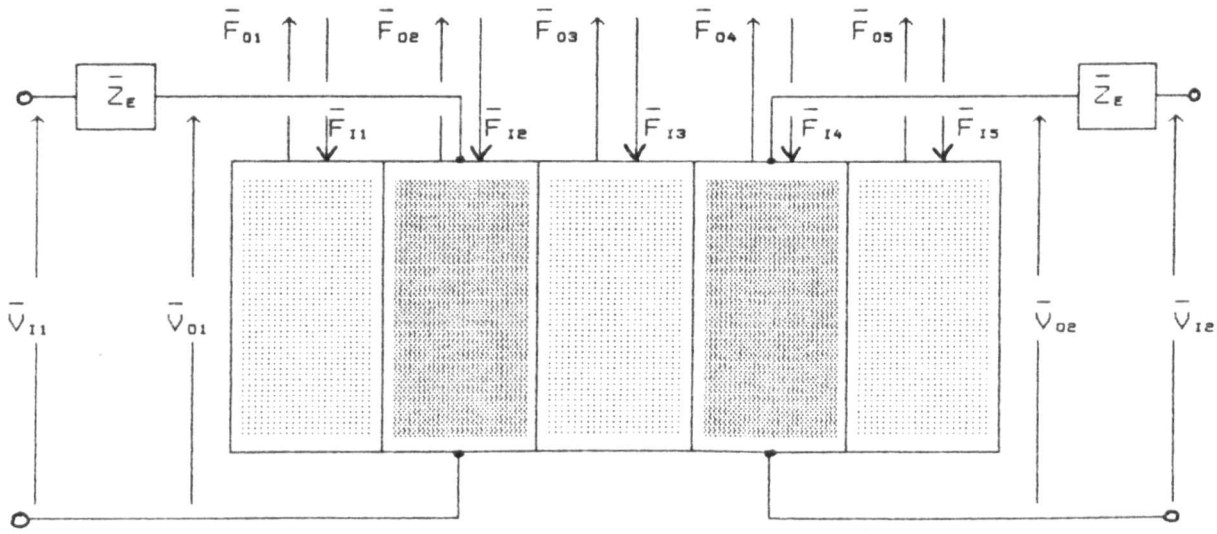

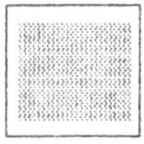

—— PIEZOELECTRIC

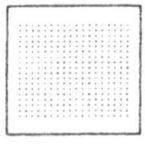

—— NON-PIEZOELECTRIC

Figure 4.5 The configuration for lateral layers.

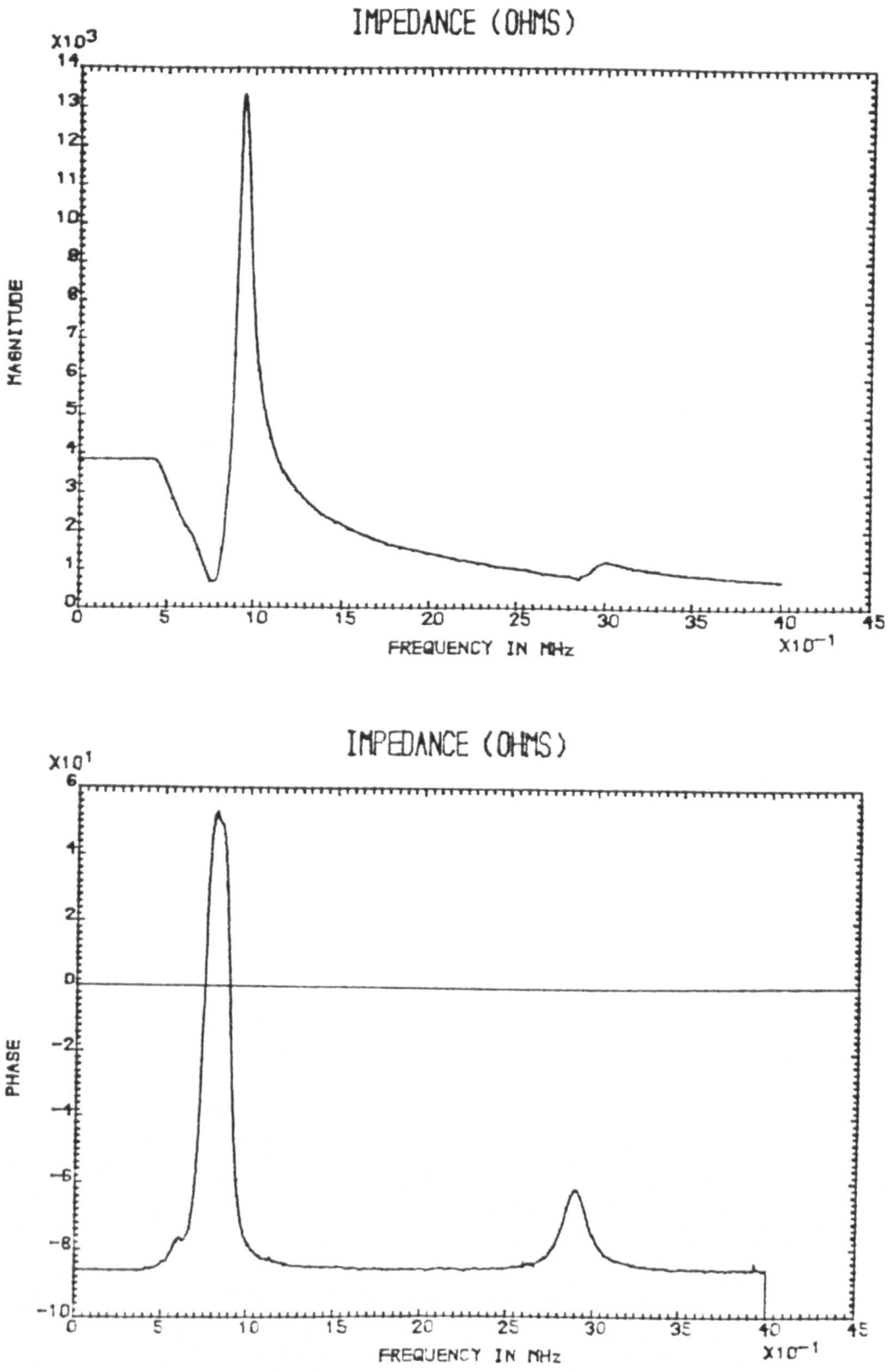

Figure 5.1a Measured electrical impedance characteristics of a two-dimensional, PZT-5A transducer with configuration ratio equal to 0.14.

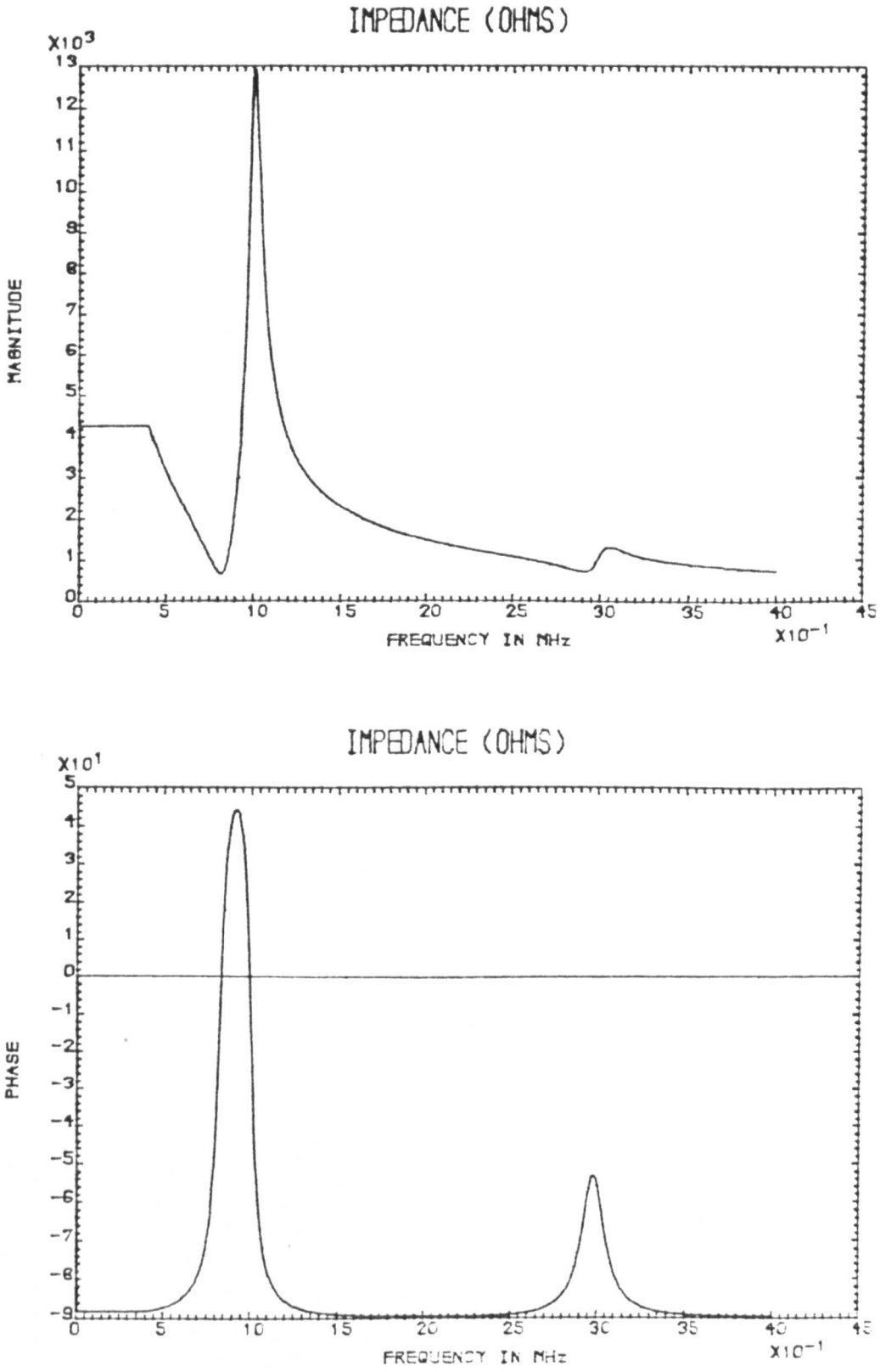

Figure 5.1b Simulated electrical impedance characteristics of a two-dimensional, PZT-5A transducer with configuration ratio equal to 0.14. Simulated according to the modified unidimensional model.

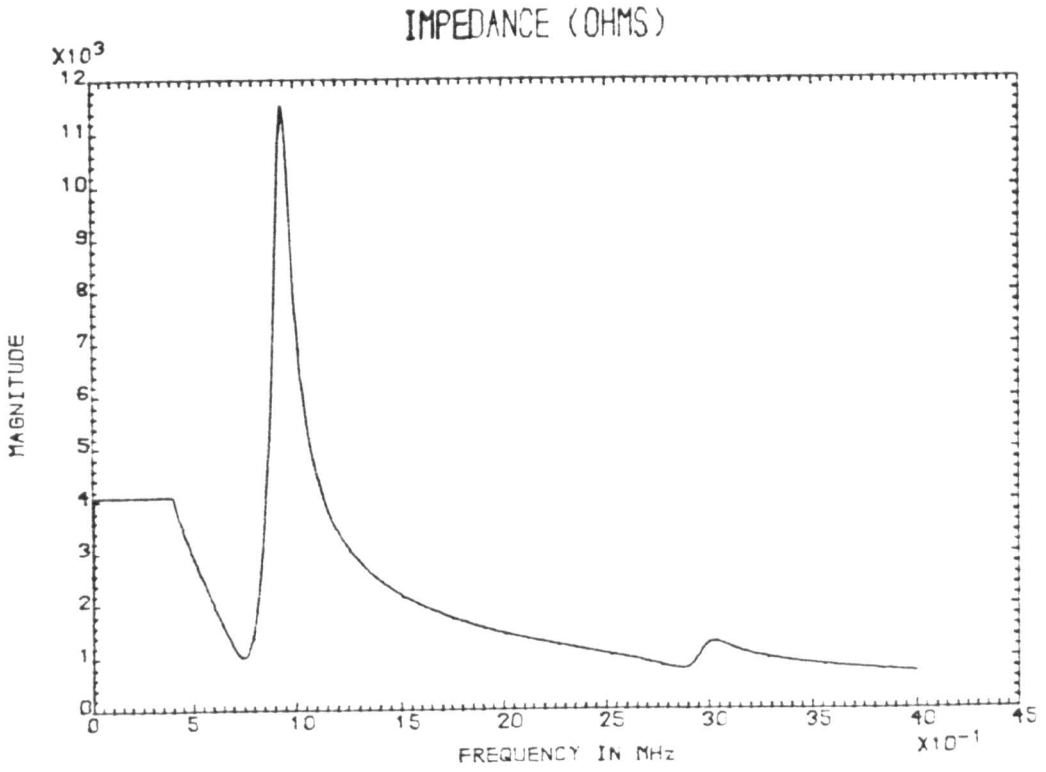

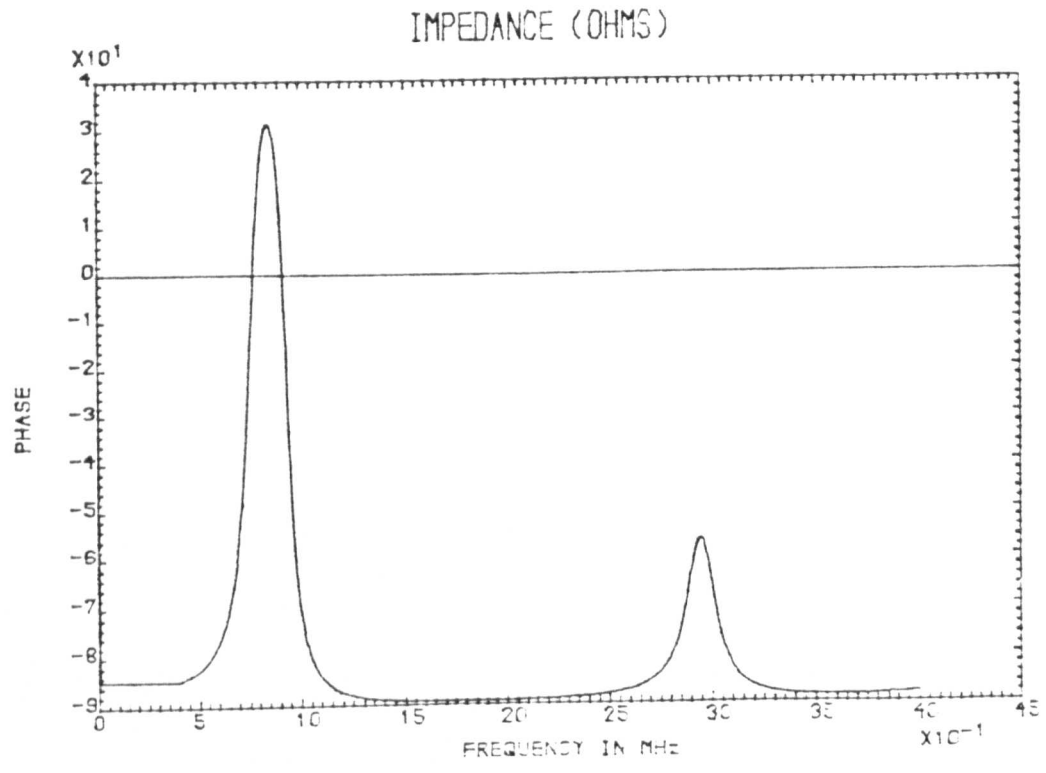

Figure 5.1c Simulated electrical impedance characteristics of a two-dimensional, PZT-5A transducer with configuration ratio equal to 0.14. Simulated according to the two-dimensional linear systems model.

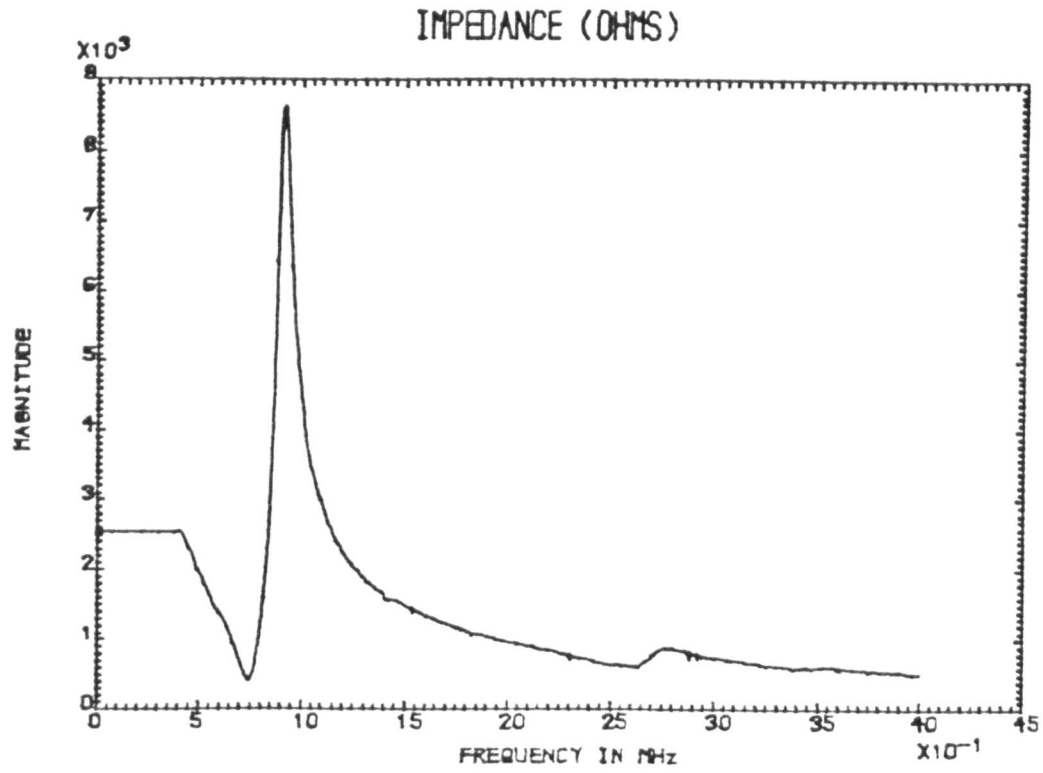

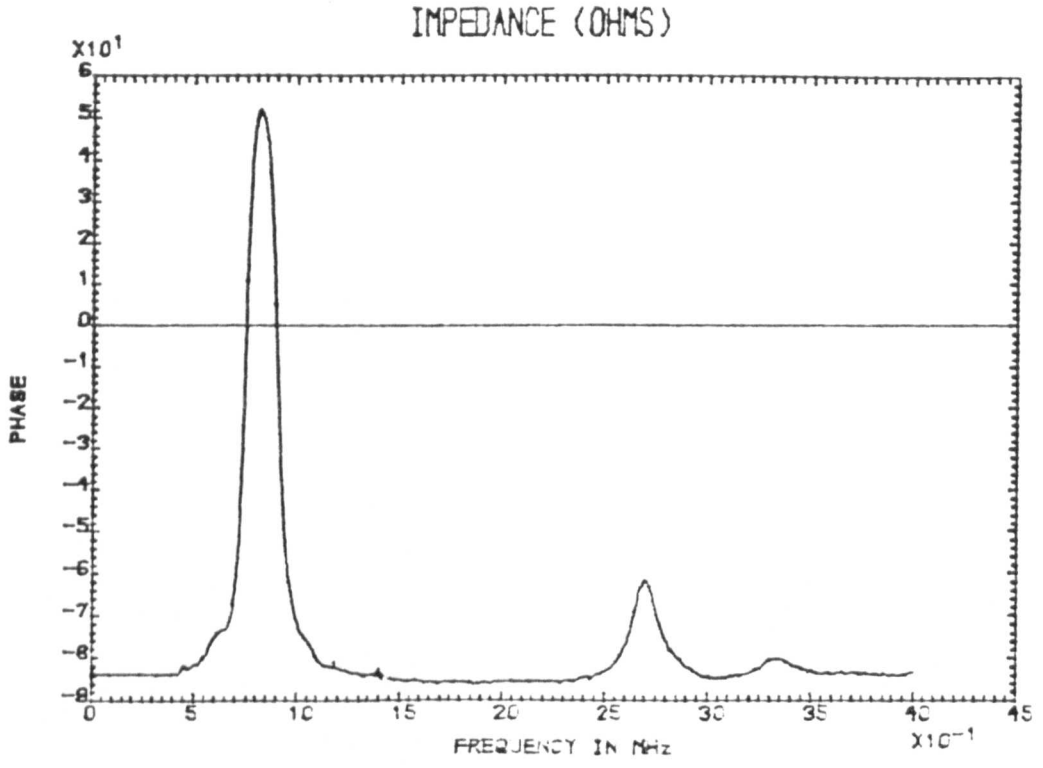

Figure 5.2a Measured electrical impedance characteristics of a two-dimensional, PZT-5A transducer with configuration ratio equal to 0.23.

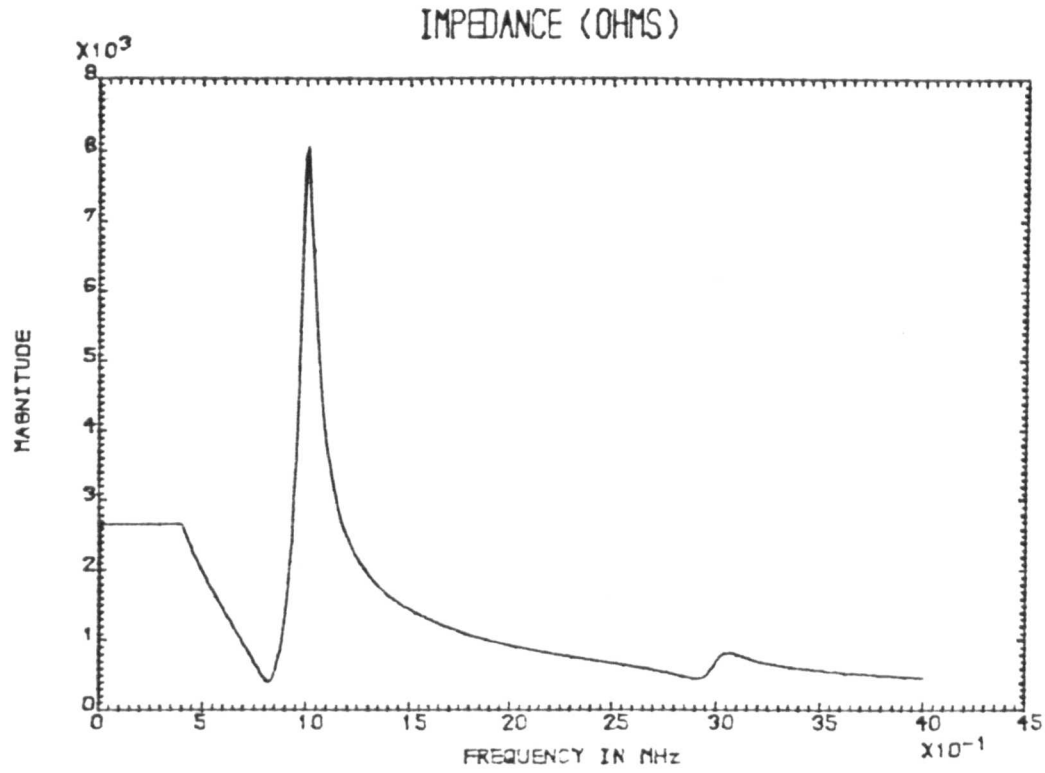

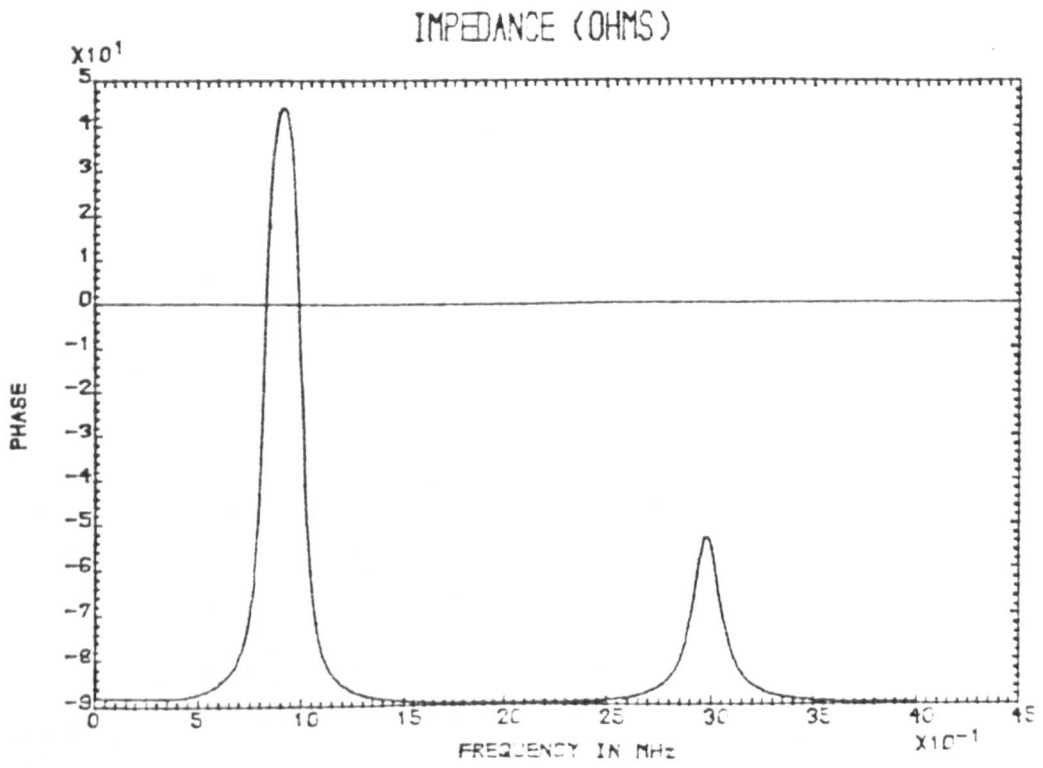

Figure 5.2b Simulated electrical impedance characteristics of a two-dimensional, PZT-5A transducer with configuration ratio equal to 0.23. Simulated according to the modified unidimensional model.

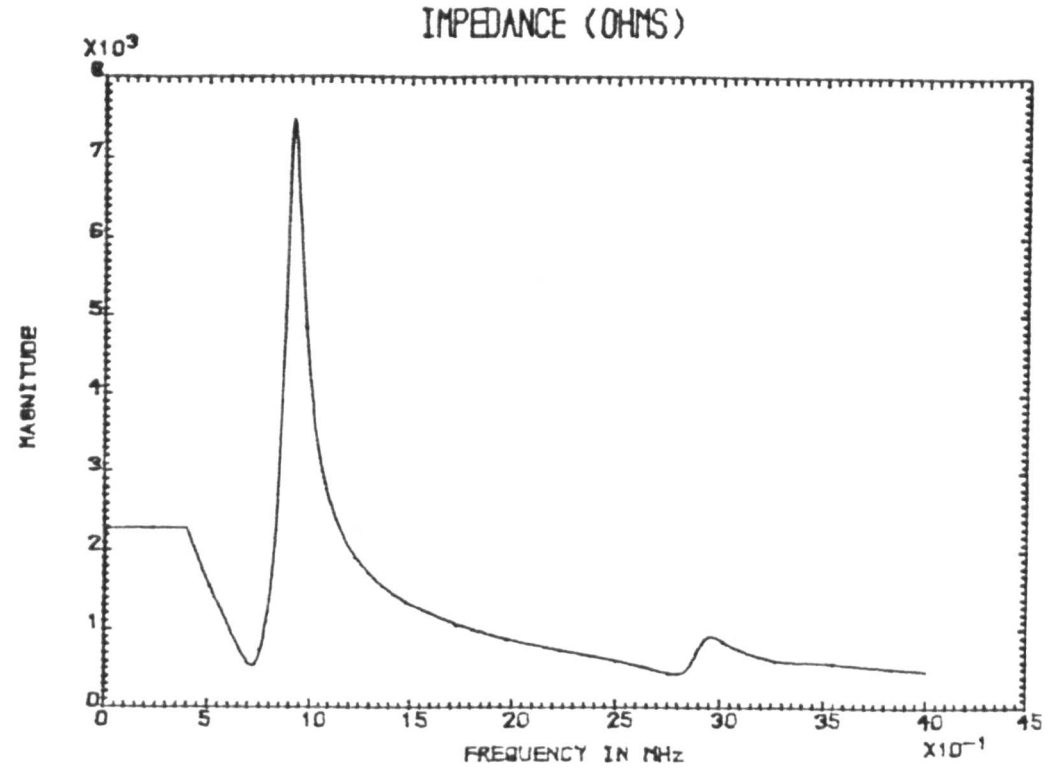

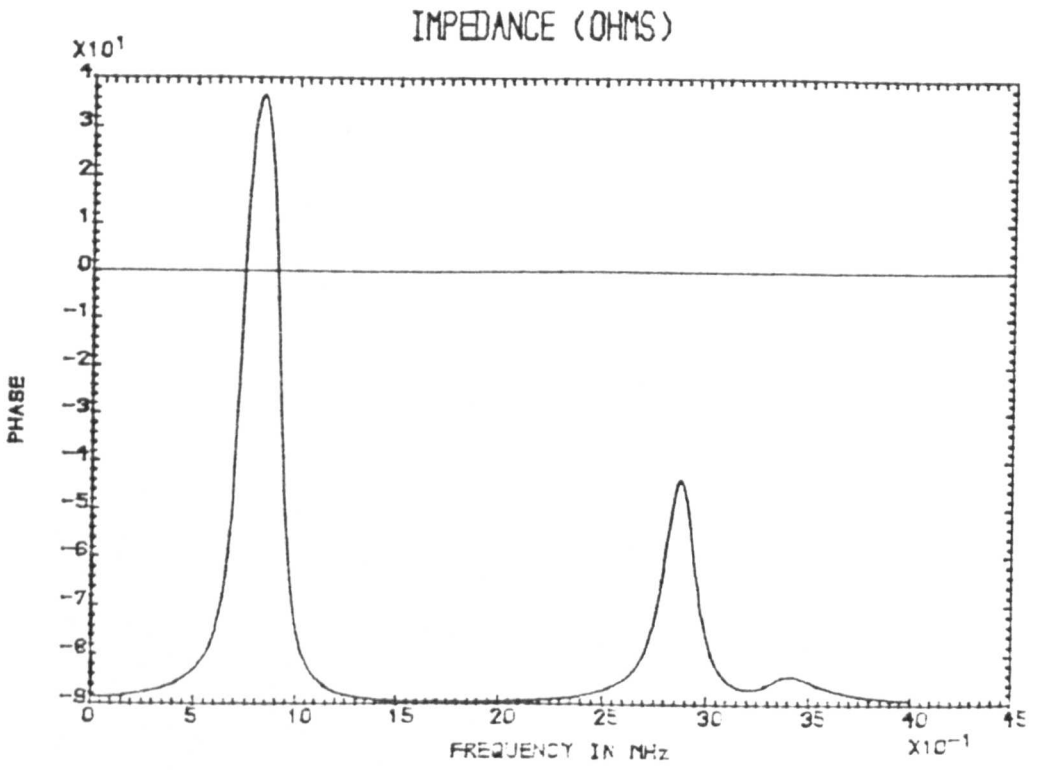

Figure 5.2c Simulated electrical impedance characteristics of a two-dimensional, PZT-5A transducer with configuration ratio equal to 0.23. Simulated according to the two-dimensional linear systems model.

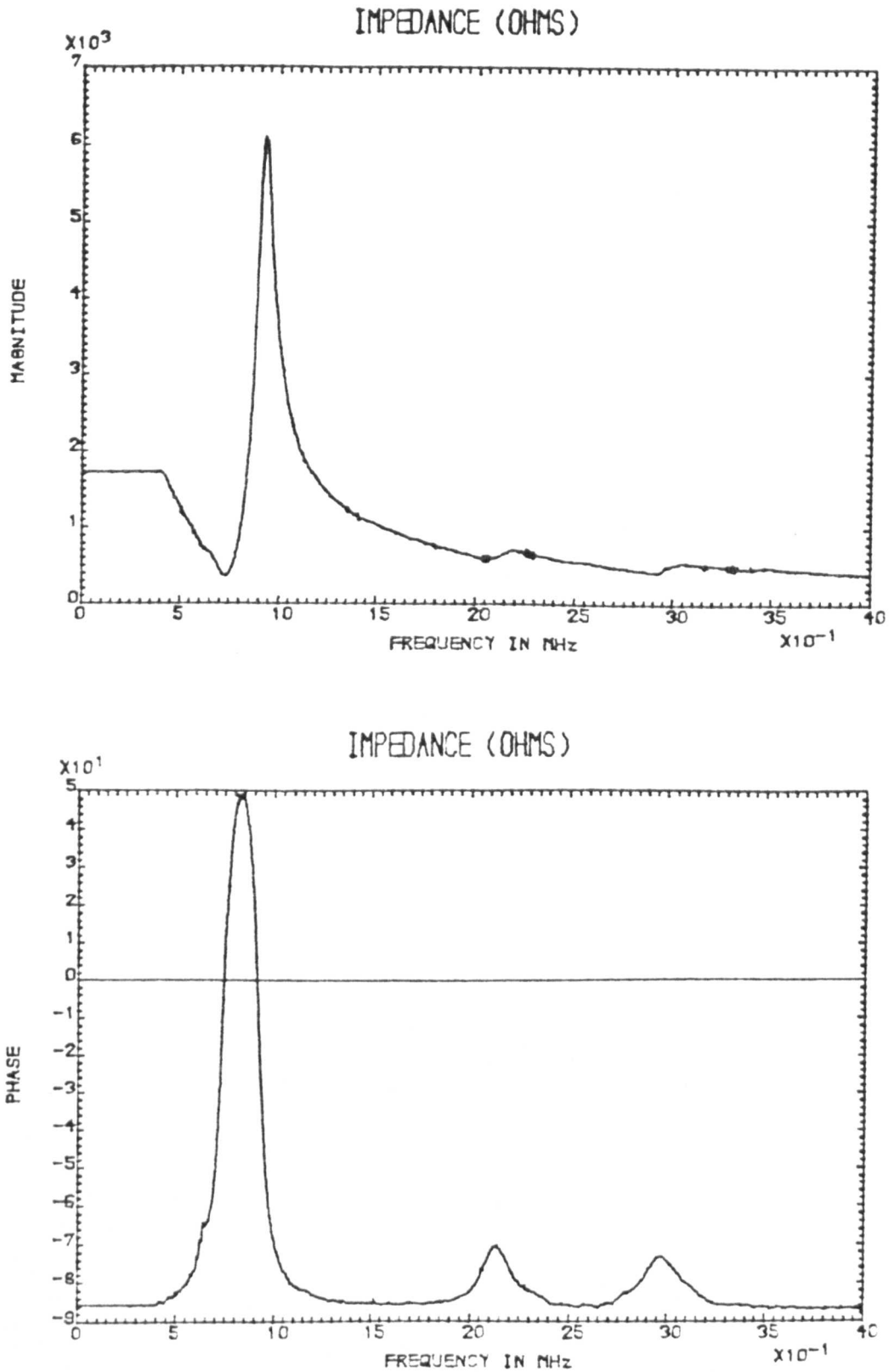

Figure 5.3a Measured electrical impedance characteristics of a two-dimensional, PZT-5A transducer with configuration ratio equal to 0.35.

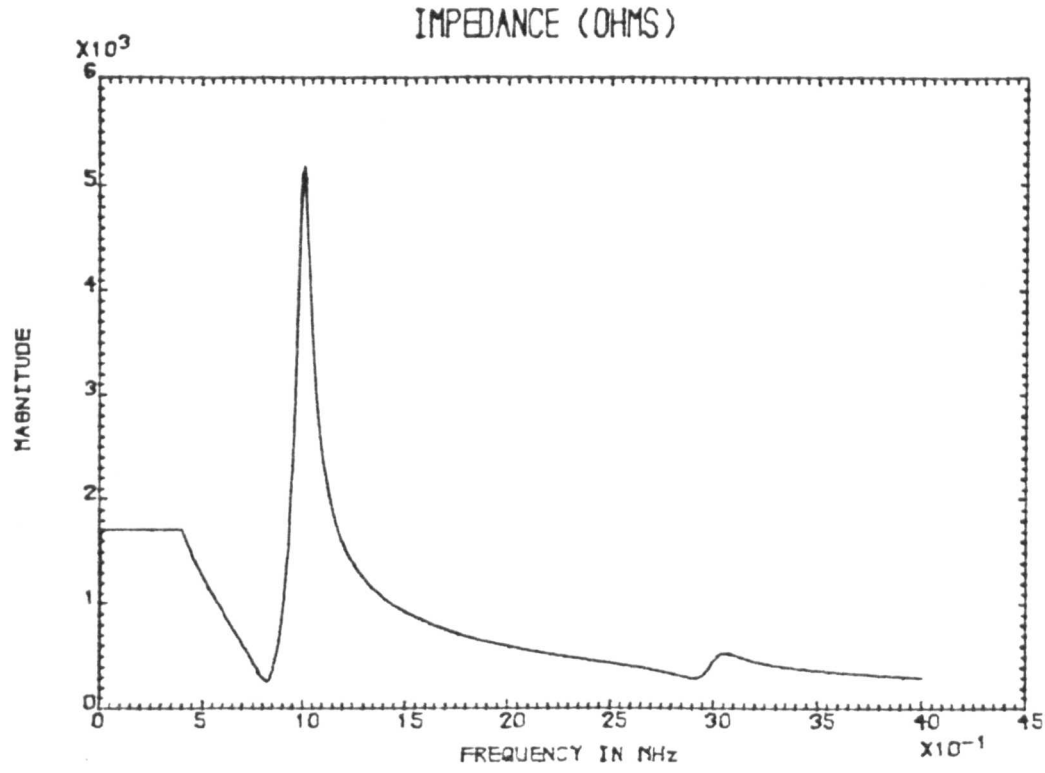

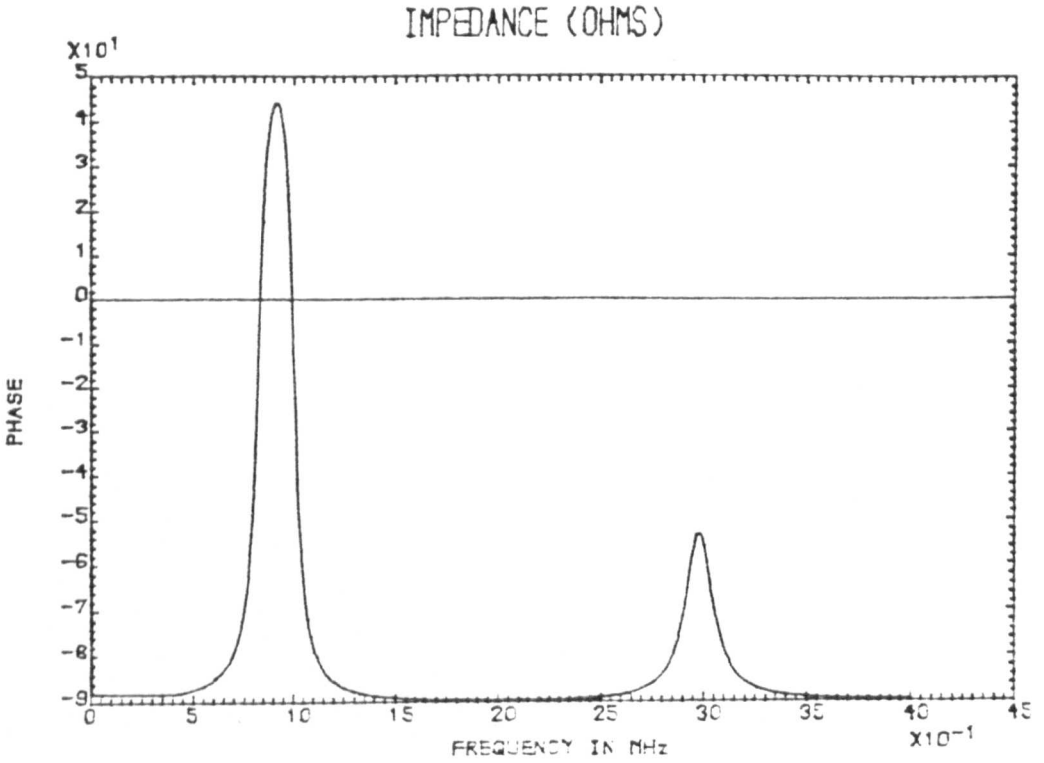

Figure 5.3b Simulated electrical impedance characteristics of a two-dimensional, PZT-5A transducer with configuration ratio equal to 0.35. Simulated according to the modified unidimensional model.

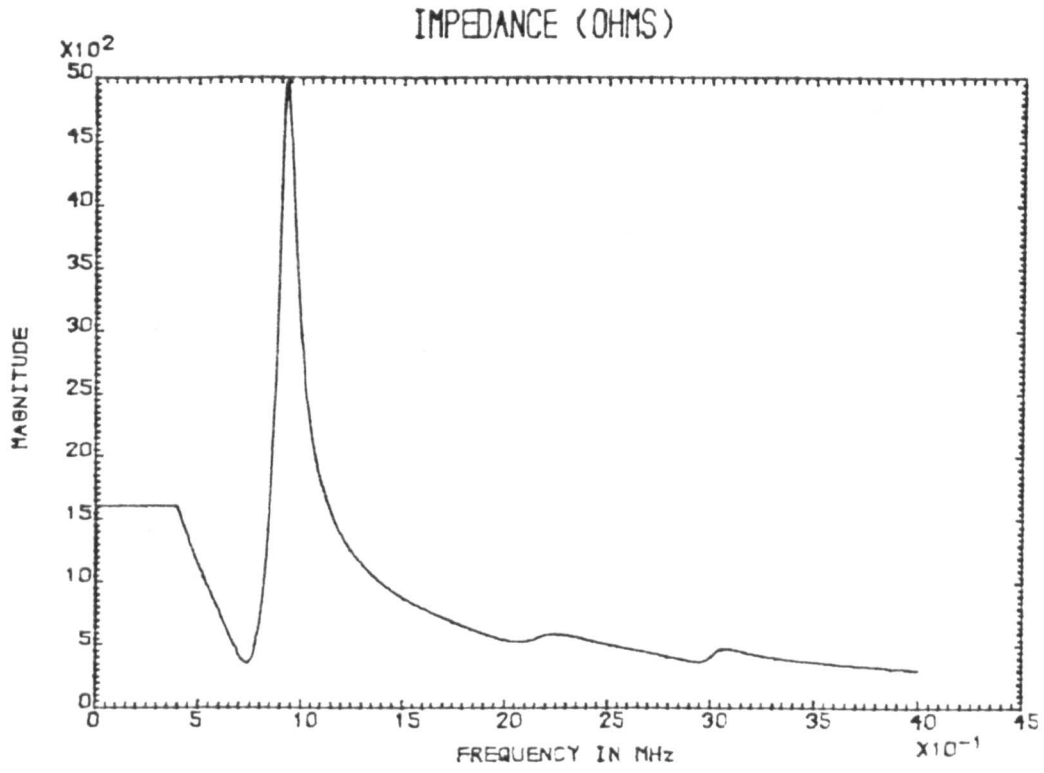

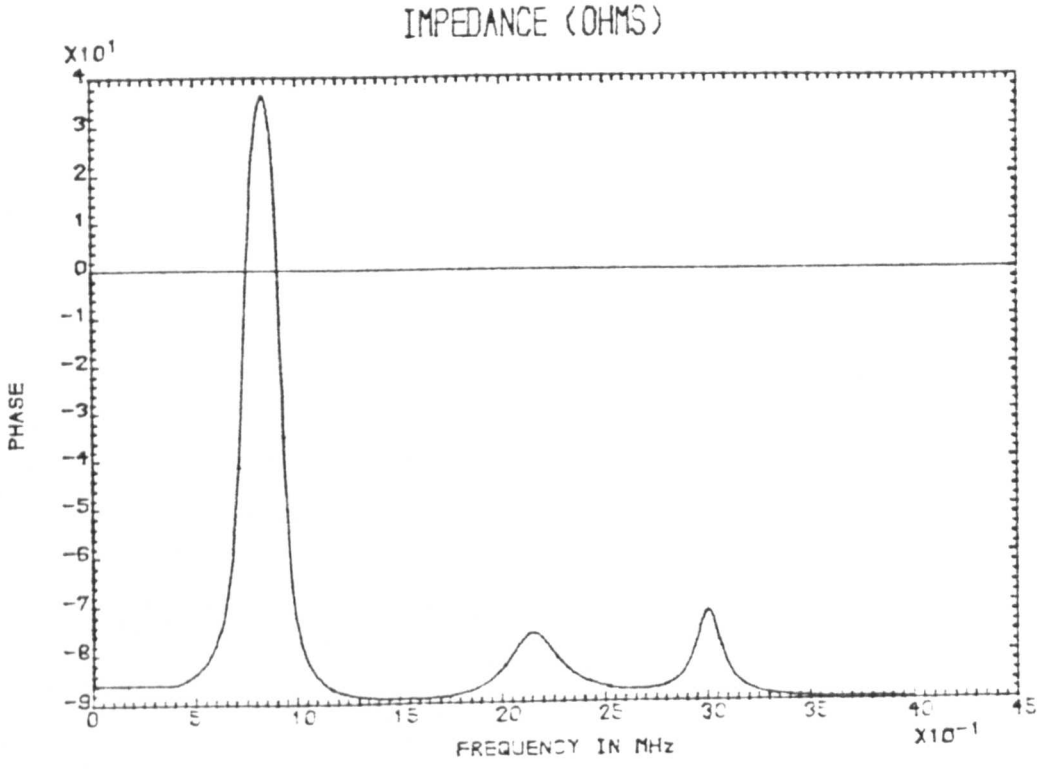

Figure 5.3c Simulated electrical impedance characteristics of a two-dimensional, PZT-5A transducer with configuration ratio equal to 0.35. Simulated according to the two-dimensional linear systems model.

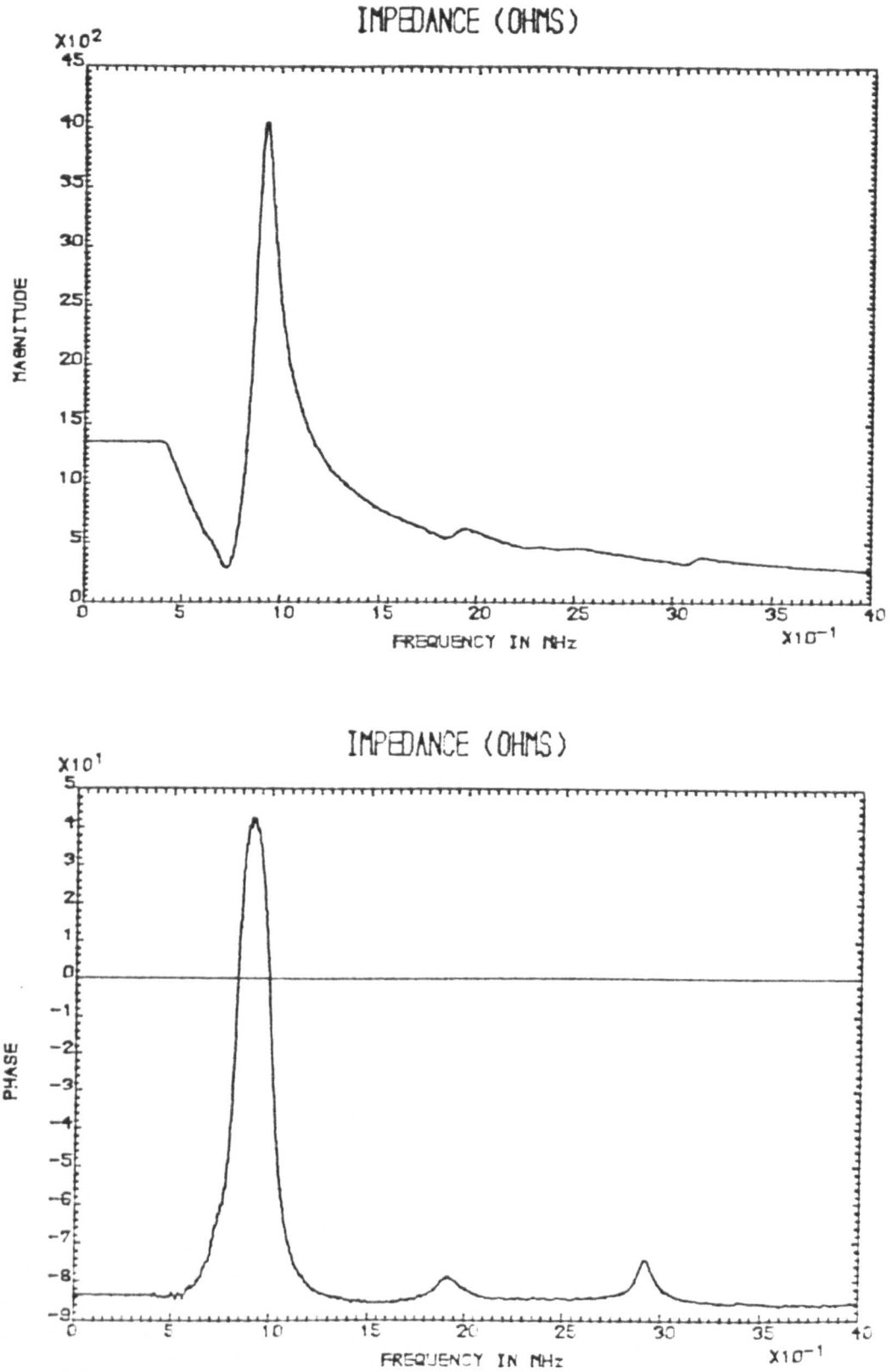

Figure 5.4a Measured electrical impedance characteristics of a two-dimensional, PZT-5A transducer with configuration ratio equal to 0.42.

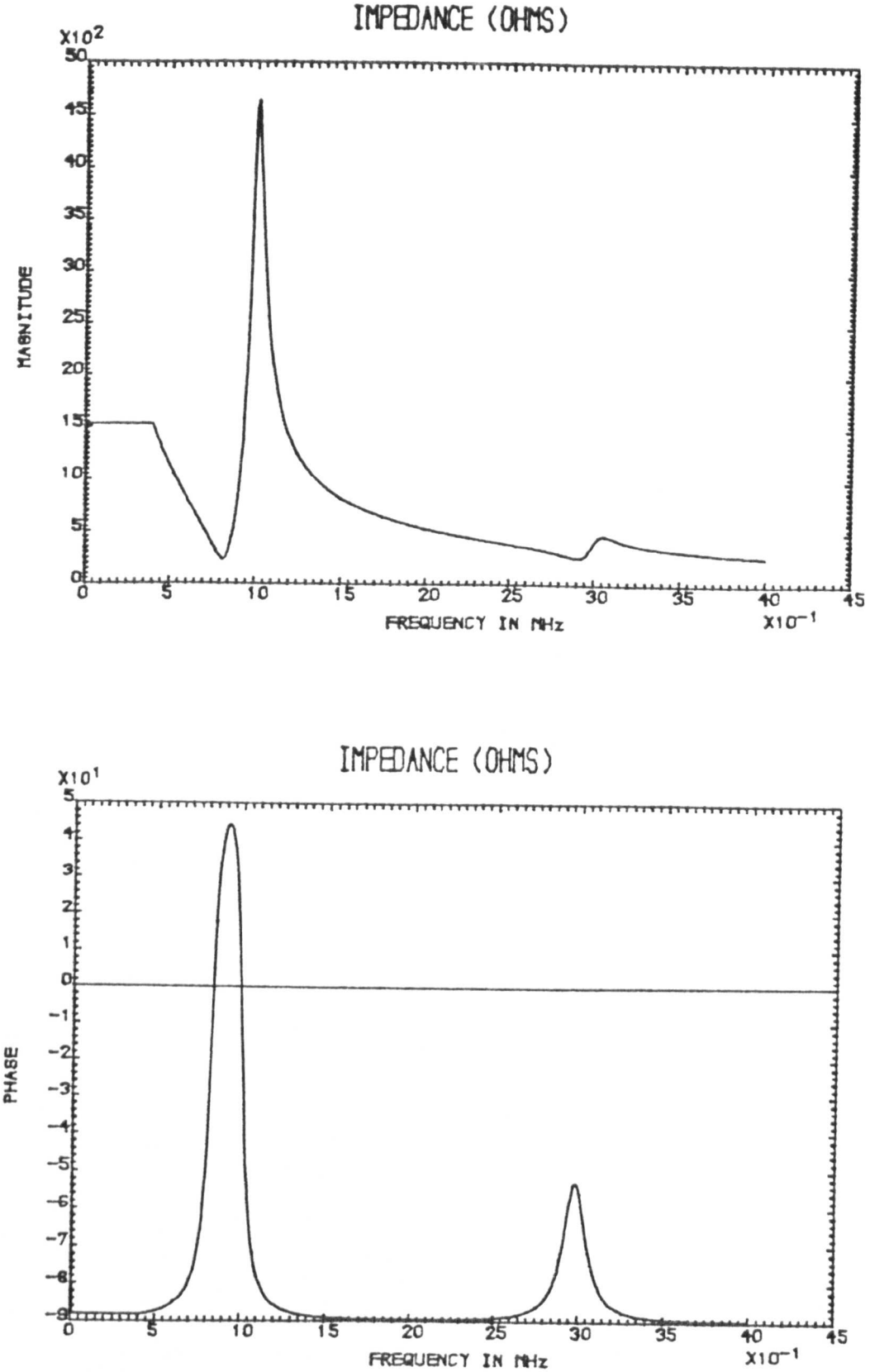

Figure 5.4b Simulated electrical impedance characteristics of a two-dimensional, PZT-5A transducer with configuration ratio equal to 0.42. Simulated according to the modified unidimensional model.

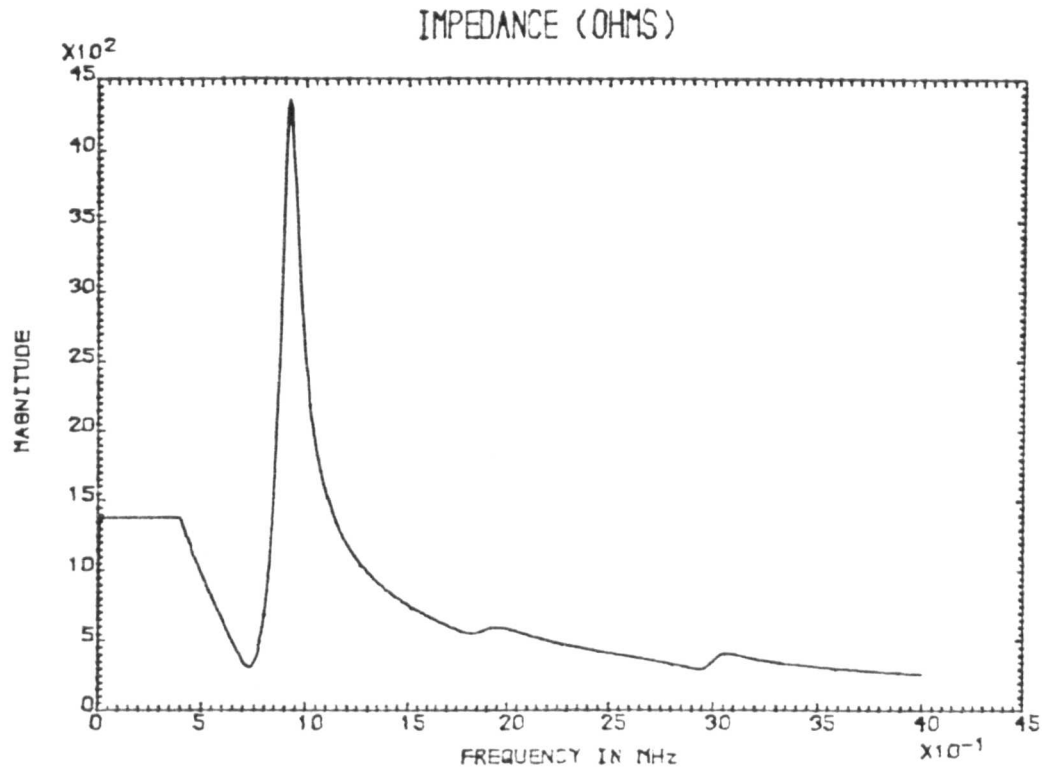

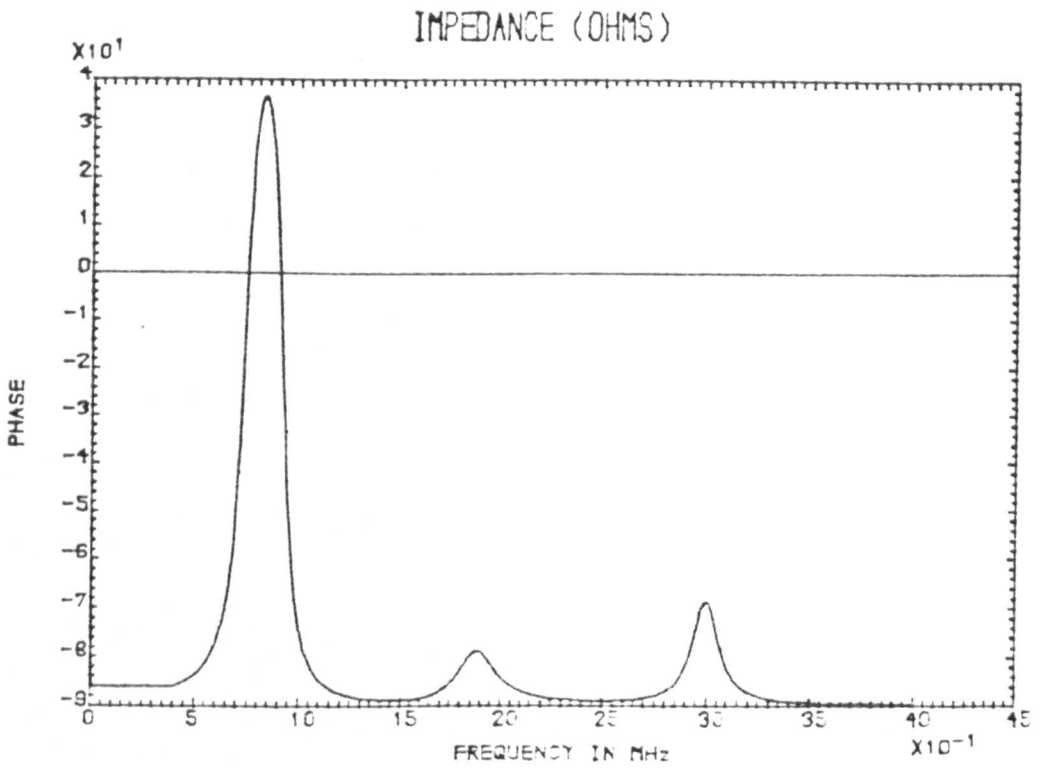

Figure 5.4c Simulated electrical impedance characteristics of a two-dimensional, PZT-5A transducer with configuration ratio equal to 0.42. Simulated according to the two-dimensional linear systems model.

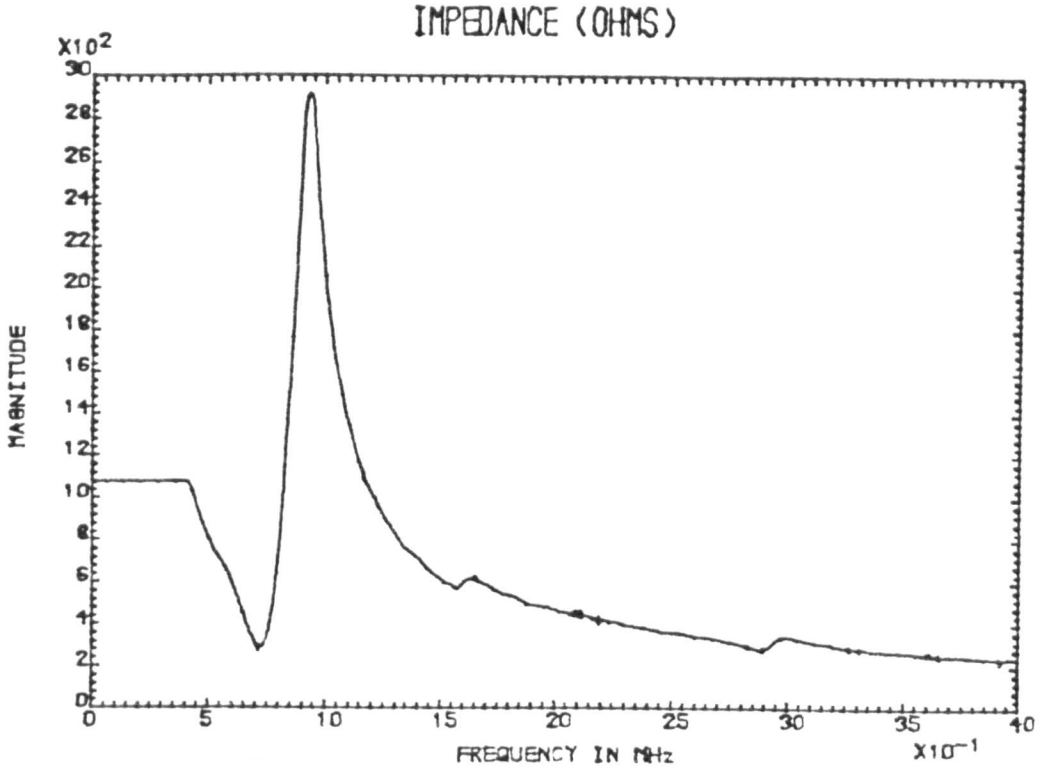

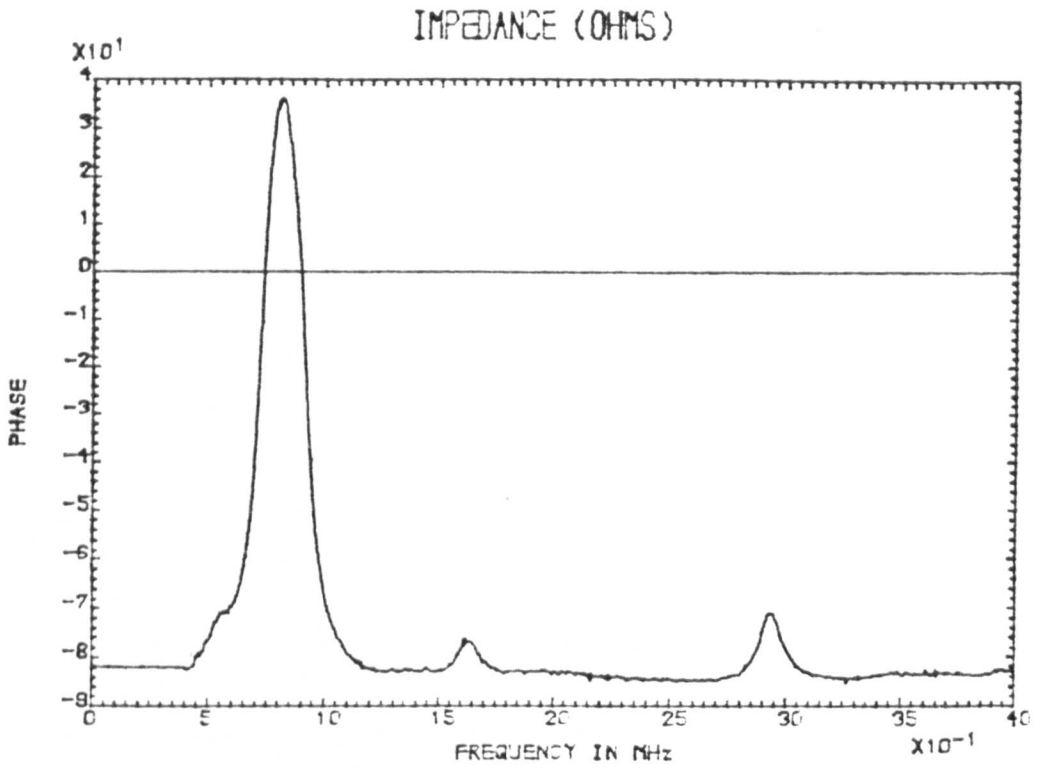

Figure 5.5a Measured electrical impedance characteristics of a two-dimensional, PZT-5A transducer with configuration ratio equal to 0.51.

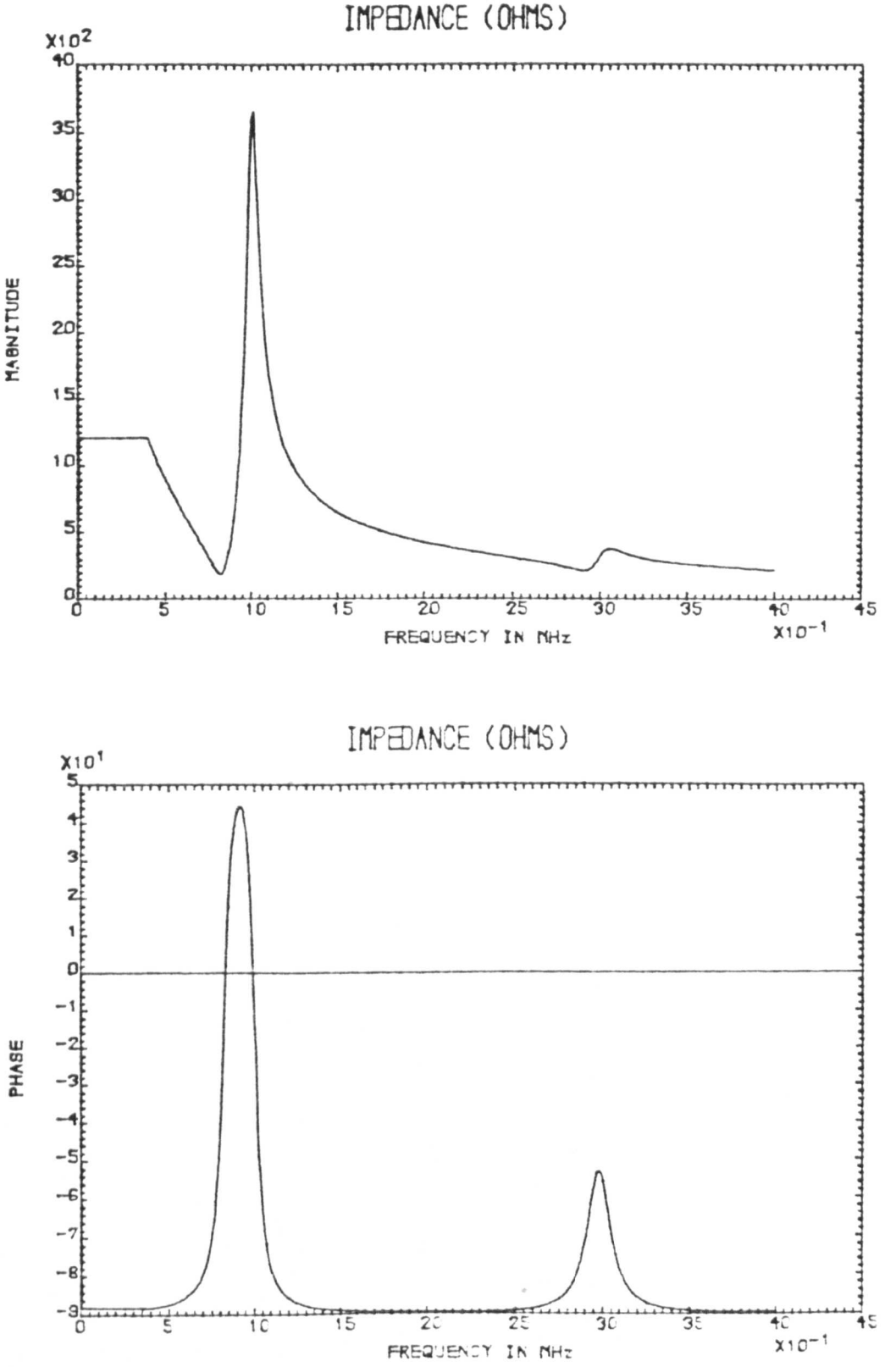

Figure 5.5b Simulated electrical impedance characteristics of a two-dimensional, PZT-5A transducer with configuration ratio equal to 0.51. Simulated according to the modified unidimensional model.

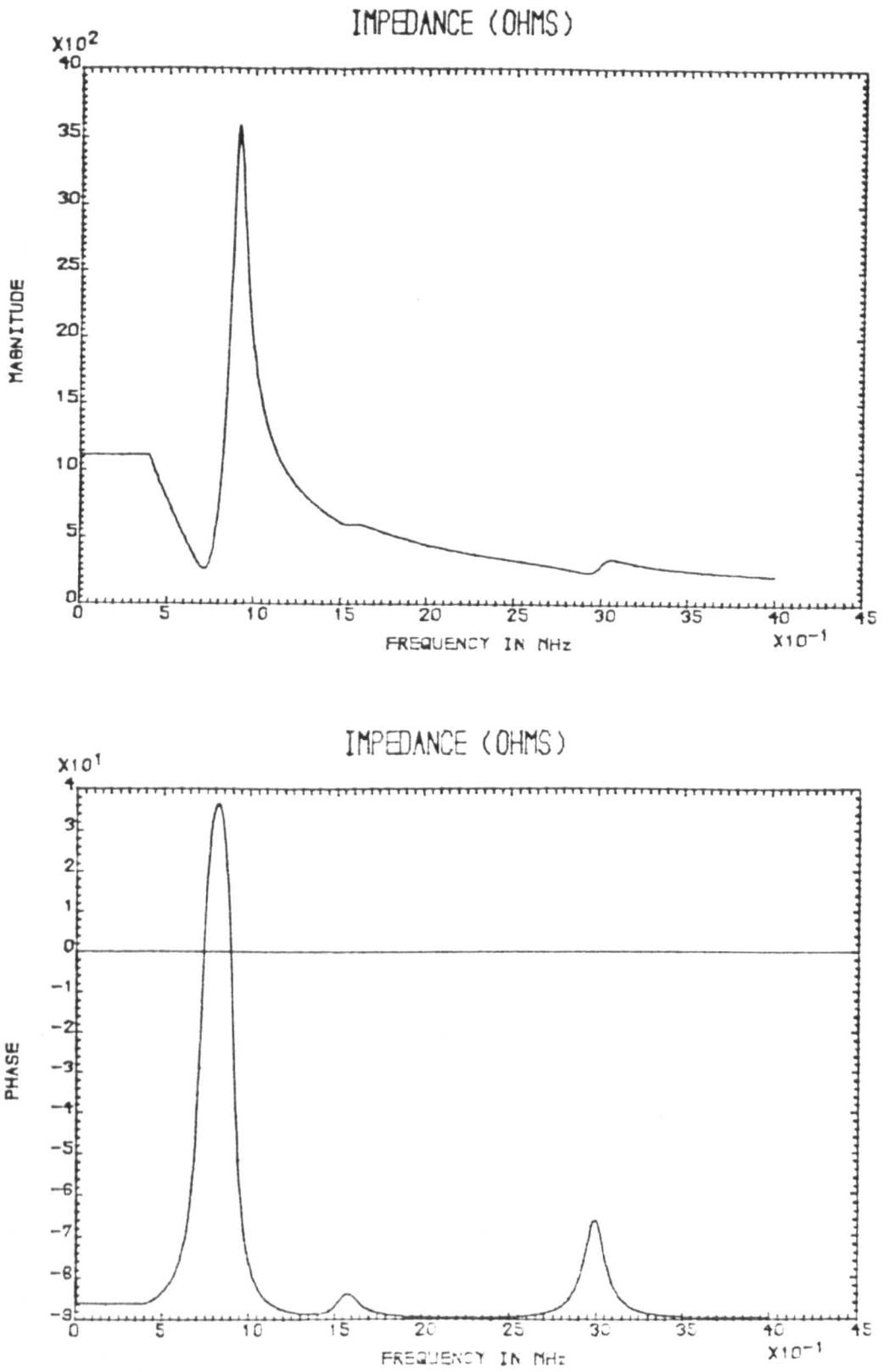

Figure 5.5c Simulated electrical impedance characteristics of a two-dimensional, PZT-5A transducer with configuration ratio equal to 0.51. Simulated according to the two-dimensional linear systems model.

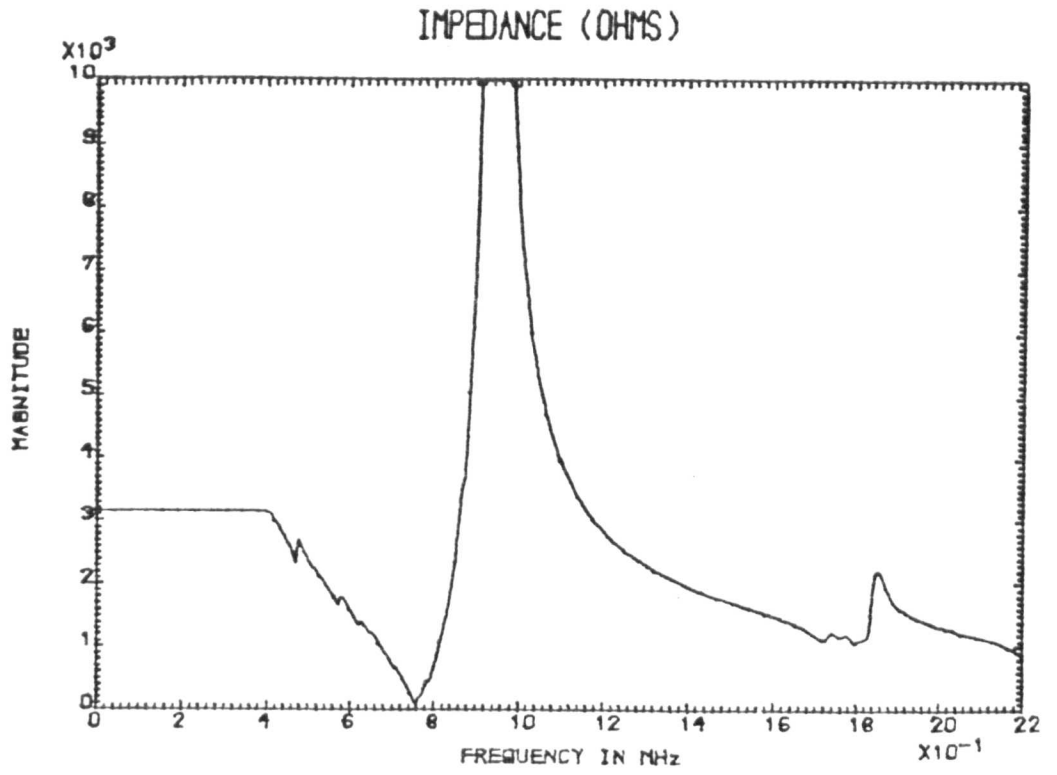

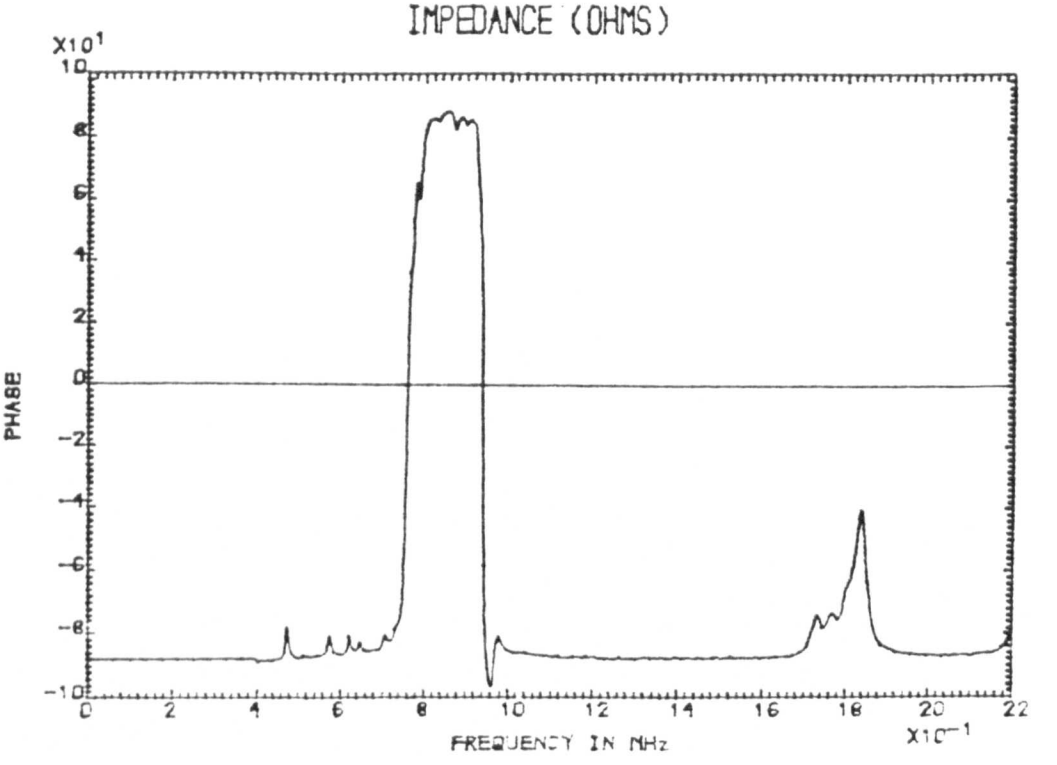

Figure 5.6a Measured electrical impedance characteristics of an air-damped two-dimensional, PZT-5A transducer possessing a configuration ratio of 0.43.

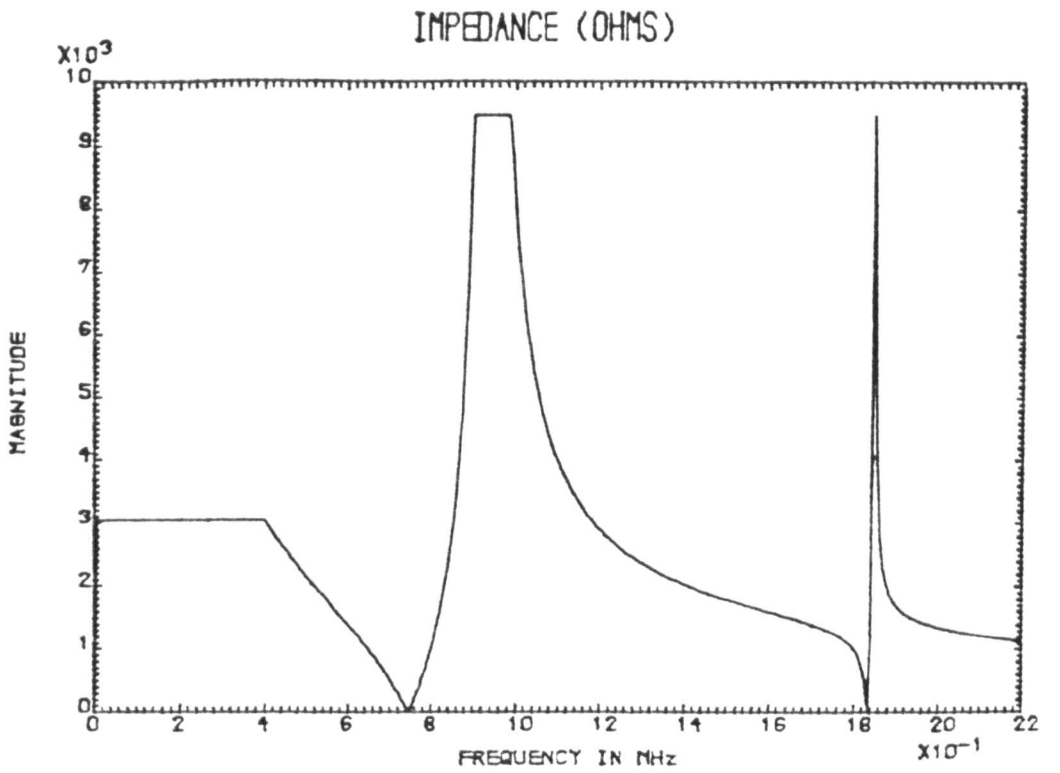

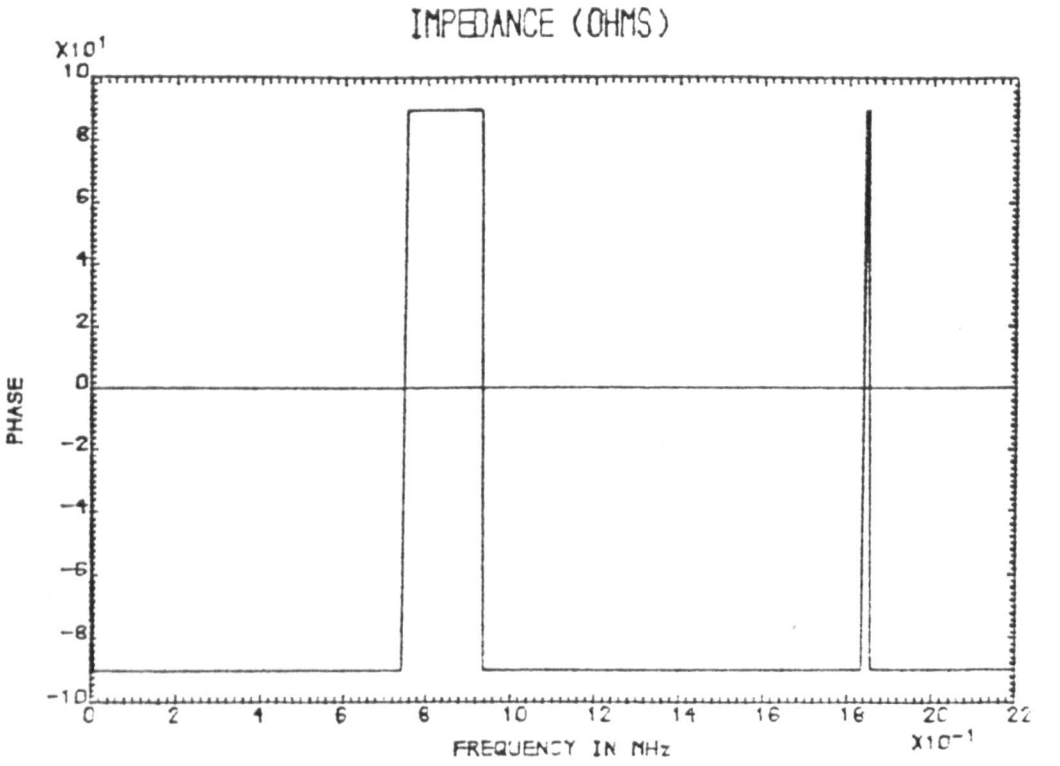

Figure 5.6b Simulated electrical impedance characteristics of an air-damped two-dimensional, PZT-5A transducer possessing a configuration ratio of 0.43. Simulated according to the two-dimensional linear systems model.

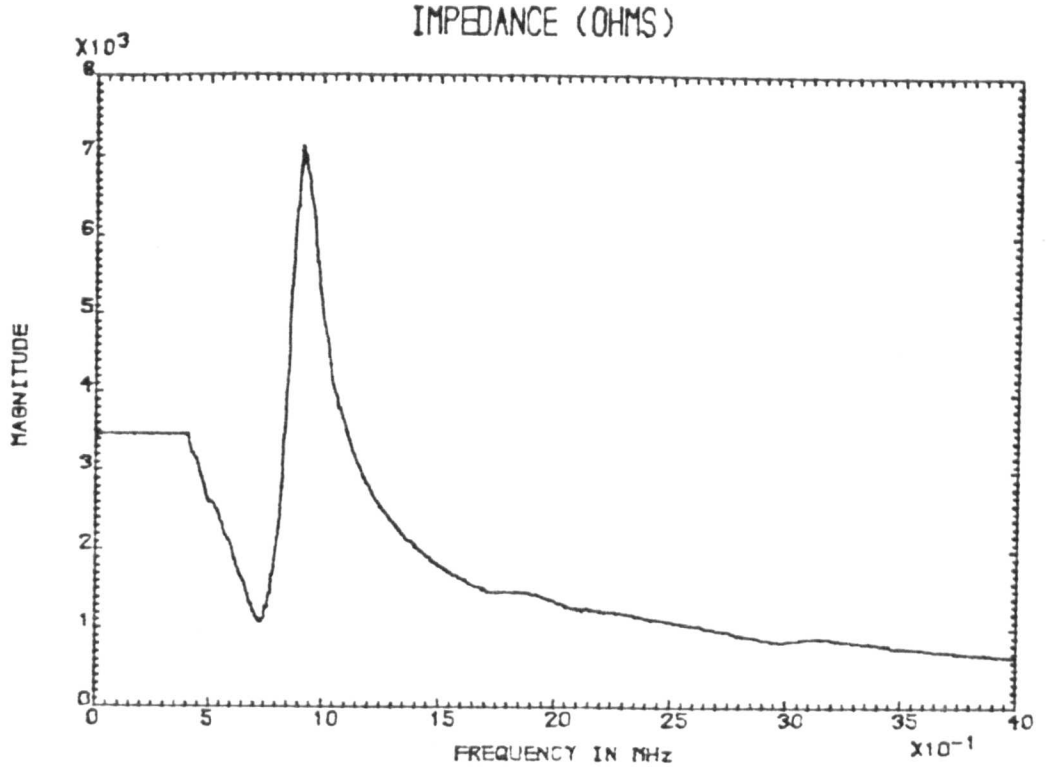

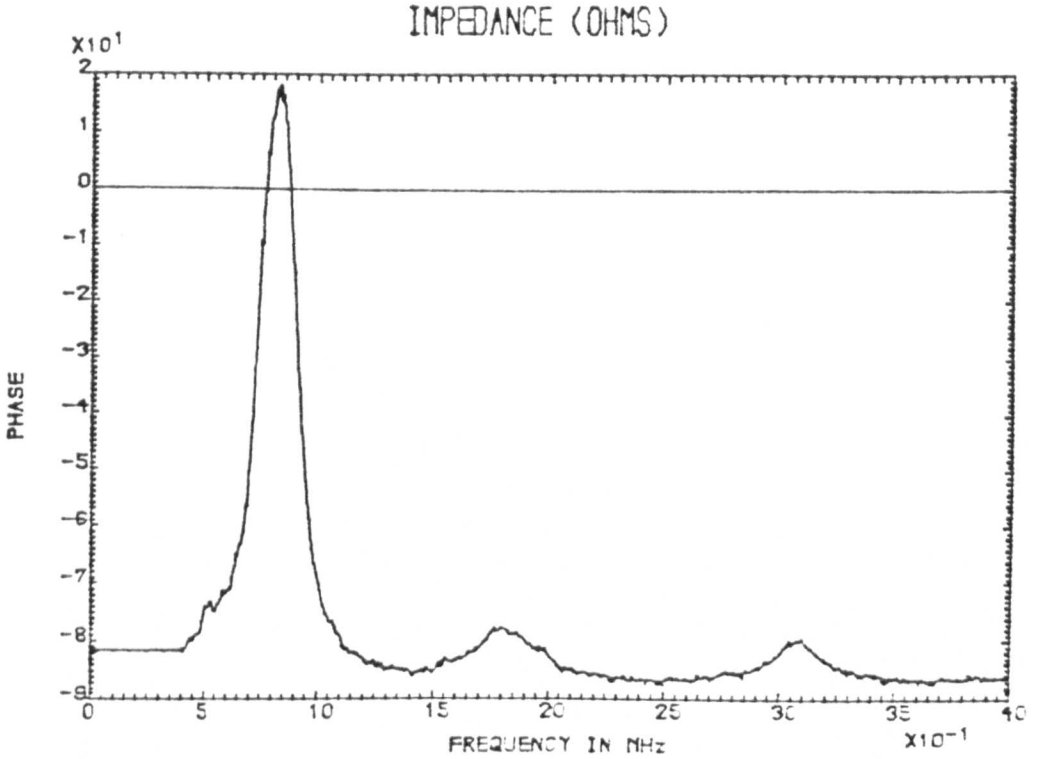

Figure 5.7a Measured electrical impedance characteristics of a two-dimensional, PZT-5A transducer with configuration ratio of 0.41. The left face of the device is damped with loaded epoxy. (Zc=4)

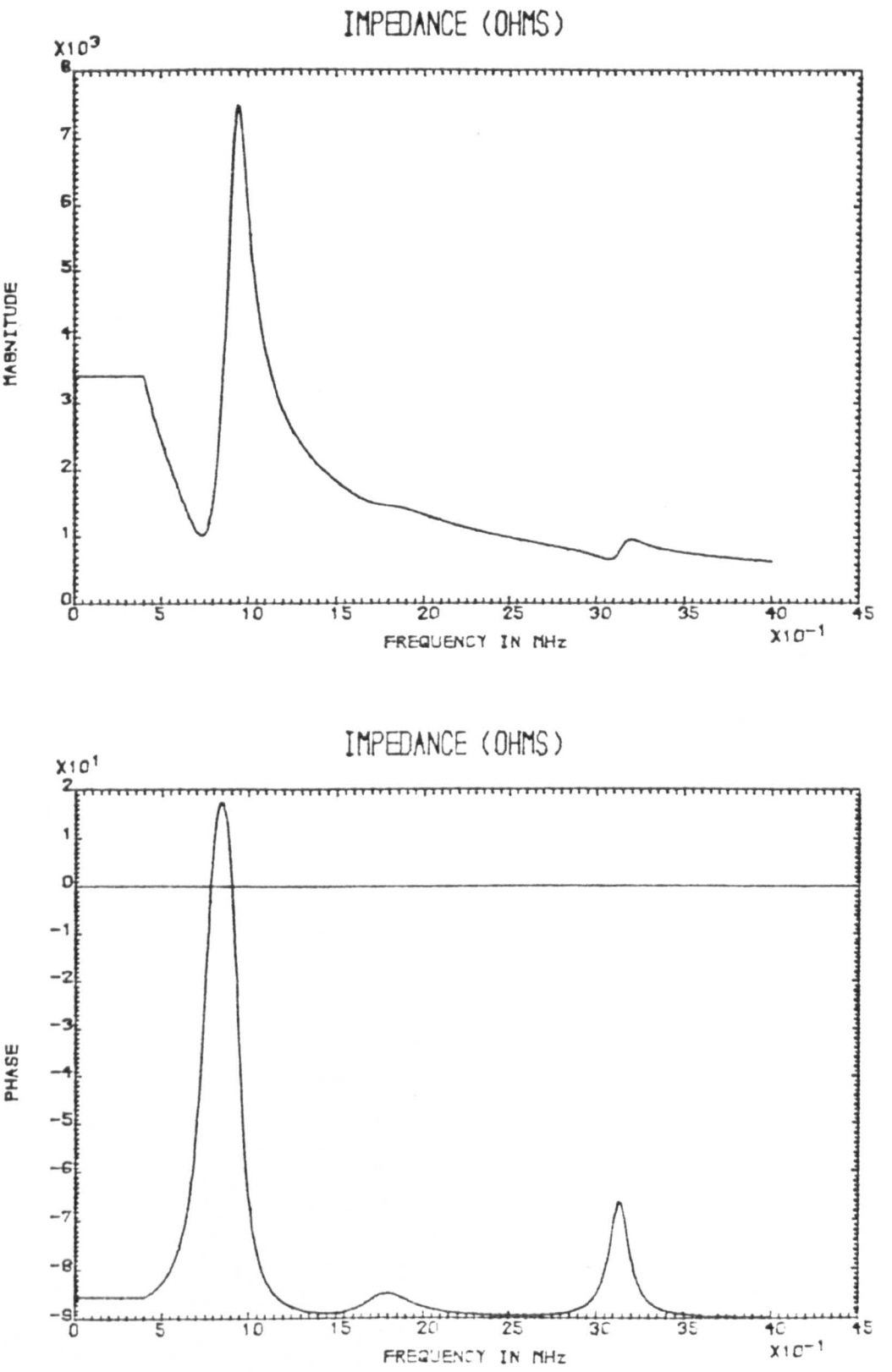

Figure 5.7b Simulated electrical impedance characteristics of a two-dimensional, PZT-5A transducer with configuration ratio of 0.41. The left face of the device is damped with loaded epoxy. (Zc=4) Simulated according to the two-dimensional linear systems model.

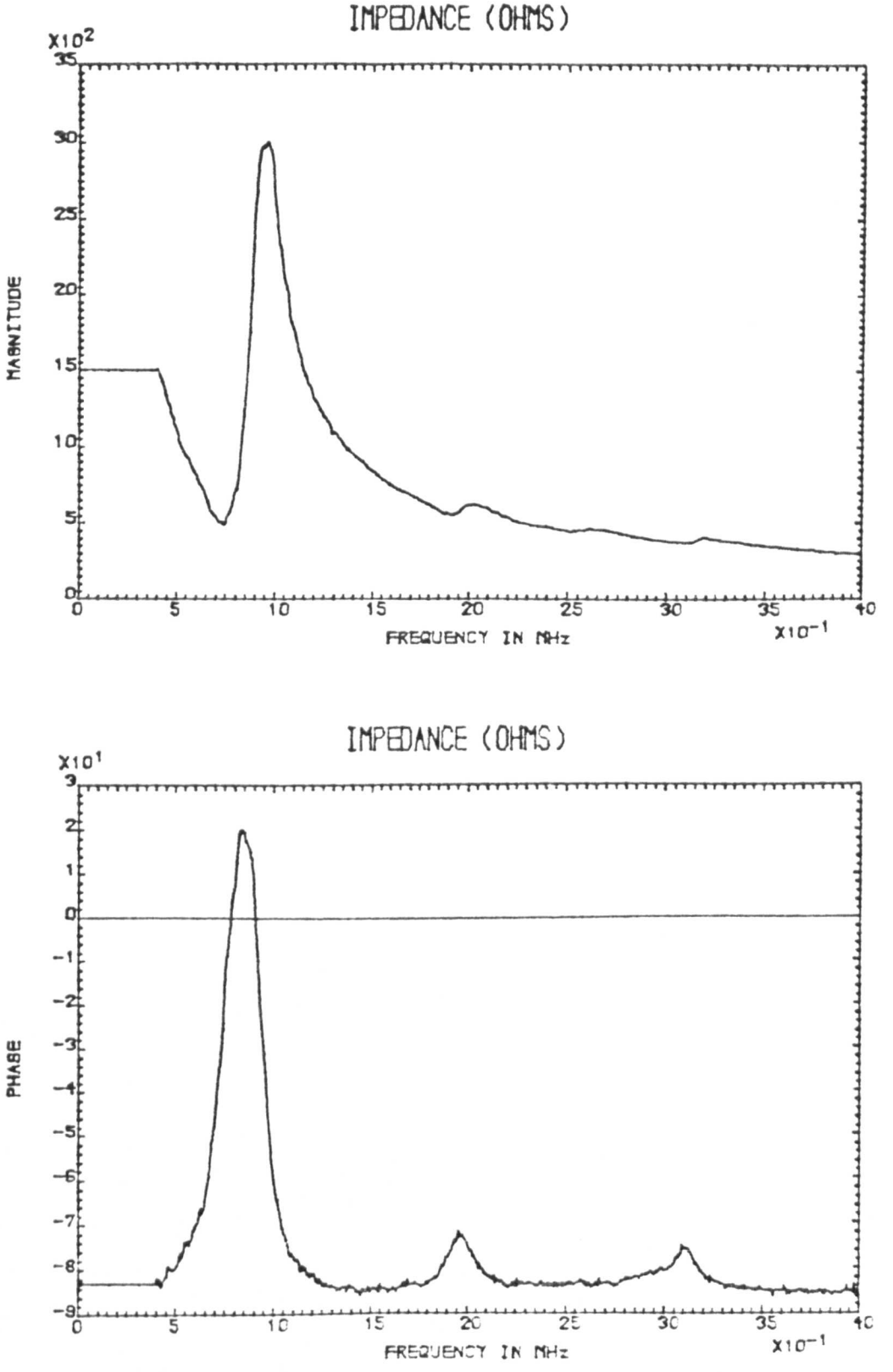

Figure 5.8a Measured electrical impedance characteristics of a two-dimensional, PZT-5A transducer with configuration ratio of 0.39. The rear face of the device is damped with loaded epoxy. (Zc=4)

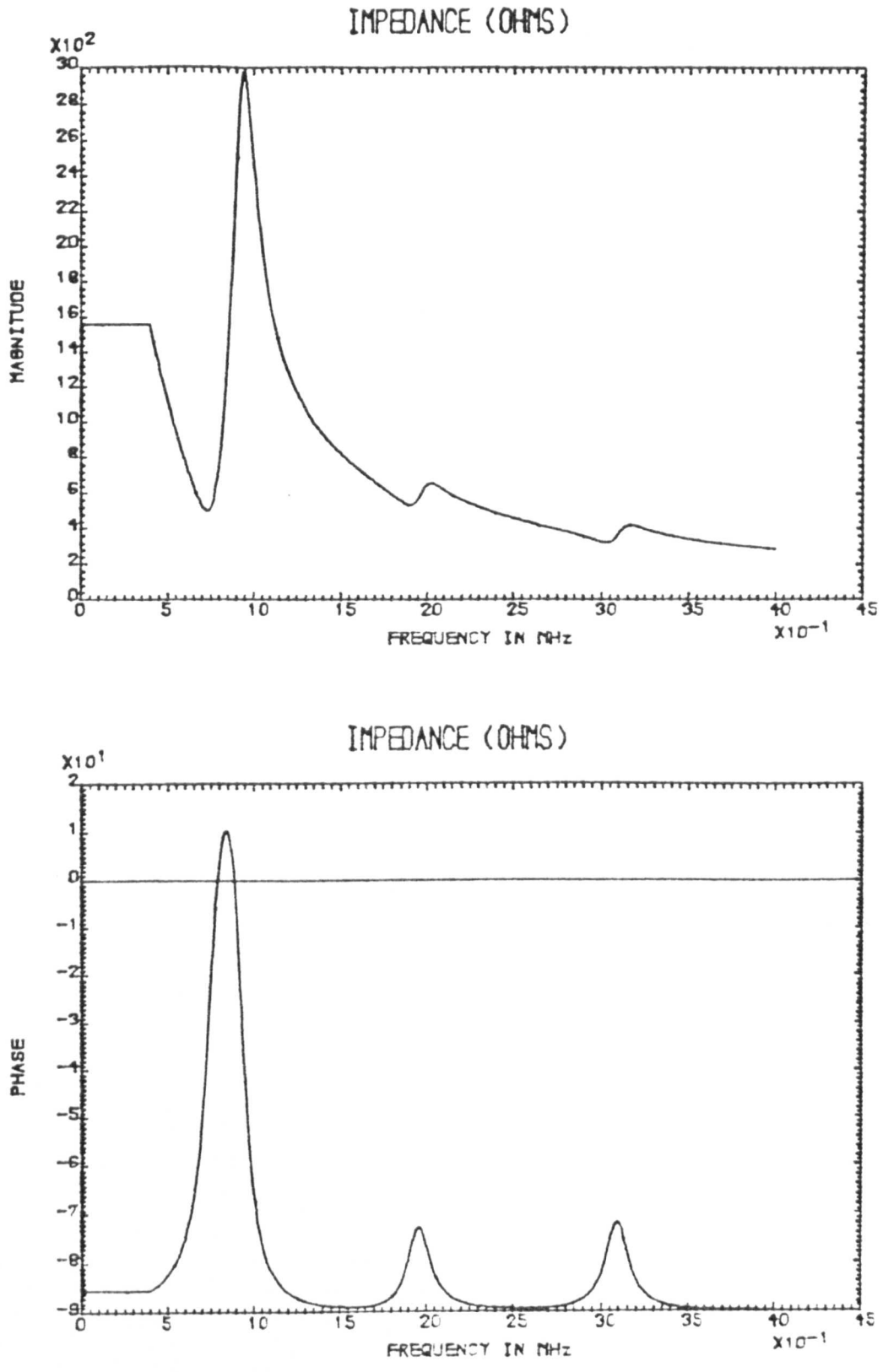

Figure 5.8b Simulated electrical impedance characteristics of a two-dimensional, PZT-5A transducer with configuration ratio of 0.39. The rear face of the device is damped with loaded epoxy. (Zc=4) Simulated according to the two-dimensional linear systems model.

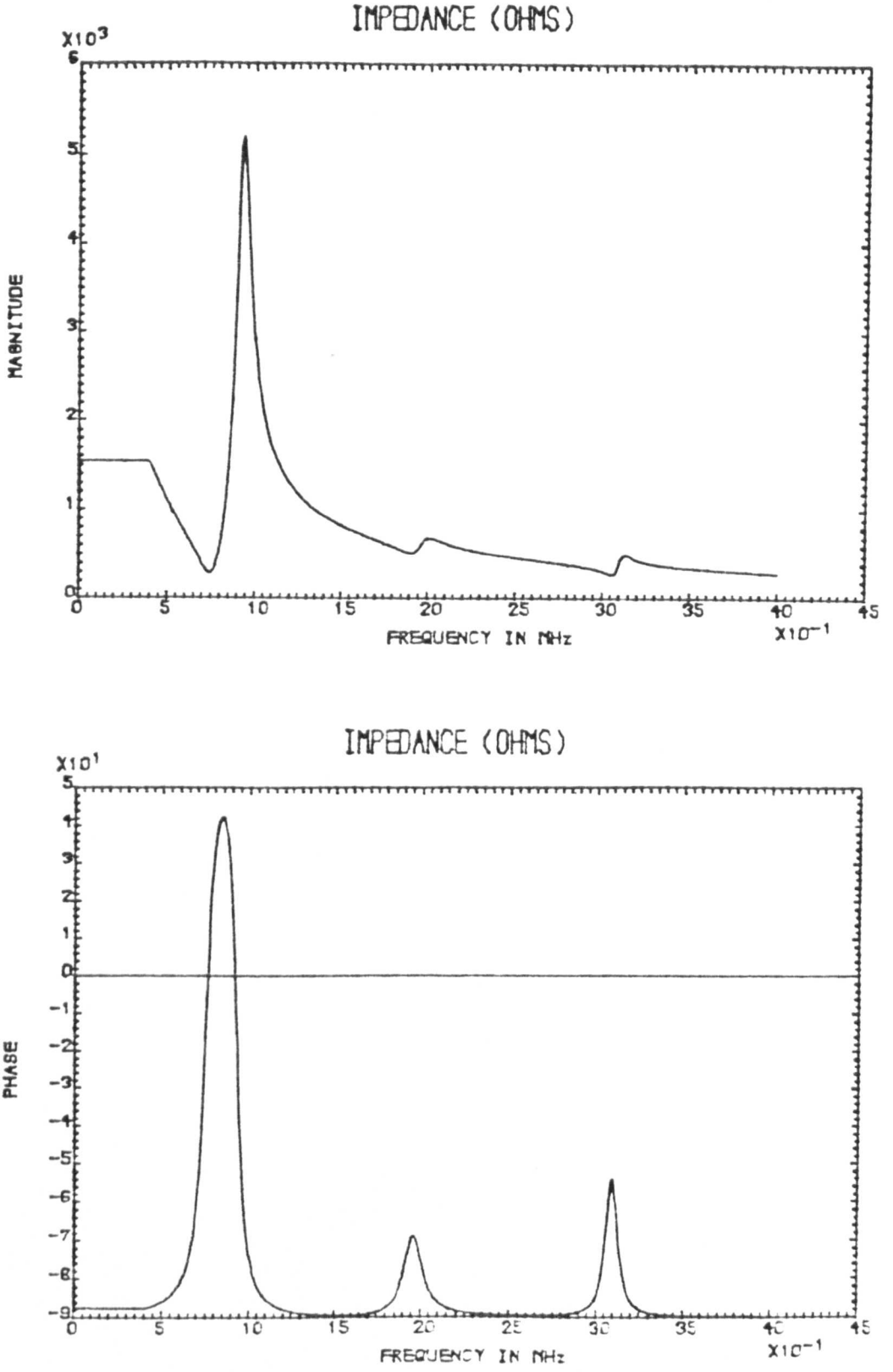

Figure 5.8c Simulated electrical impedance characteristics of a two-dimensional, PZT-5A transducer with configuration ratio of 0.39. All faces are damped with an acoustic impedance of 1.5. Simulated according to the two-dimensional linear systems model.

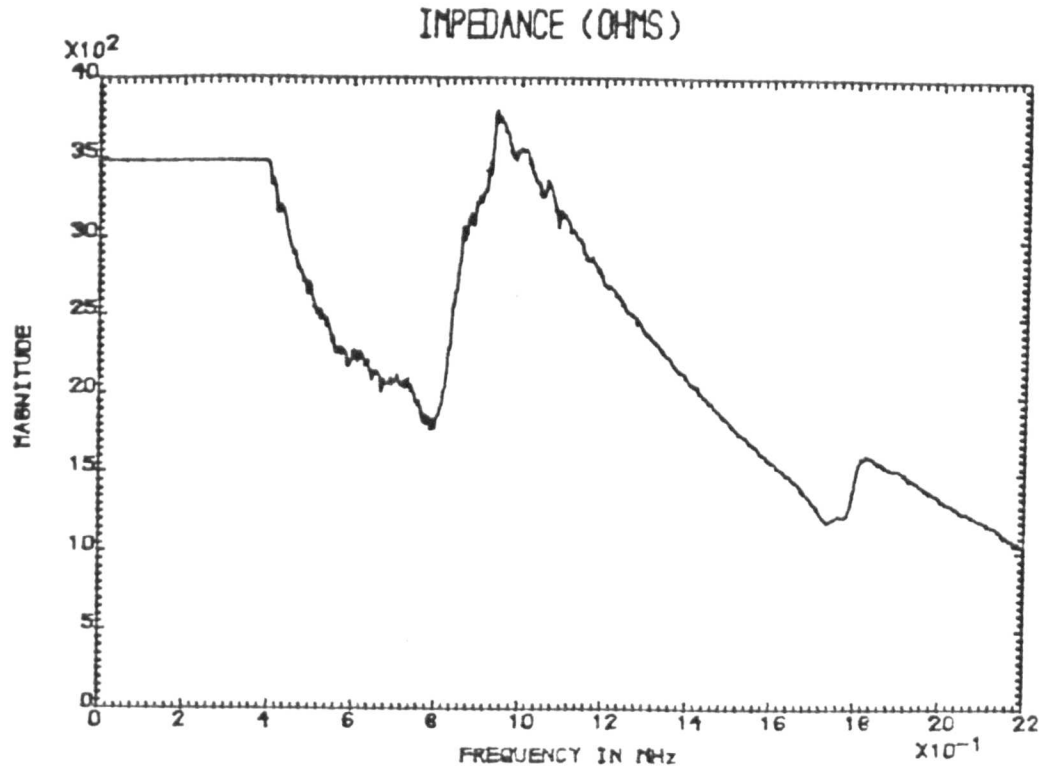

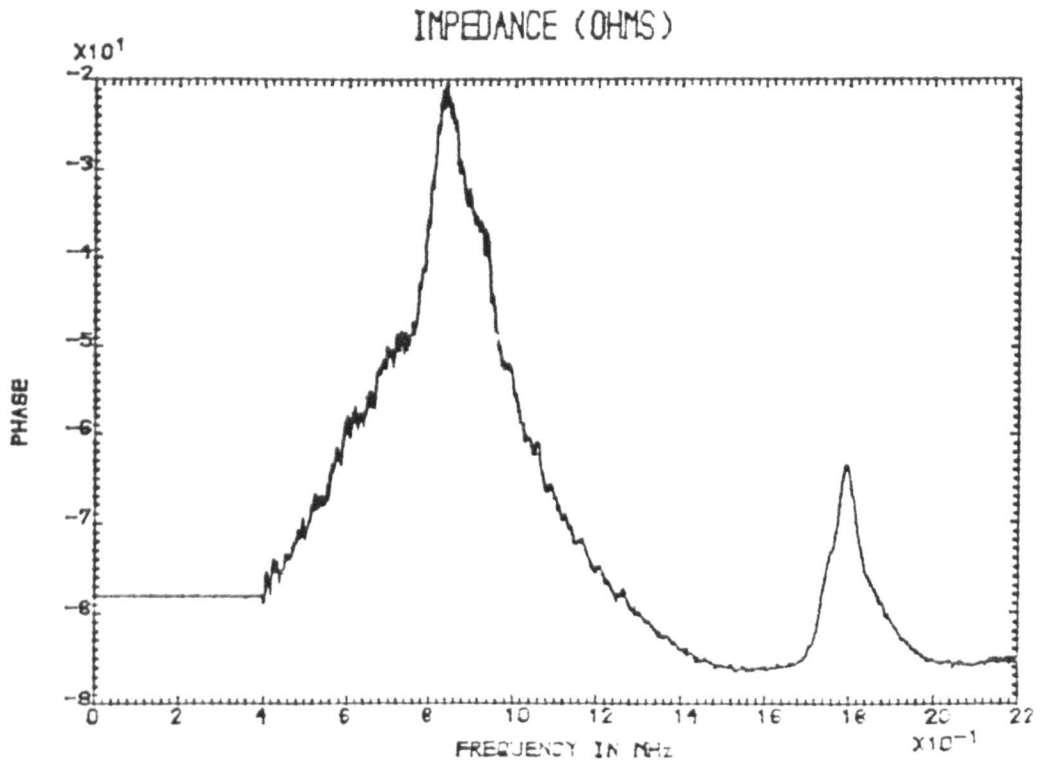

Figure 5.9a Measured electrical impedance characteristics of a two-dimensional, PZT-5A transducer with configuration ratio of 0.43. The rear face of the device is damped with lead.(Zc=24)

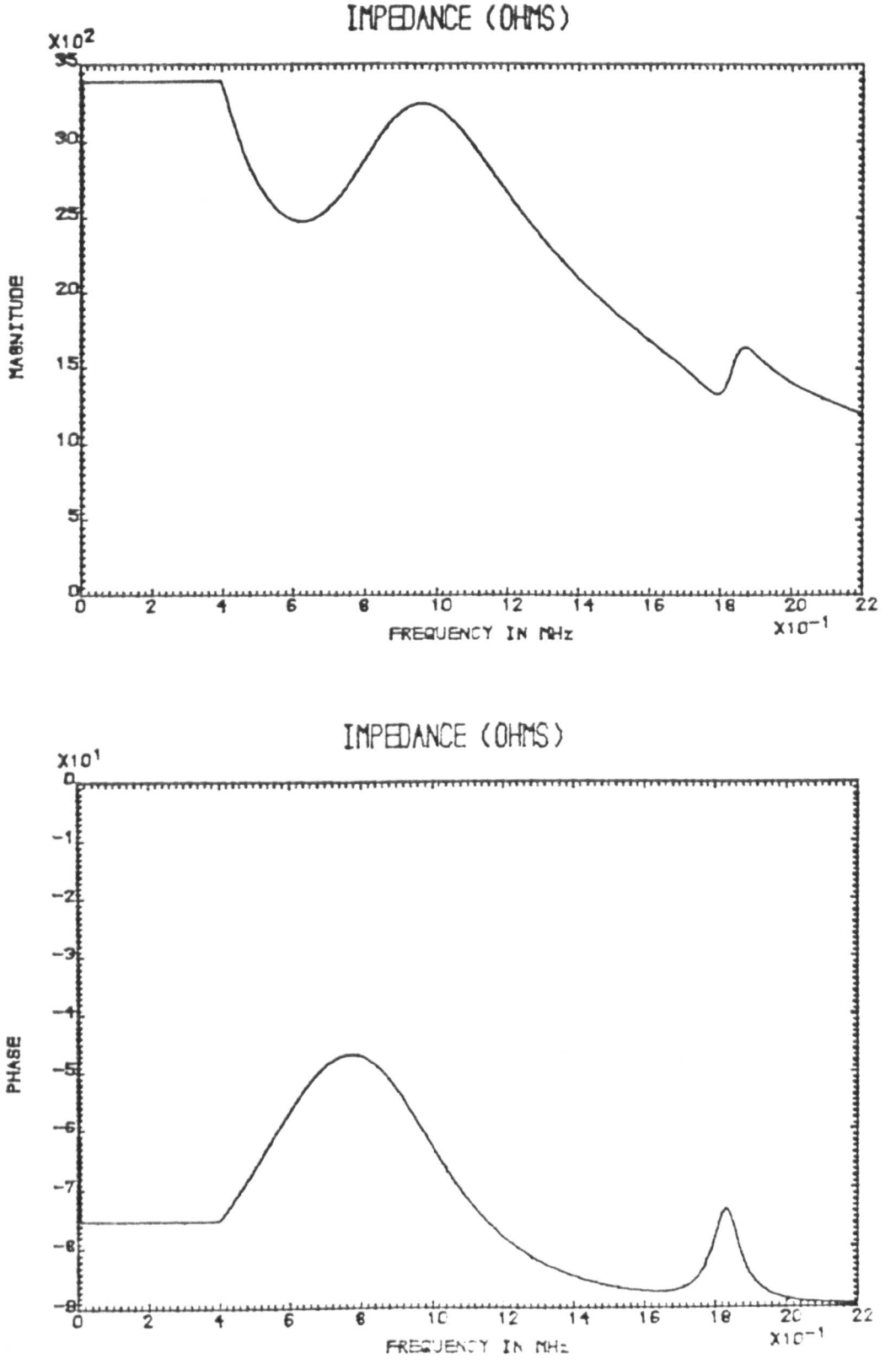

Figure 5.9b Simulated electrical impedance characteristics of a two-dimensional, PZT-5A transducer with configuration ratio of 0.43. The rear face of the device is damped with lead. (Zc = 24) Simulated according to the two-dimensional linear systems model.

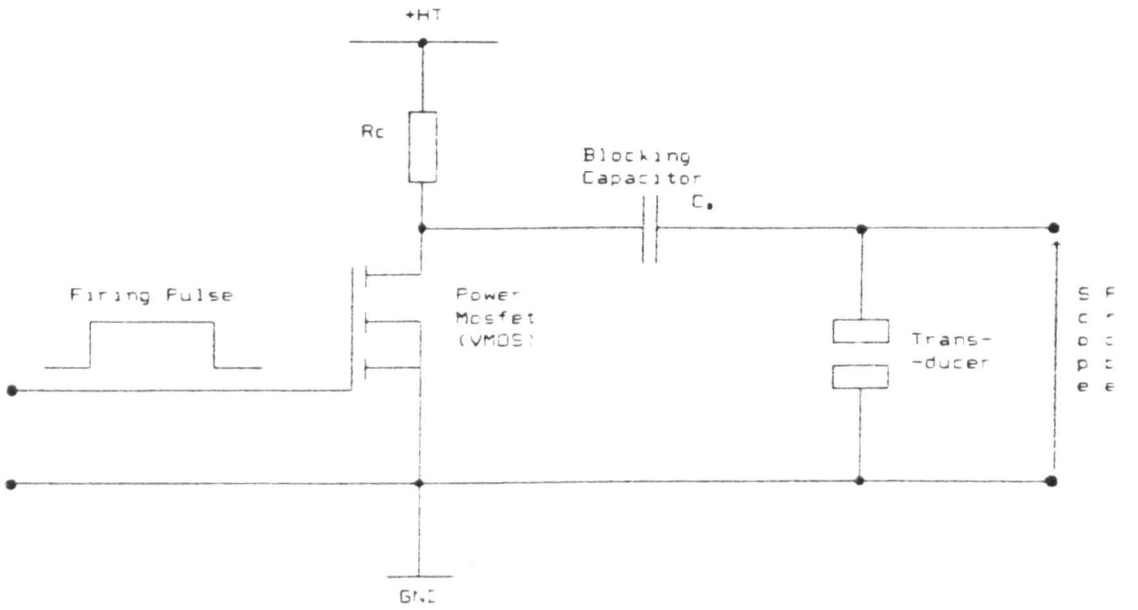

Figure 5.10 Firing circuit #1

5.11(a)

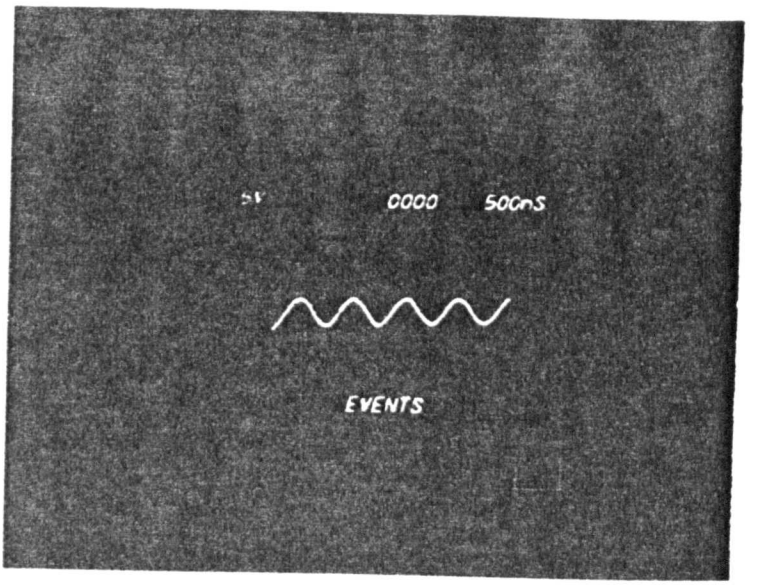

TRANSMITTER VOLTAGE 5.11(b)

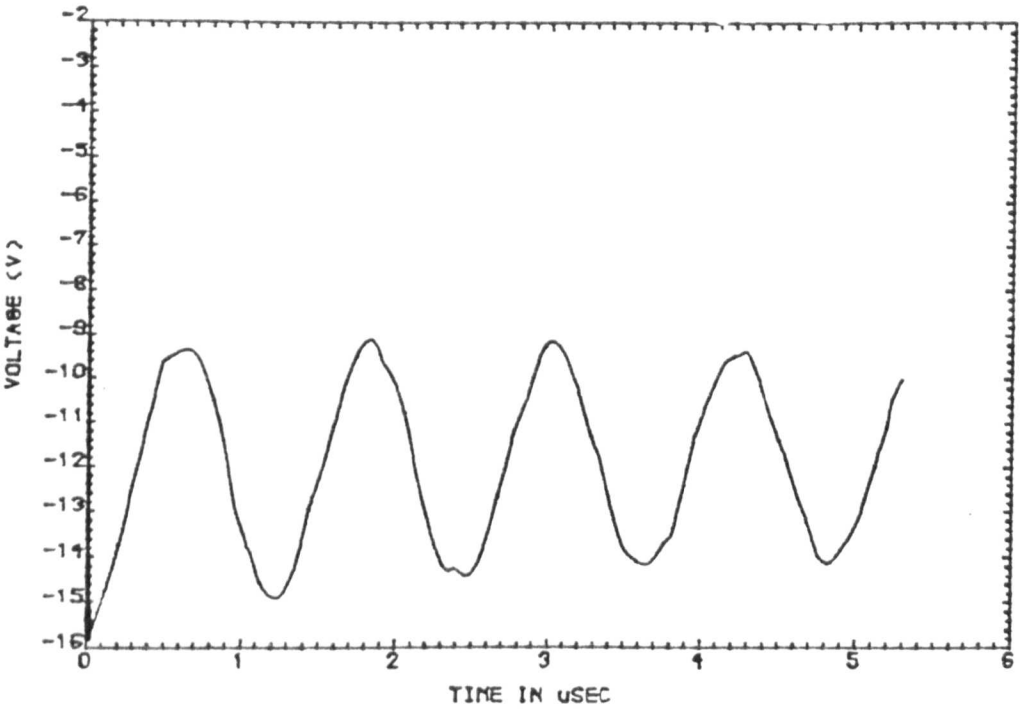

Figure 5.11 Measured and simulated transducer voltage response when excited by firing circuit #1.

5.12(a)

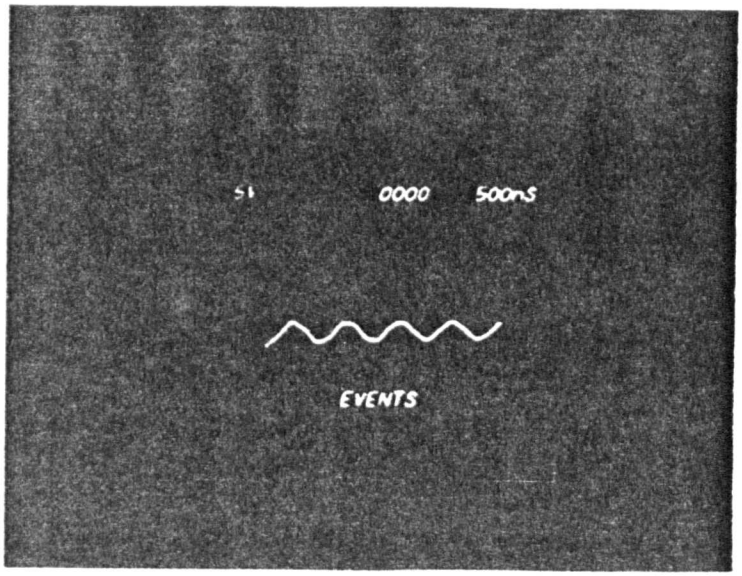

TRANSMITTER VOLTAGE 5.12(b)

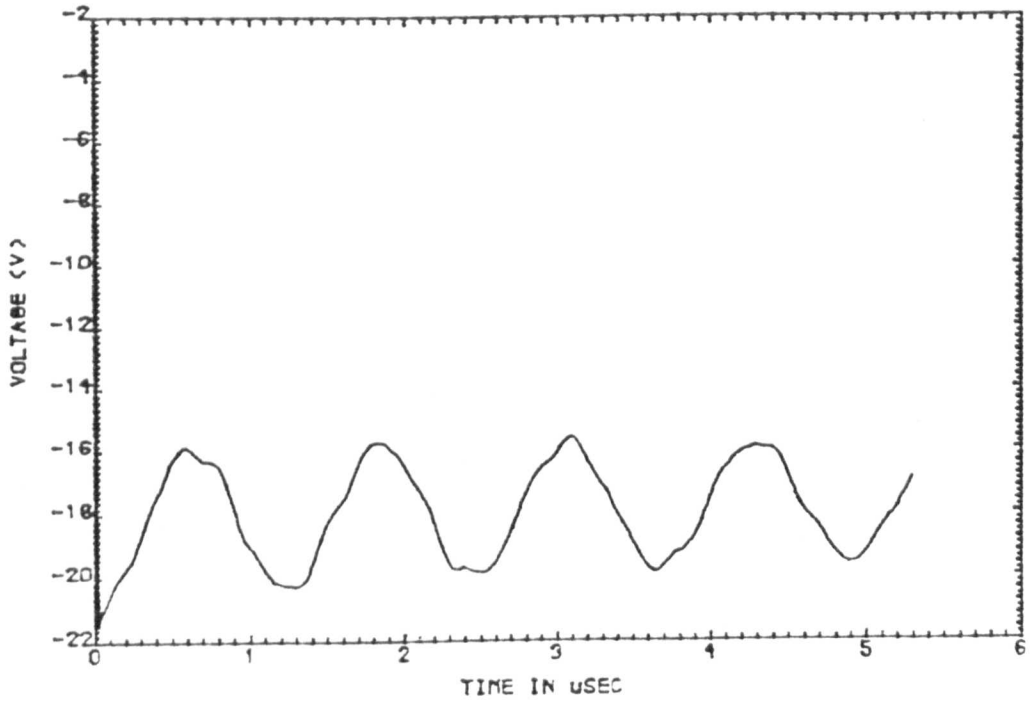

Figure 5.12 Measured and simulated transducer voltage response when excited by firing circuit #1.

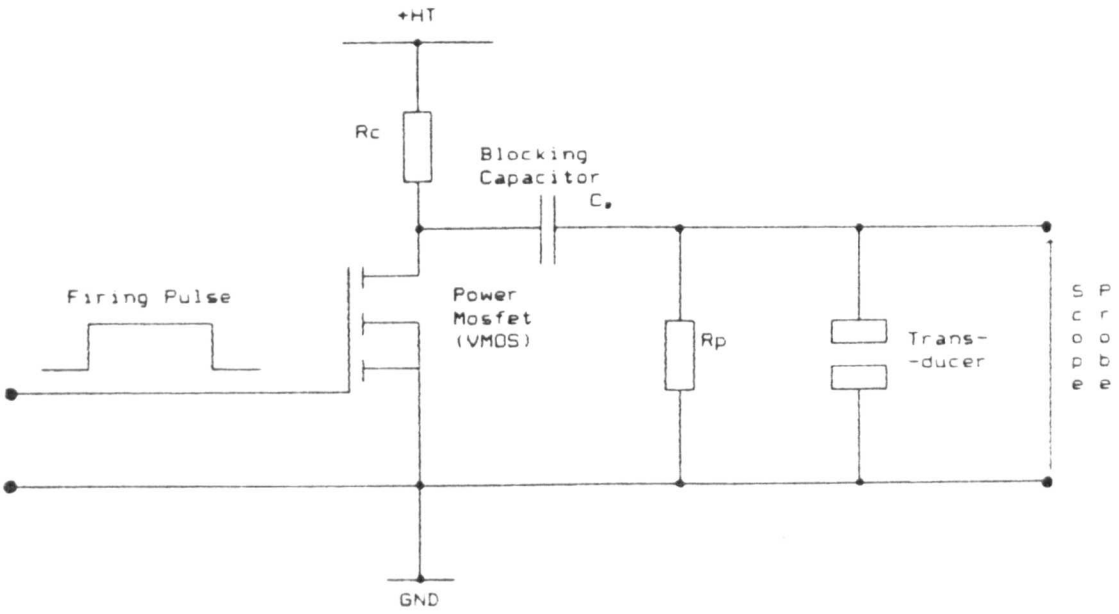

Figure 5.13 Firing circuit #2

5.14(a)

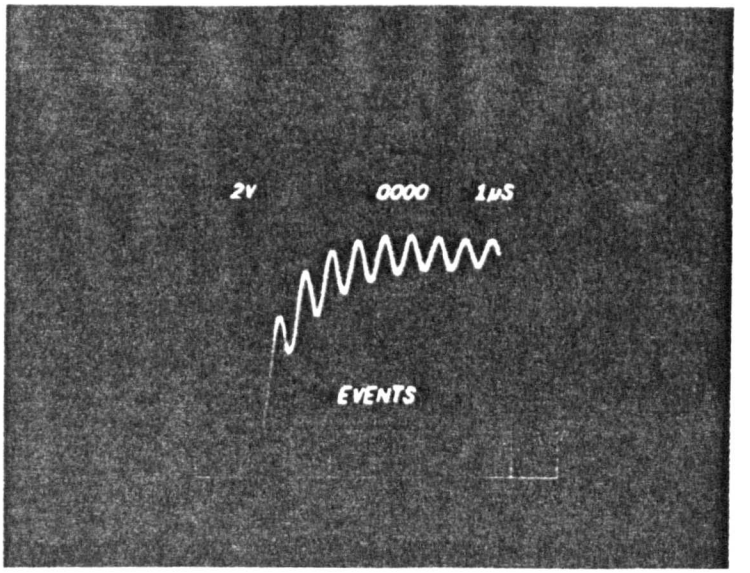

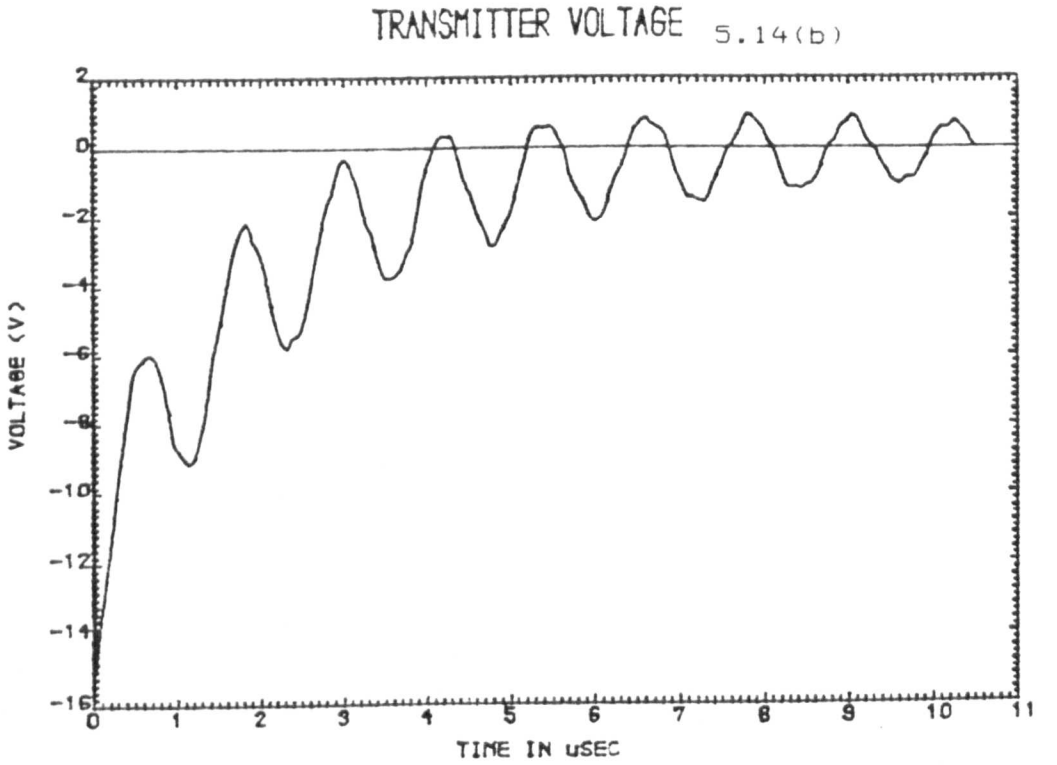

Figure 5.14 Measured and simulated transducer voltage response when excited by firing circuit #2.

5.15(a)

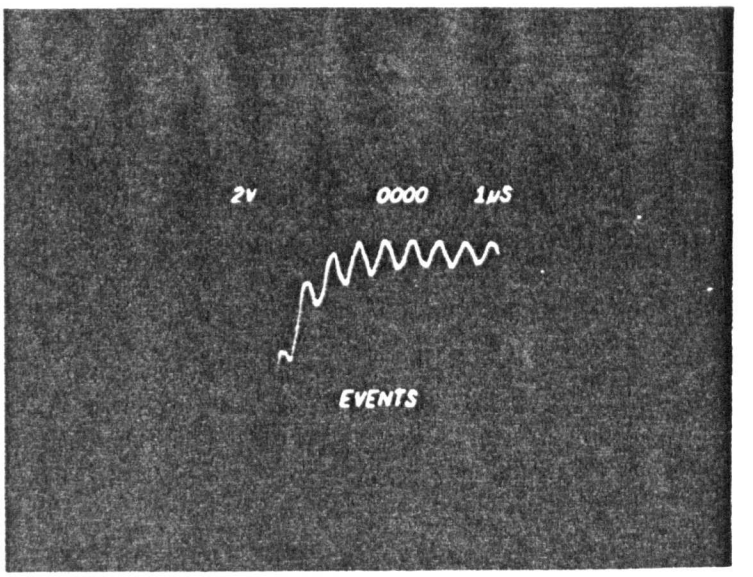

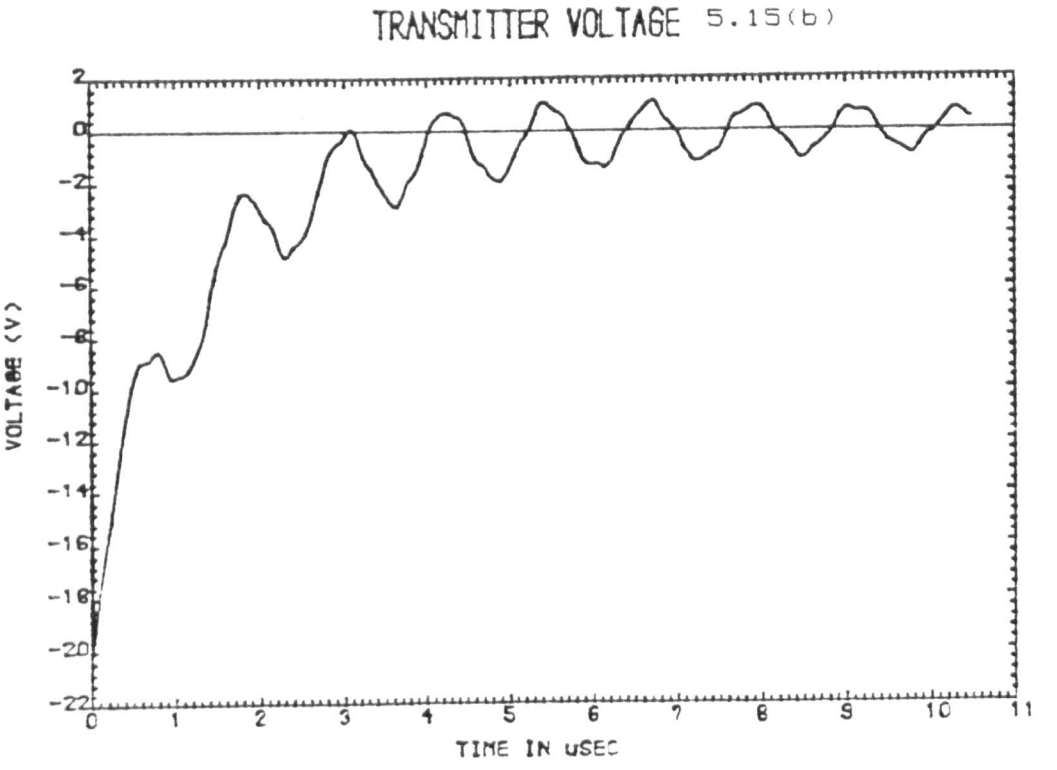

Figure 5.15 Measured and simulated transducer voltage response when excited by firing circuit #2.

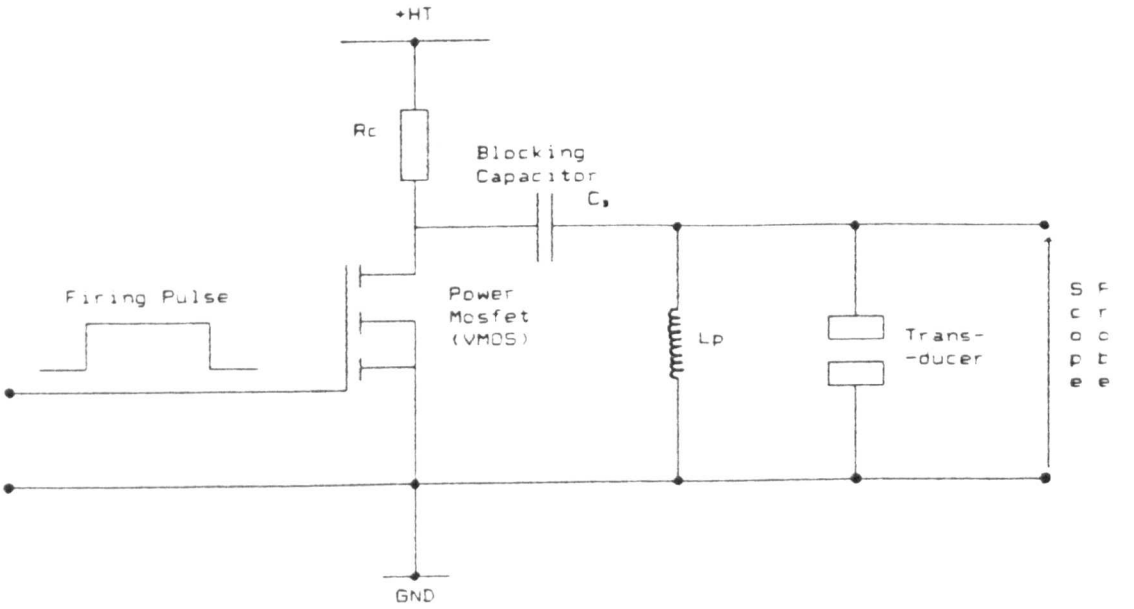

Figure 5.16 Firing circuit #3

5.17(a)

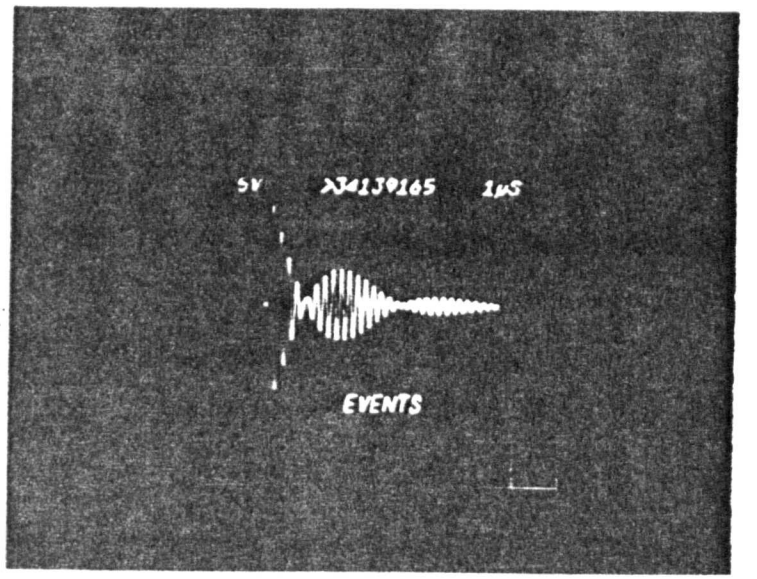

VOLTAGE (V) 5.17(b)

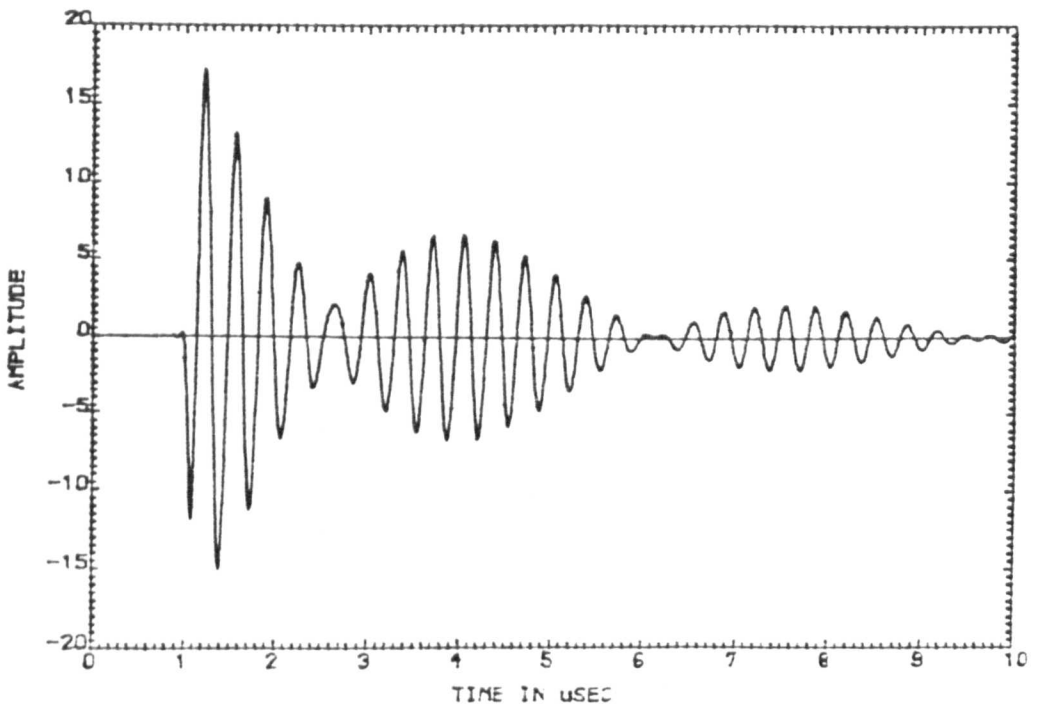

Figure 5.17 Measured and simulated transducer voltage response when excited by firing circuit #3.

5.18(a)

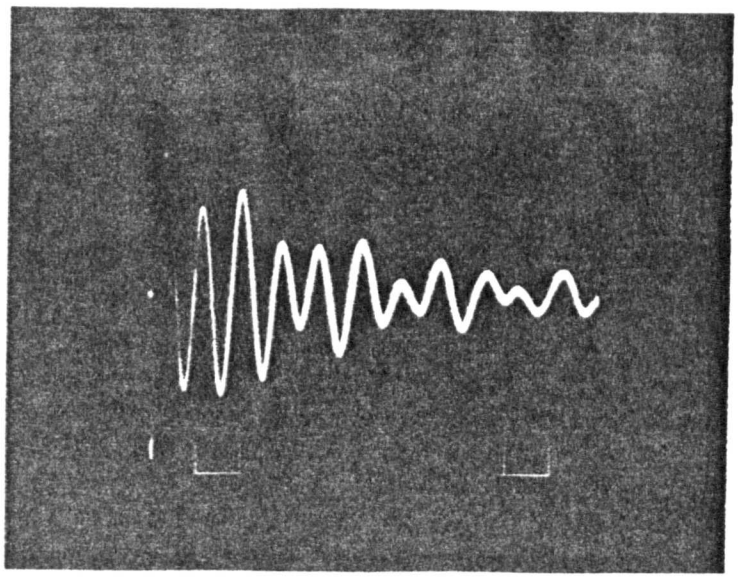

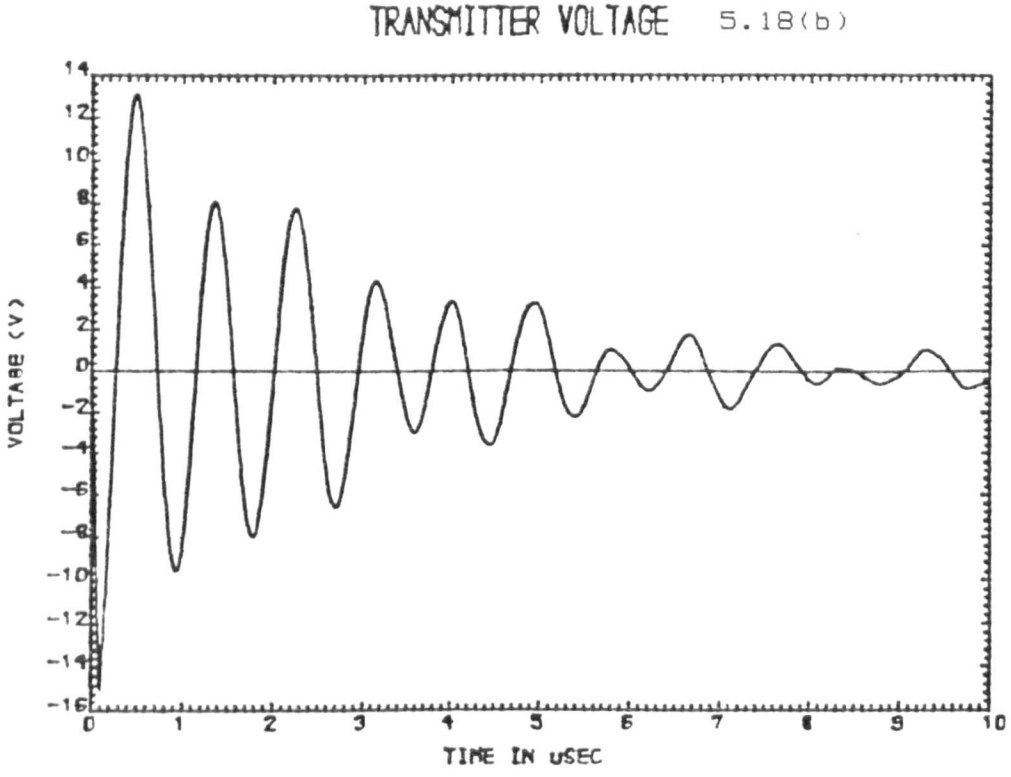

Figure 5.18 Measured and simulated transducer voltage response when excited by firing circuit #3.

5.19(a)

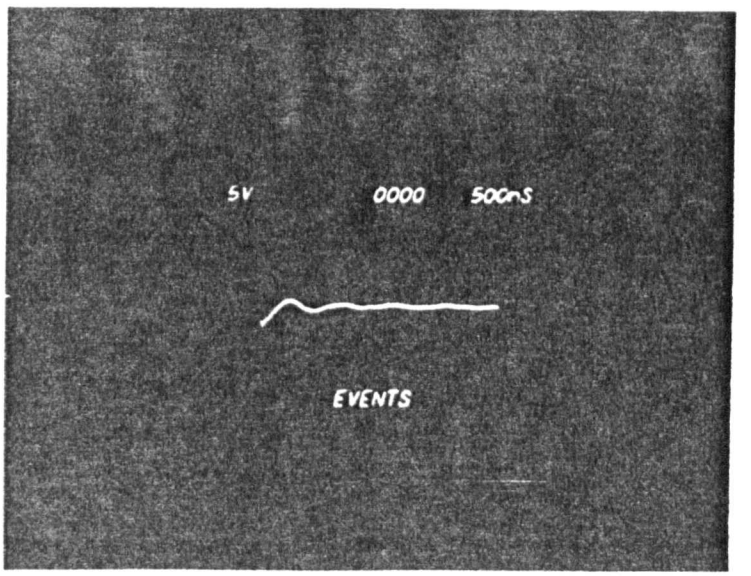

5.19(b)

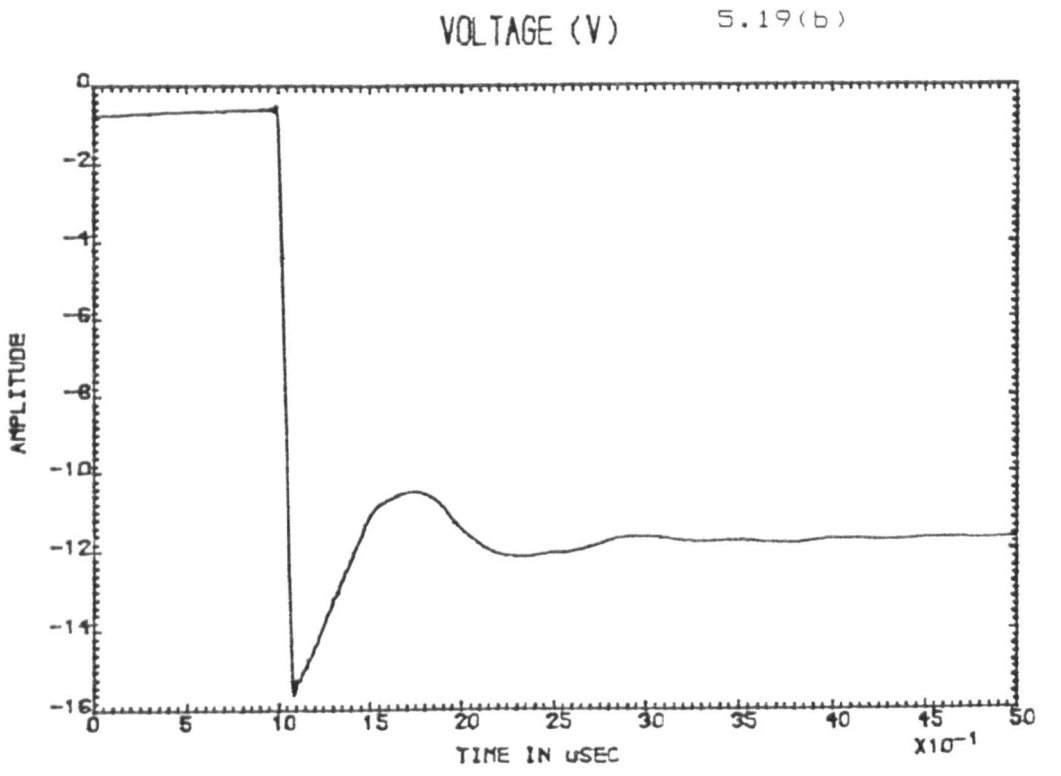

Figure 5.19 Measured and simulated transducer voltage response when excited by firing circuit #1. The transducer is mechanically damped on the rear face with lead.

5.20(a)

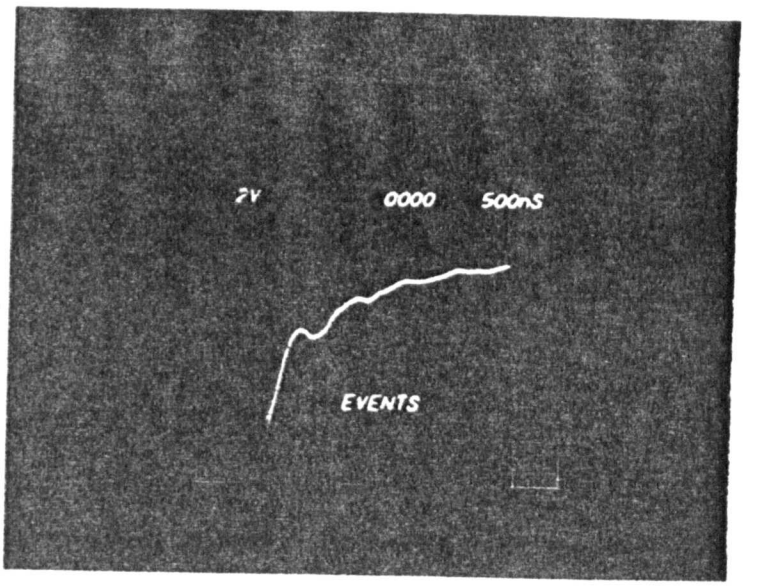

VOLTAGE (V) 5.20(b)

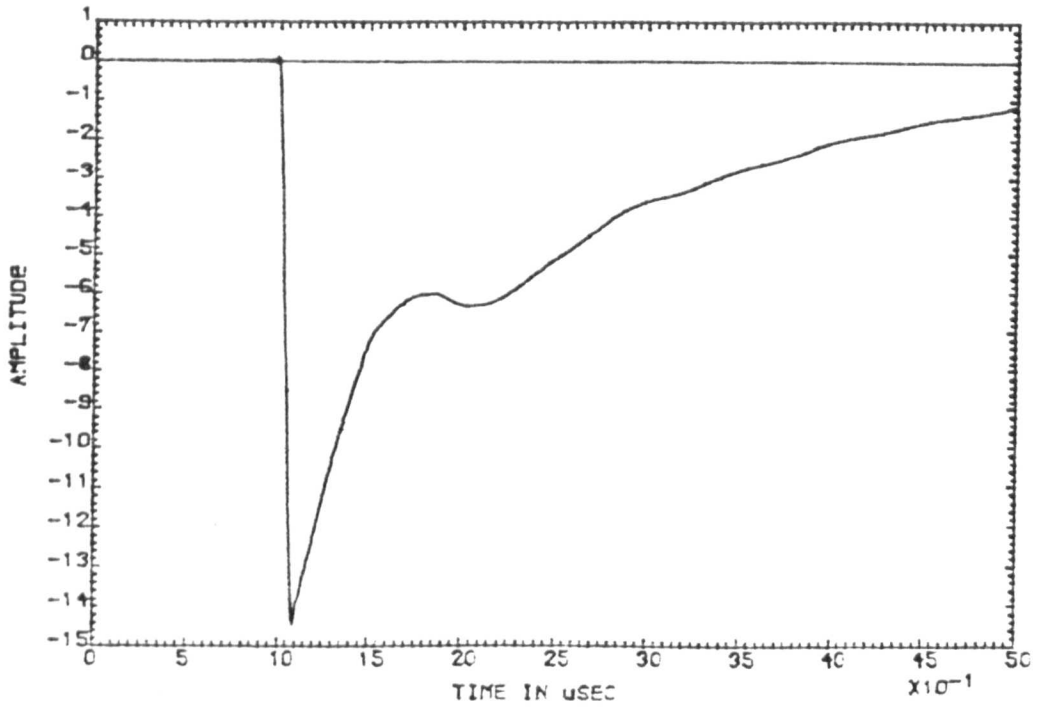

Figure 5.20 Measured and simulated transducer voltage response when excited by firing circuit #2. The transducer is mechanically damped on the rear face with lead.

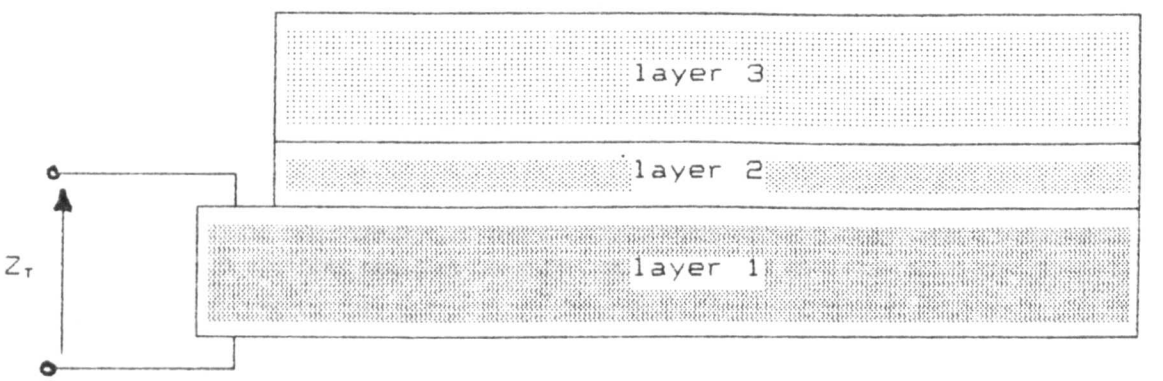

Figure 5.21 Configuration of the layered structure in the thickness dimension

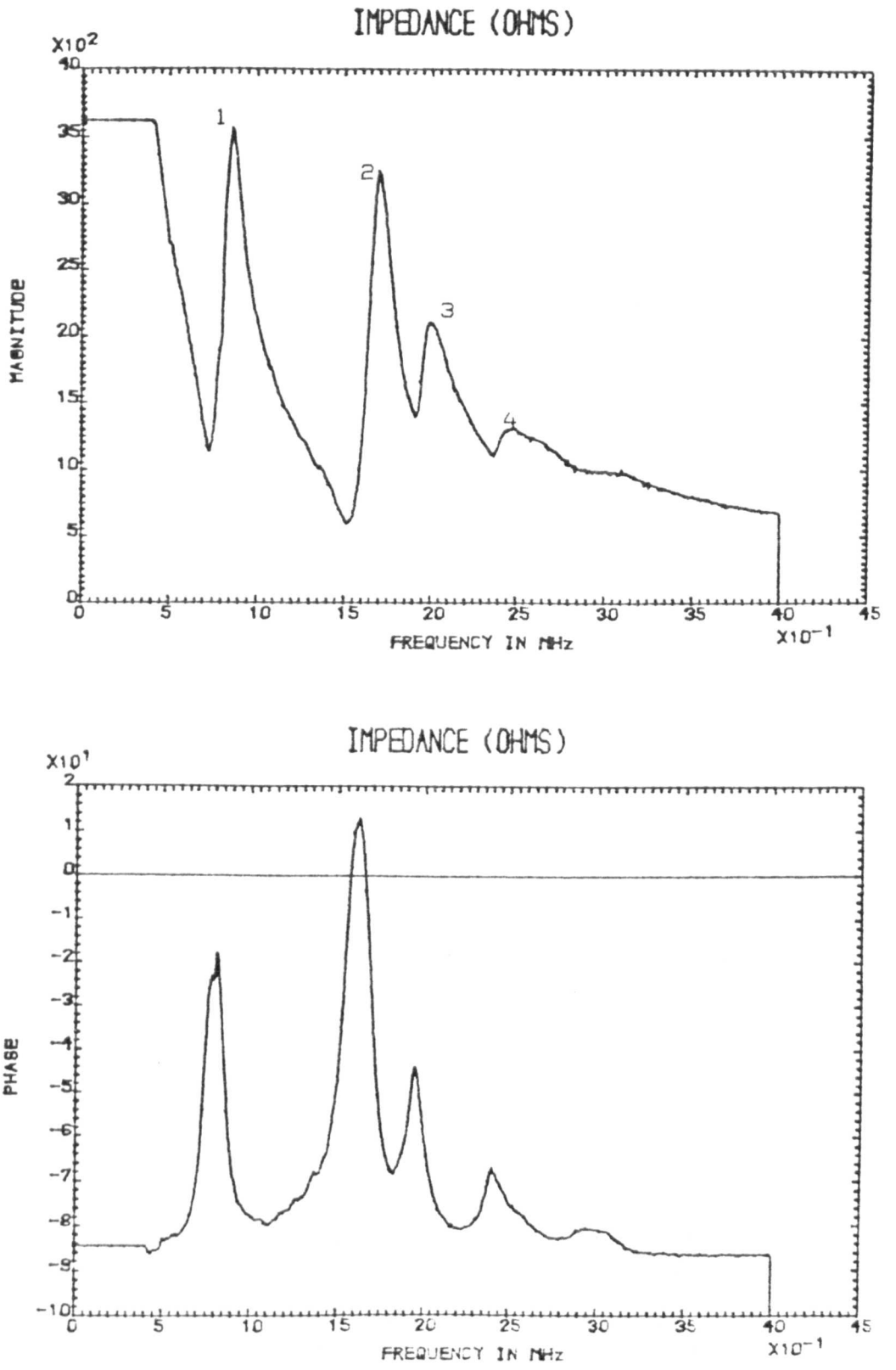

Figure 5.22a Measured electrical impedance characteristics of layered structure #1.

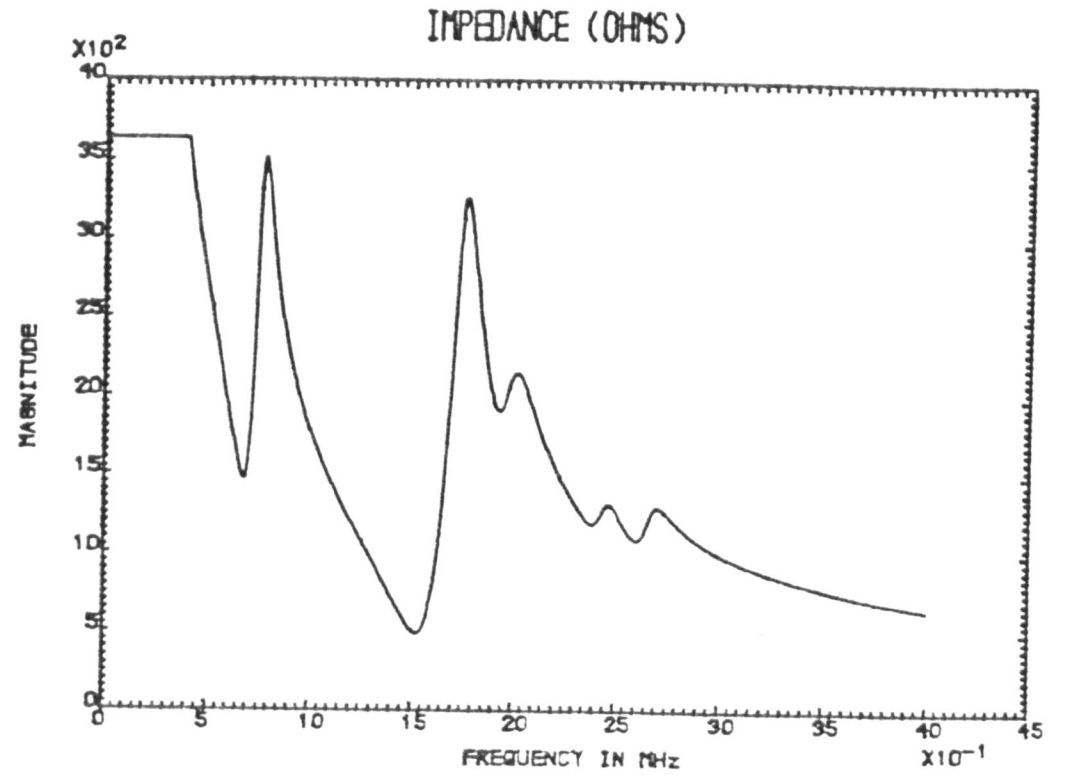

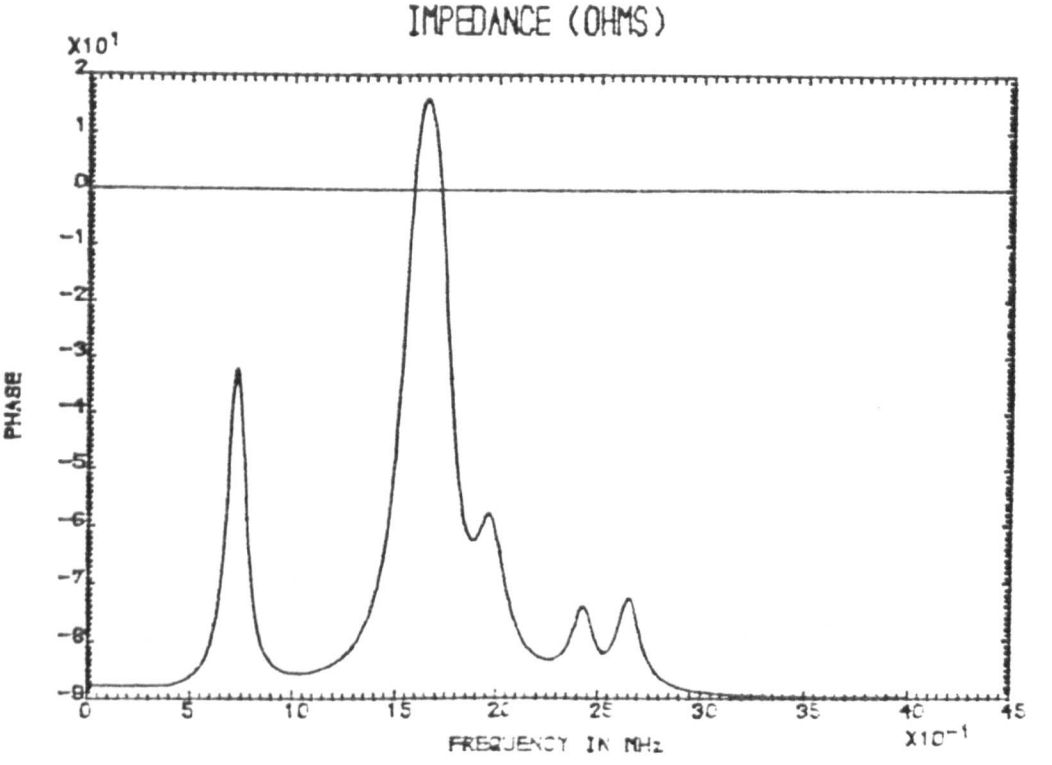

Figure 5.22b Simulated electrical impedance characteristics of layered structure #1.

5.23(a)

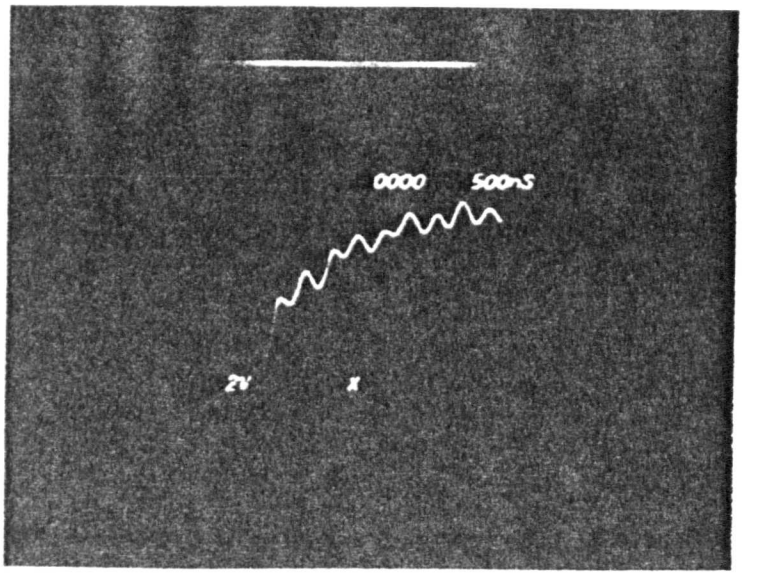

VOLTAGE (V) 5.23(b)

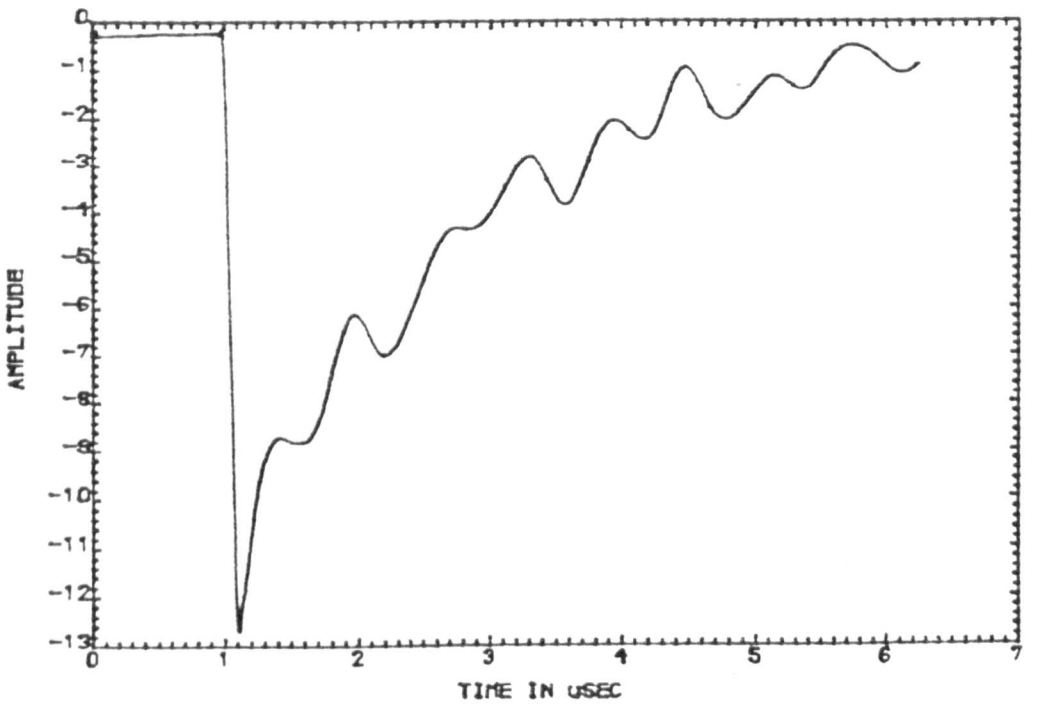

Figure 5.23 Measured and simulated voltage response of layered structure #1 when excited by firing circuit #2.

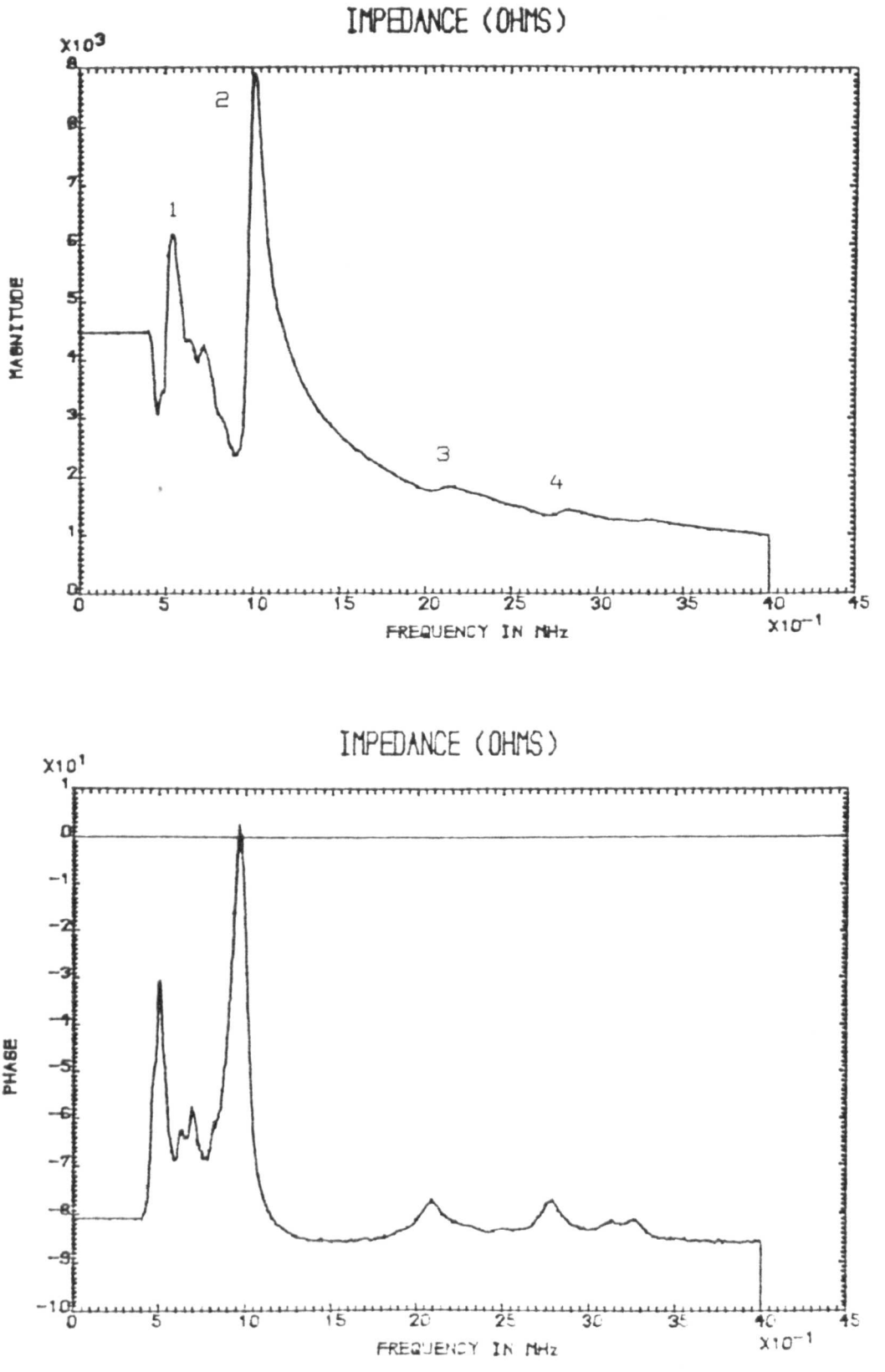

Figure 5.24a Measured electrical impedance characteristics of layered structure #2.

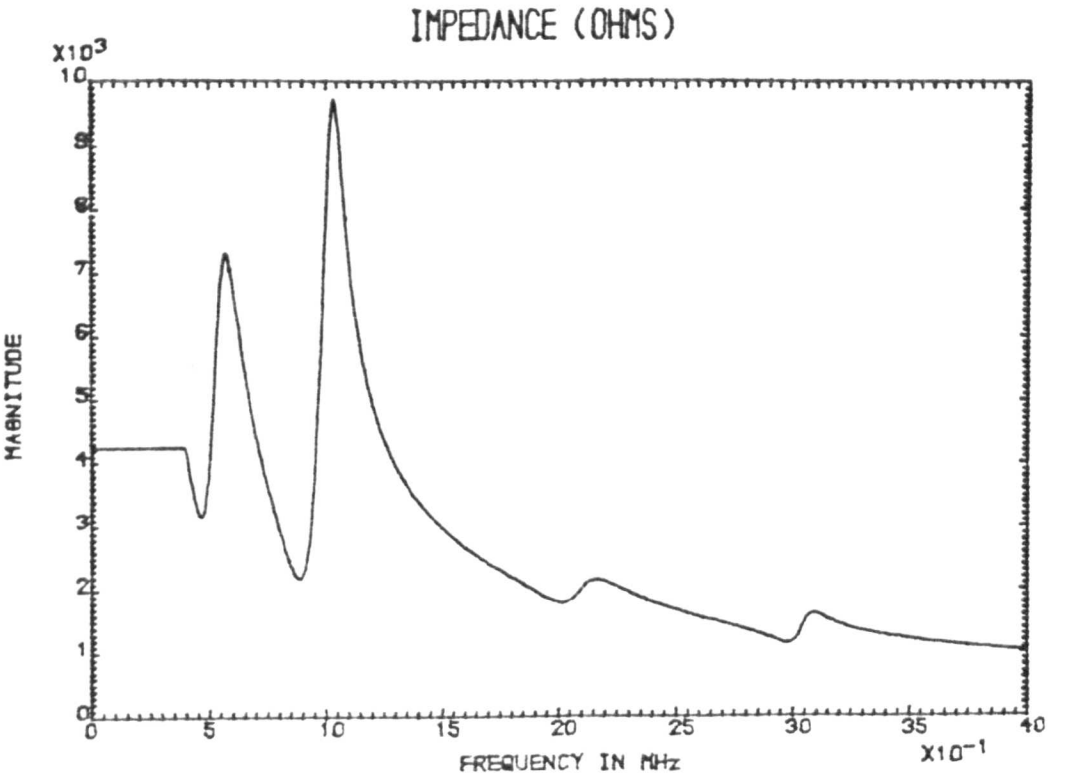

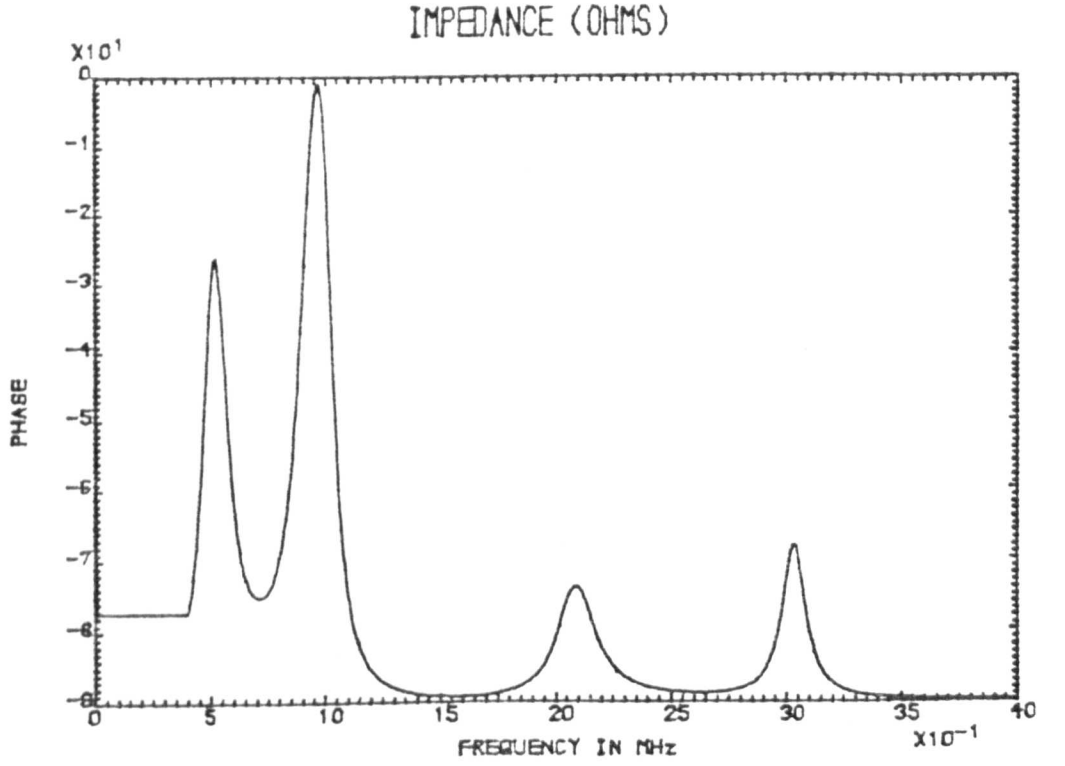

Figure 5.24b Simulated electrical impedance characteristics of layered structure #2.

5.25(a)

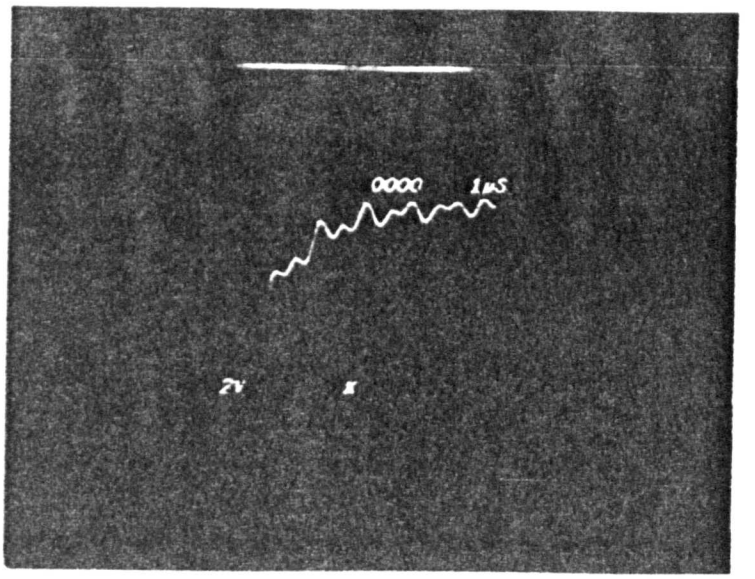

VOLTAGE (V)

5.53(b)

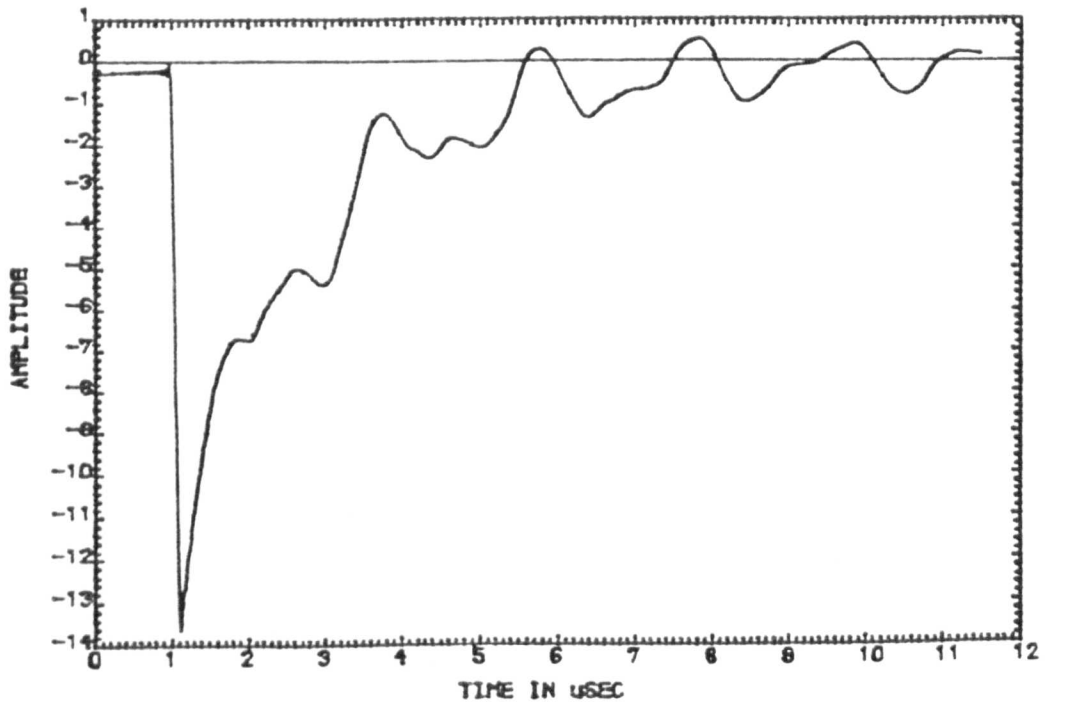

Figure 5.25 Measured and simulated voltage response of layered structure #2 when excited by firing circuit #2.

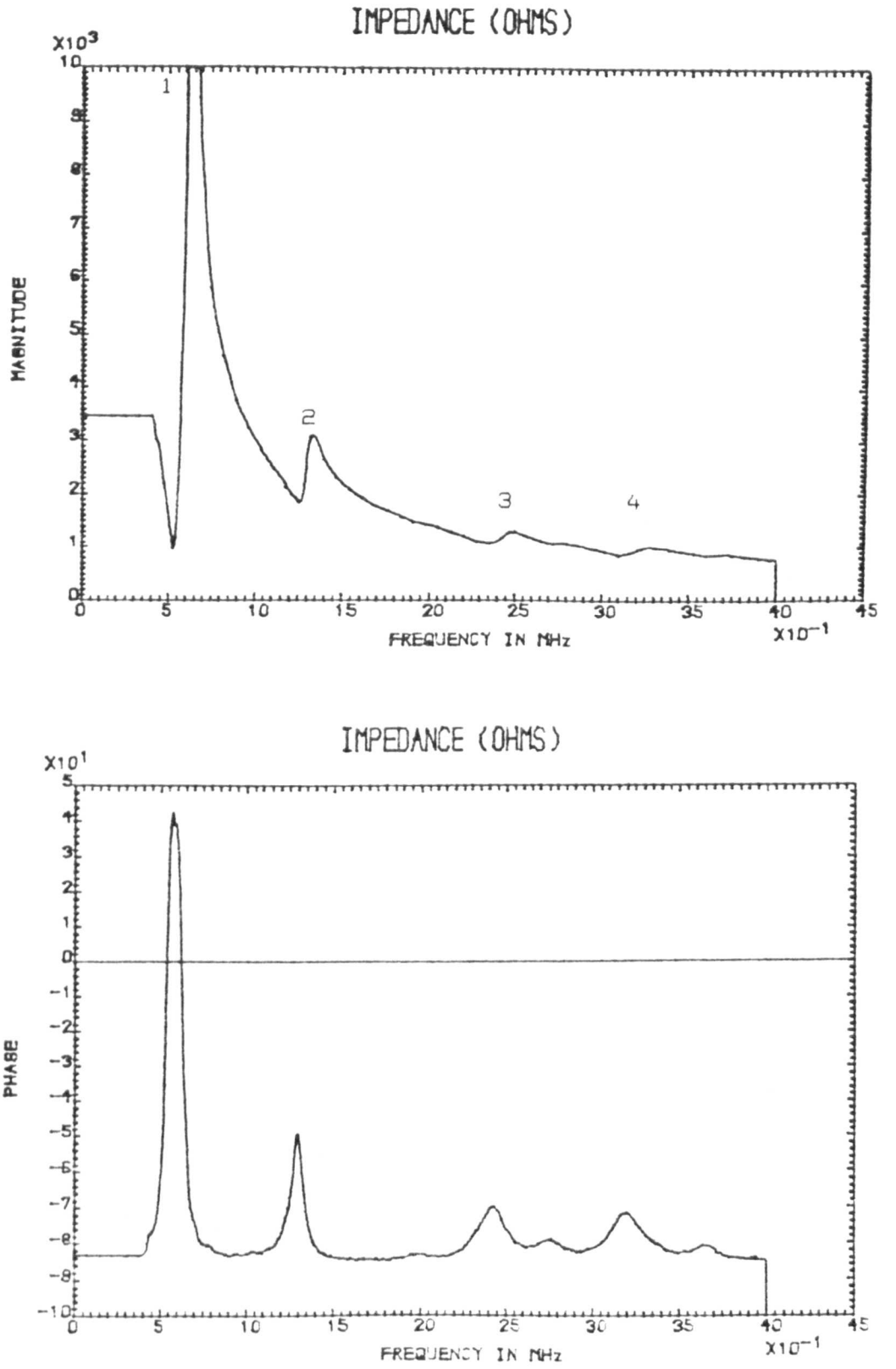

Figure 5.26a Measured electrical impedance characteristics of layered structure #3.

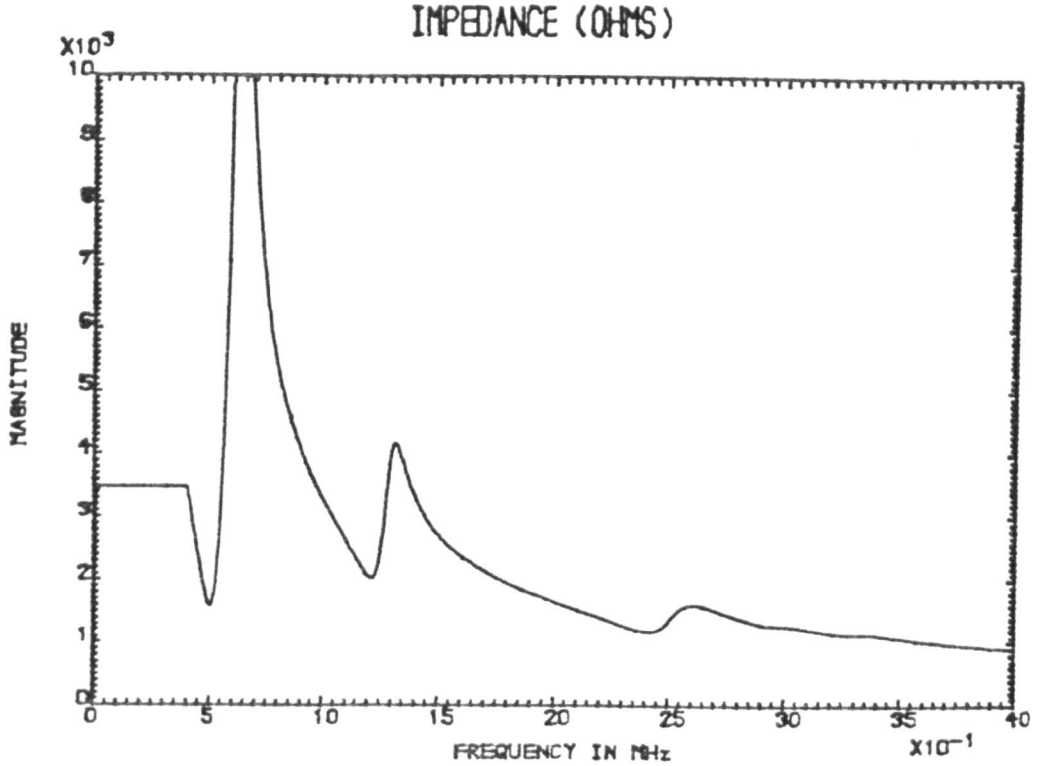

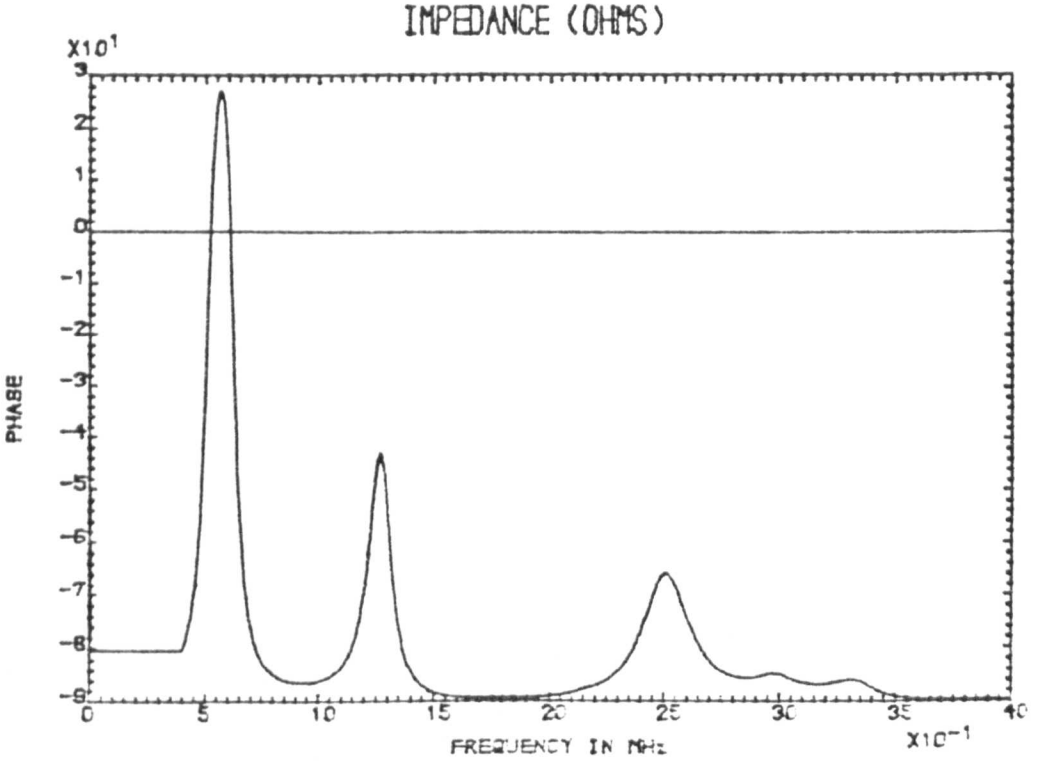

Figure 5.26b Simulated electrical impedance characteristics of layered structure #3.

5.27(a)

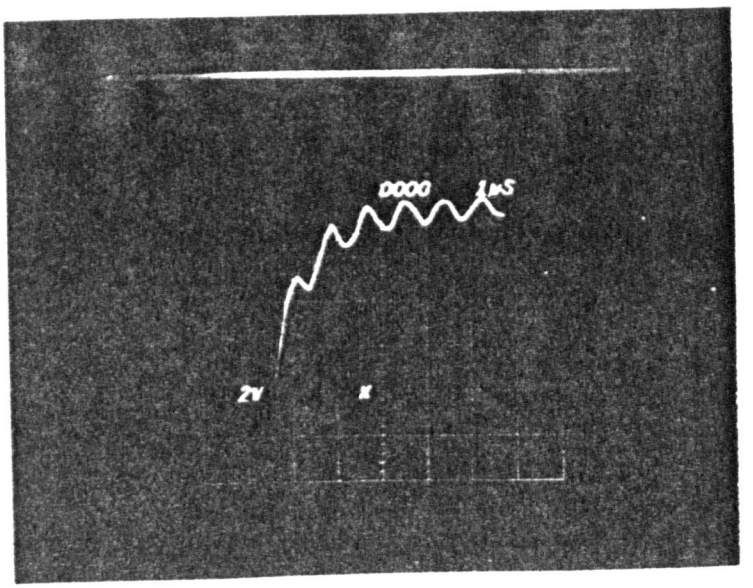

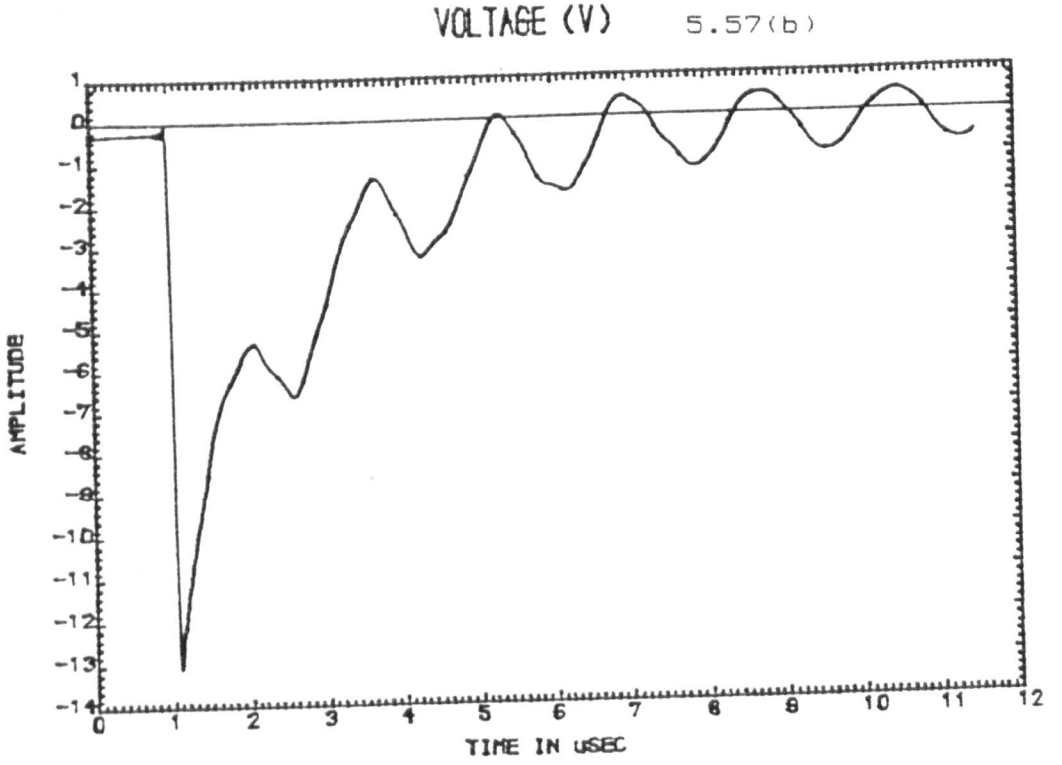

Figure 5.27 Measured and simulated voltage response of layered structure #3 when excited by firing circuit #2.

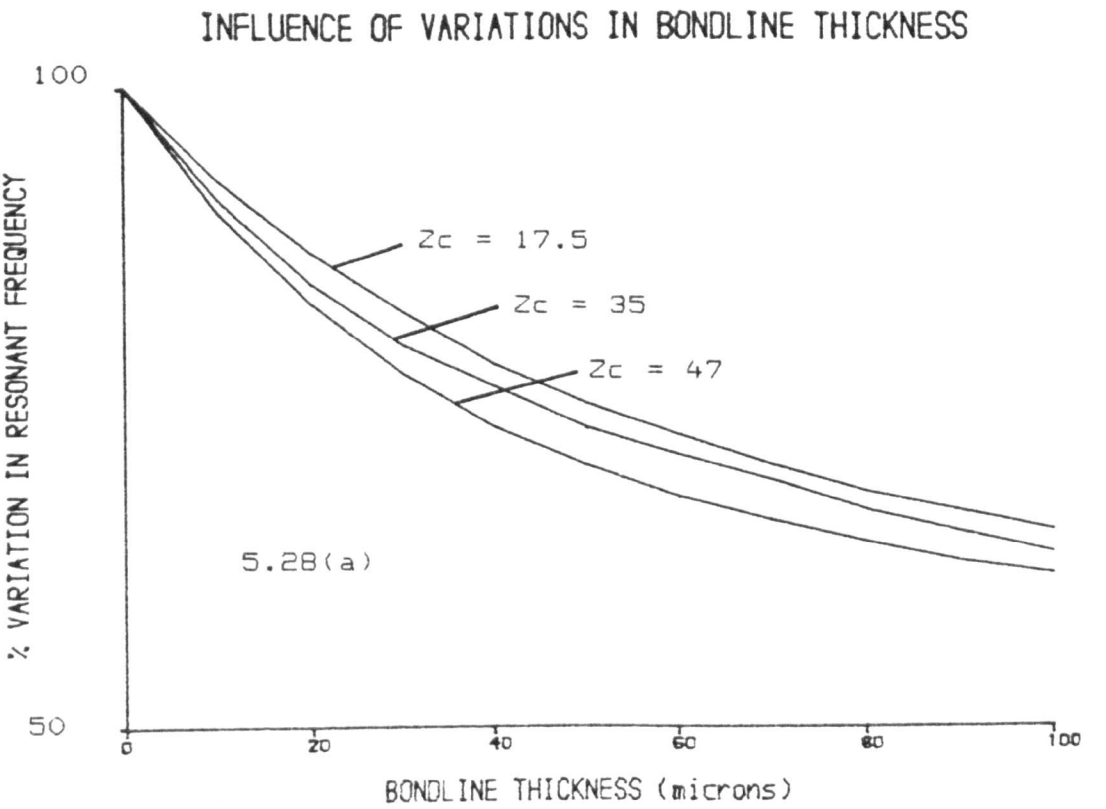

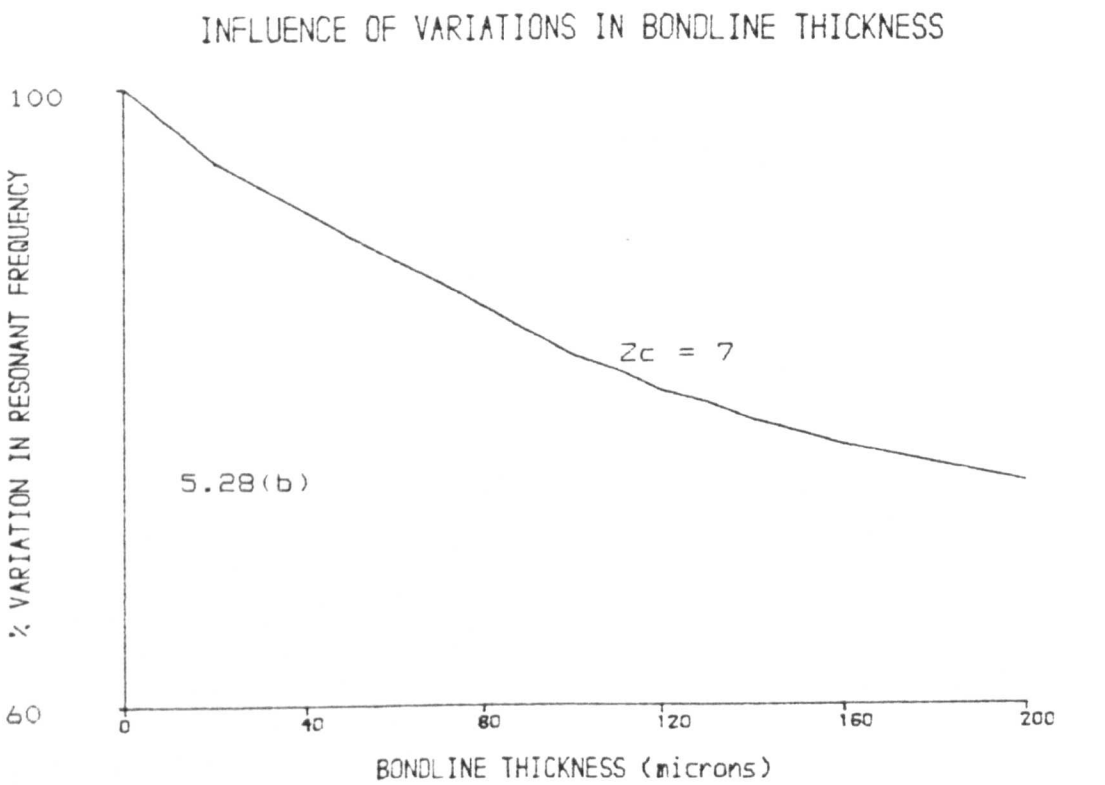

Figure 5.28 Variations in resonant frequency as a result of bondline thickness changes.

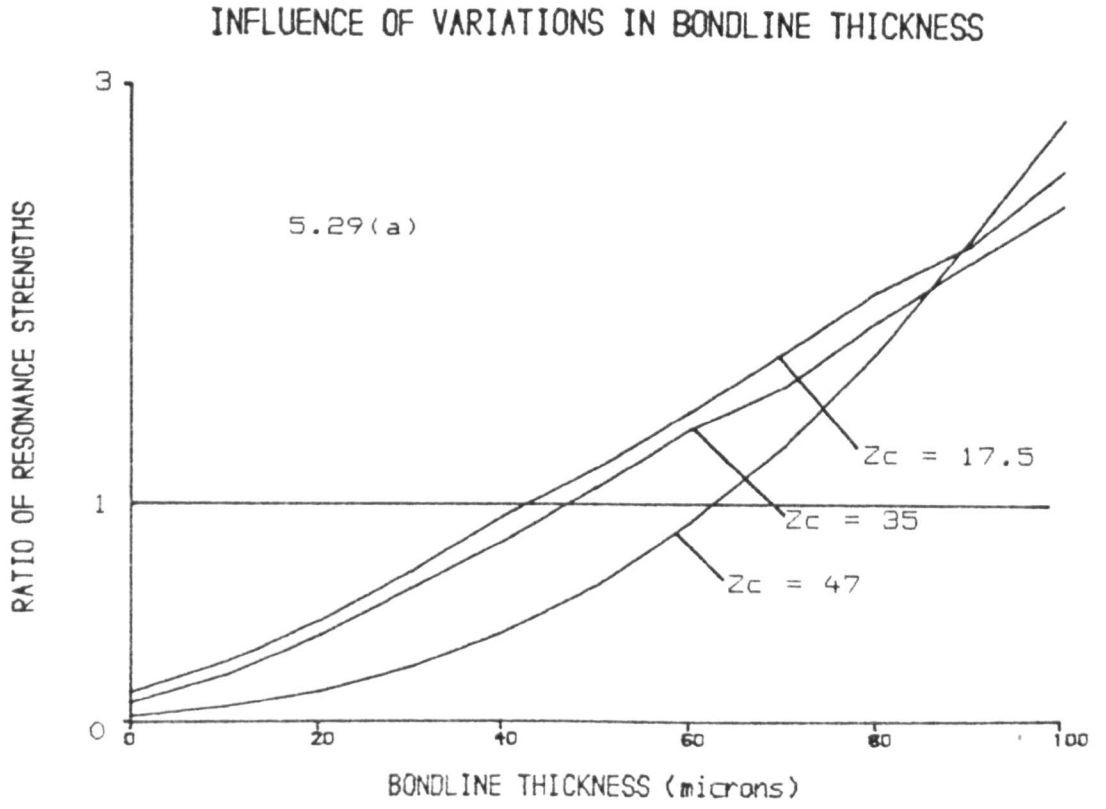

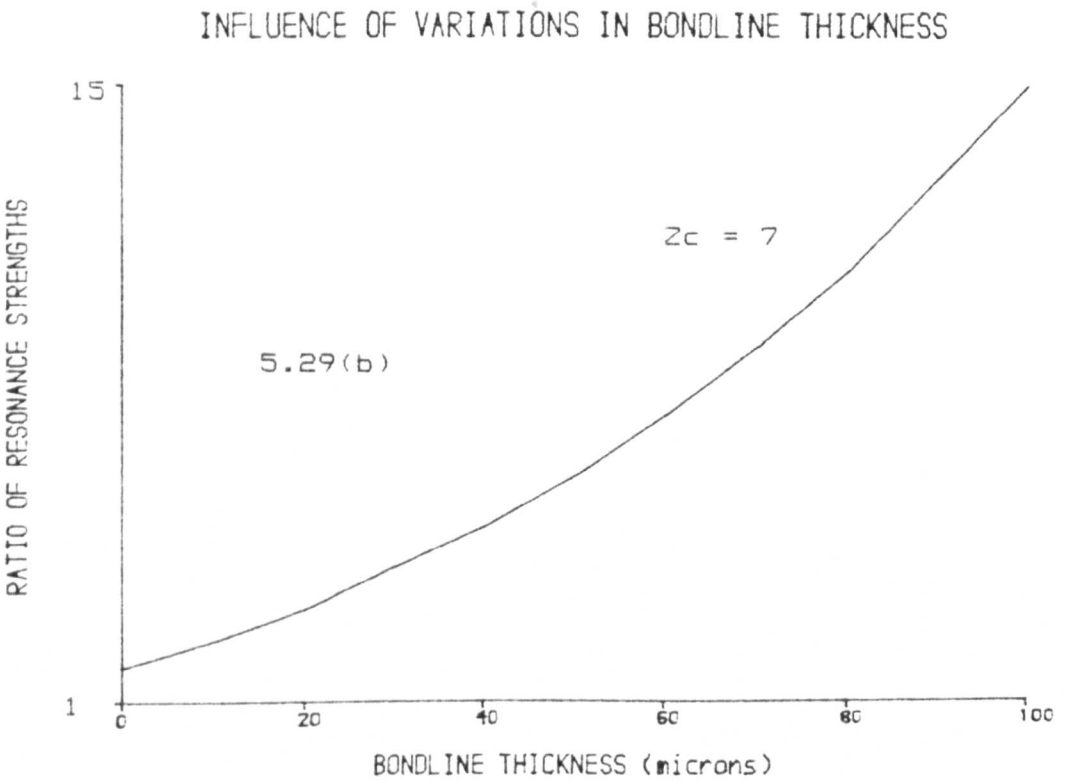

Figure 5.29 Variations in resonant strength as a result of bondline thickness changes.

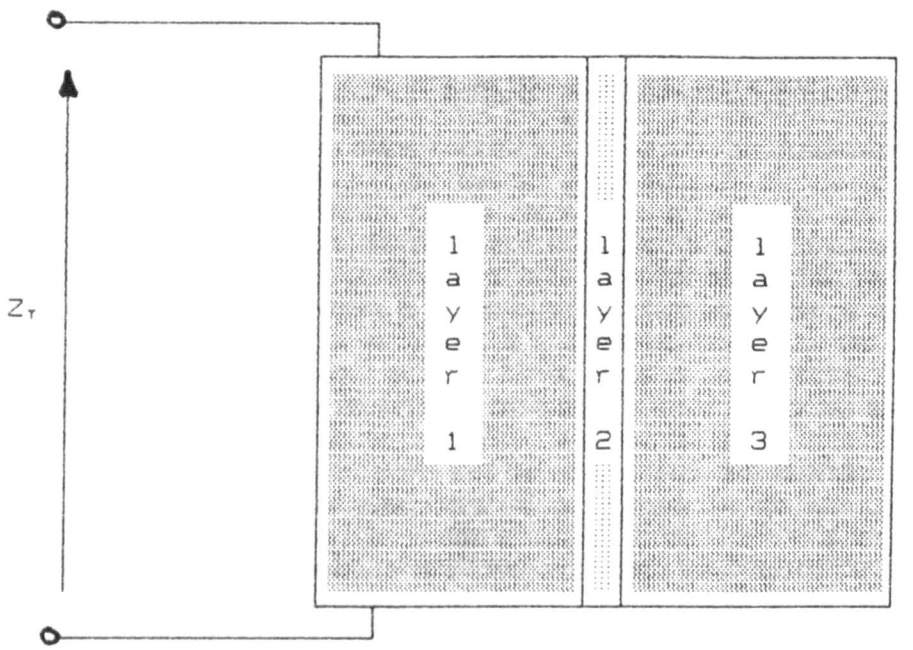

Figure 5.30 Configuration of the layered structure in the lateral direction

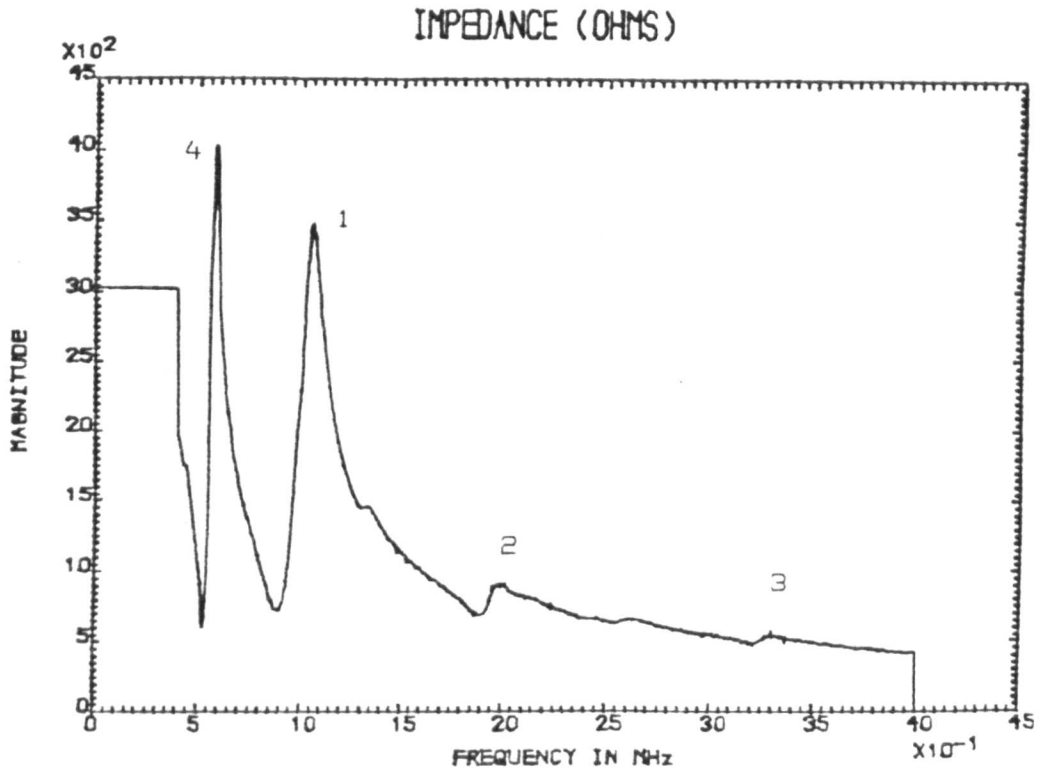

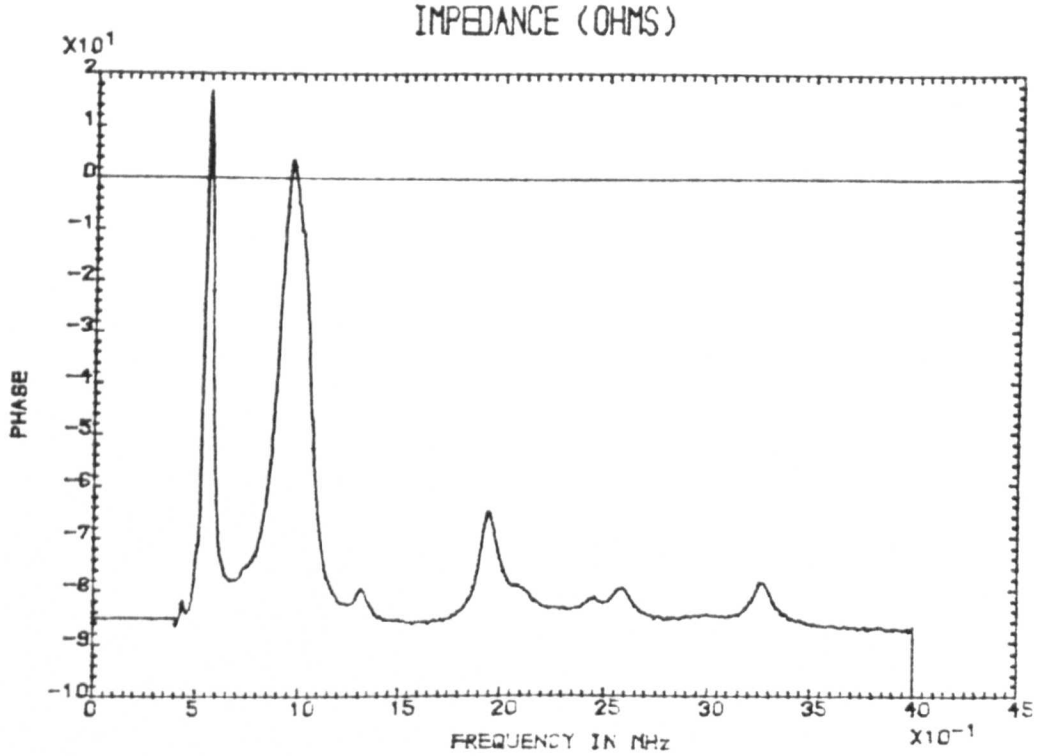

Figure 5.31a Measured electrical impedance characteristics of layered structure #4.

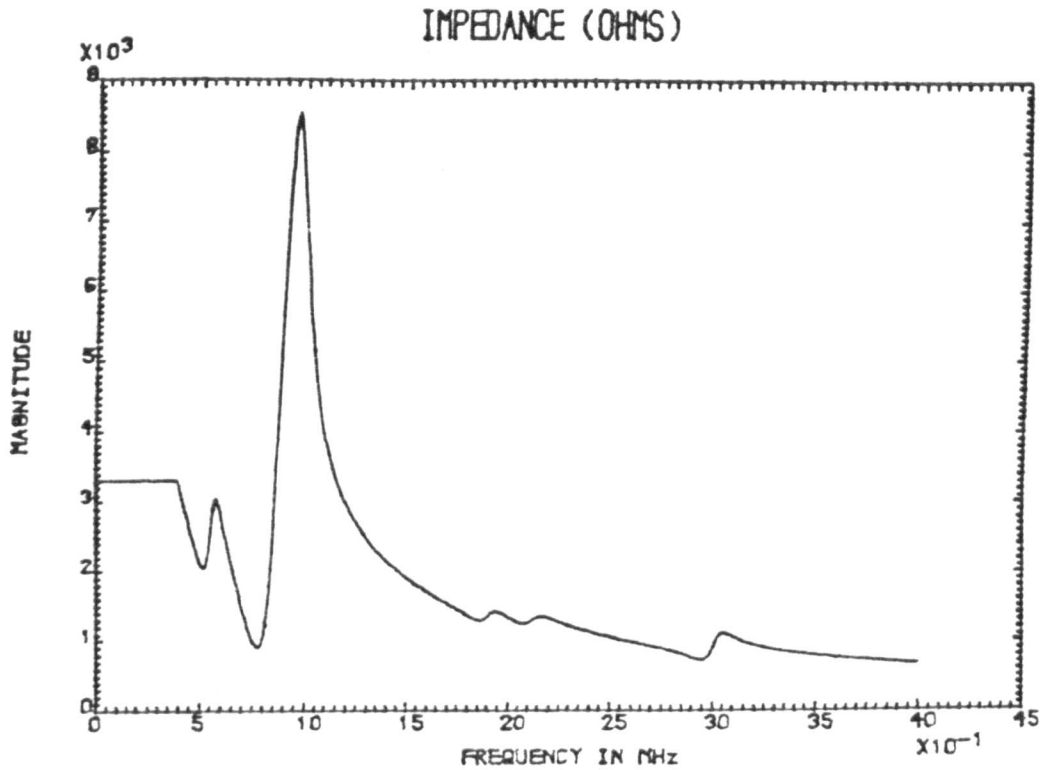

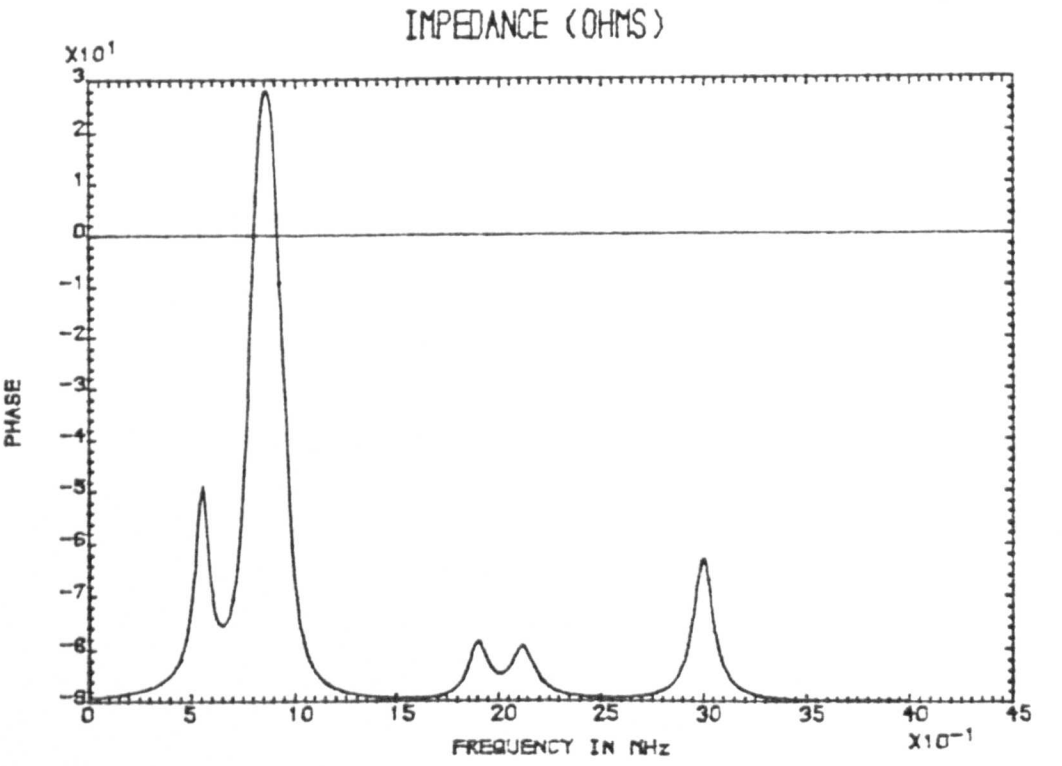

Figure 5.31b Simulated electrical impedance characteristics of layered structure #4.

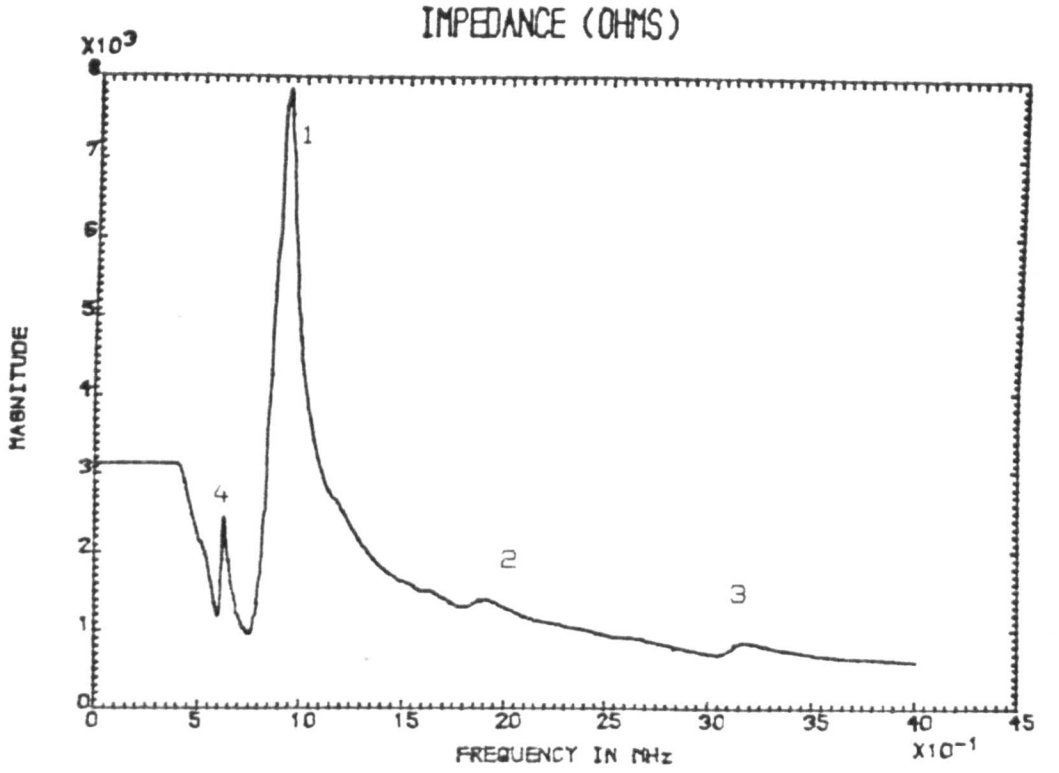

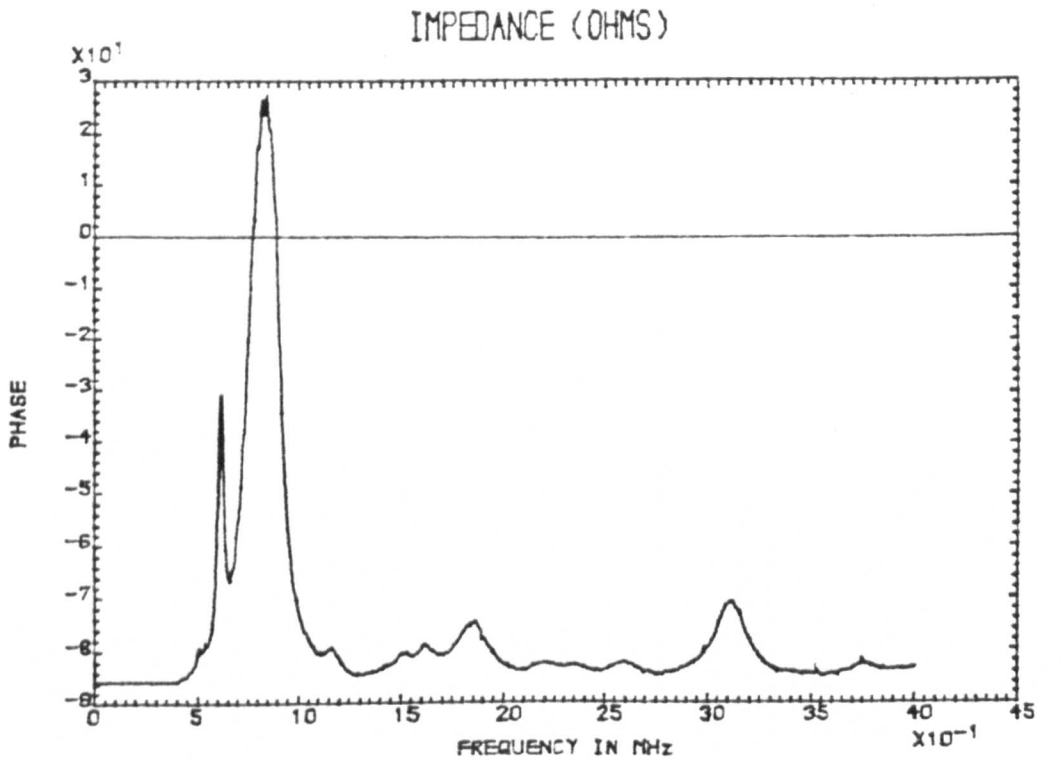

Figure 5.32a Measured electrical impedance characteristics of layered structure #5.

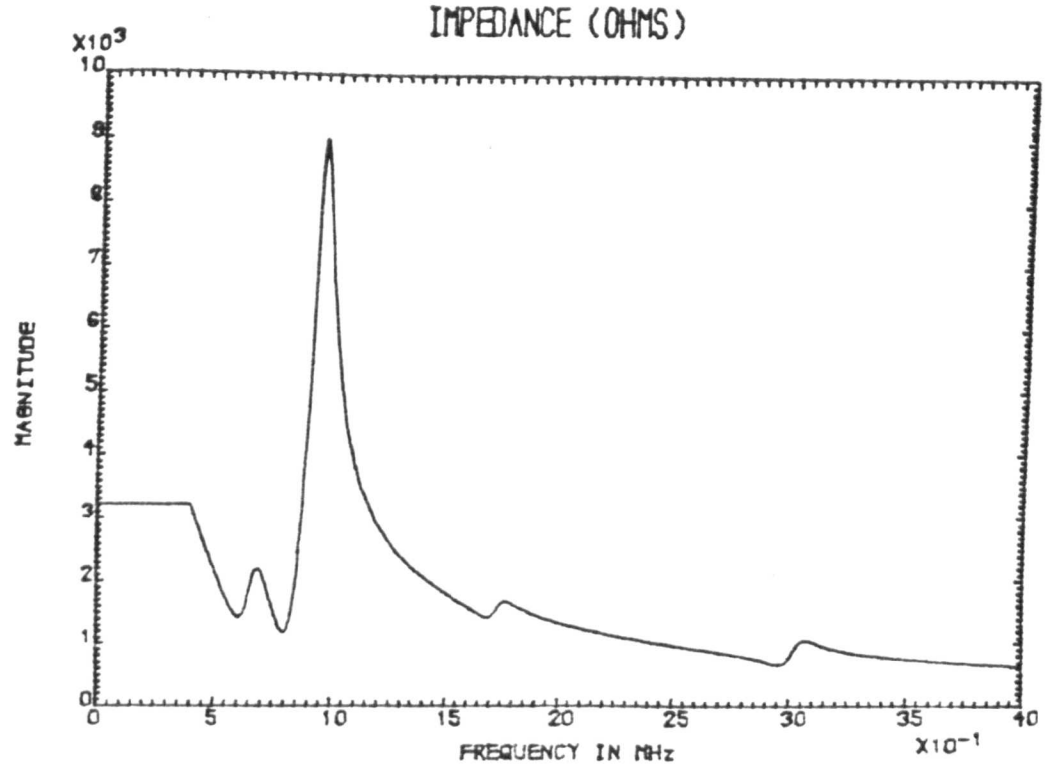

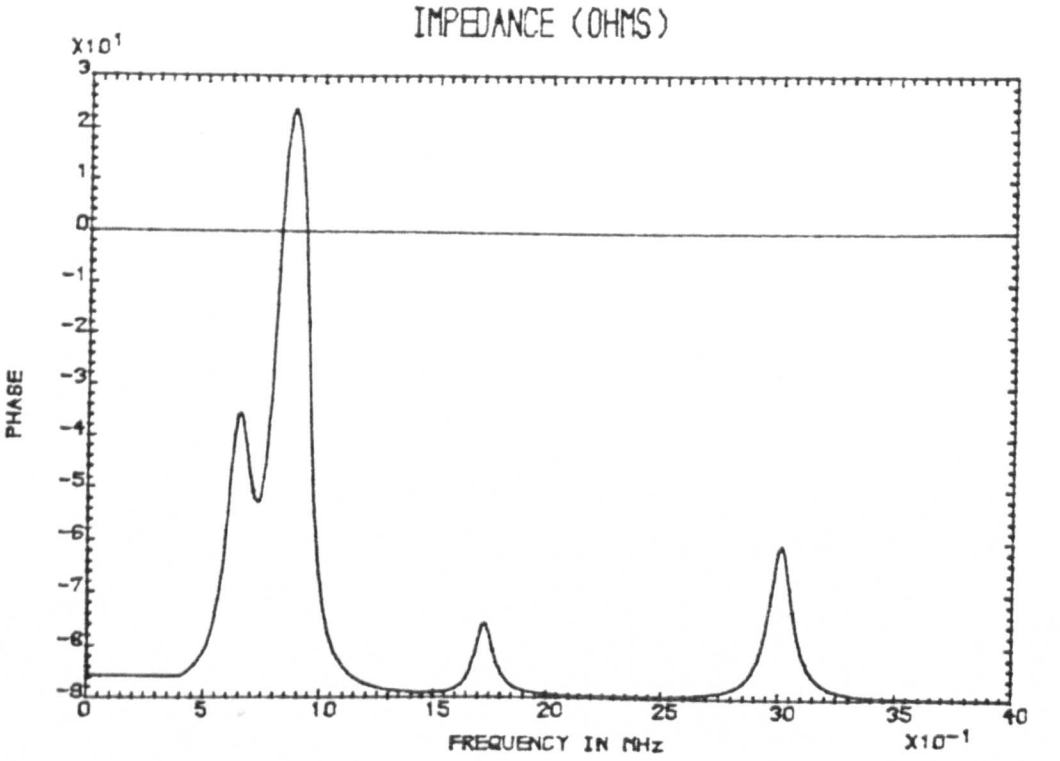

Figure 5.32b Simulated electrical impedance characteristics of layered structure #5.

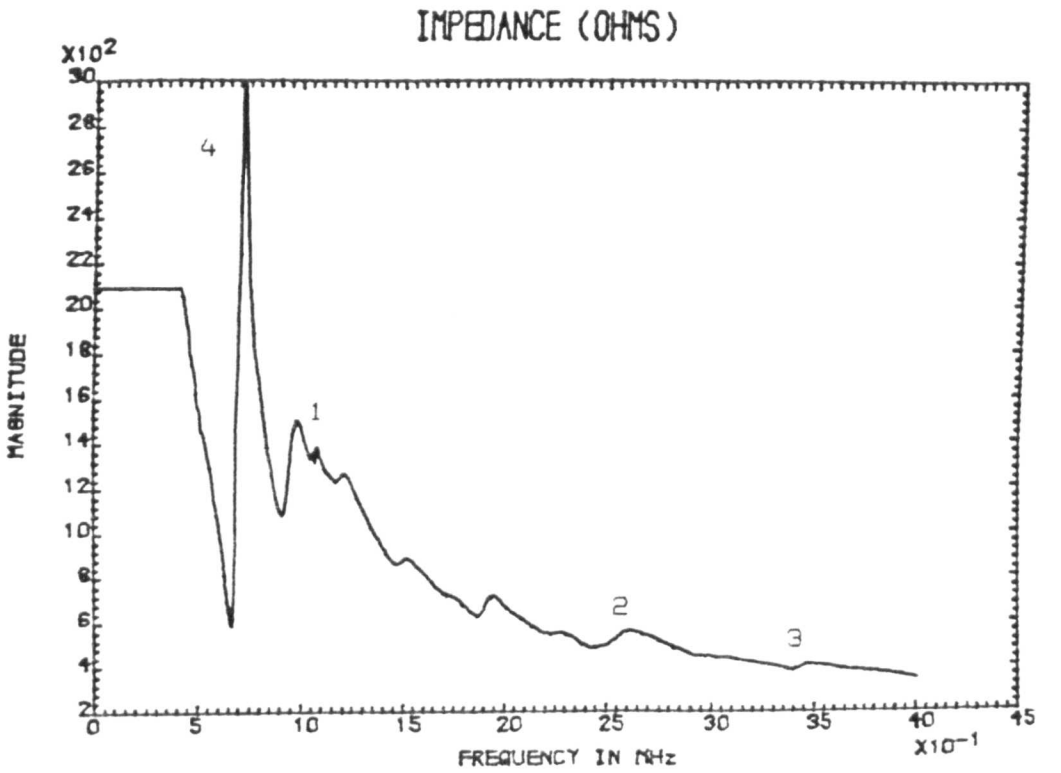

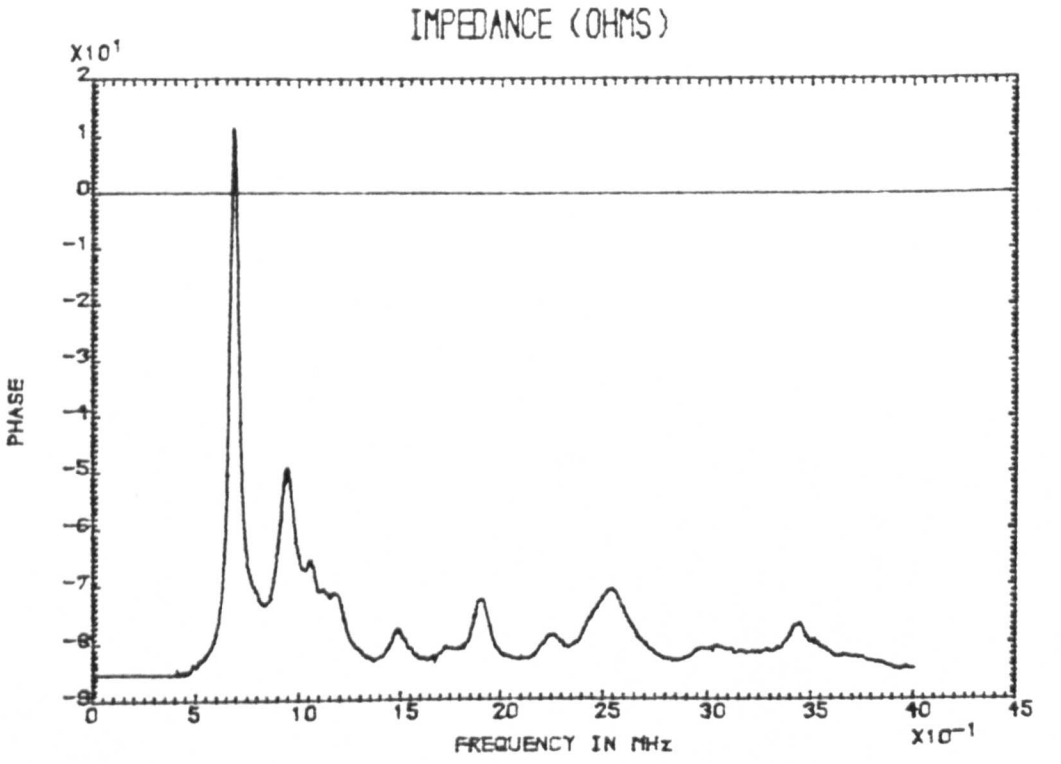

Figure 5.33a Measured electrical impedance characteristics of layered structure #6.

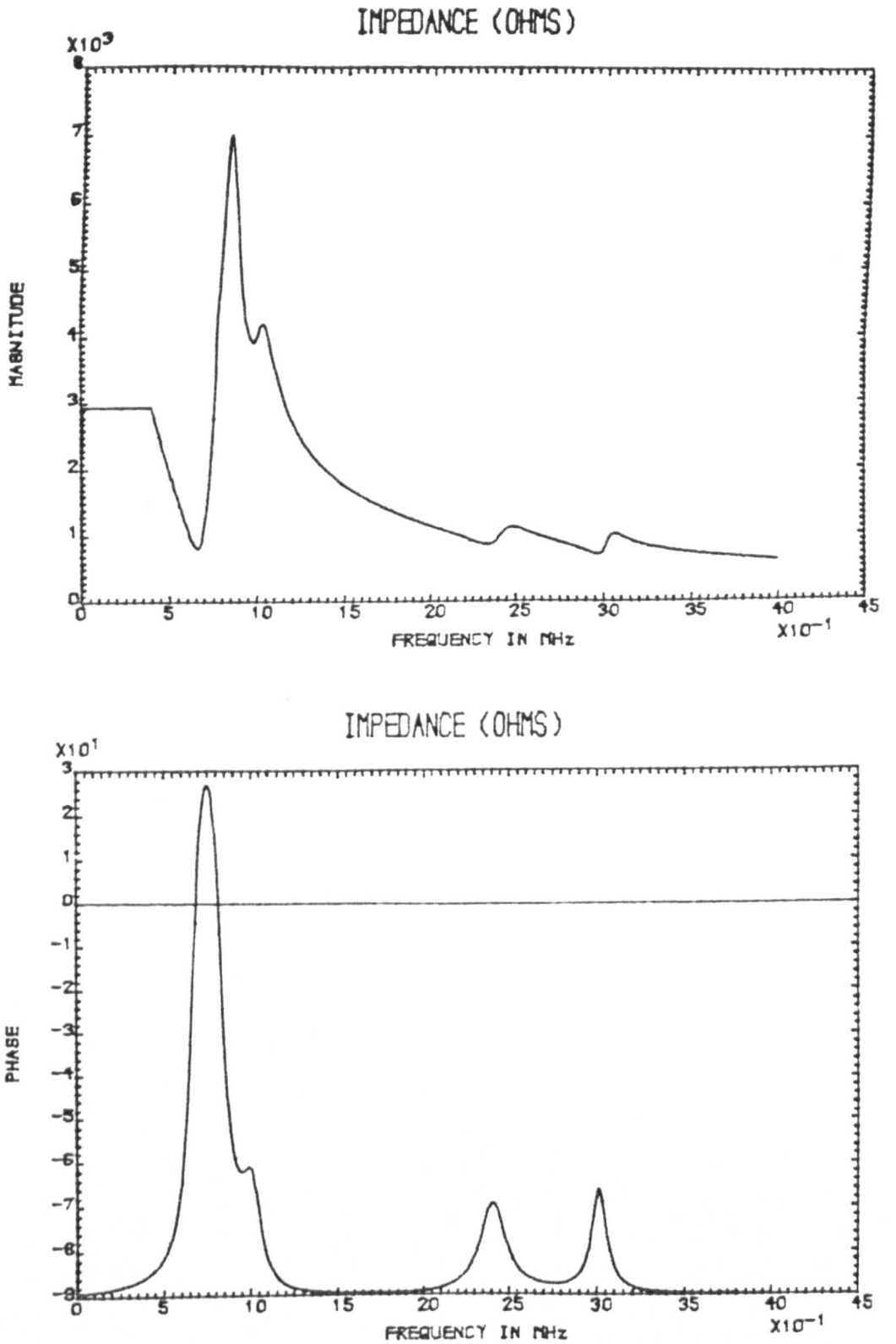

Figure 5.33b Simulated electrical impedance characteristics of layered structure #6.

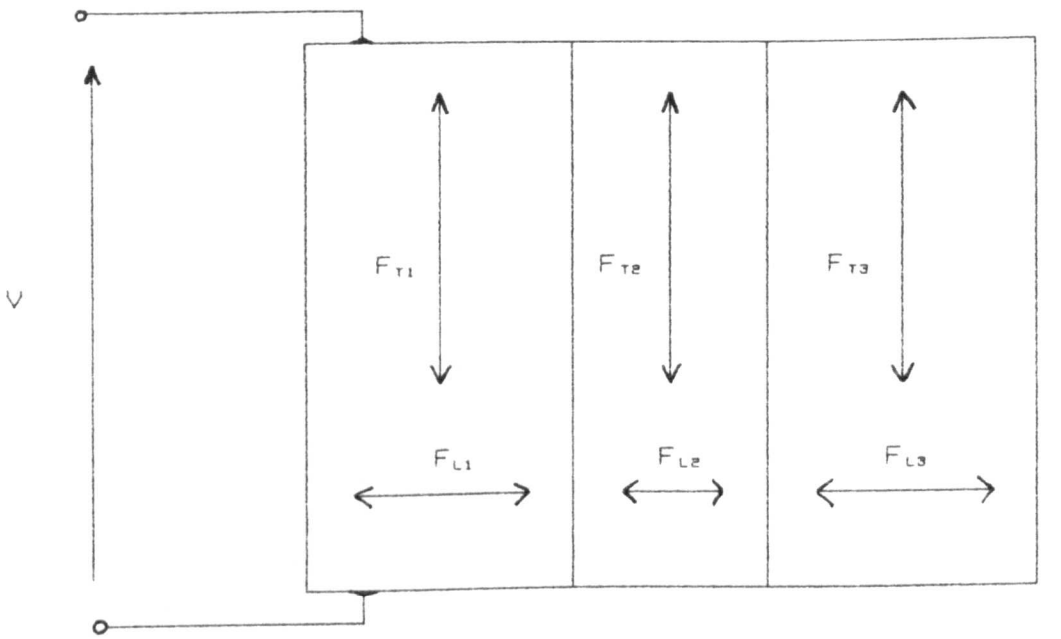

Figure 5.34 The force components inside a lateral three layered structure.

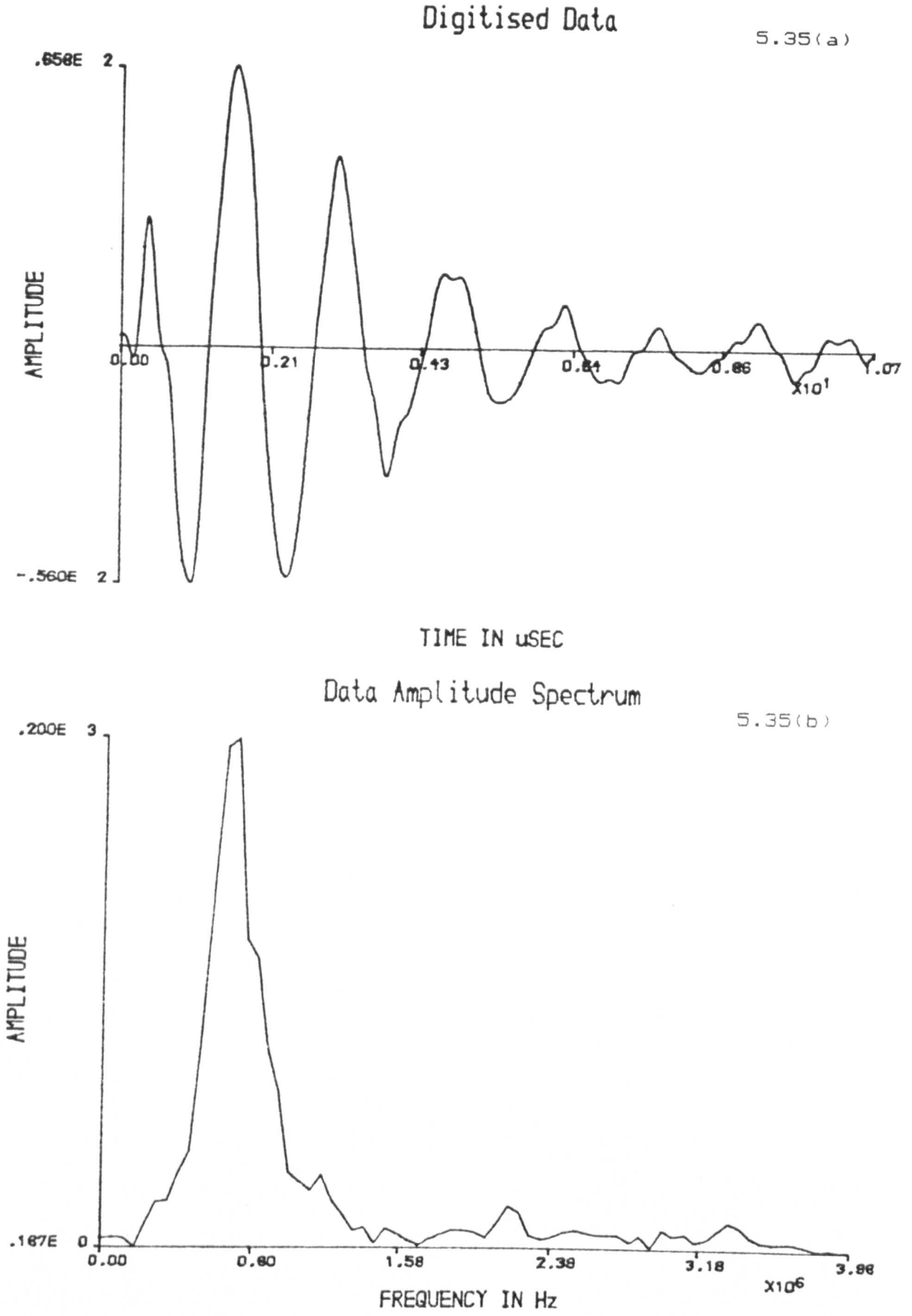

Figure 5.35 Measured time and frequency domain force output from the transducer with no layers.

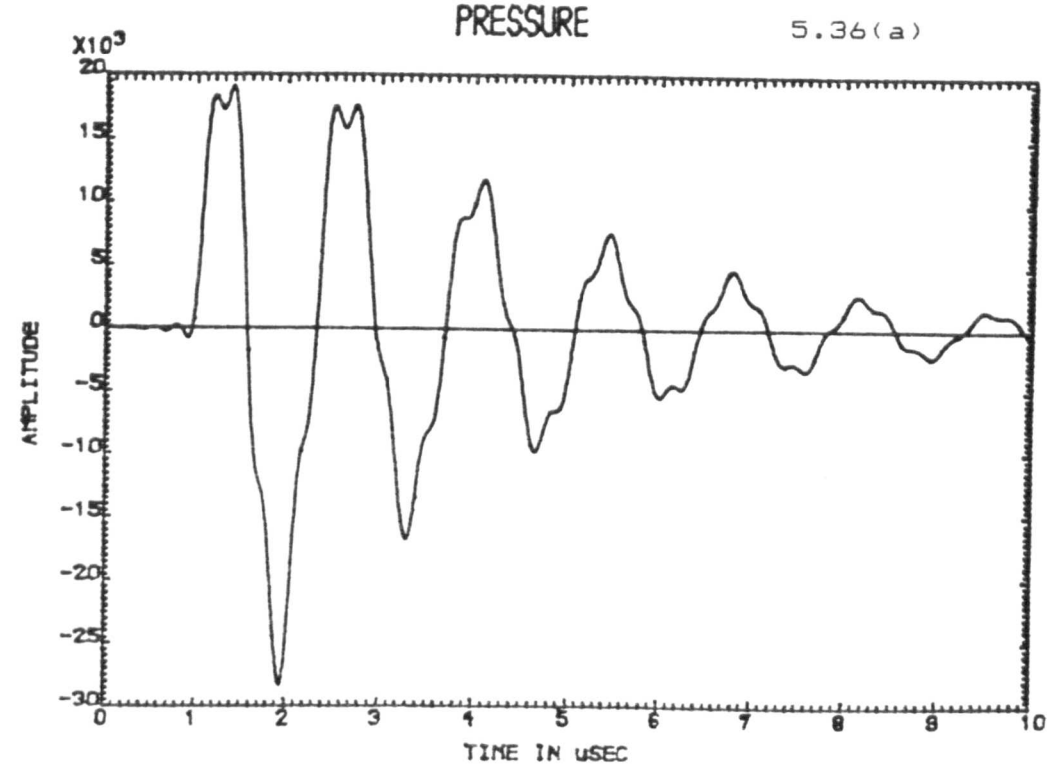

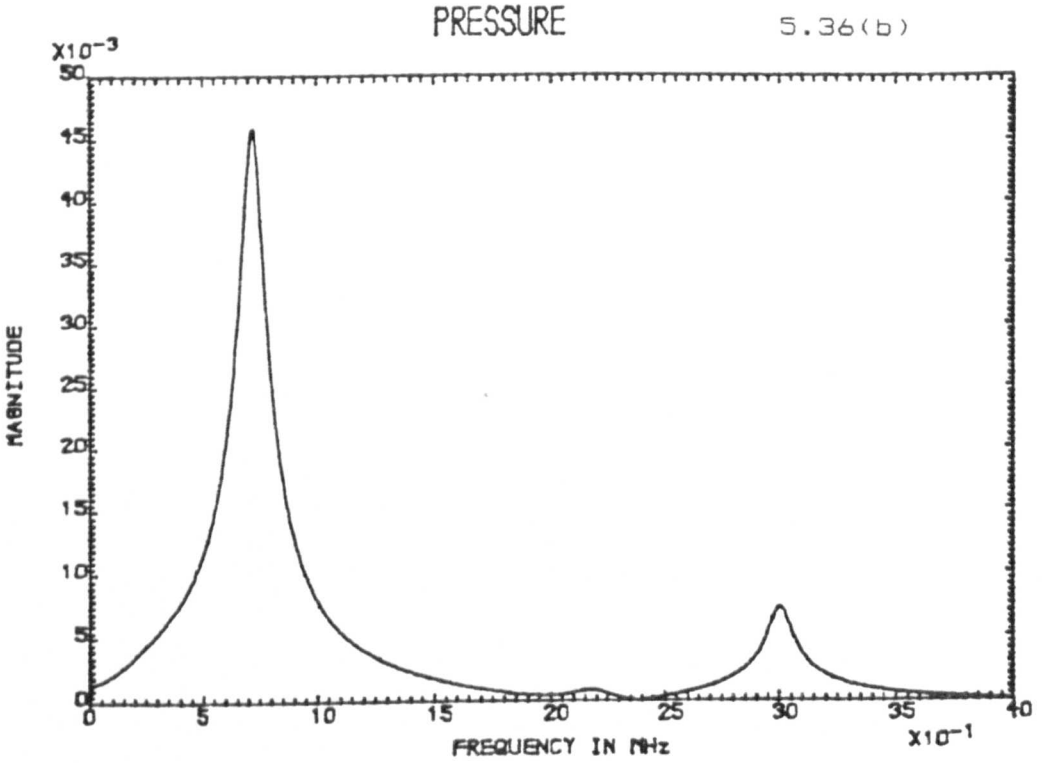

Figure 5.36 Simulated time and frequency domain force output from the transducer with no layers.

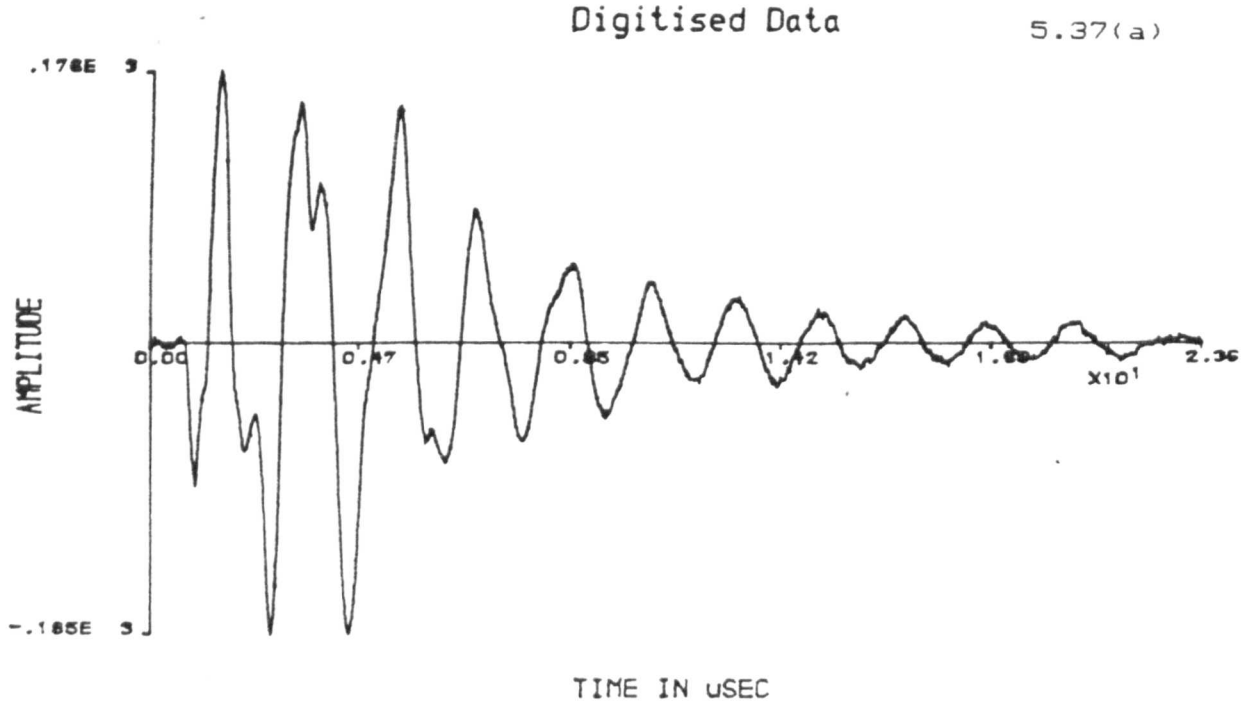

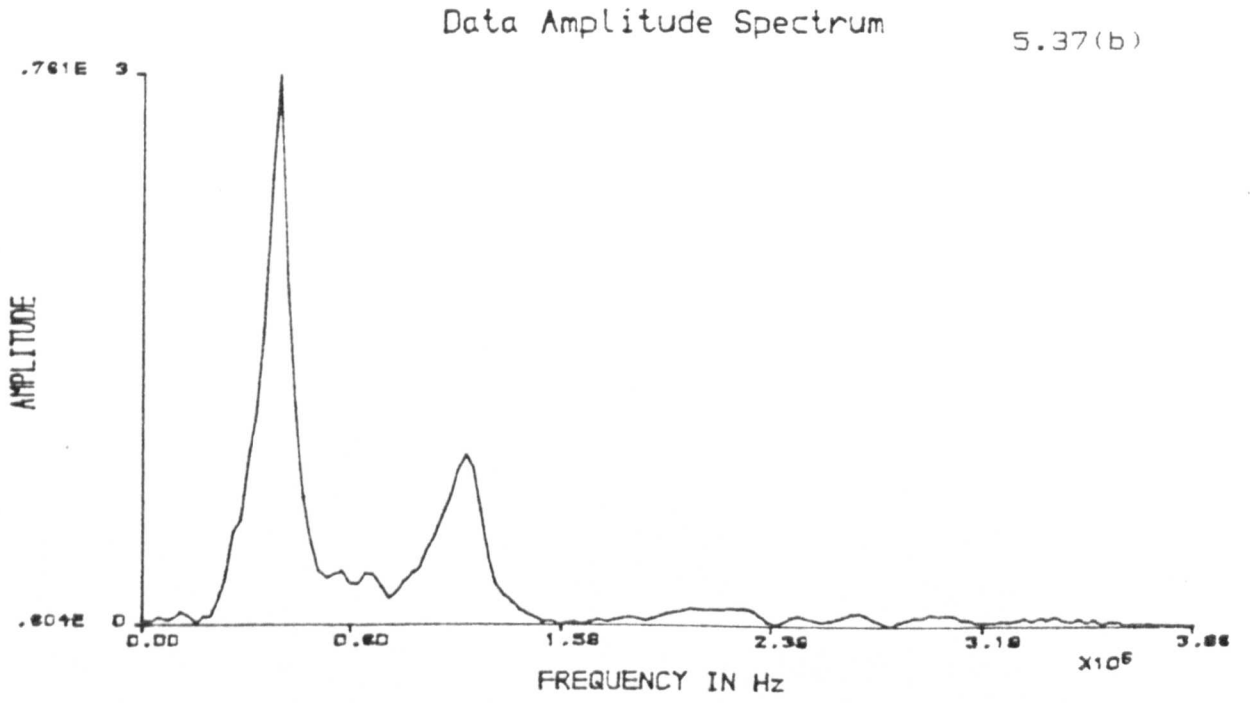

Figure 5.37 Measured time and frequency domain force output from the transducer with steel layer.

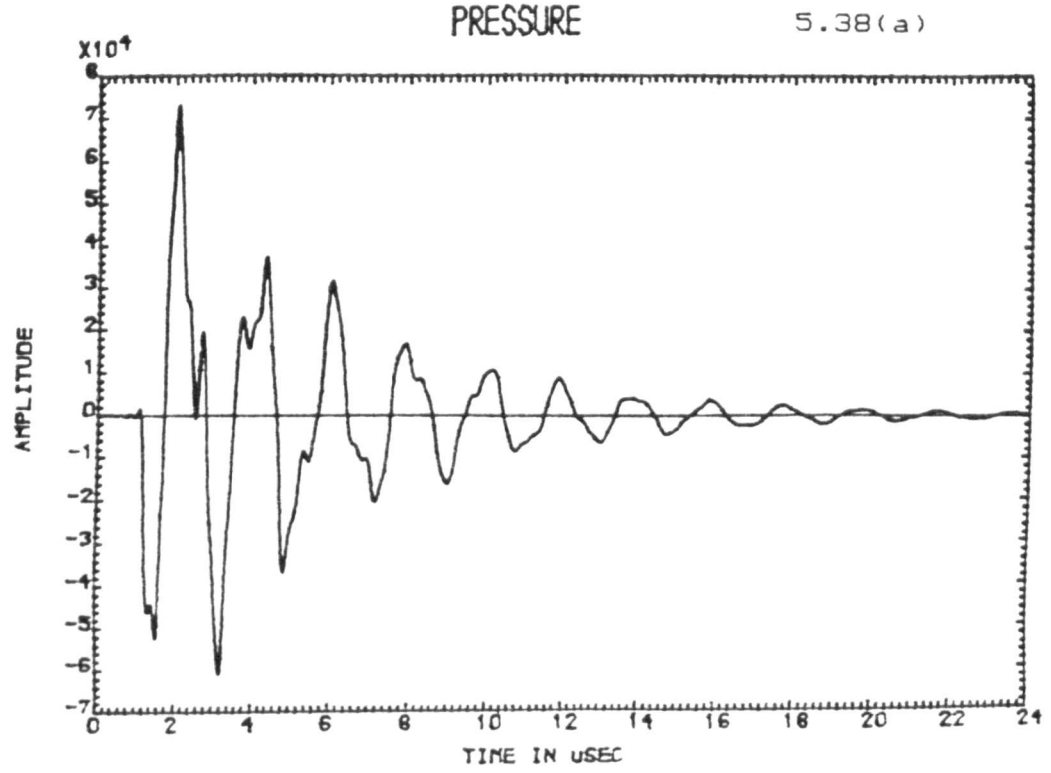

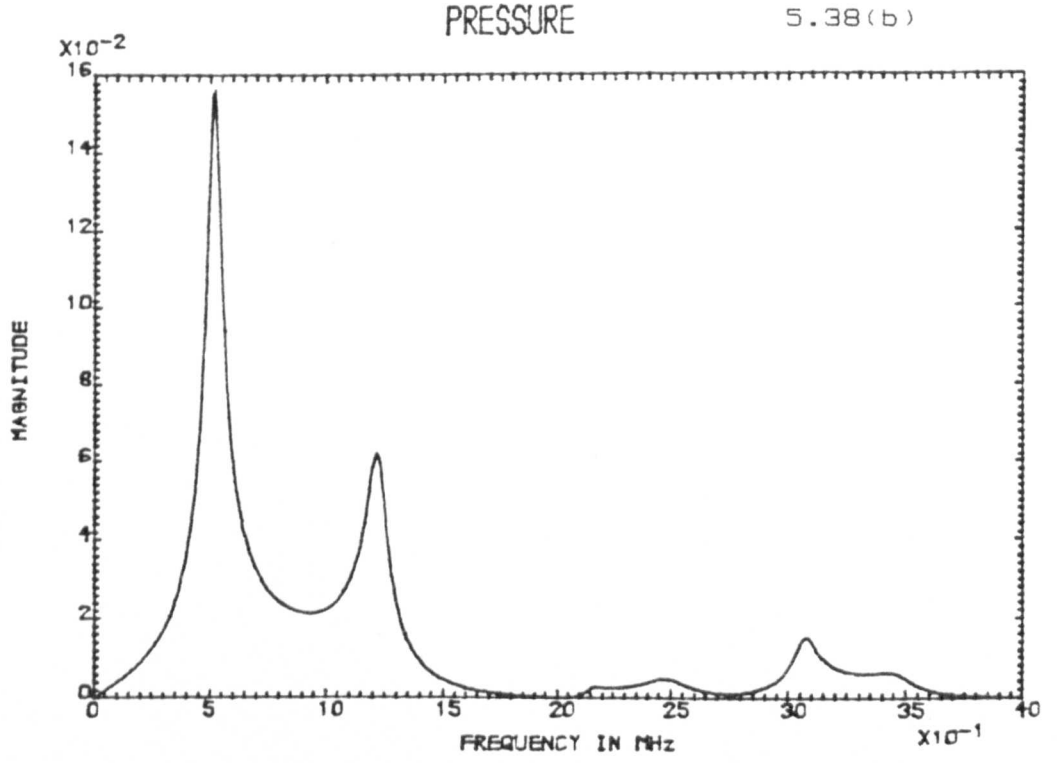

Figure 5.38 Simulated time and frequency domain force output from the transducer with steel layer.

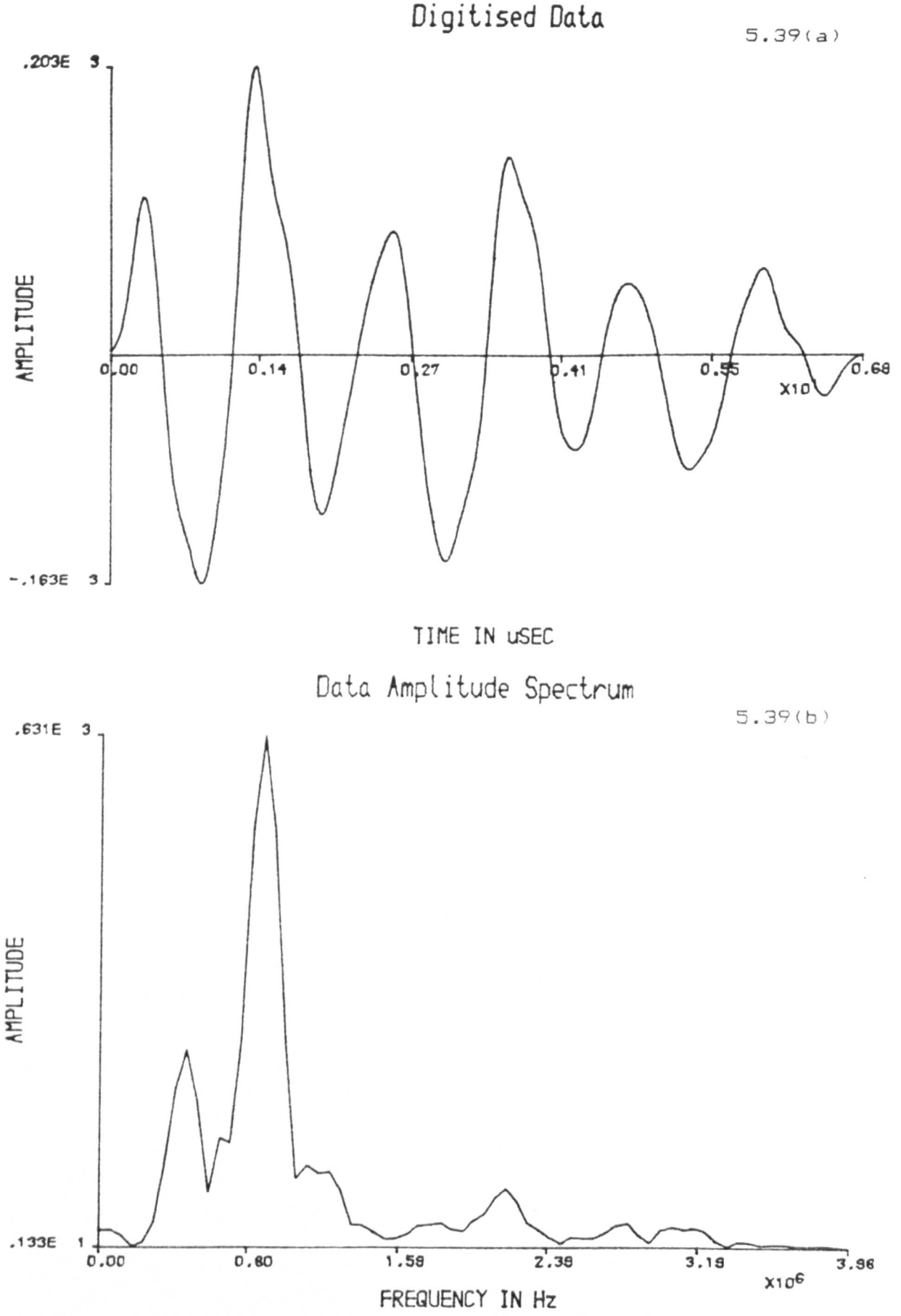

Figure 5.39 Measured time and frequency domain force output from the transducer with aluminium layer.

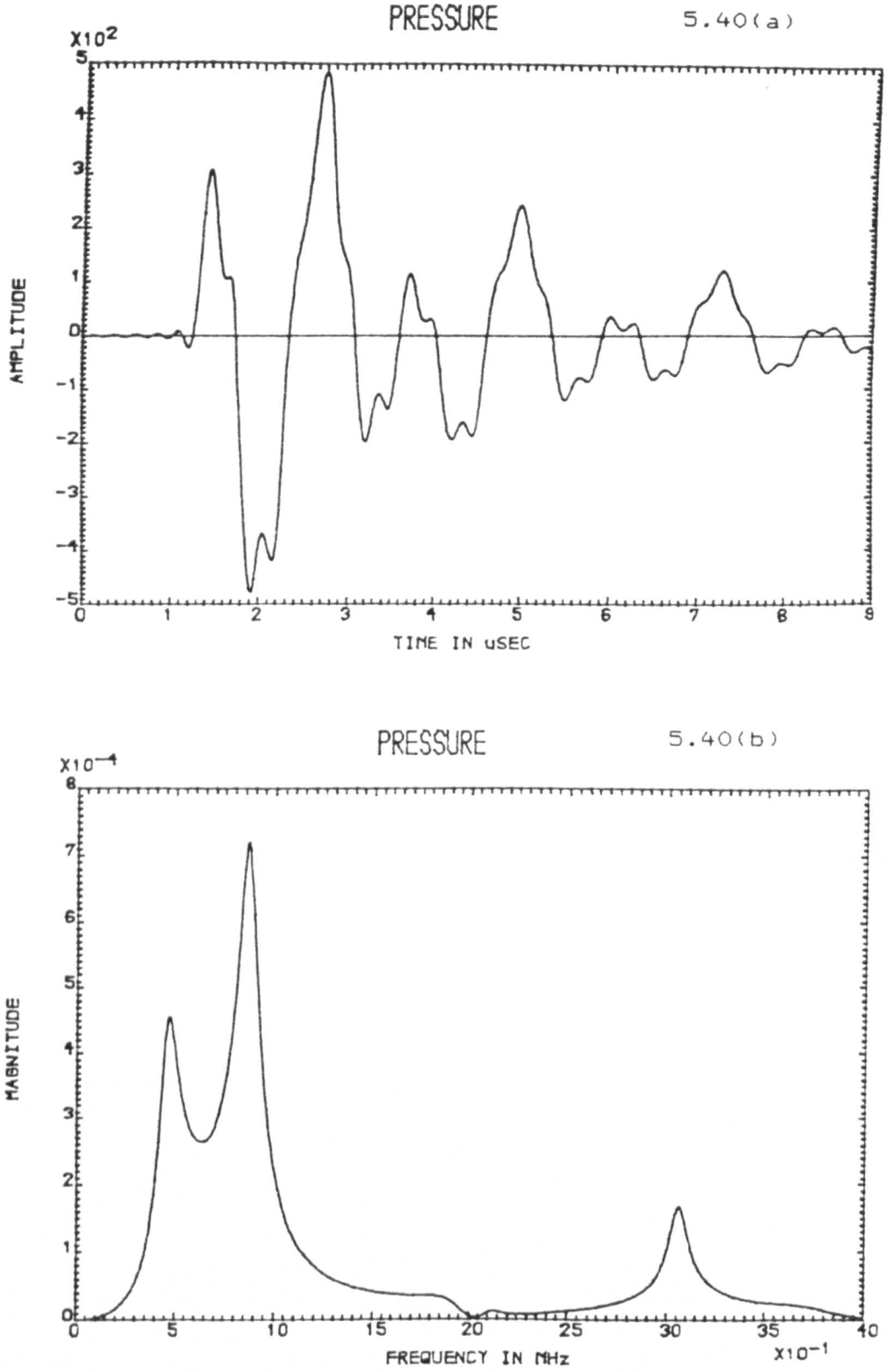

Figure 5.40 Simulated time and frequency domain force output from the transducer with aluminium layer.

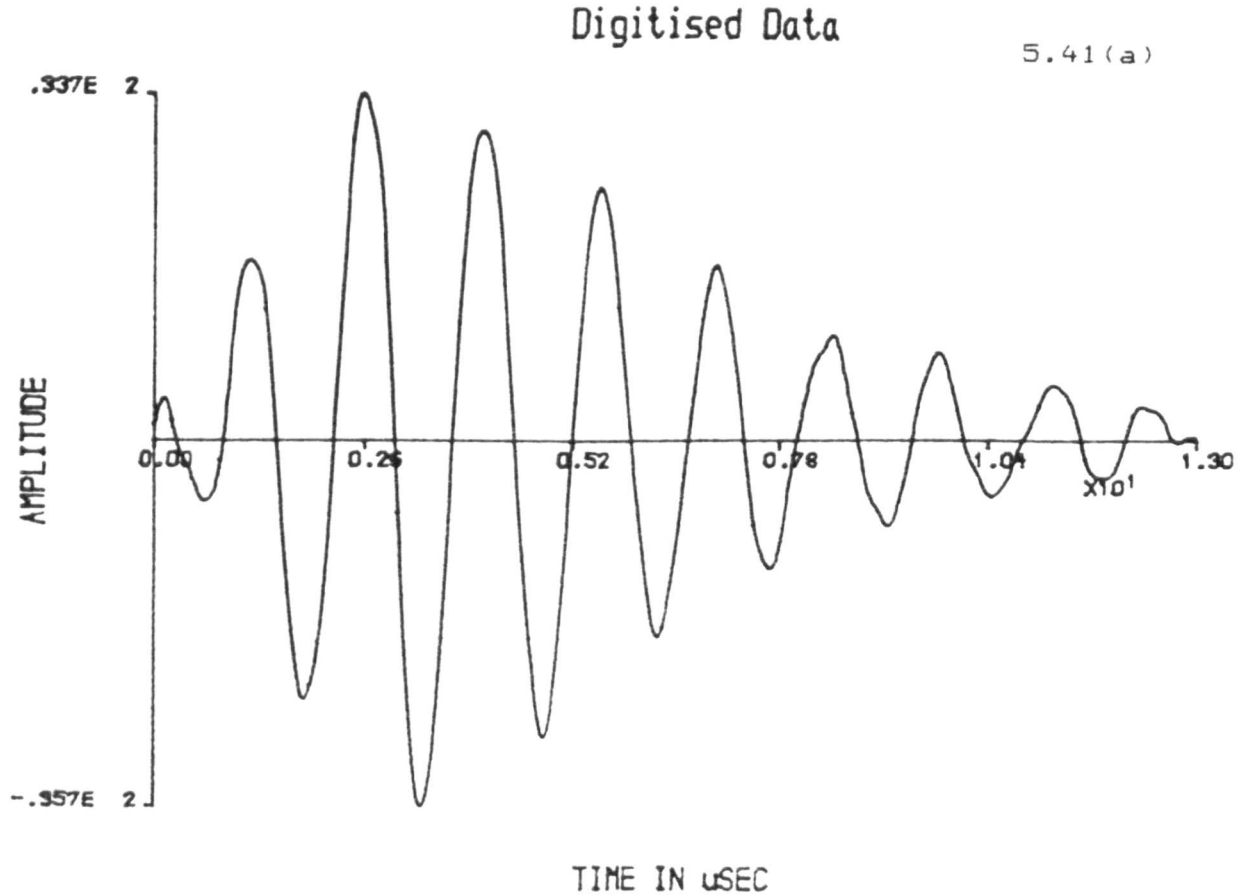

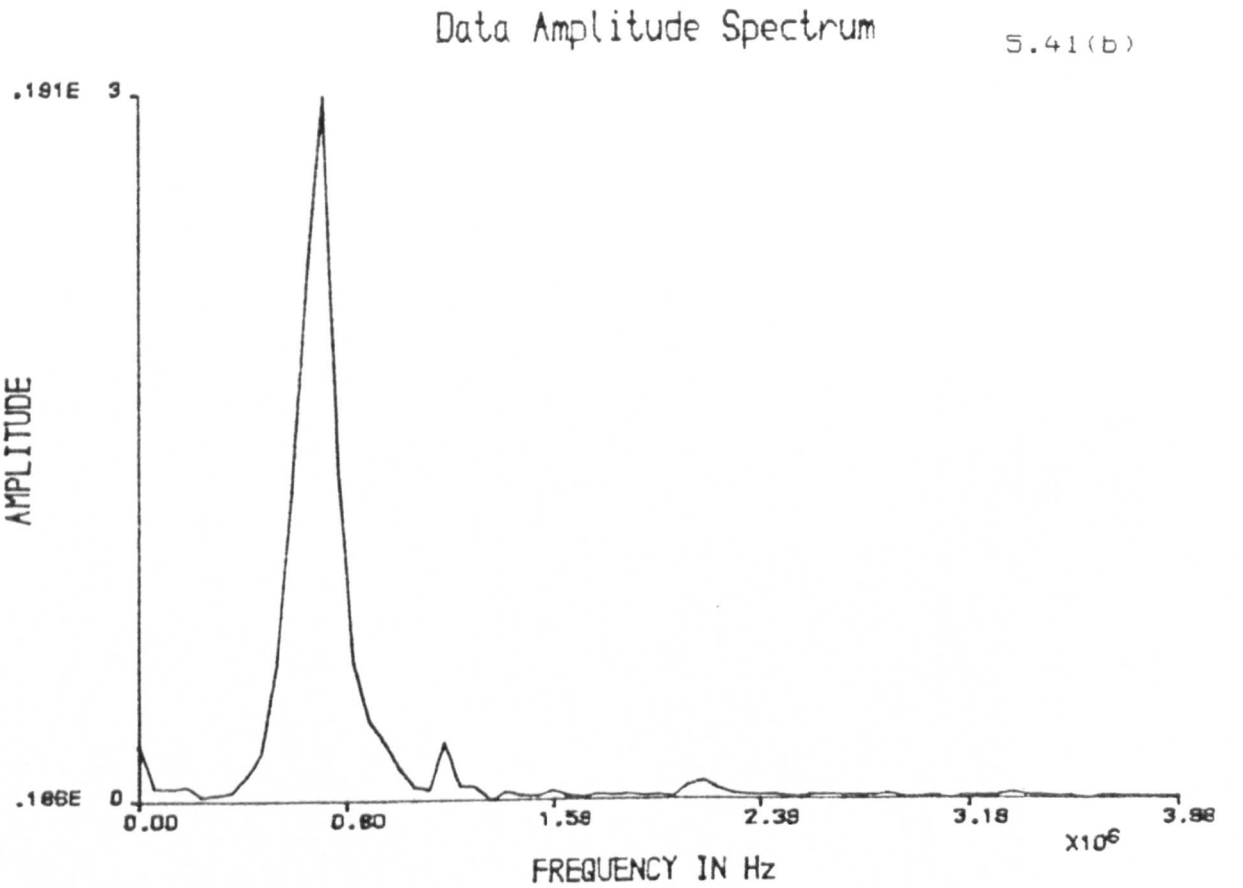

Figure 5.41 Measured time and frequency domain pulse-echo response of the transducer with no layers. Measured in water.

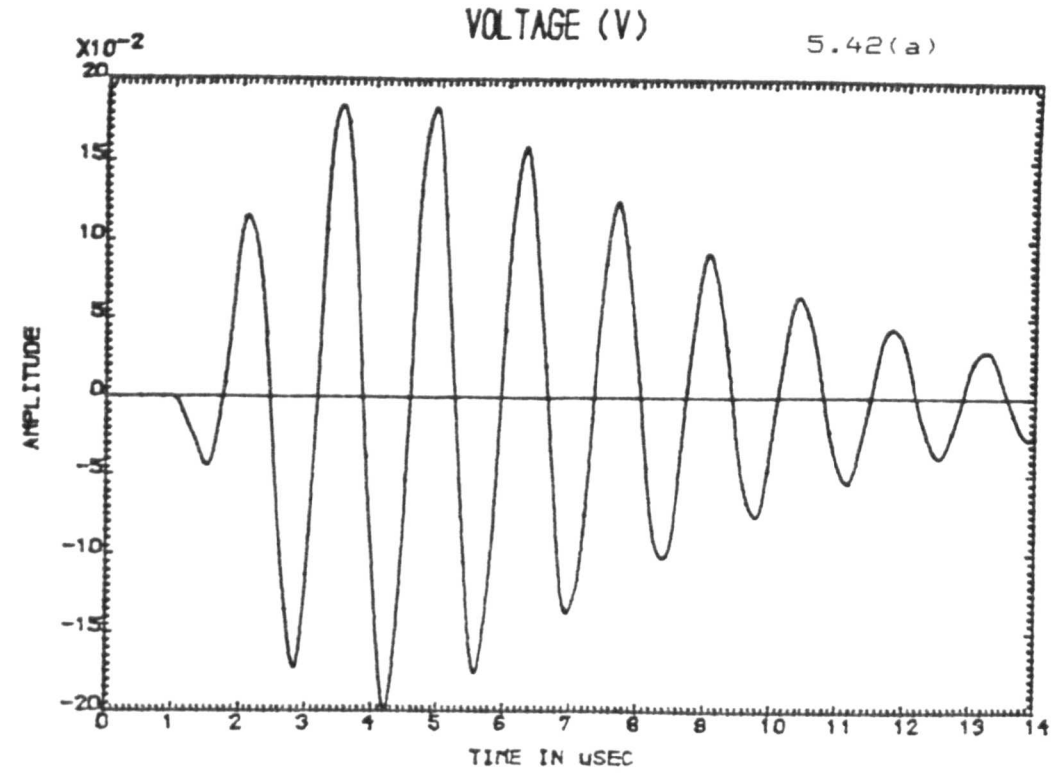

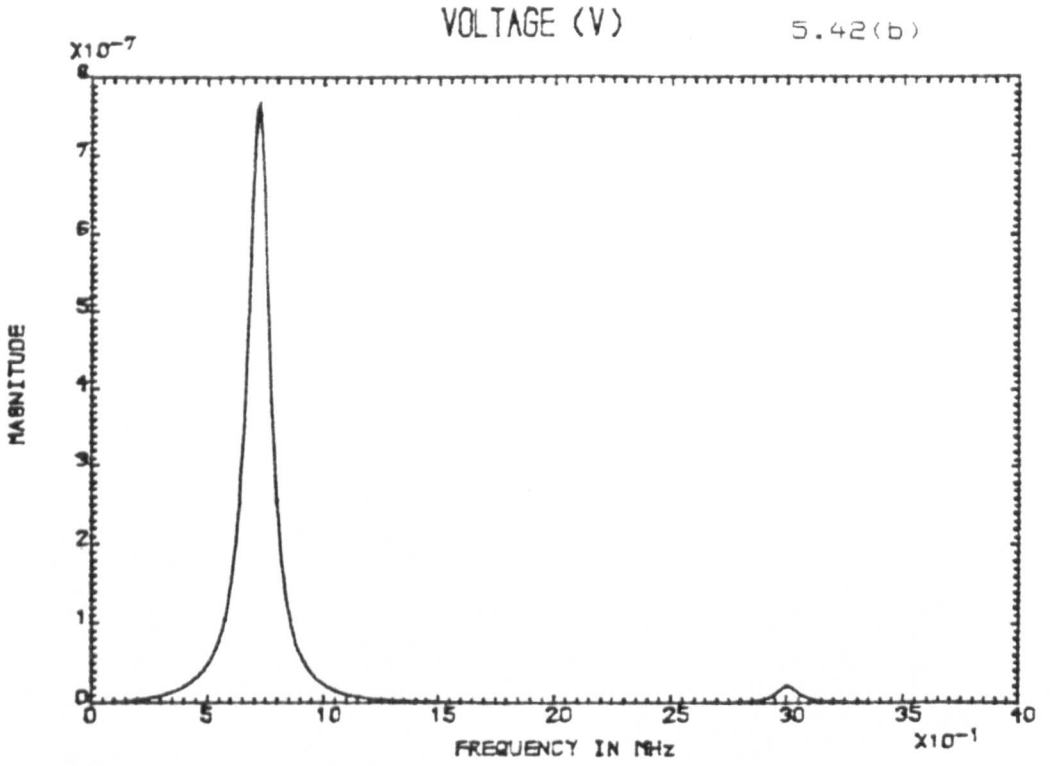

Figure 5.42 Simulated time and frequency domain pulse-echo response of the transducer with no layers.

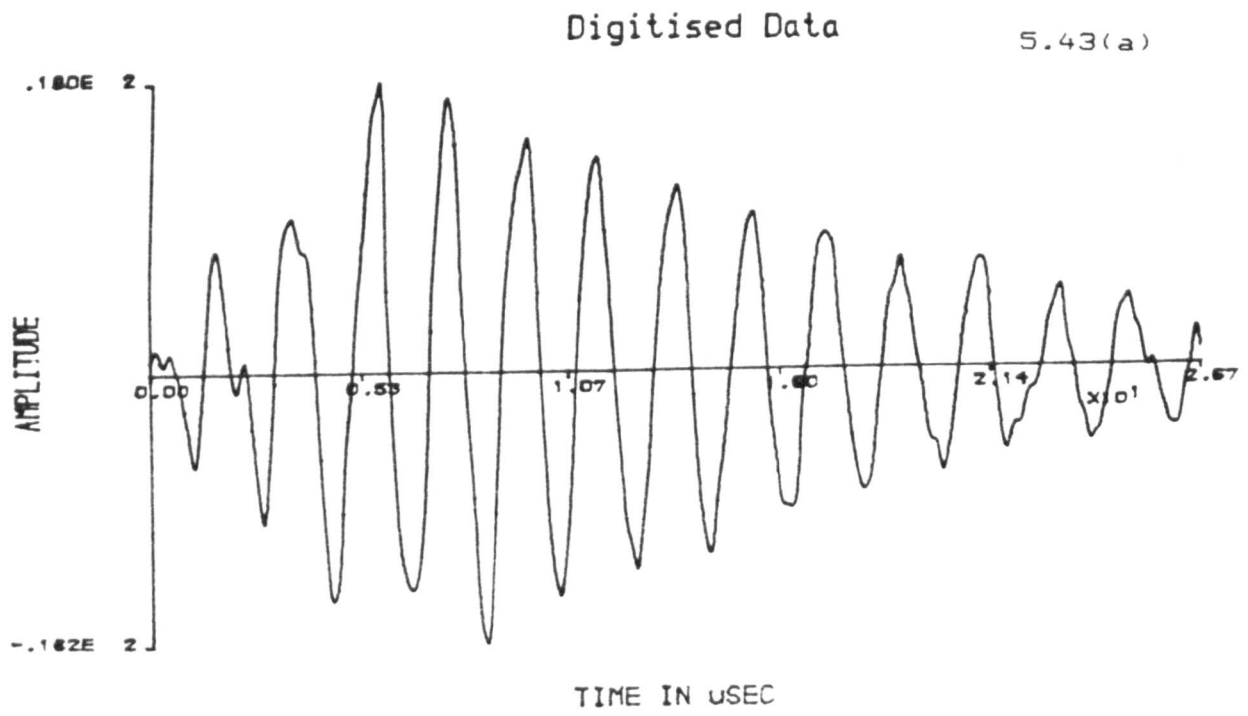

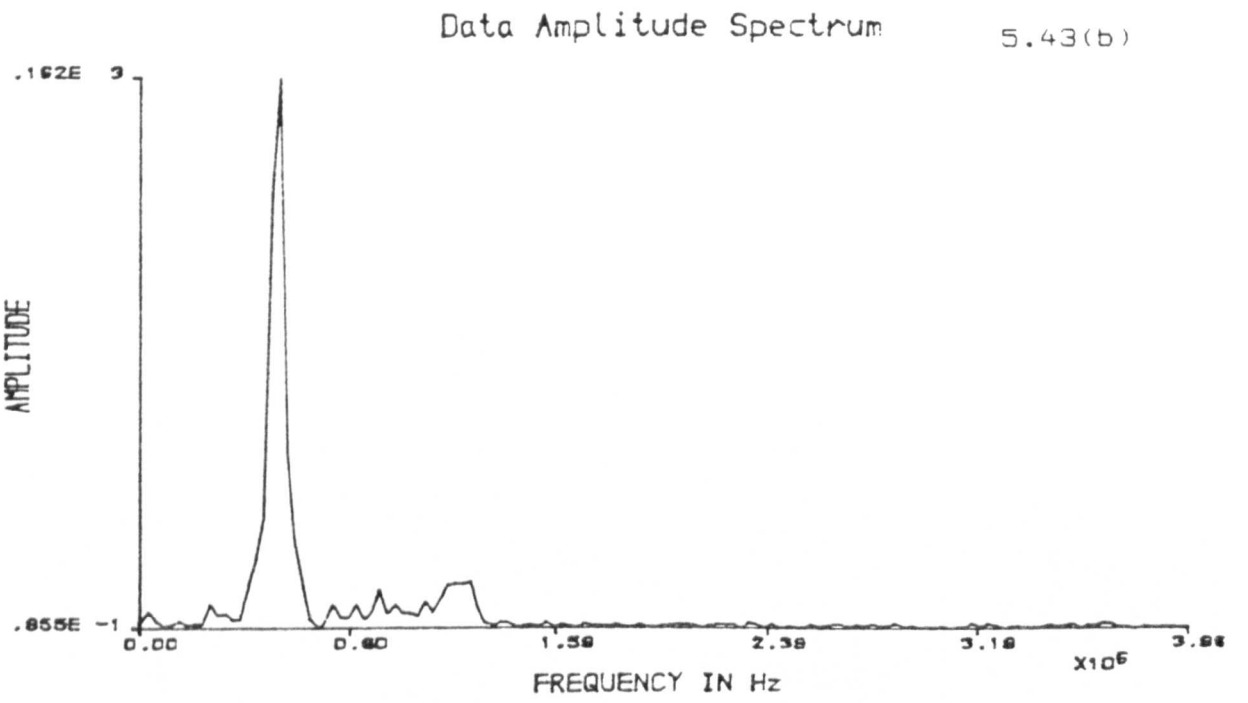

Figure 5.43 Measured time and frequency domain pulse-echo response of the transducer with steel layer. Measured in water.

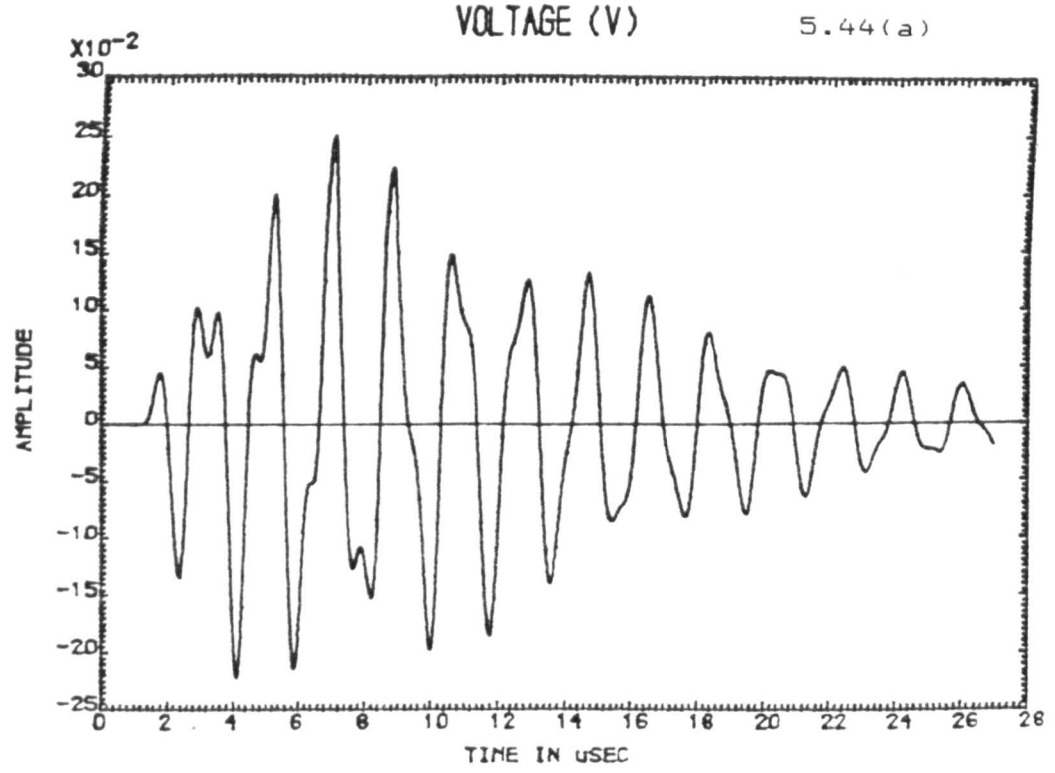

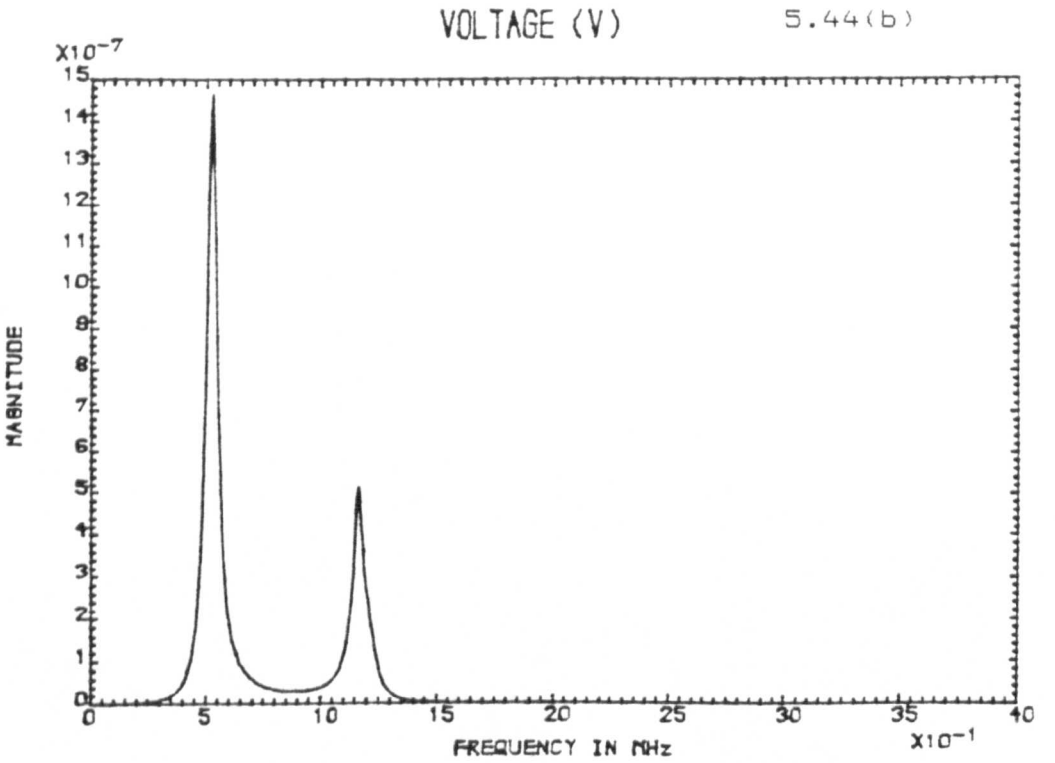

Figure 5.44 Simulated time and frequency domain pulse-echo response of the transducer with steel layer.

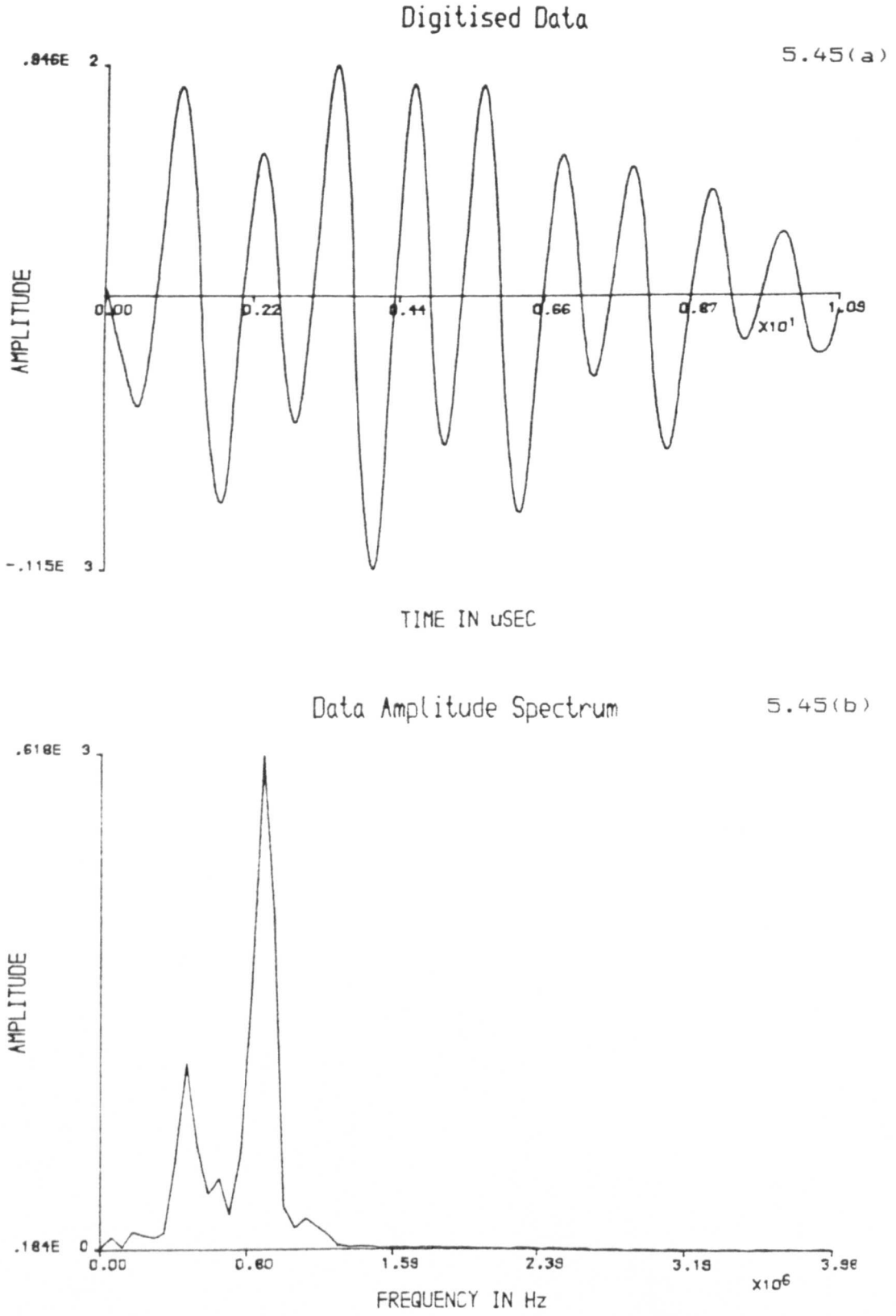

Figure 5.45 Measured time and frequency domain pulse-echo response of the transducer with aluminium layer. Measured in water.

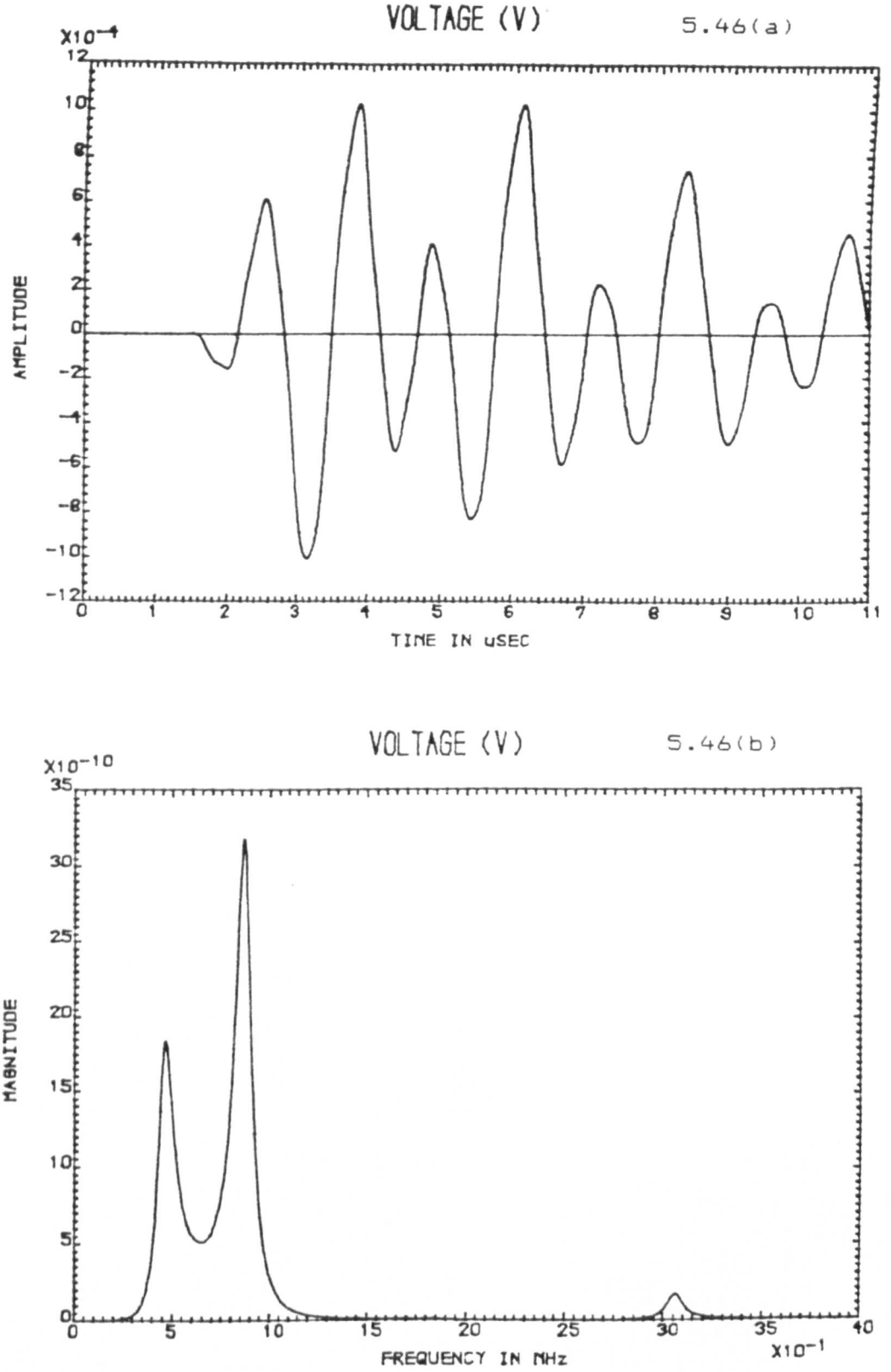

Figure 5.46 Simulated time and frequency domain pulse-echo response of the transducer with aluminium layer.

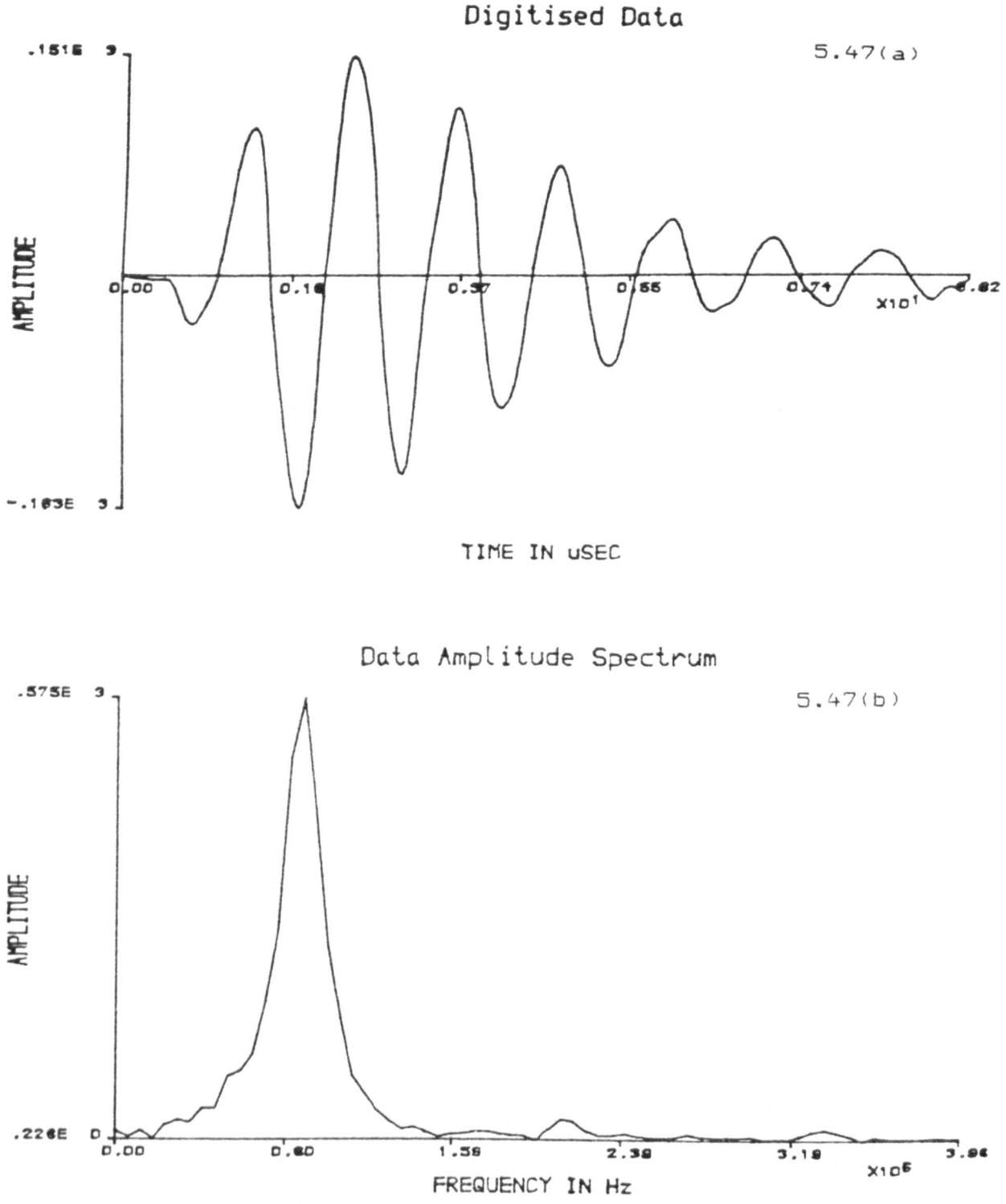

Figure 5.47 Measured time and frequency domain pulse-echo response of the transducer with no layers. Measured in crown glass.

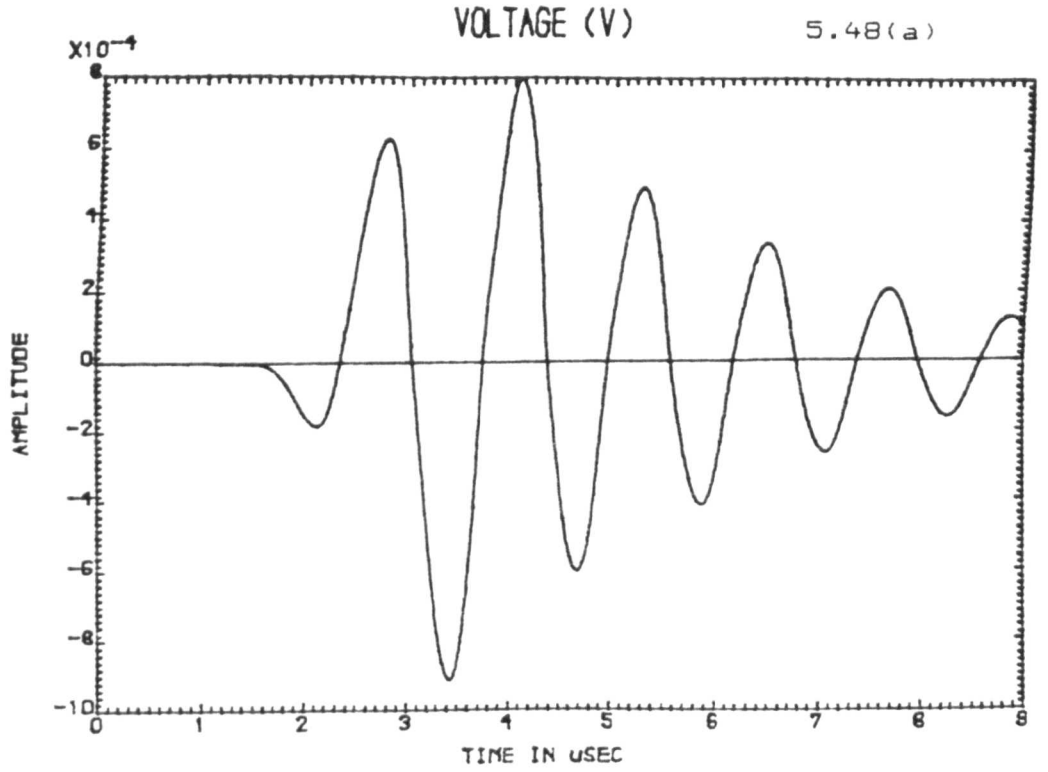

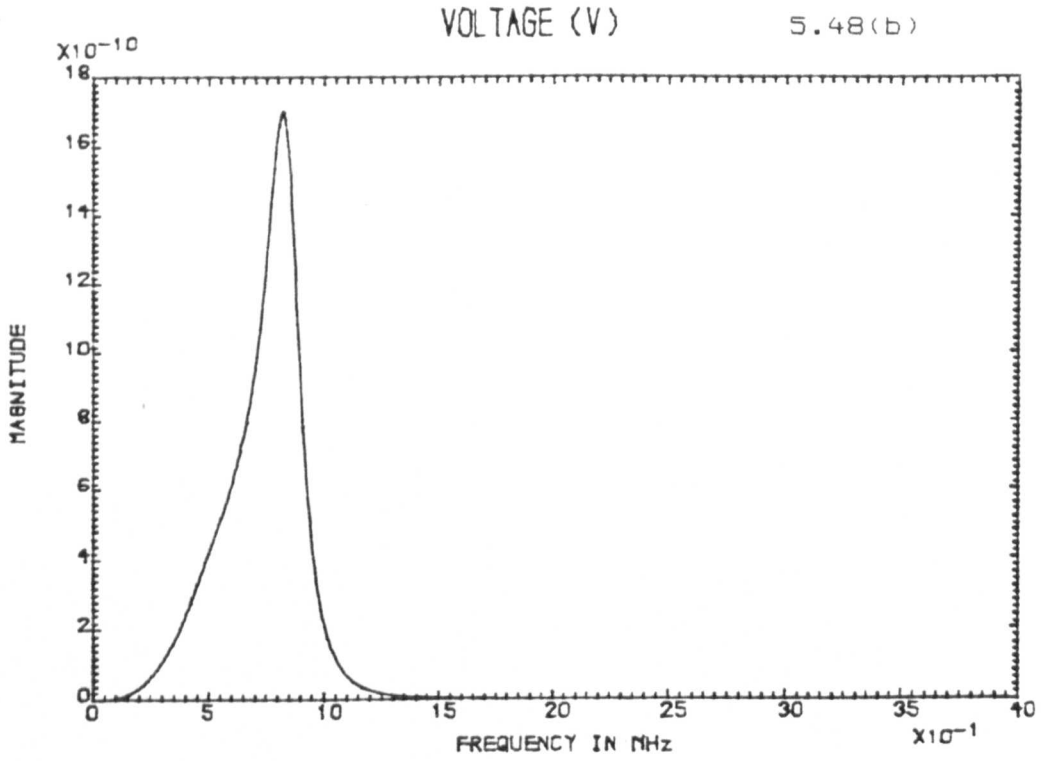

Figure 5.48 Simulated time and frequency domain pulse-echo response of the transducer with no layers.

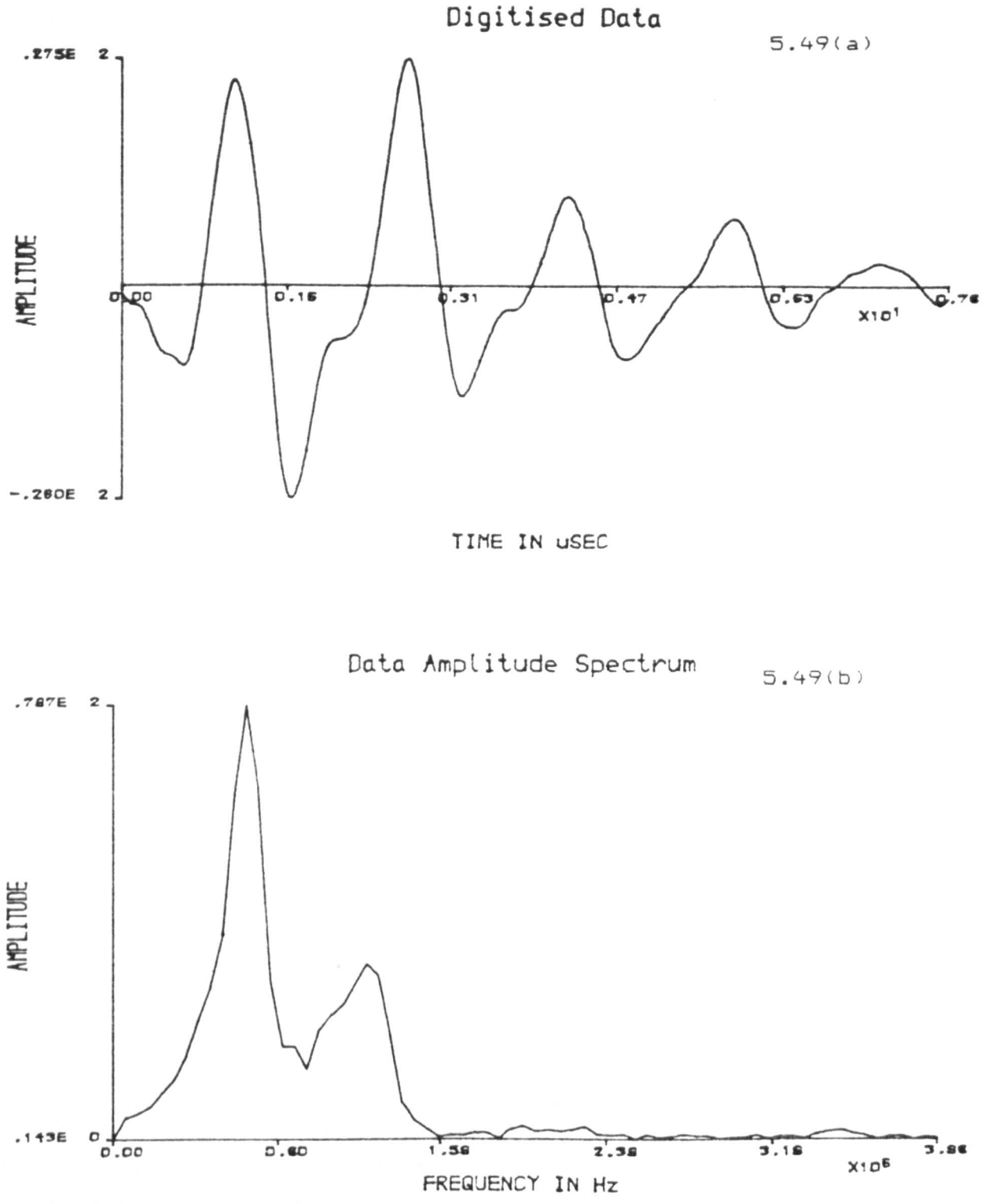

Figure 5.49 Measured time and frequency domain pulse-echo response of the transducer with steel layer. Measured in crown glass.

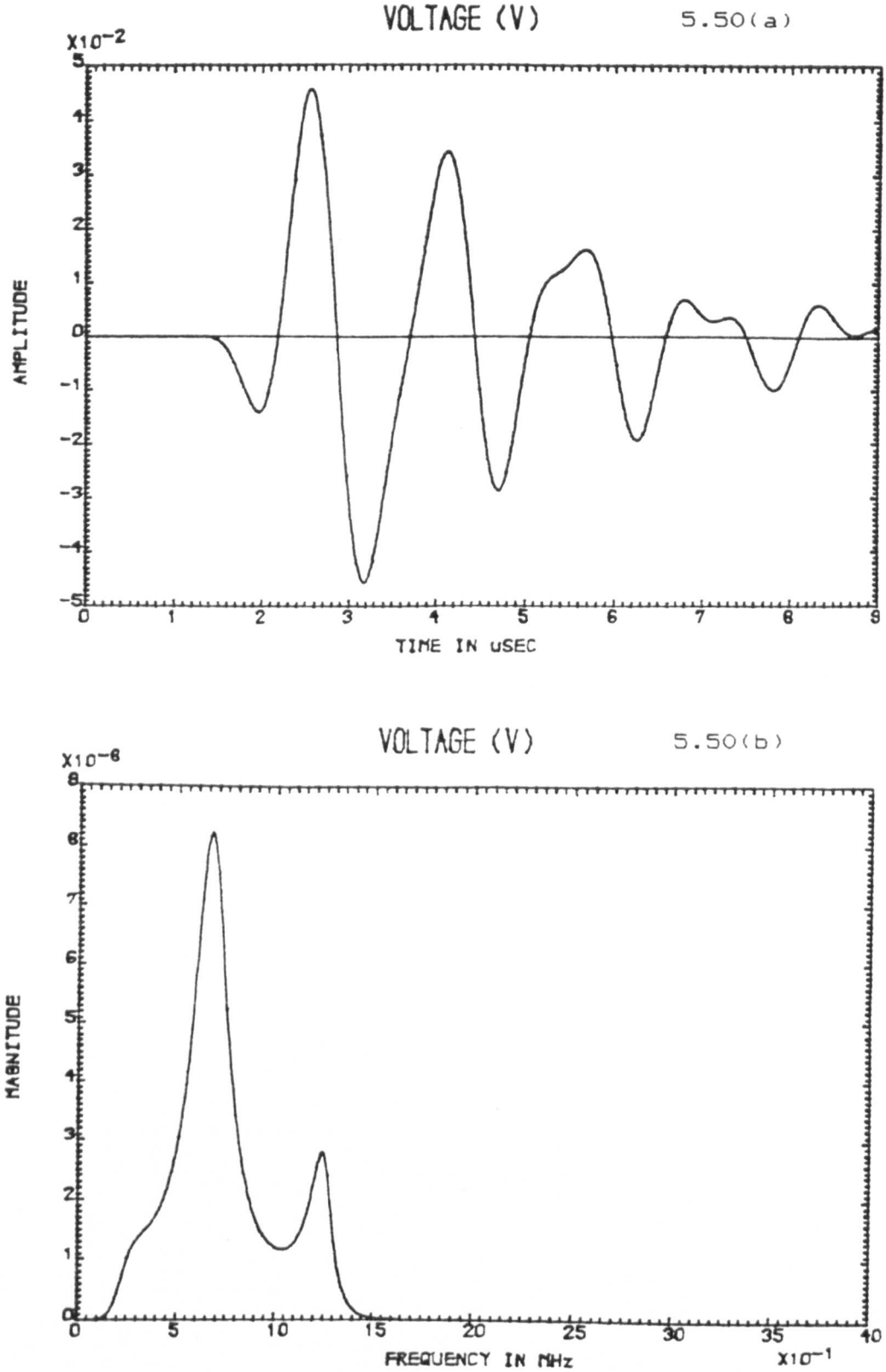

Figure 5.50 Simulated time and frequency domain pulse-echo response of the transducer with steel layer

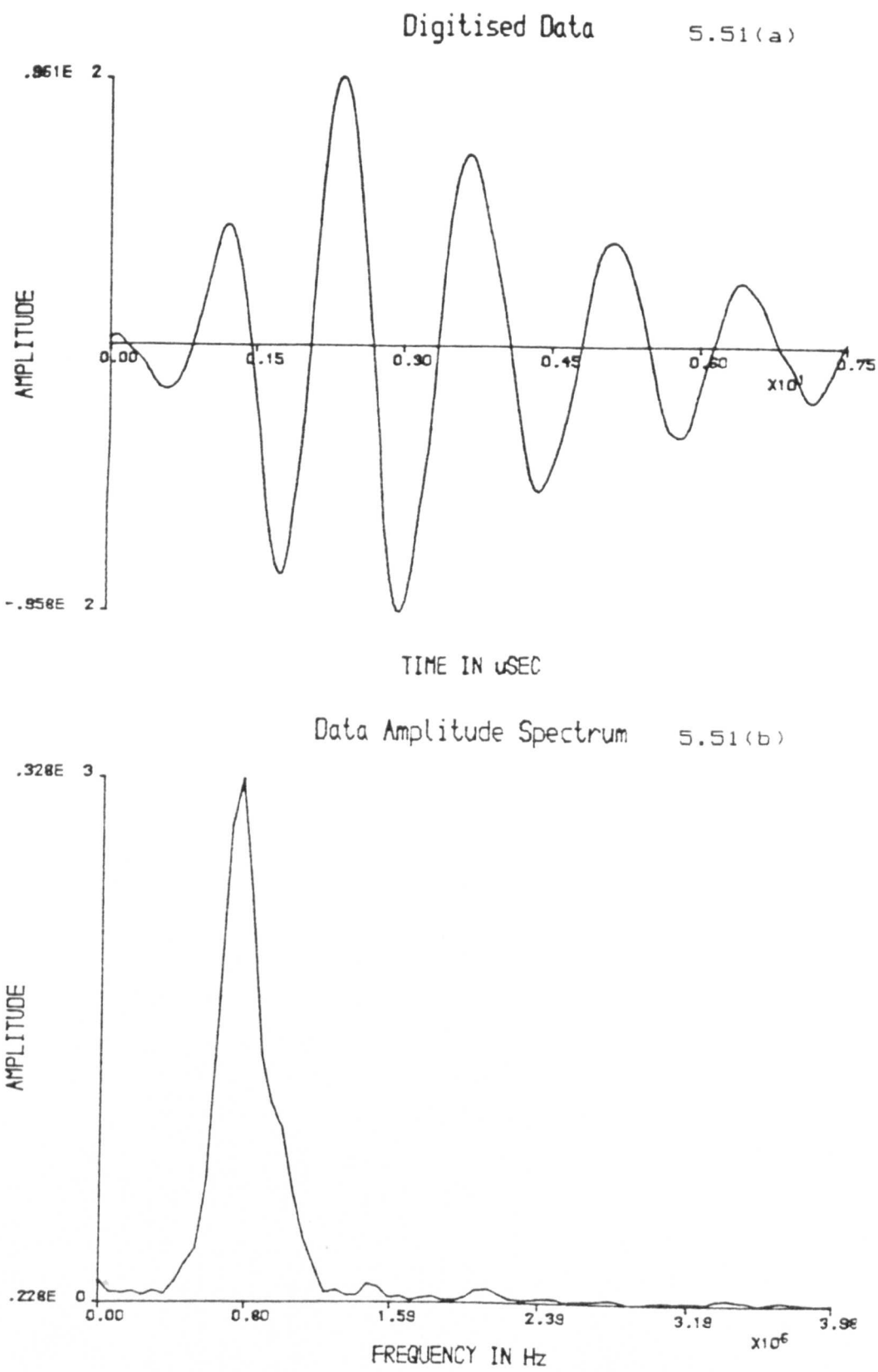

Figure 5.51 Measured time and frequency domain pulse-echo response of the transducer with aluminium layer. Measured in crown glass.

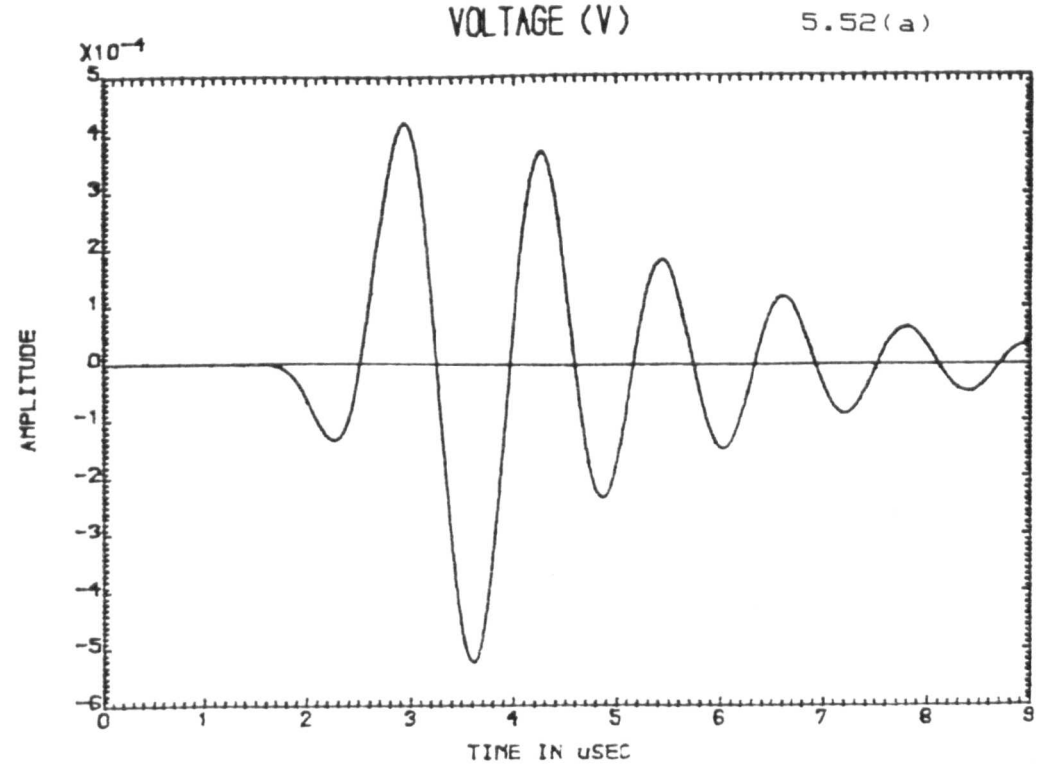

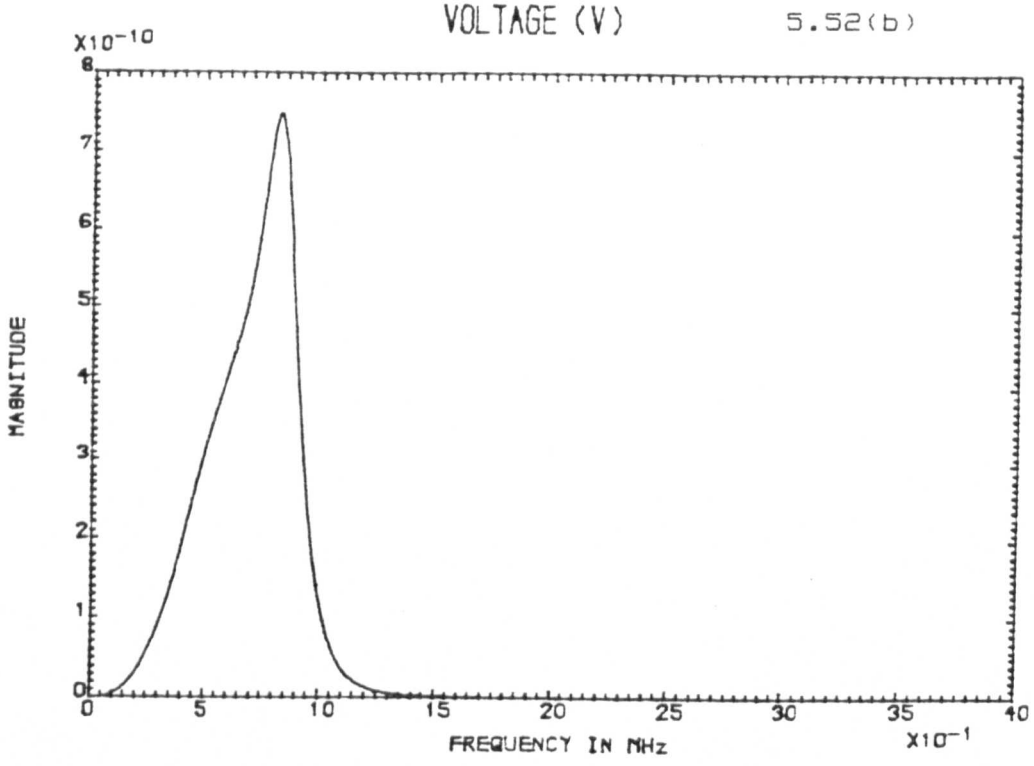

Figure 5.52 Simulated time and frequency domain pulse-echo response of the transducer with aluminium layer.

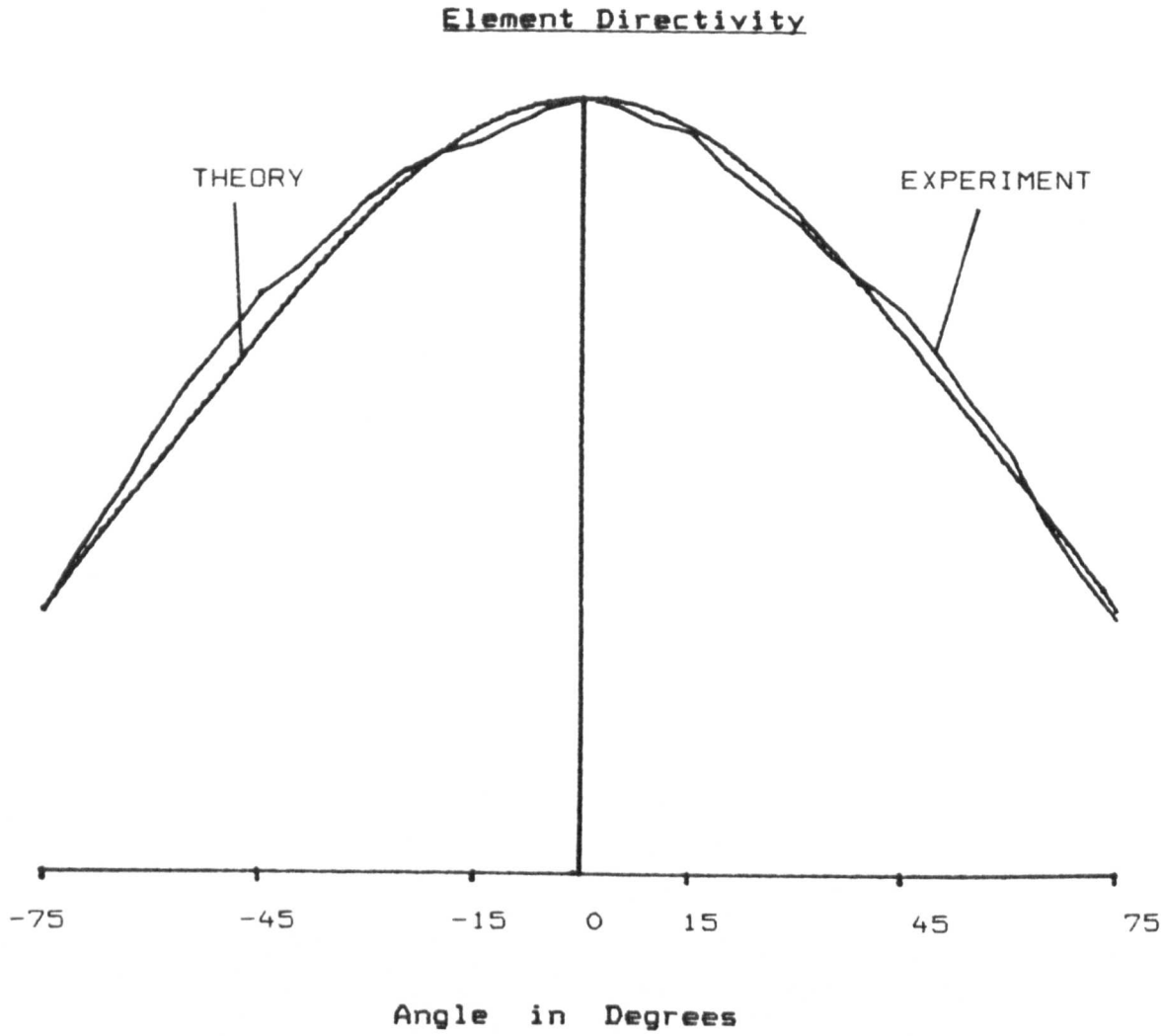

Figure 5.53 Typical experimental and theoretical directivity functions for a two-dimensional transducer.

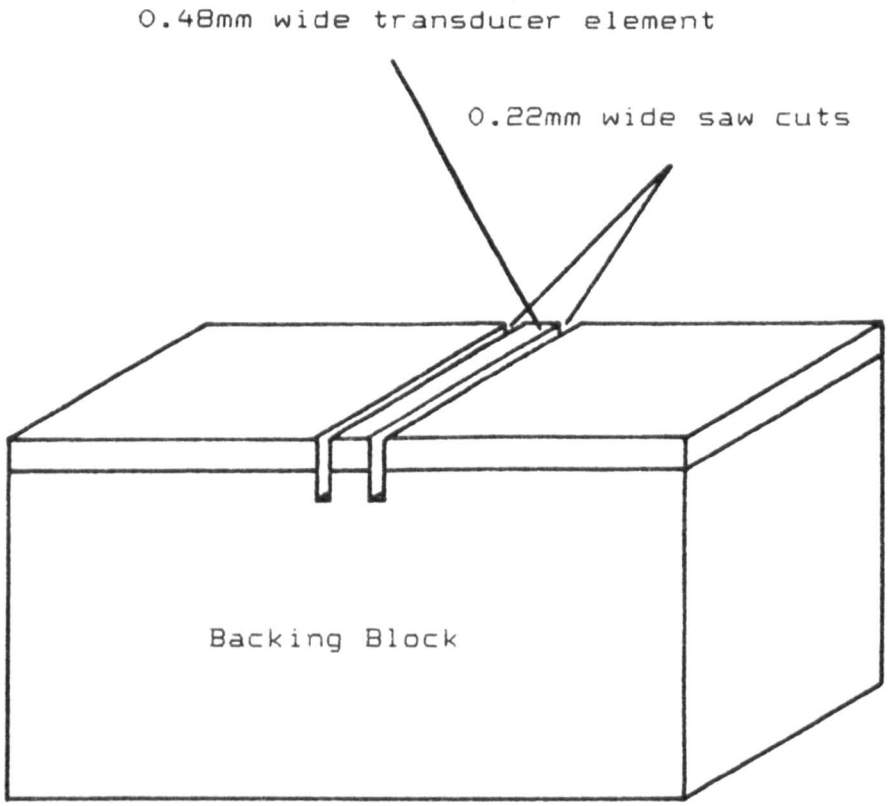

Figure 6.1 Diagram showing the 0.22mm sawcuts and the resultant 0.48mm transducer element.

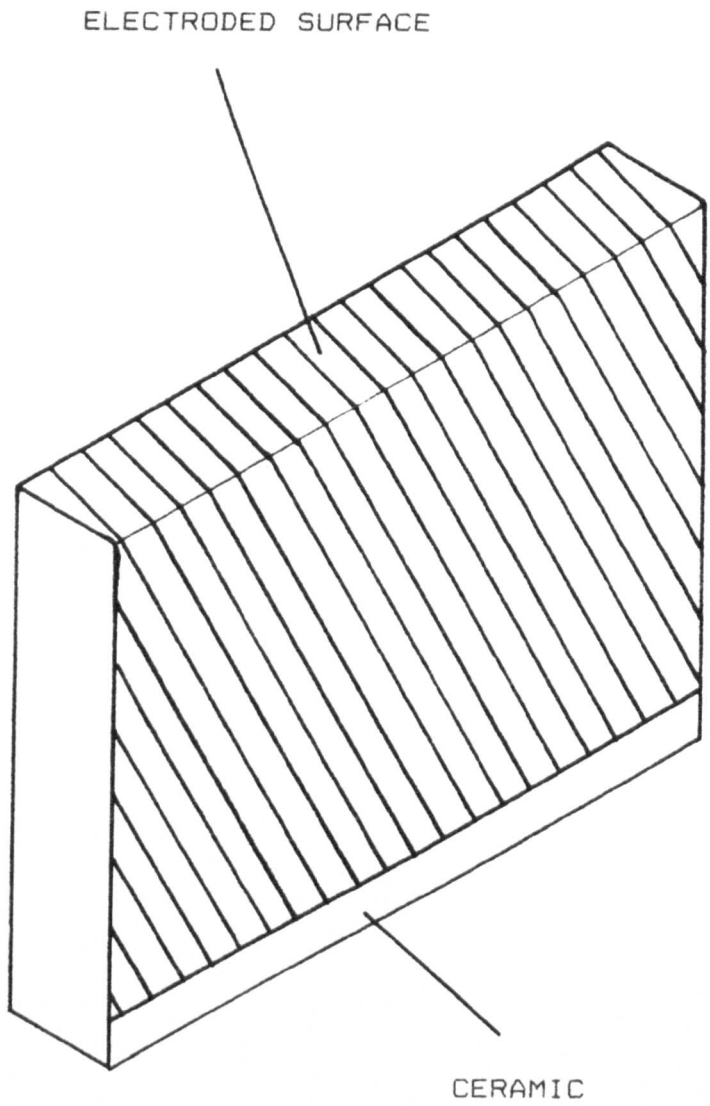

Figure 6.2 The array transducer with the customised electrode. The electrode pattern is identical on the opposite face.

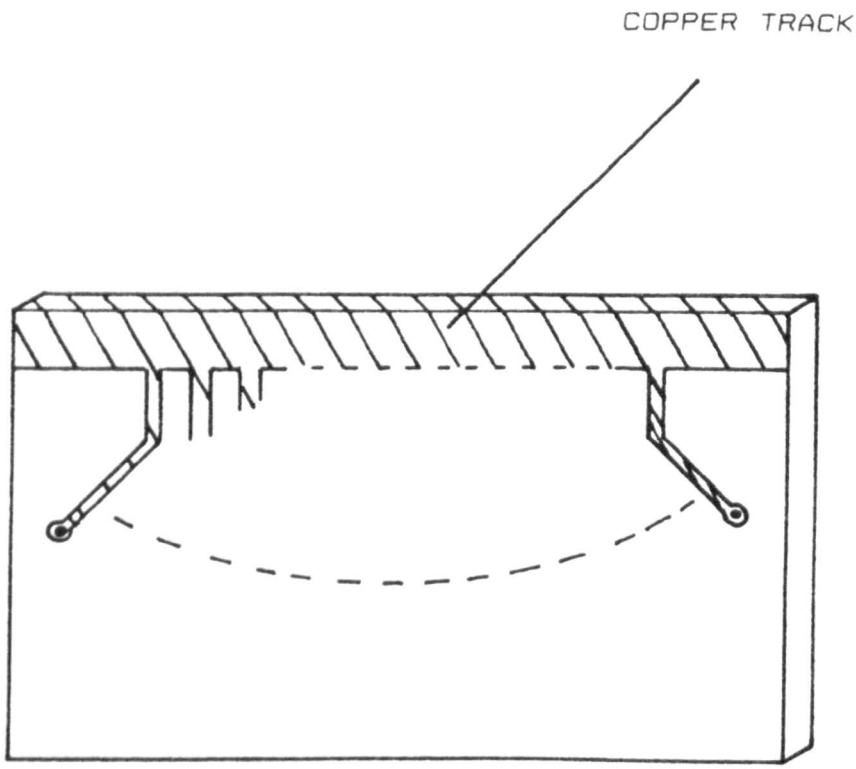

Figure 6.3 The printed circuit board used for making electrical connection to the array elements.

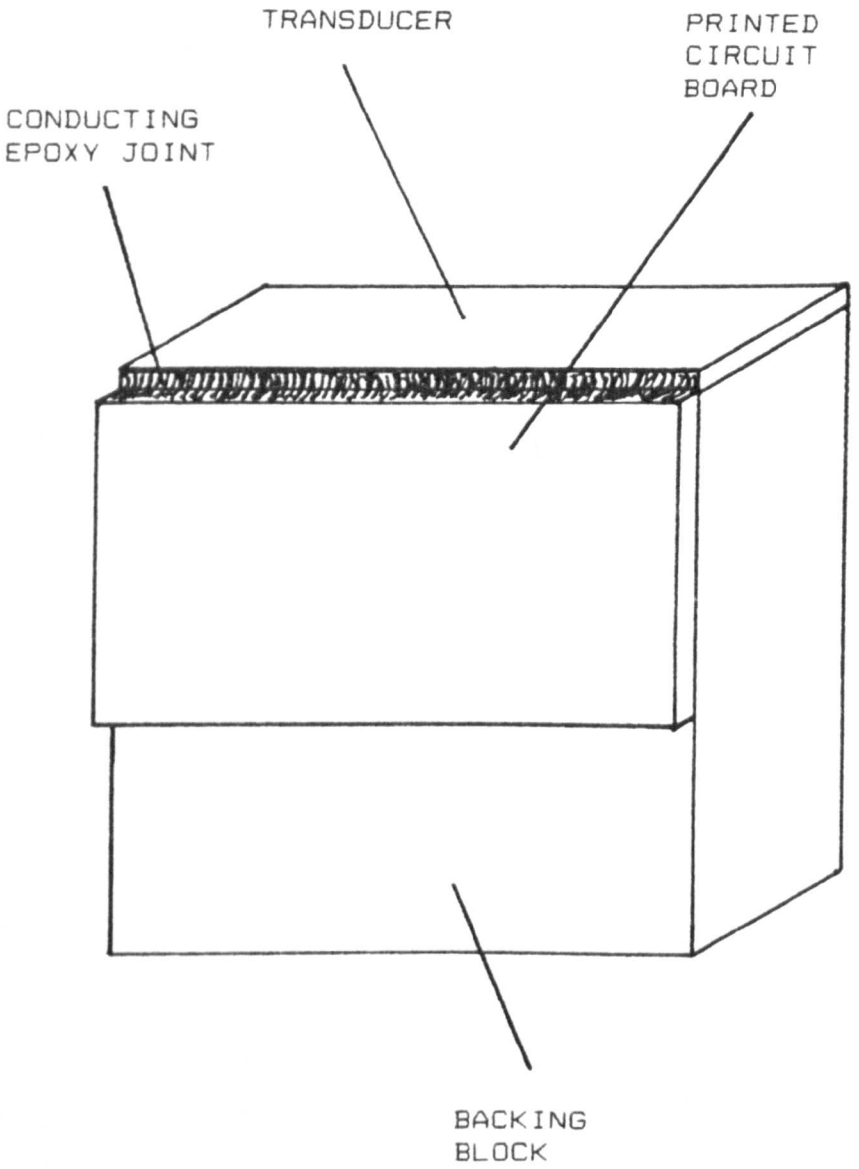

Figure 6.4 Diagram showing position of the conducting epoxy joint.

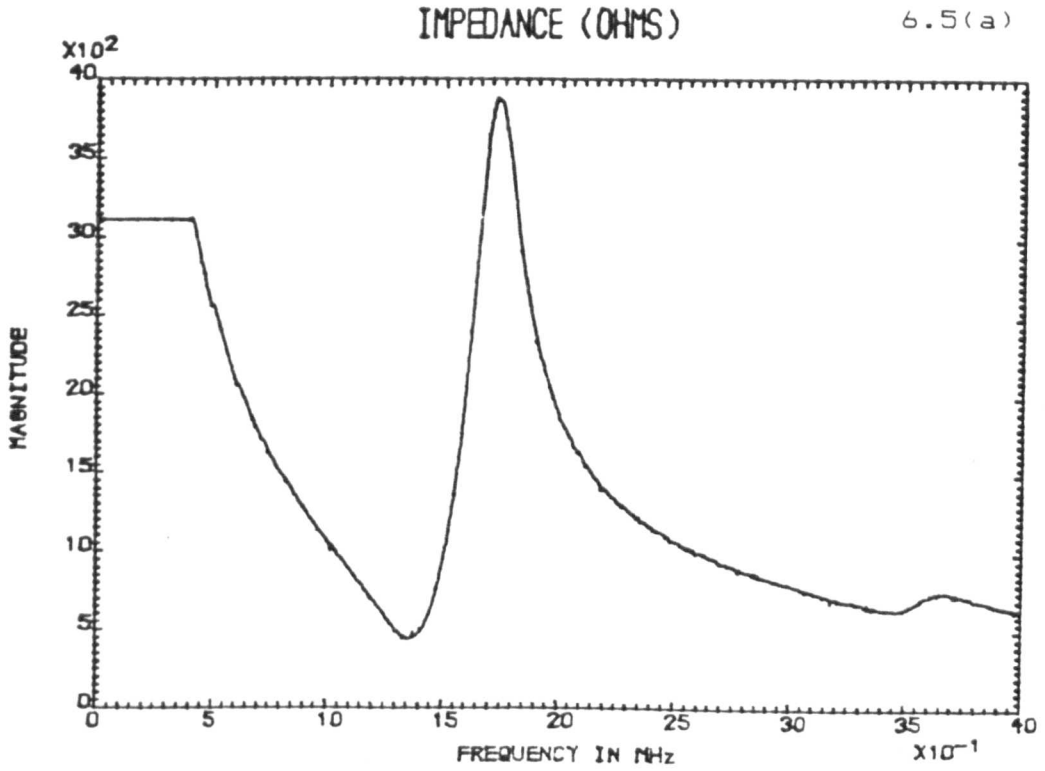

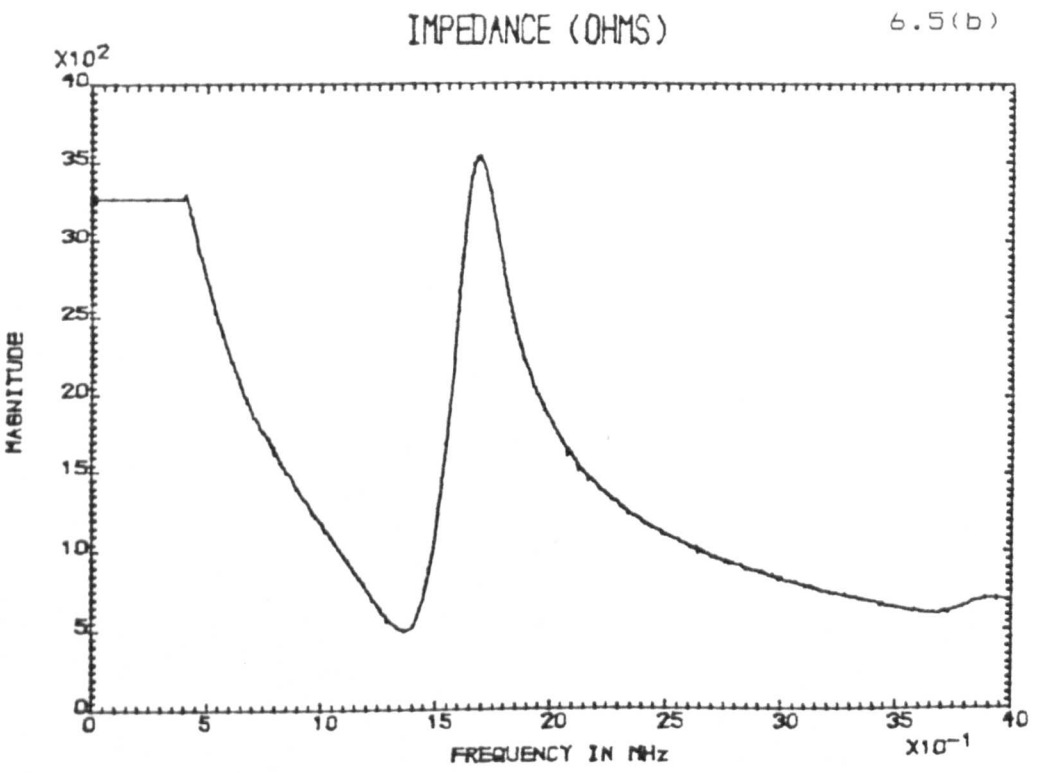

Figure 6.5 Measured impedance magnitude spectra for the transducer with end electrode, and the transducer without end electrode respectively.

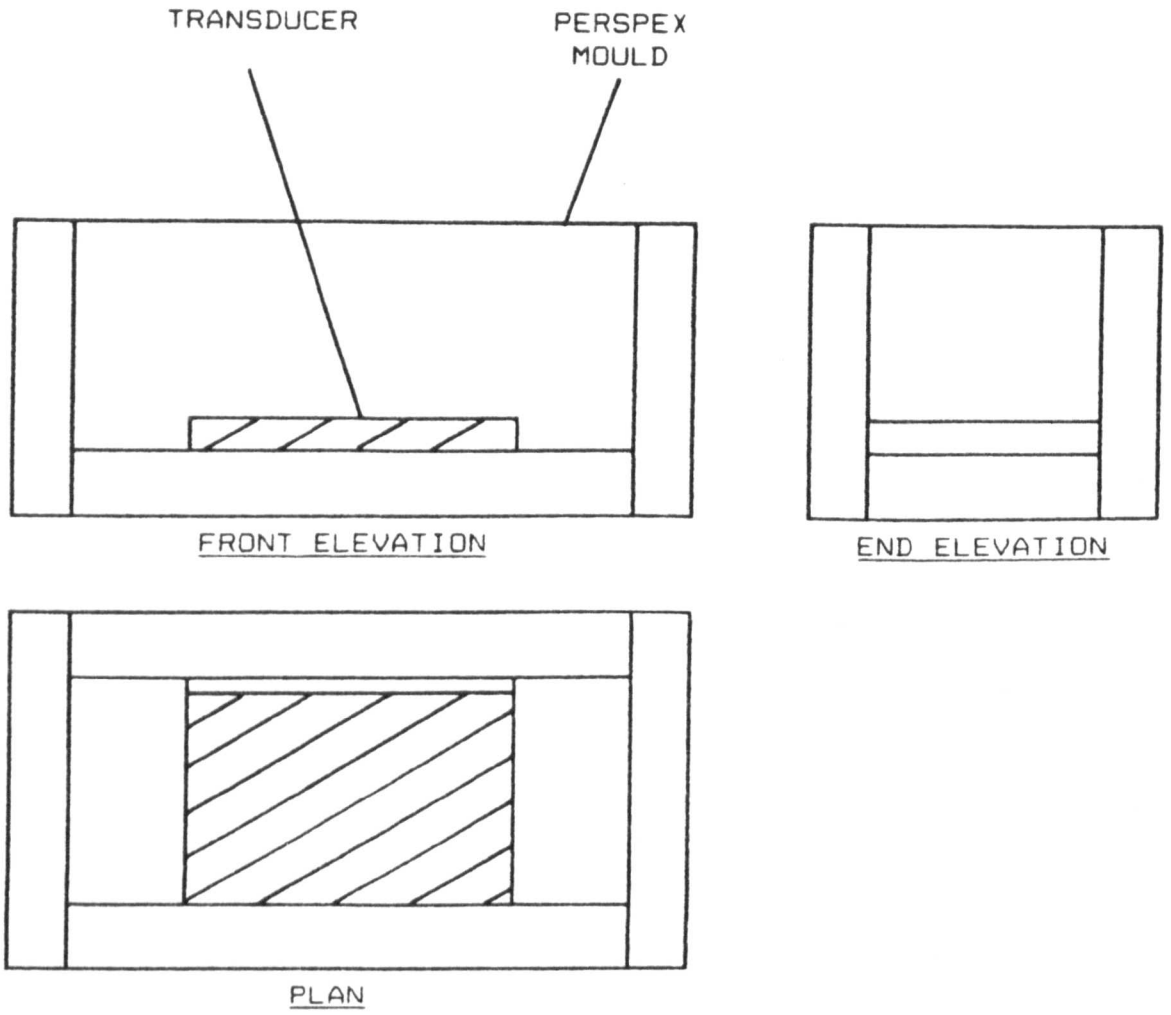

Figure 6.6 Drawing of the transducer in the perspex mould. The aluminium loaded epoxy is poured into the top of the mould.

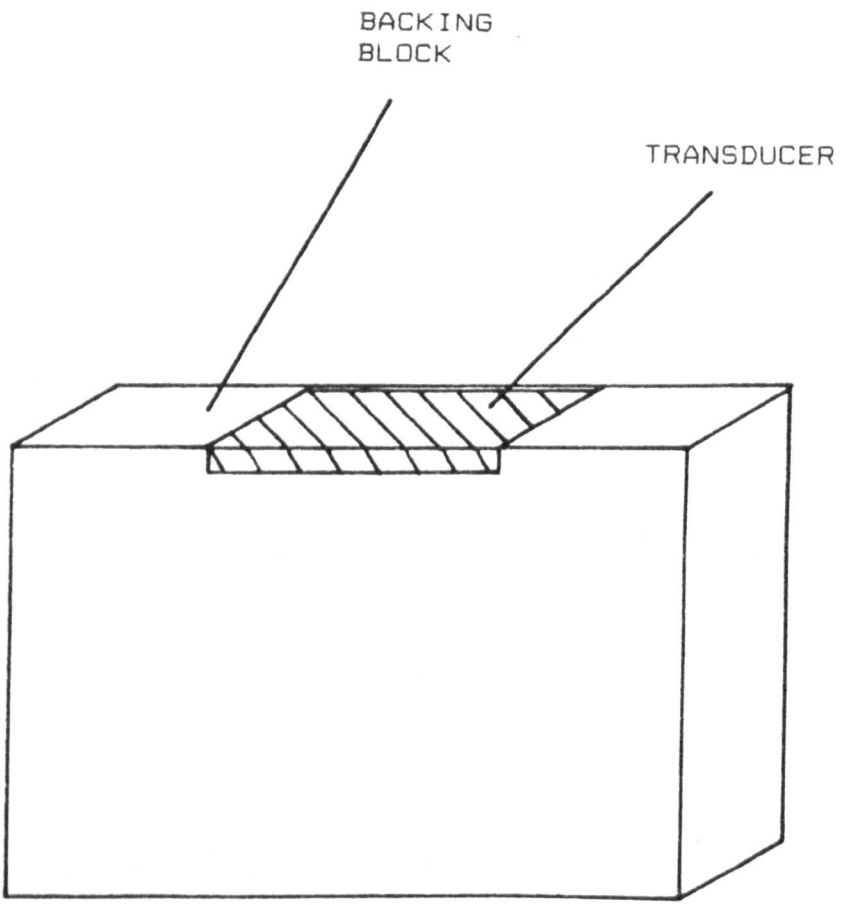

Figure 6.7 The mounted array transducer.

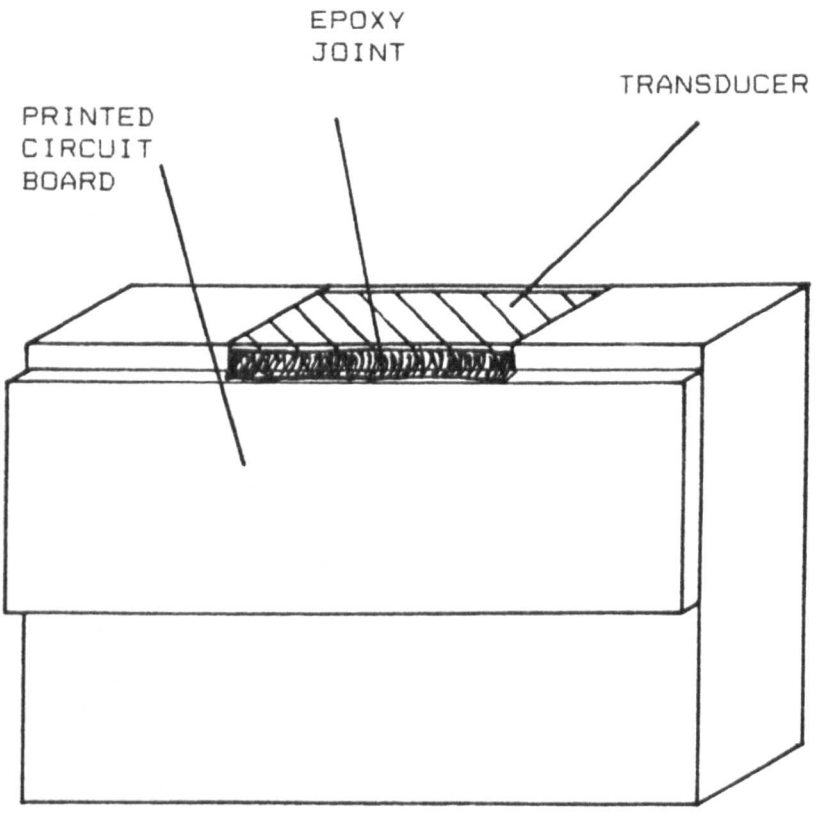

Figure 6.8 Connection of the printed circuit board to the mounted transducer.

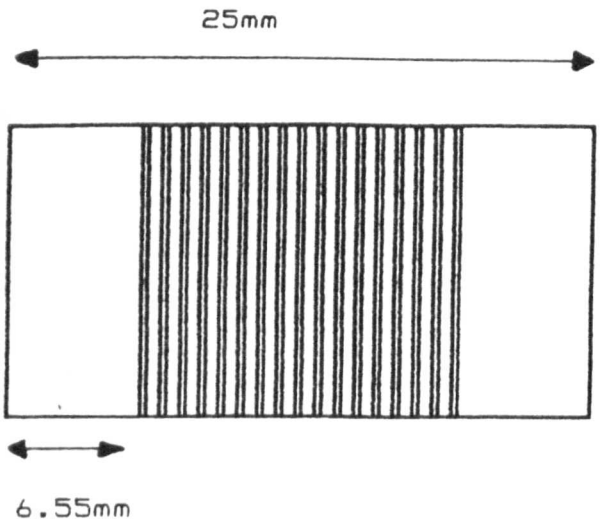

Figure 6.9 Diagram showing the seventeen 0.22mm cuts, and sixteen 0.48mm wide transducer elements on the 25mm PZT-5A slab.

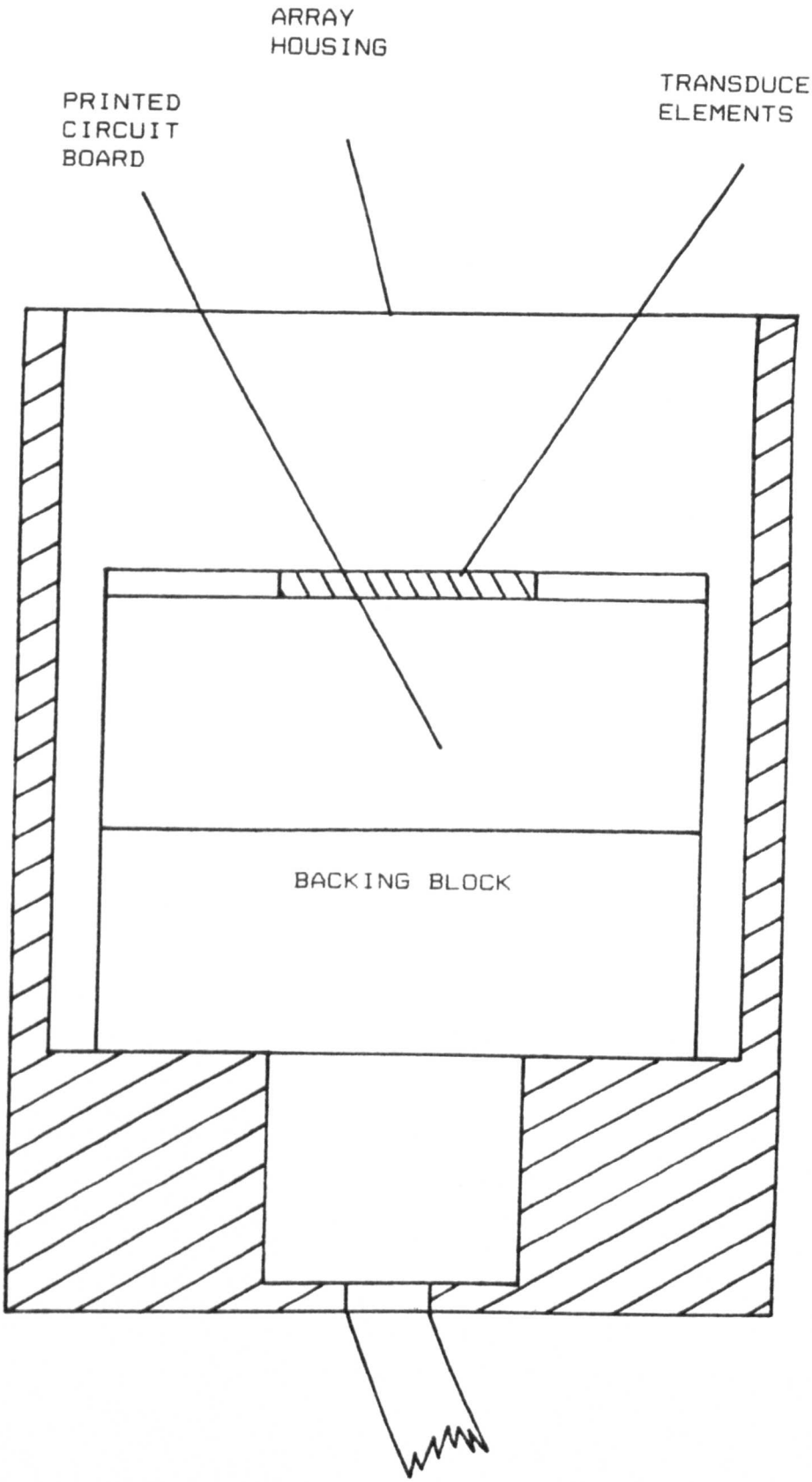

Figure 6.10 Cross sectional view of the array housing, with the array in place.

6.11a The mechanical structure of array #1.

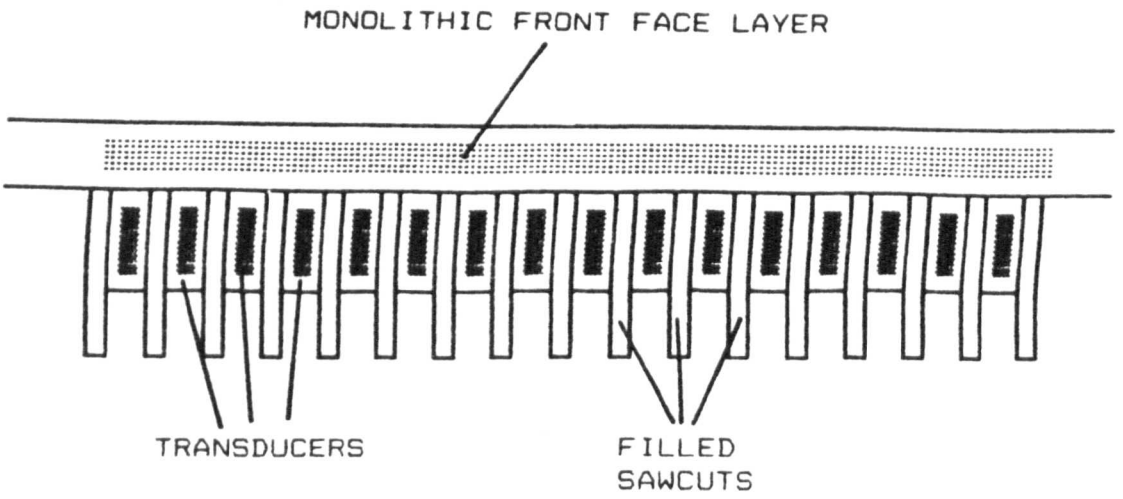

6.11b The mechanical structure of array #2.

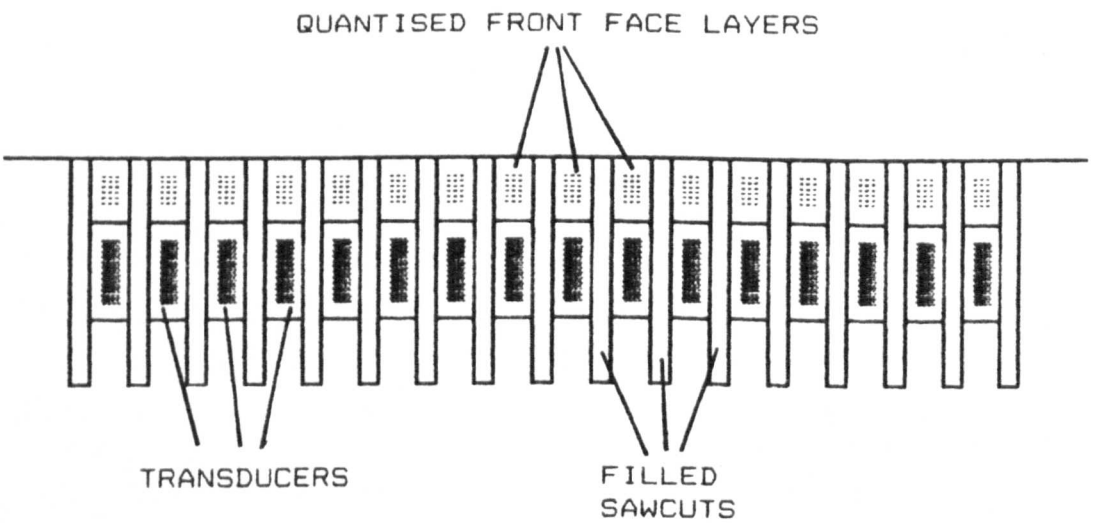

Figure 6.11 A diagrammatical comparison of the mechanical structure of the two arrays.

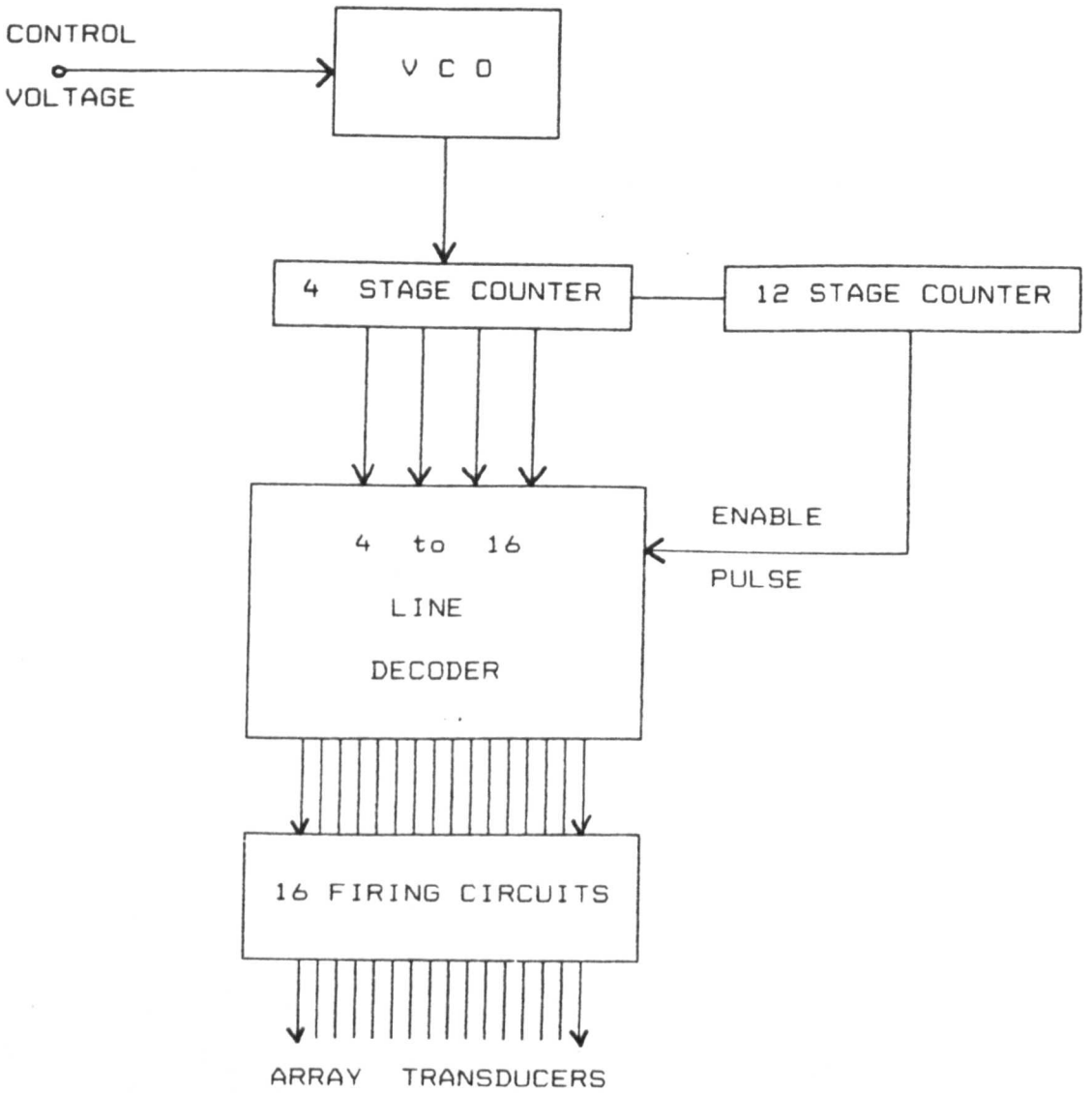

Figure 6.12 Block diagram of the array control hardware.

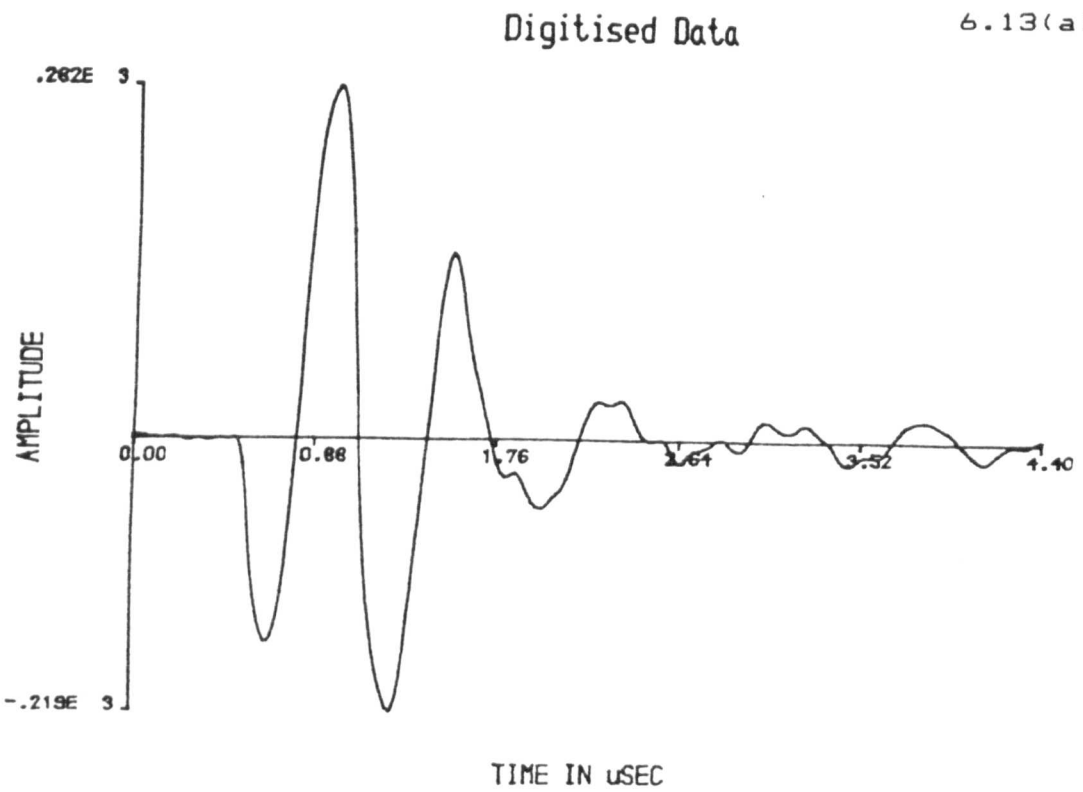

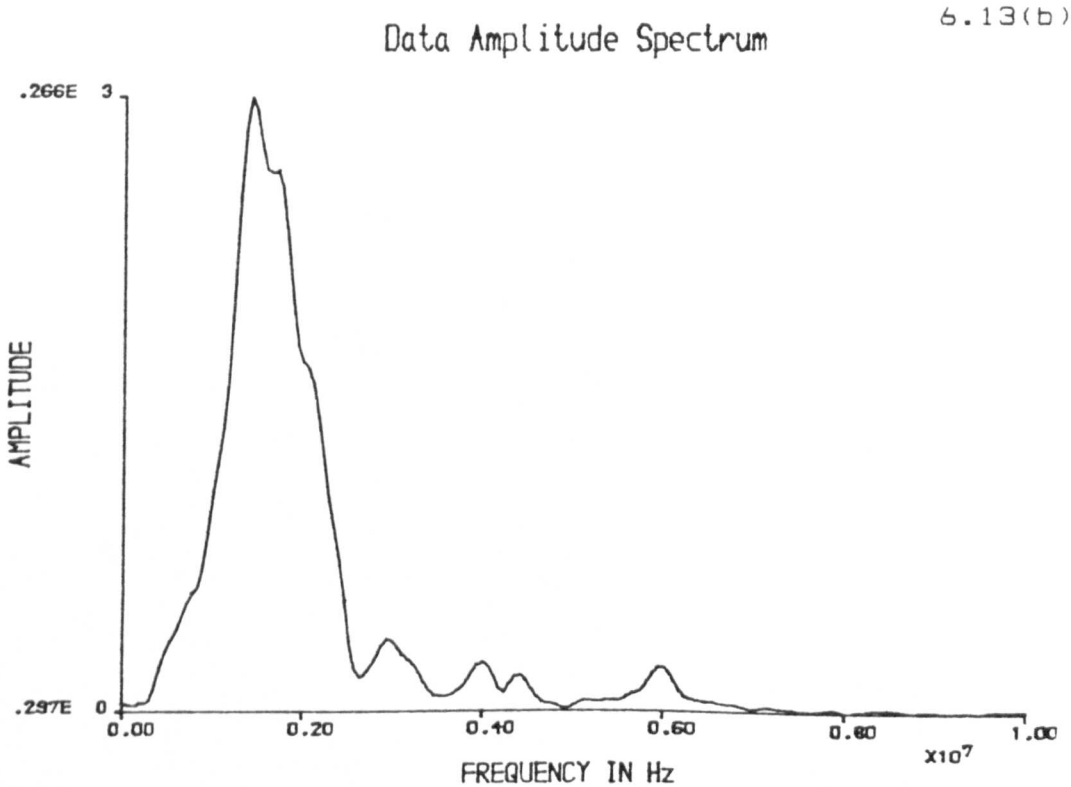

Figure 6.13 Measured time and frequency domain force output from element 9 in array #1.

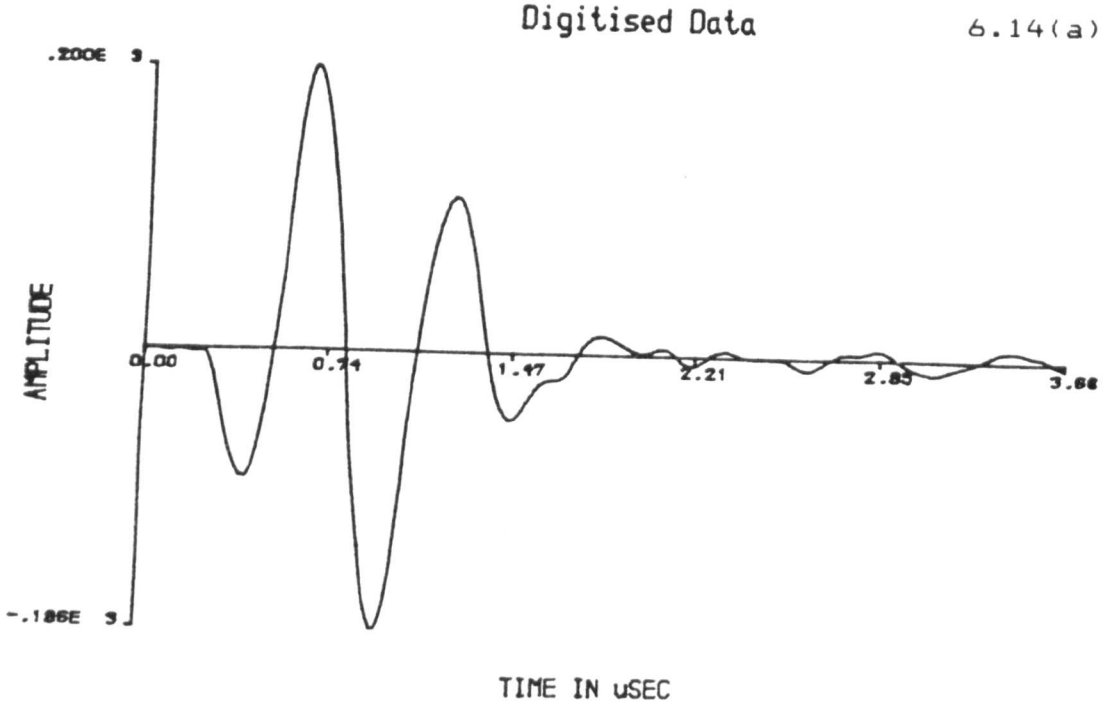

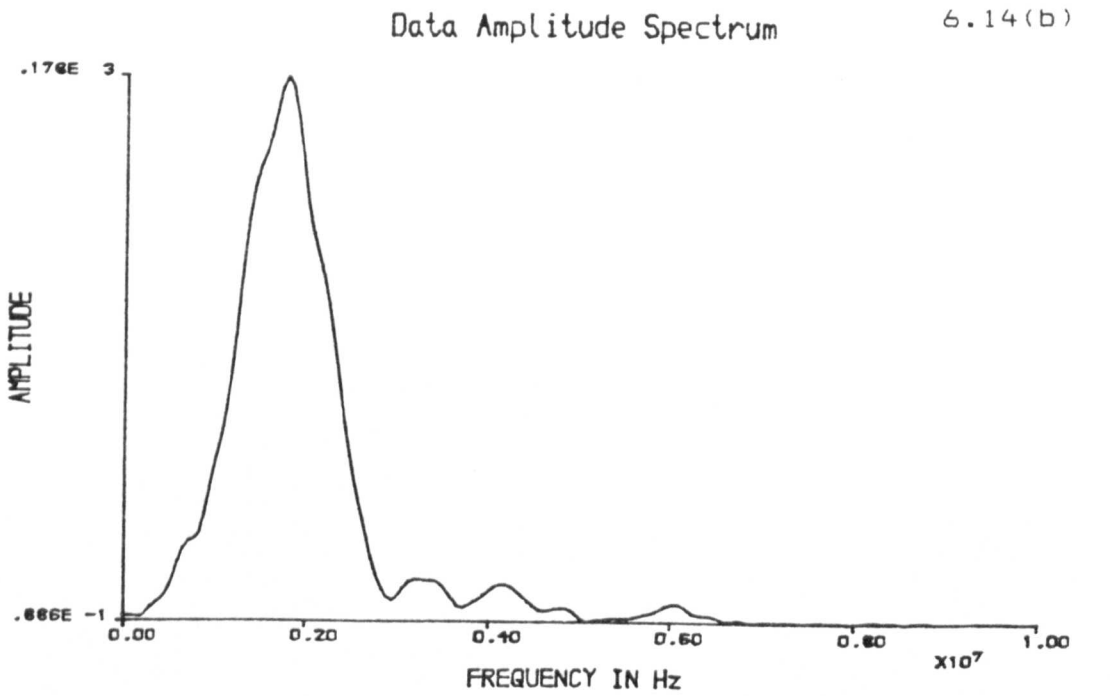

Figure 6.14 Measured time and frequency domain force output from element 9 in array #2.

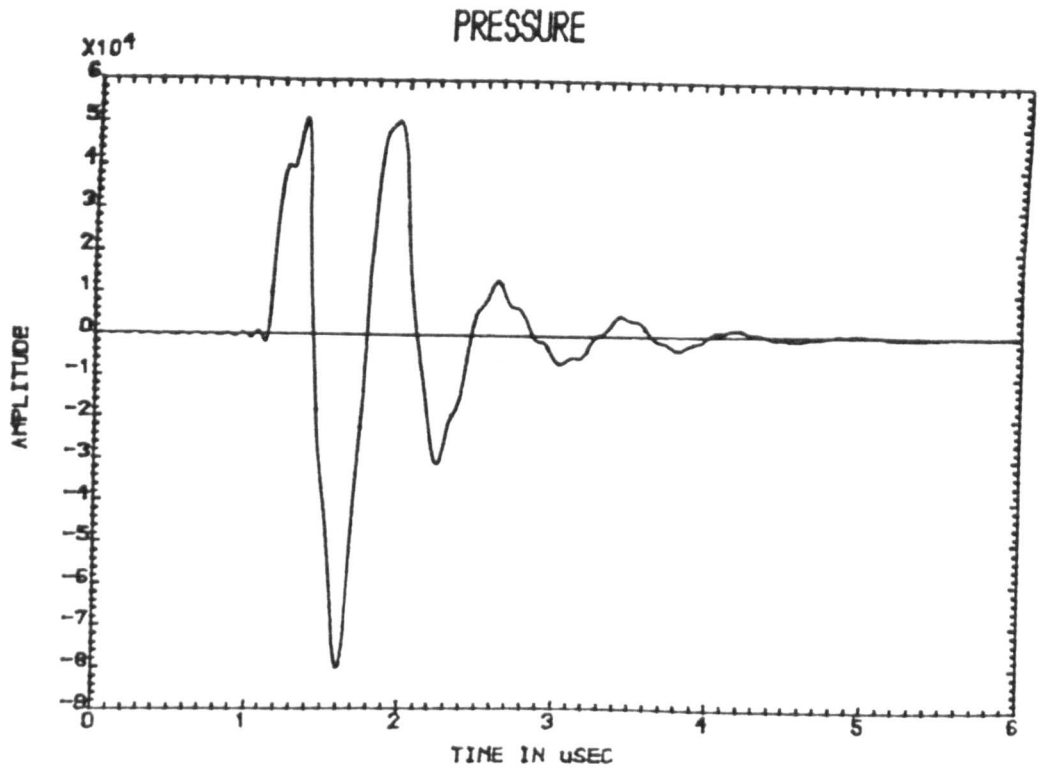

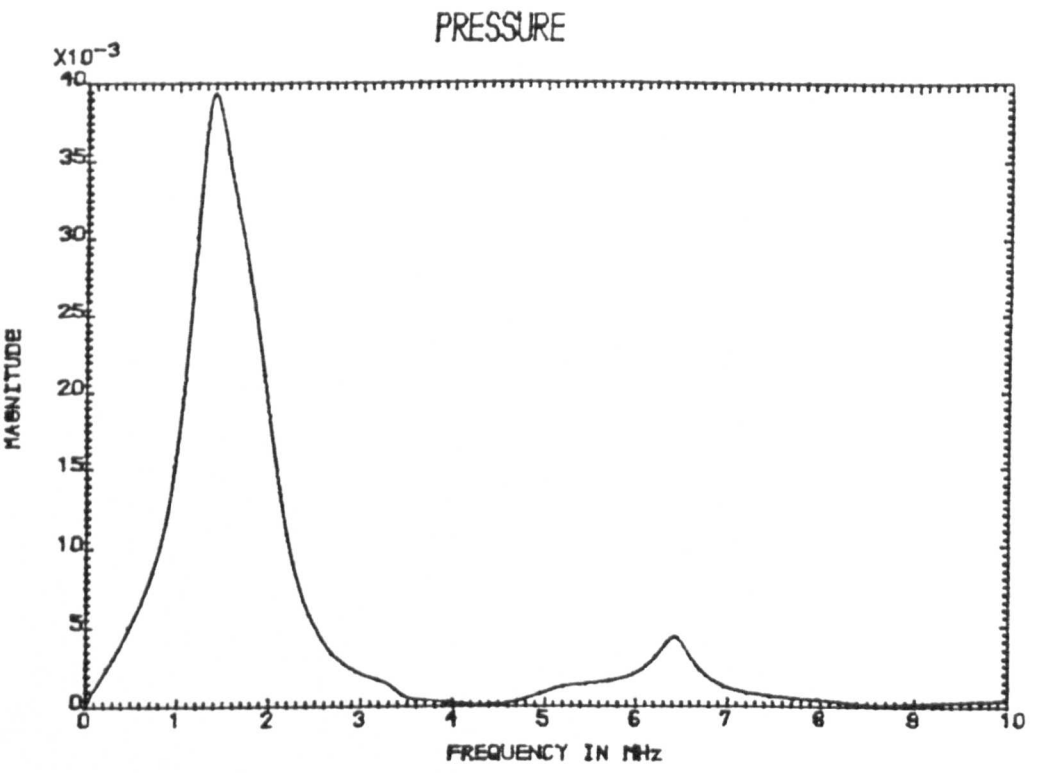

Figure 6.15(a) Simulated time and frequency domain force output for a front face layer thickness of 350μm.

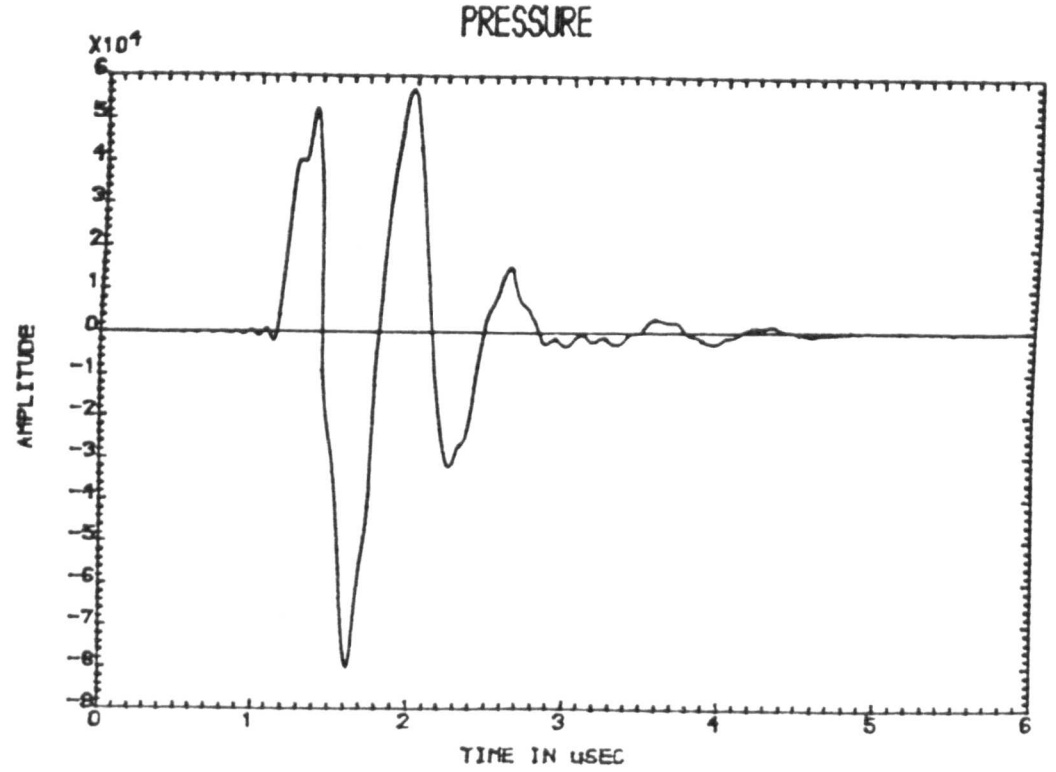

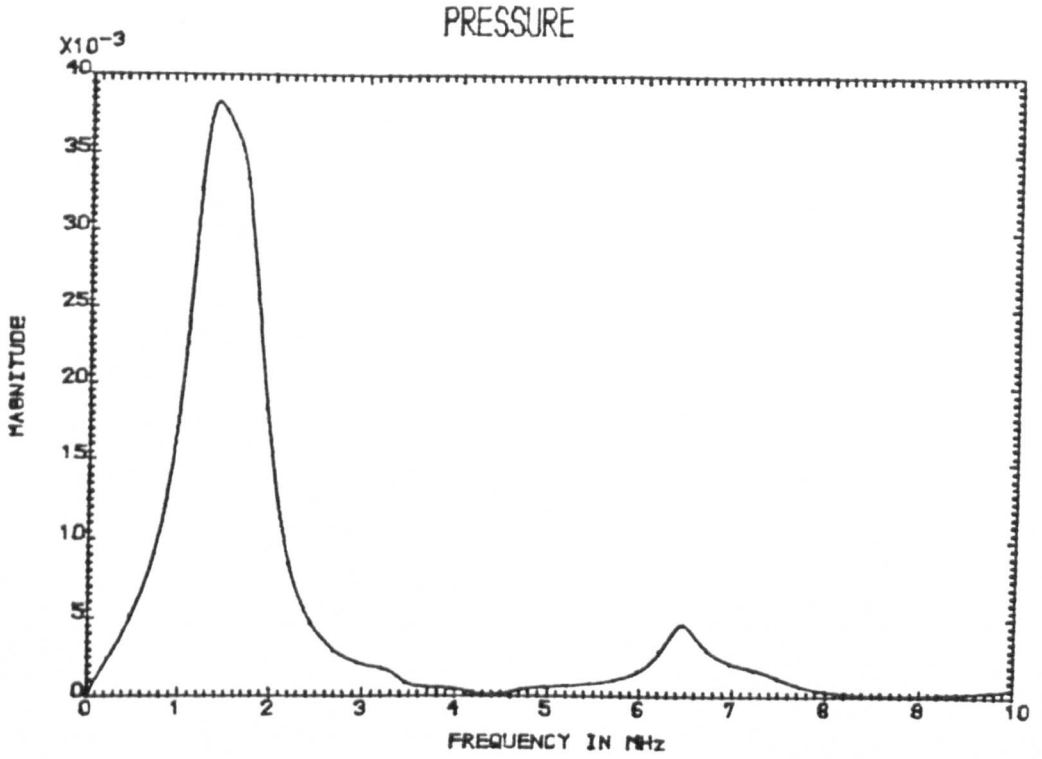

Figure 6.15(b) Simulated time and frequency domain force output for a front face layer thickness of 400μm.

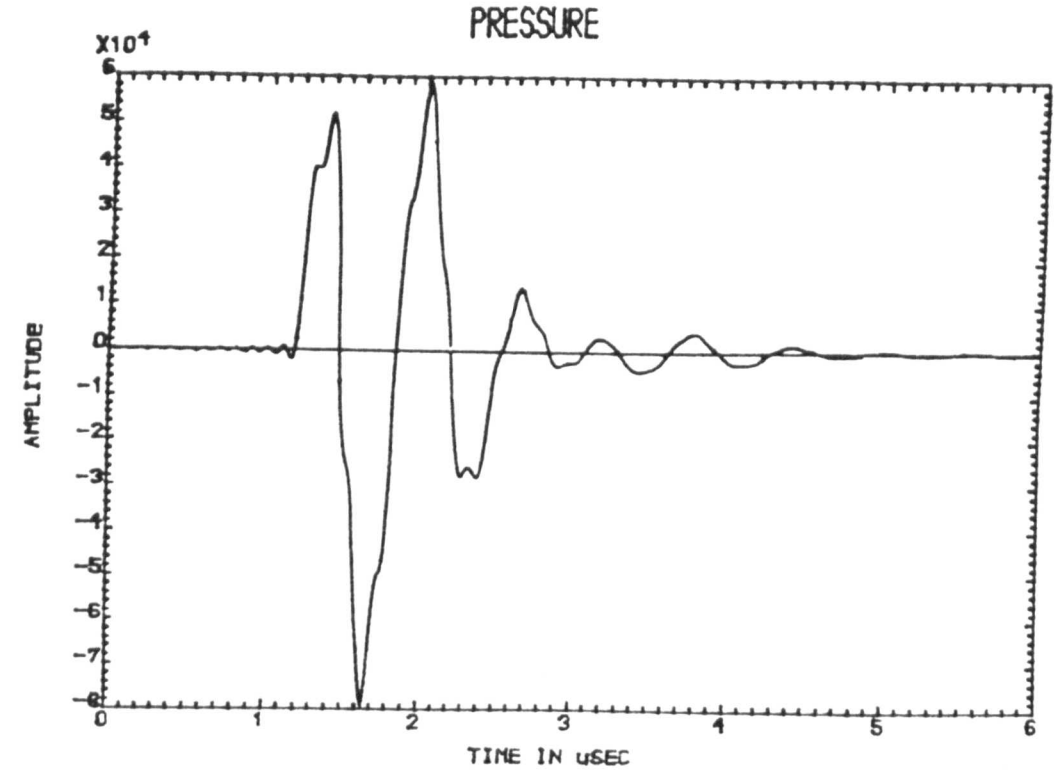

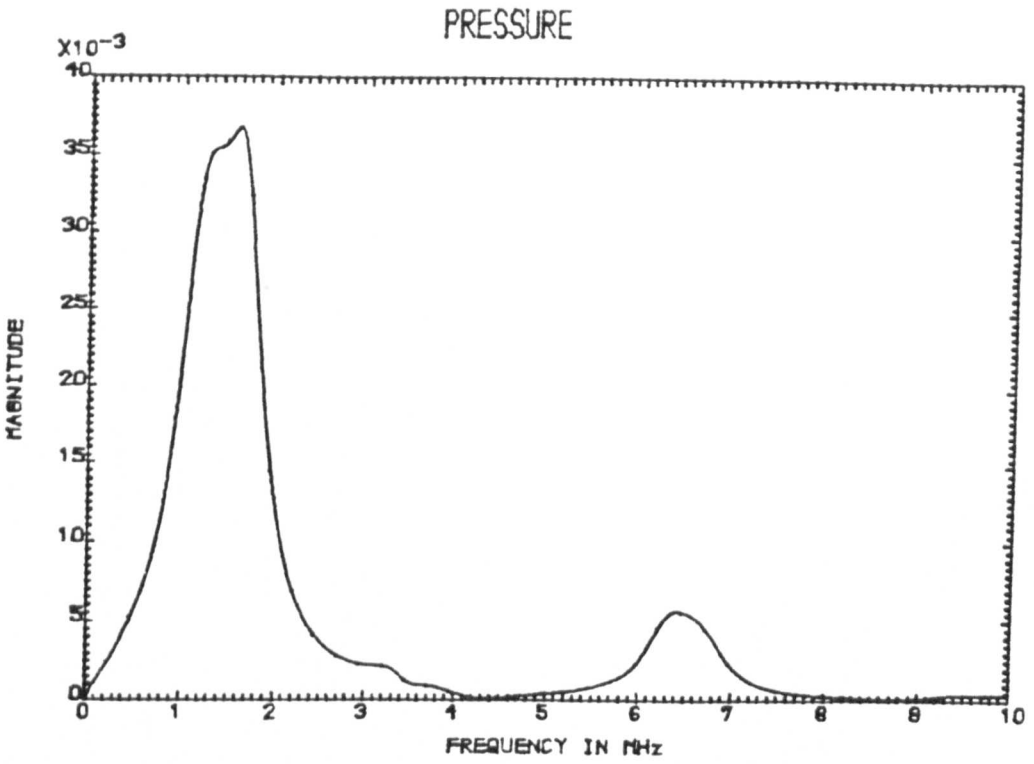

Figure 6.15(c) Simulated time and frequency domain force output for a front face layer thickness of 450μm.

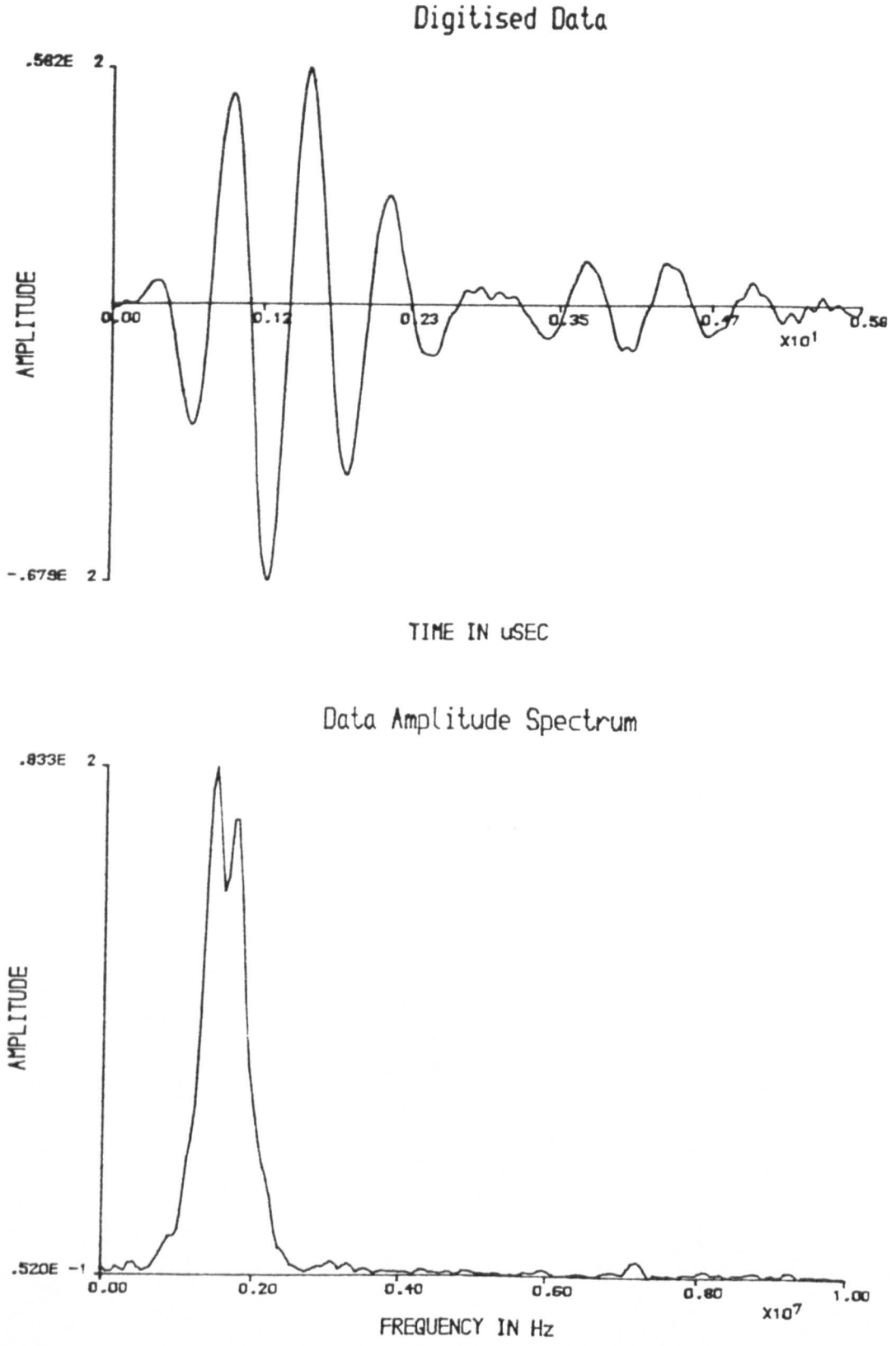

Figure 6.16 Measured time and frequency domain pulse-echo response of element 9 in array #1.

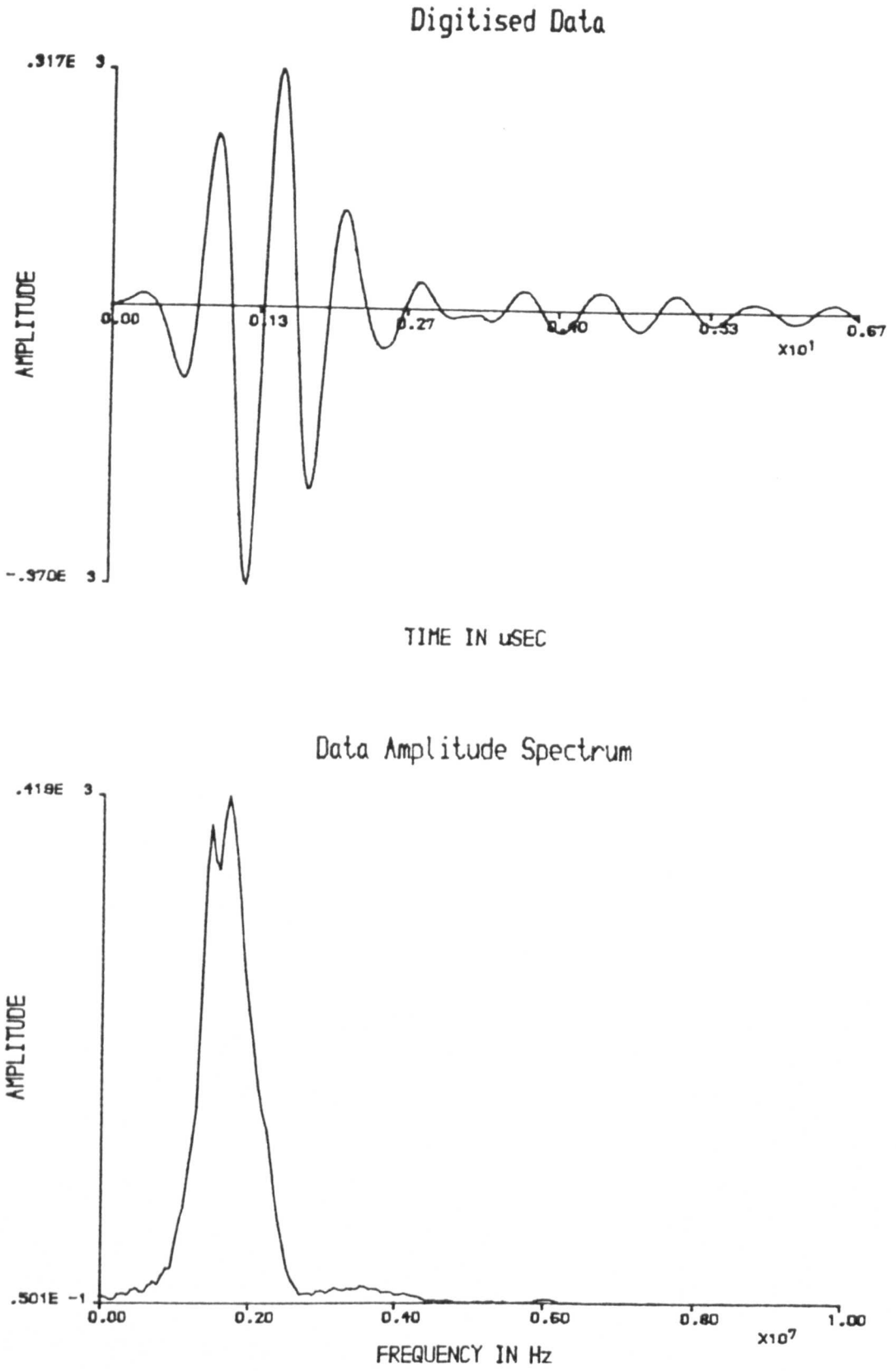

Figure 6.17 Measured time and frequency domain pulse-echo response of element 9 in array #2.

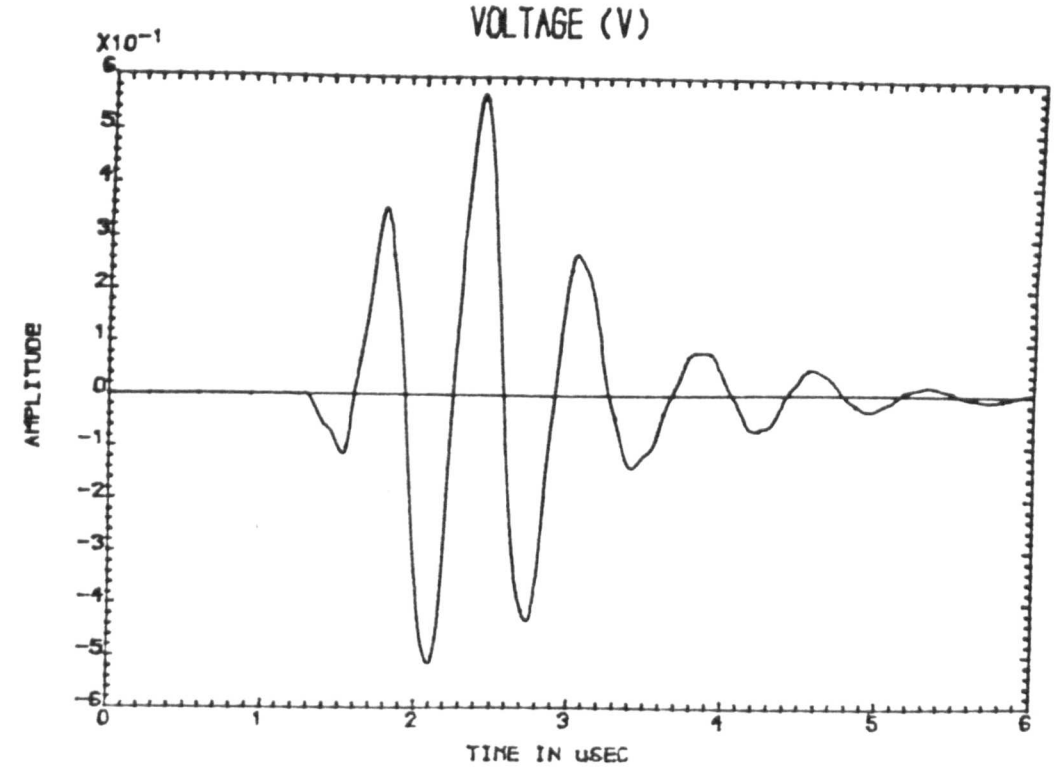

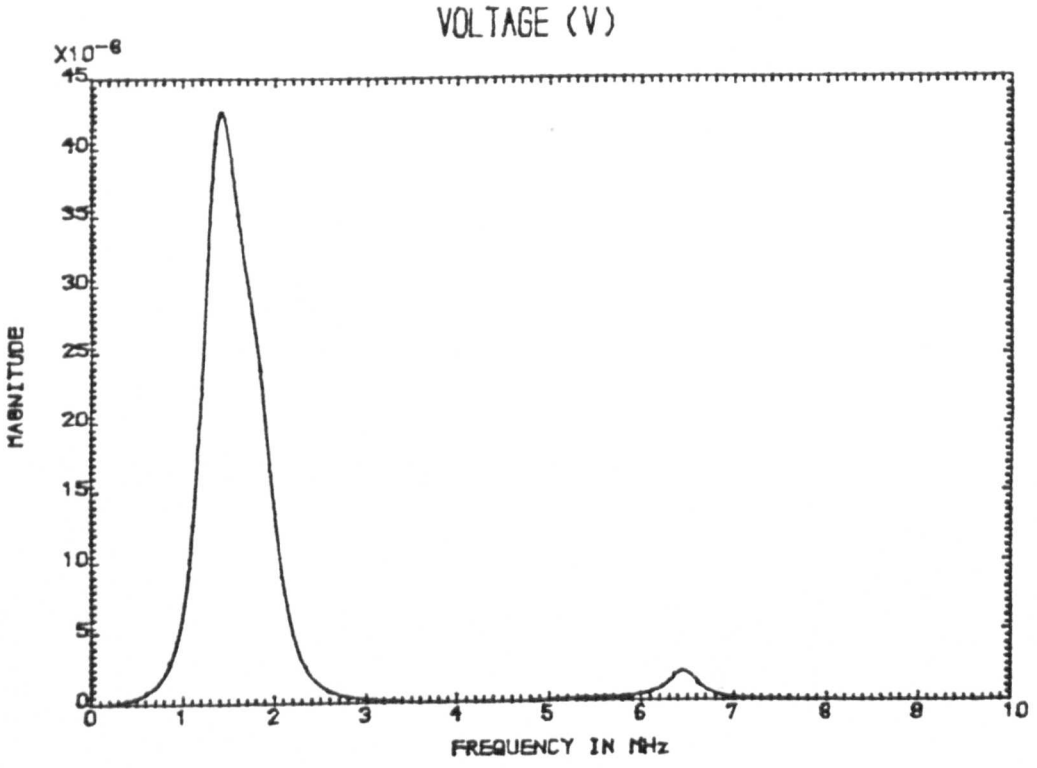

Figure 6.18(a) Simulated time and frequency domain pulse-echo response for a front face layer thickness of 350μm.

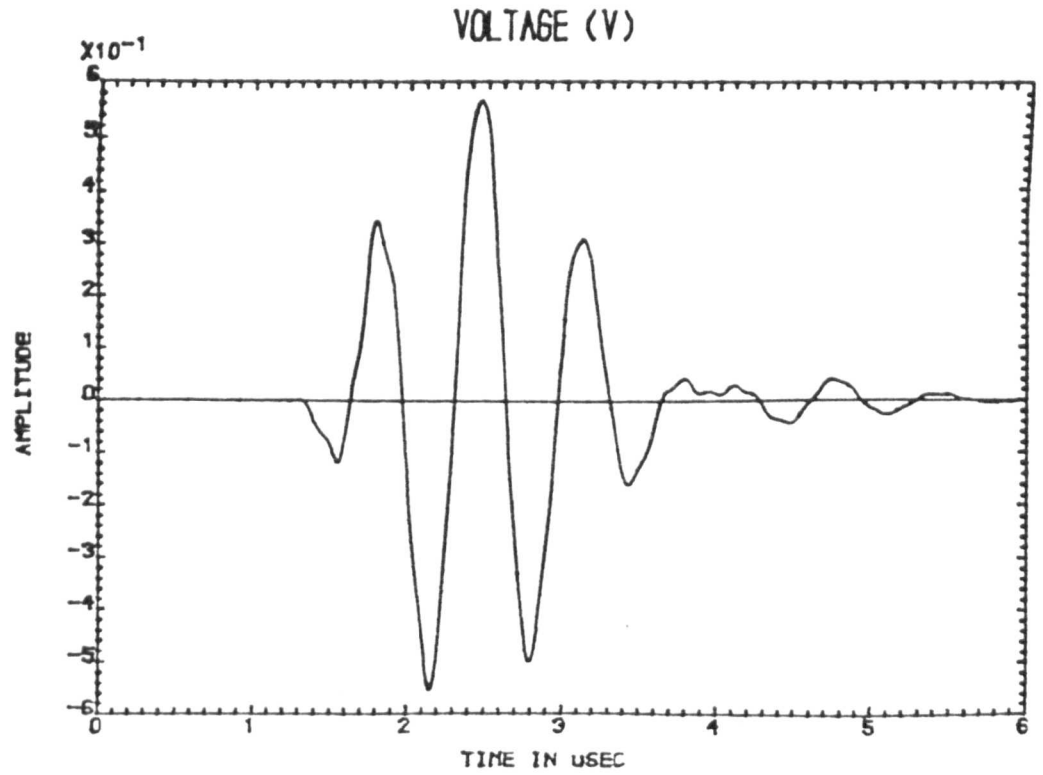

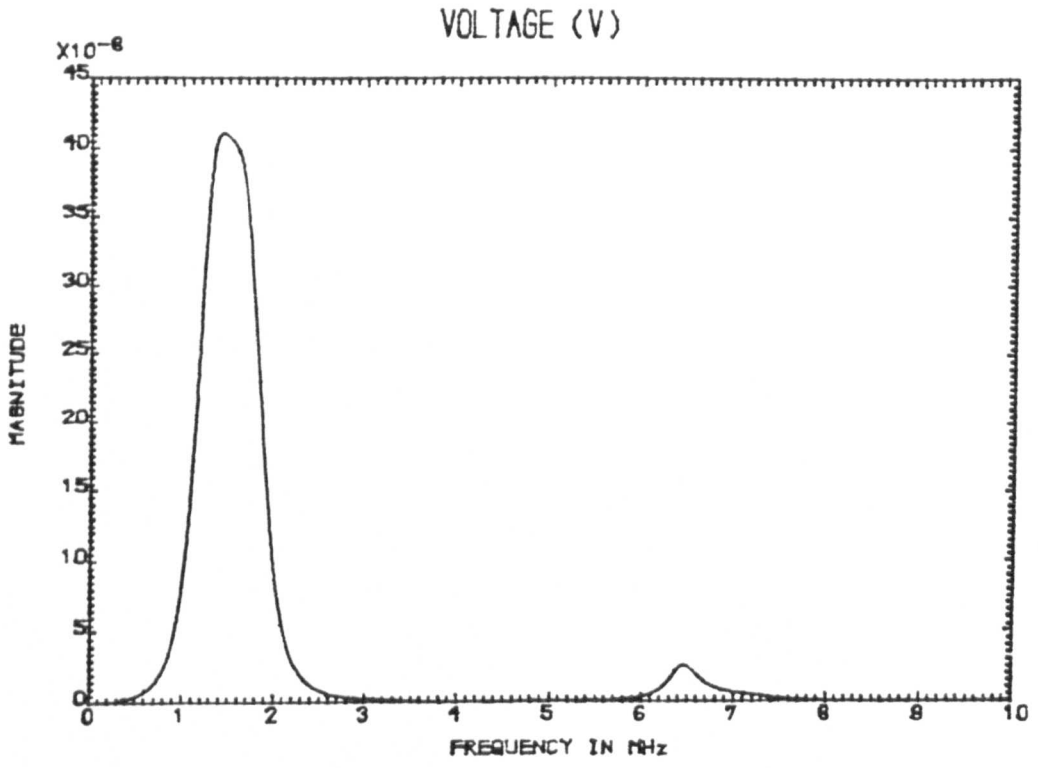

Figure 6.18(b) Simulated time and frequency domain pulse-echo response for a front face layer thickness of 400μm.

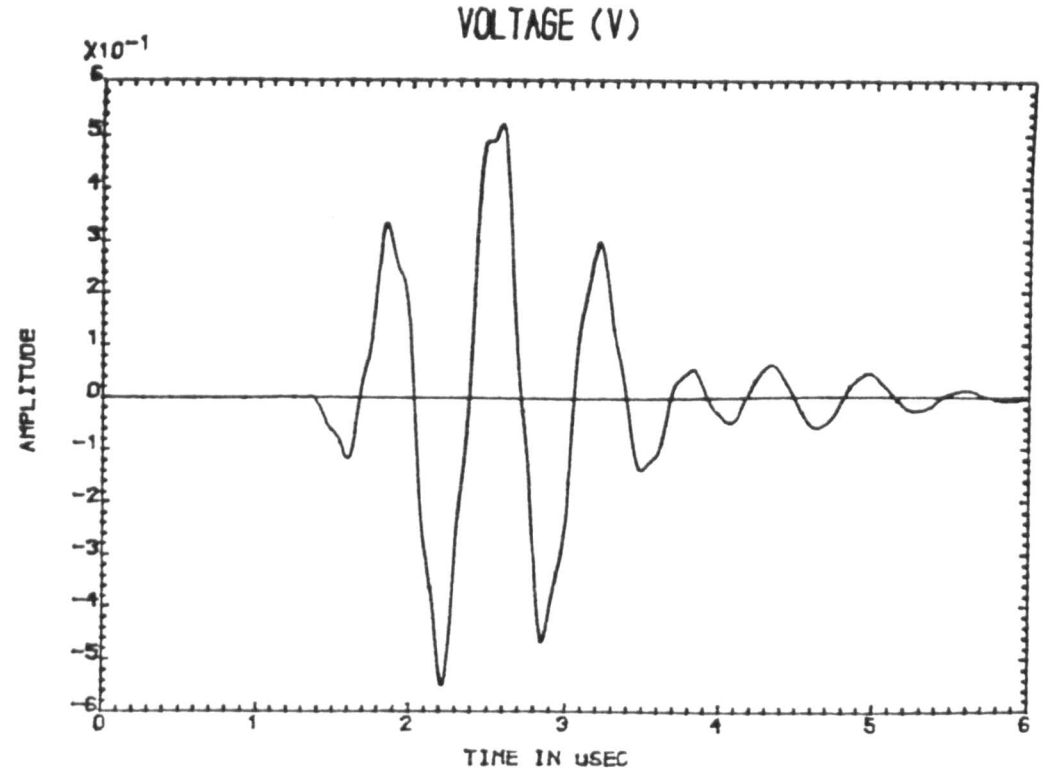

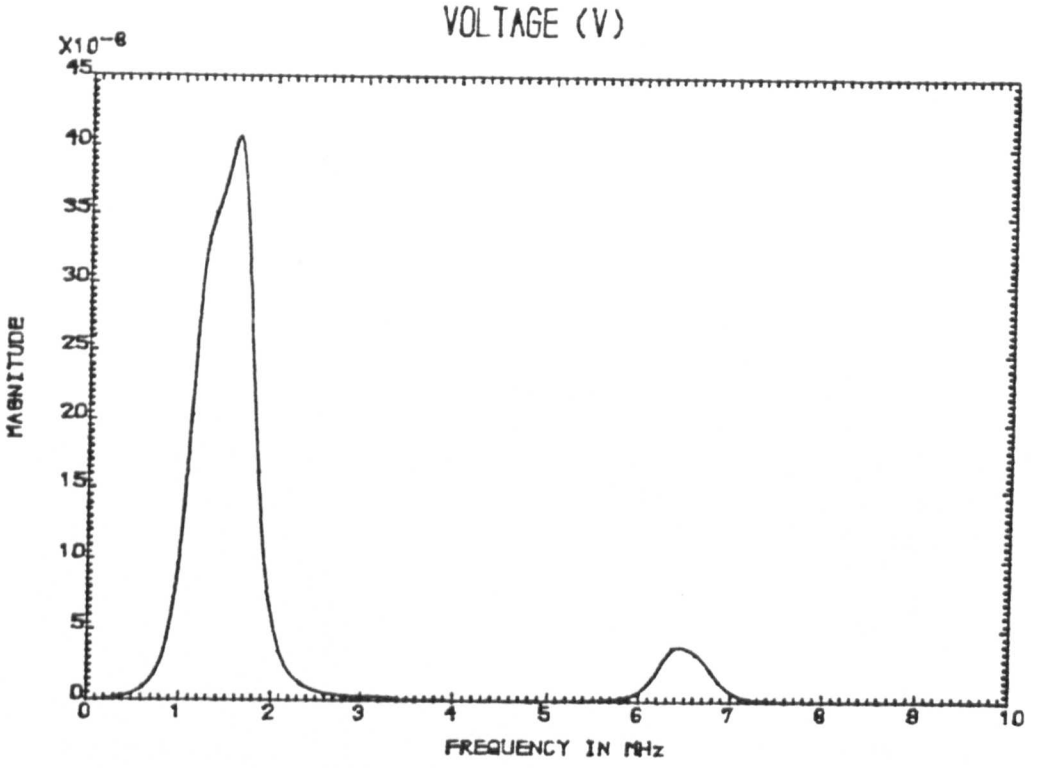

Figure 6.18(c) Simulated time and frequency domain pulse-echo response for a front face layer thickness of 450μm.

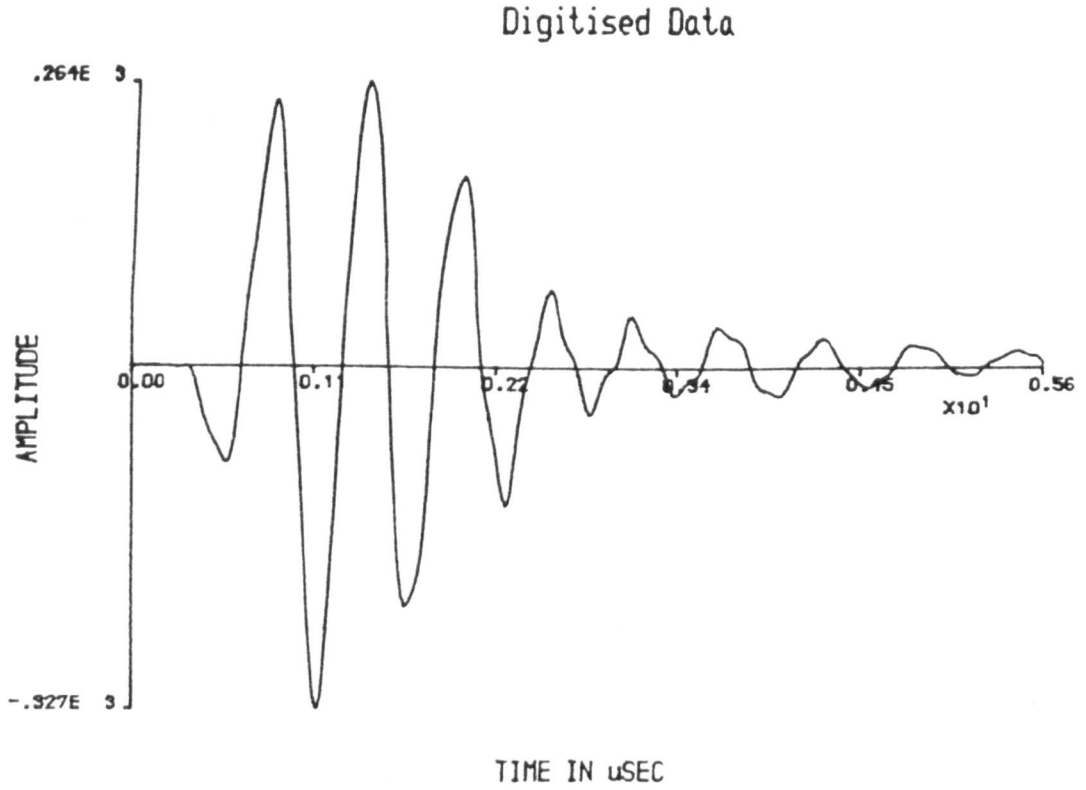

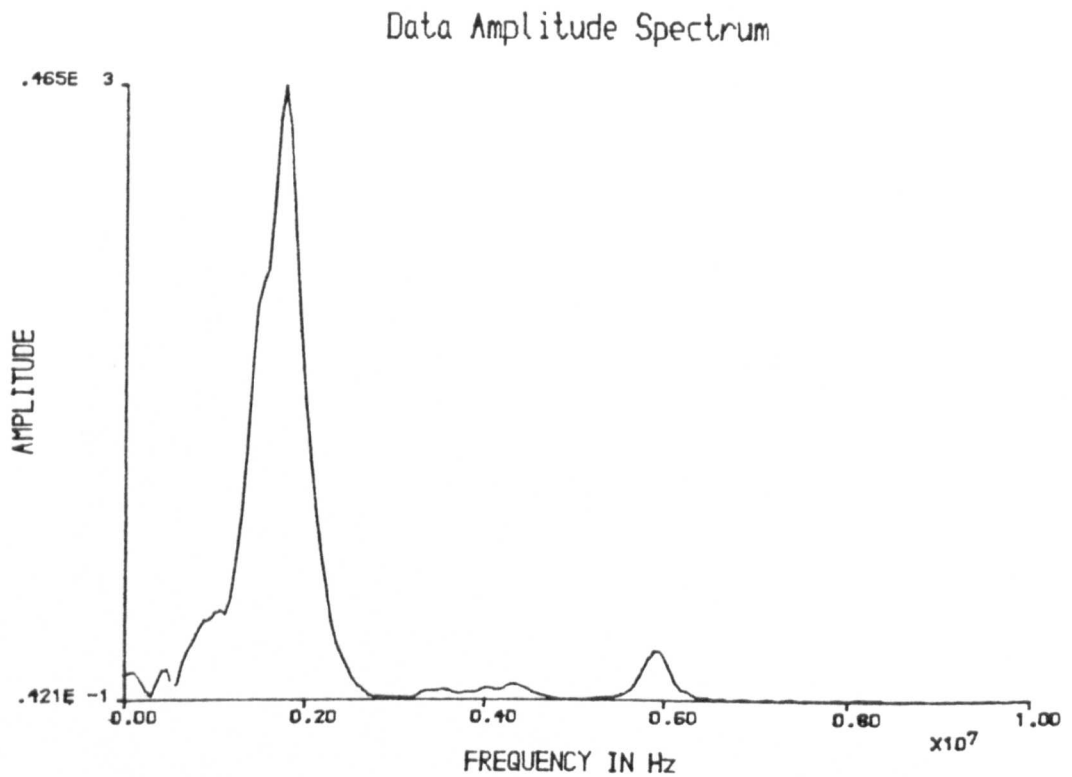

Figure 6.19 Measured time and frequency domain pulse-echo response of element 9 in array #1 operating into a glass load.

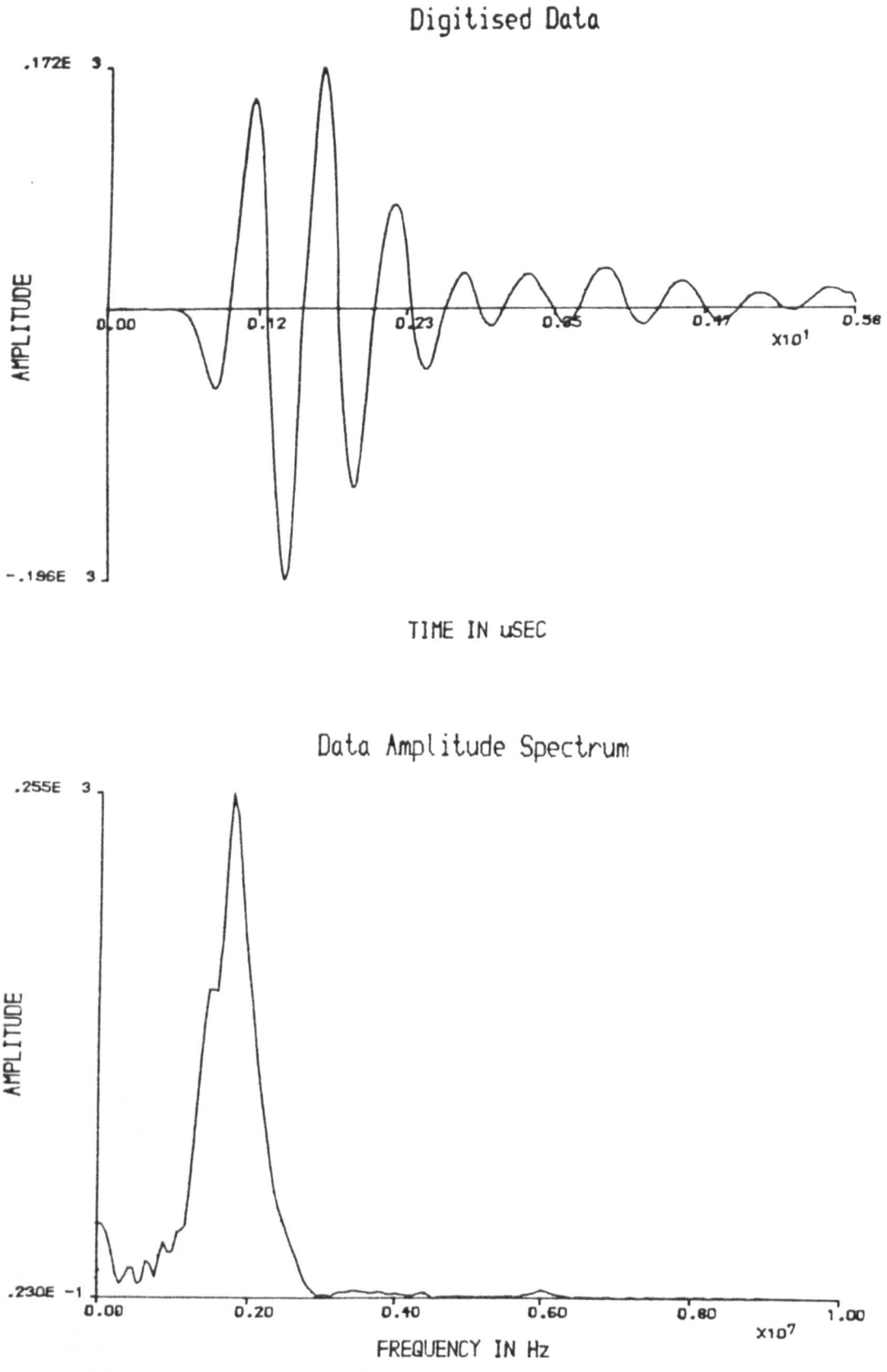

Figure 6.20 Measured time and frequency domain pulse-echo response of element 9 in array #2 operating into a glass load.

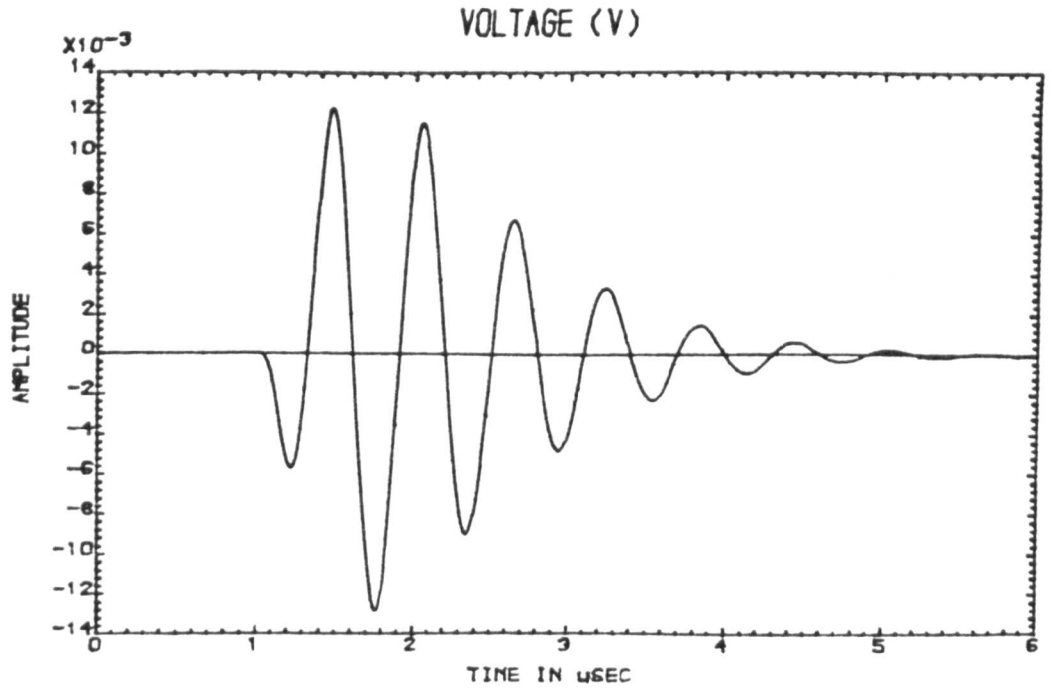

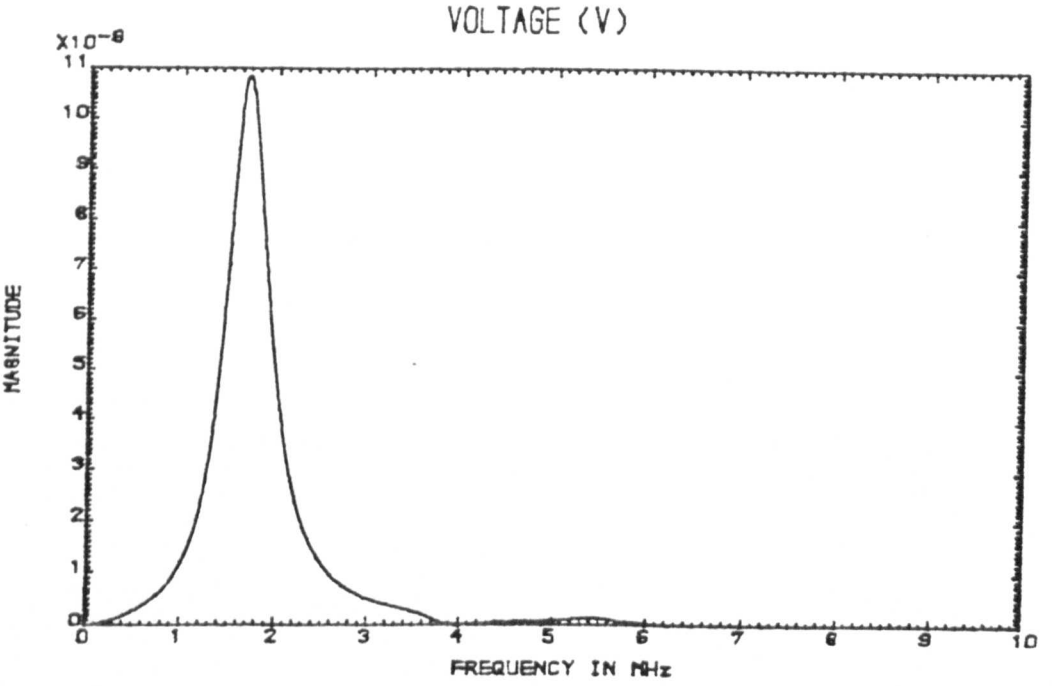

Figure 6.21 Simulated time and frequency domain pulse-echo response for a front face layer of 400μm, operating into a glass load.

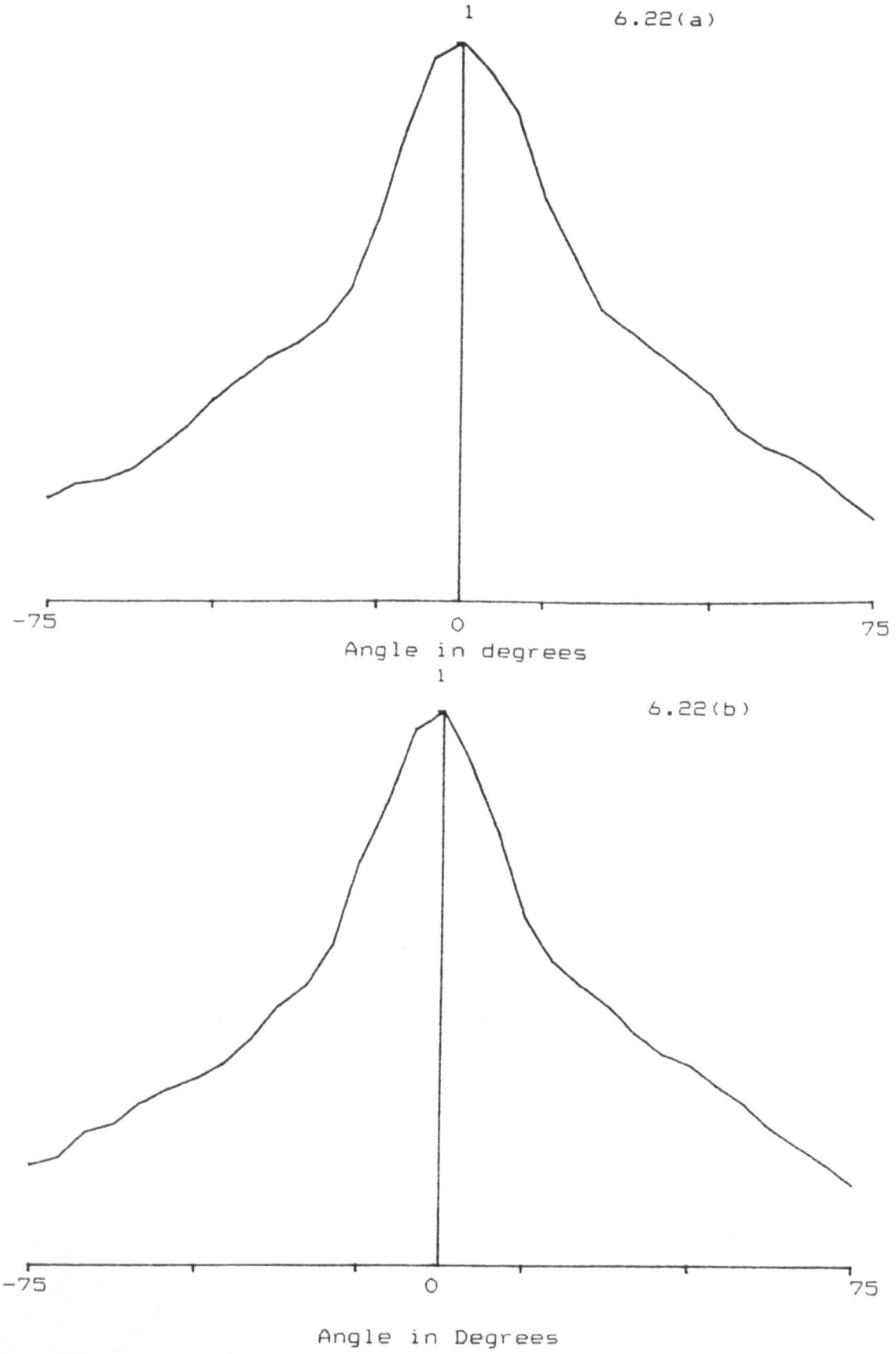

Figure 6.22 Directivity plots for element 9 of array #1 and array #2 respectively.

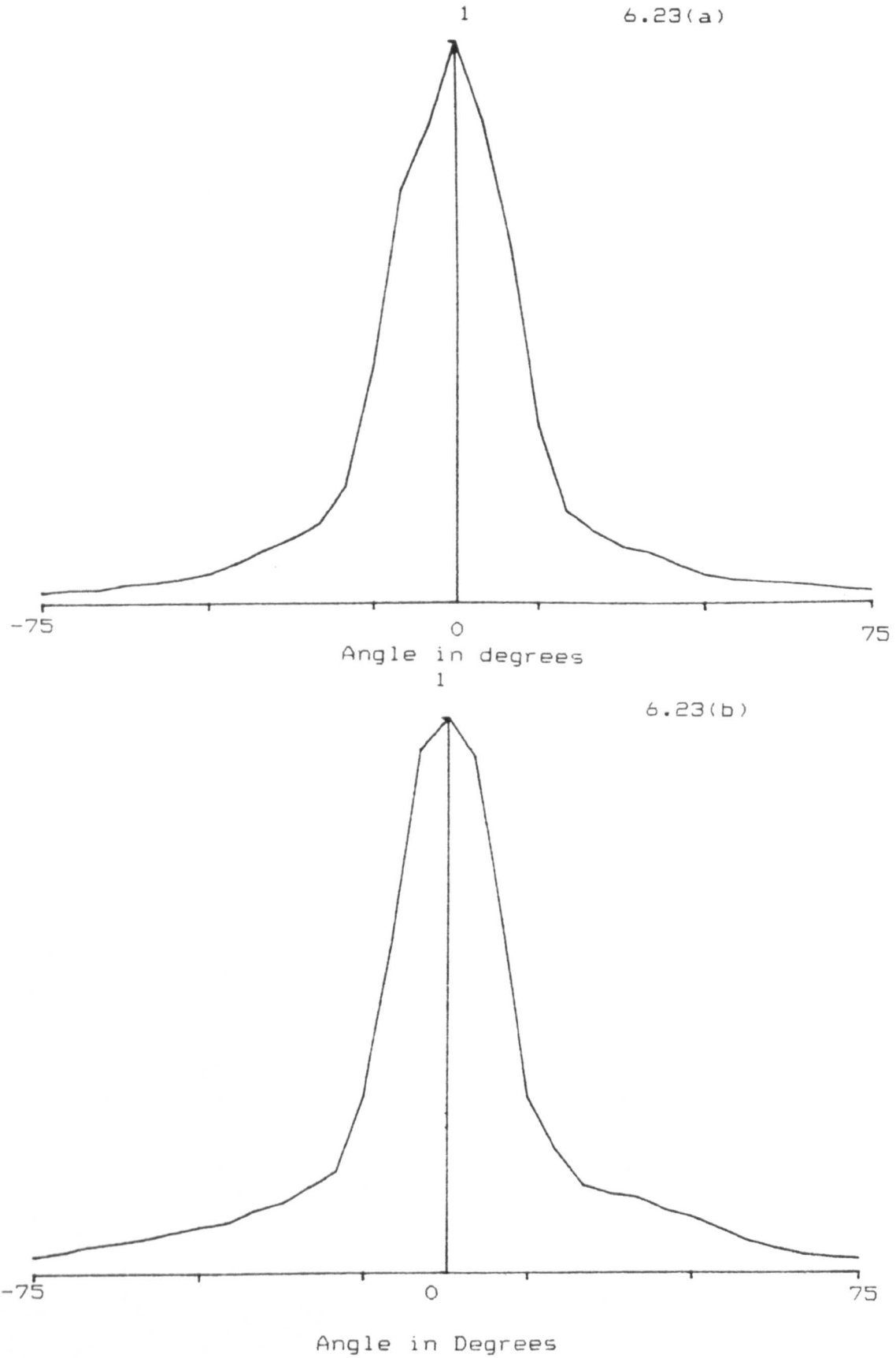

Figure 6.23 Directivity plots for array #1 and array #2 respectively, when steered at 0°.

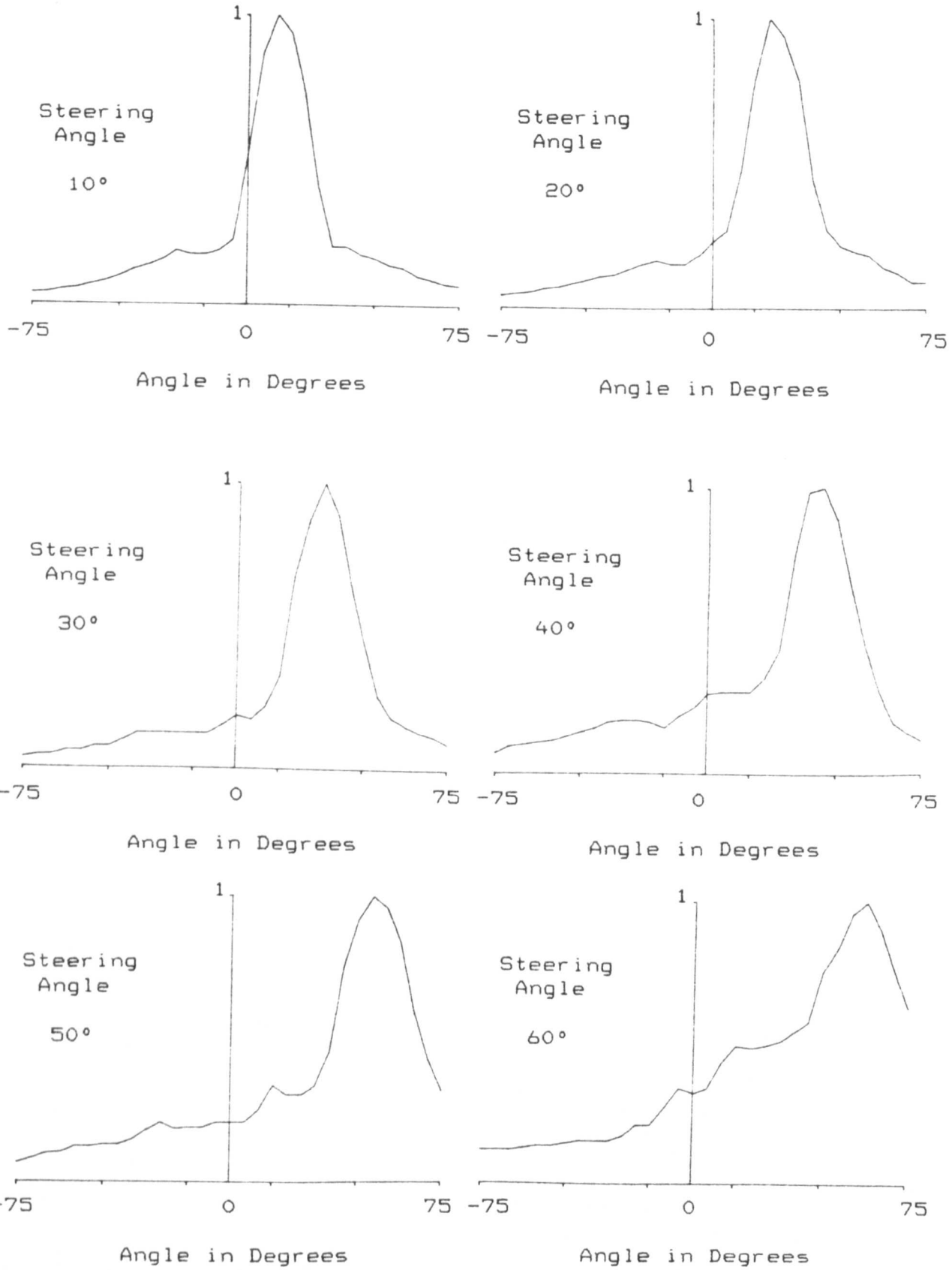

Figure 6.24 Steered beam directivity plots for array #1.

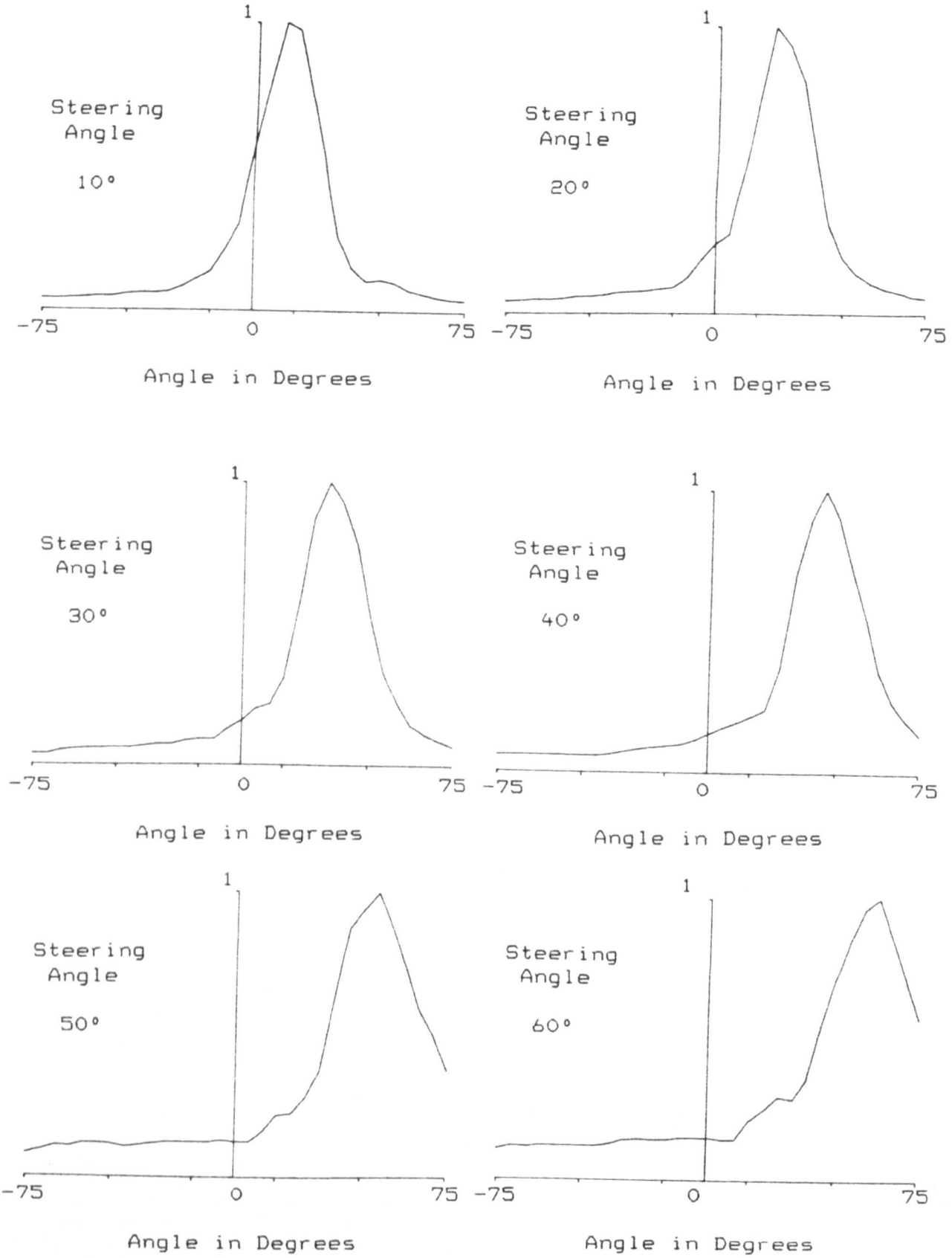

Figure 6.25 Steered beam directivity plots for array #2.

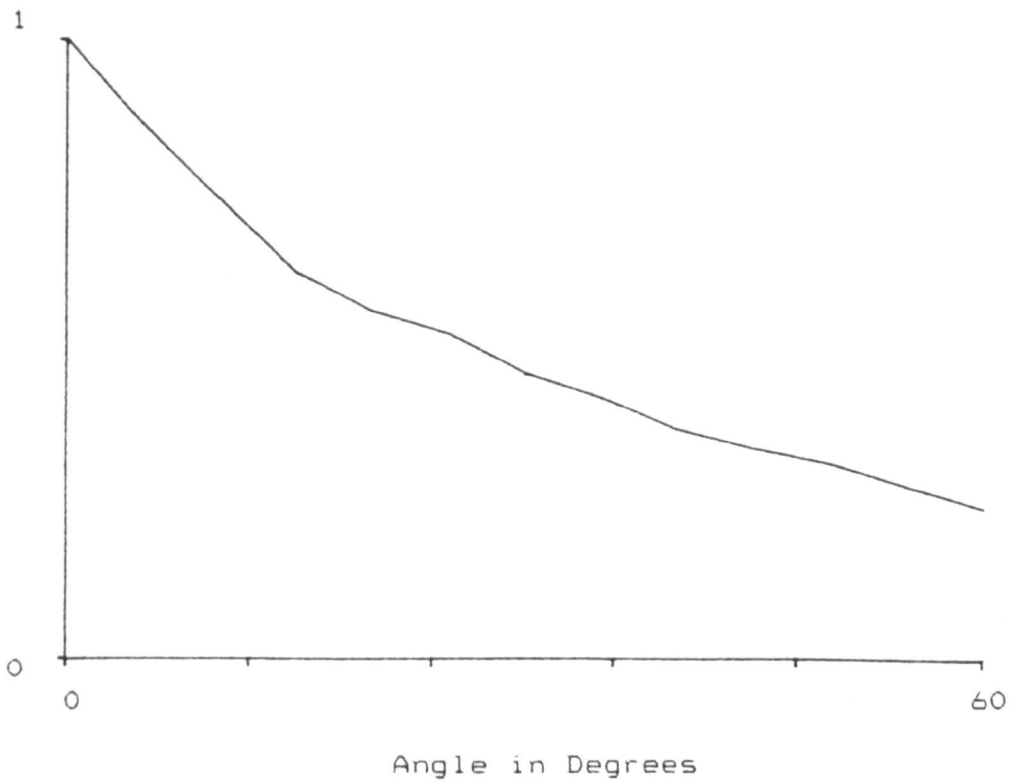

Figure 6.26 Relative strength of the steered beam between 0° and 60°.

ANGLE OF STEER degrees	ARRAY #1			ARRAY #2		
	-3dB (lower)	-3dB (upper)	-3dB (width)	-3dB (lower)	-3dB (upper)	-3dB (width
0°	-9	9	18	-9	9	18
10°	3	21	18	3	21	18
20°	14	32	18	13	30	17
30°	22	41	19	21	39	18
40°	30	50	20	30	50	20
50°	37	61	24	40	63	23
60°	44	70	26	44	72	28

Table 6.1 A comparison of the directivity of the two arrays when steered between 0° and 60°.

ELEMENT NUMBER	ARRAY #1			ARRAY #2		
	Fe (MHz)	Z @ Fe (Ω)	EFFICIENCY (%)	Fe (MHz)	Z @ Fe (Ω)	EFFICIENCY (%)
1	1.450	395	90	*	*	*
2	1.430	370	76	1.360	480	80
3	1.400	375	95	1.380	475	98
4	1.410	370	101	1.380	475	95
5	1.410	375	103	1.360	465	96
6	1.400	385	114	1.380	470	107
7	1.390	365	109	1.380	470	110
8	1.415	365	102	1.380	475	99
9	1.400	395	100	1.360	480	100
10	1.415	370	113	1.370	470	112
11	1.420	375	95	1.380	475	85
12	1.415	370	94	1.360	450	101
13	1.420	355	86	1.400	430	90
14	1.415	370	85	1.370	450	83
15	1.415	365	81	1.355	445	84
16	1.420	375	79	1.375	425	81
AVERAGE	**1.414**	**373**	**	**1.374**	**480**	**
% VARI- -ATION	**4.2**	**10.7**	**39**	**3.8**	**11.5**	**32**

* This element is faulty, and is not considered in the calculation of the average and percentage variation.

** Not applicable

Table 6.2 A comparison of the characteristics of each element in the arrays.

PROPERTY	NOMINAL	MEASURED	SIMULATION
Y_{11} .(10^{10})	12.6	———	12.0
Y_{13} .(10^{10})	6.5	———	6.0
Y_{33} .(10^{10})	14.7	14.1	14.1
h_{13} .(10^{8})	-7.3	———	-7.3
h_{33} .(10^{8})	21.5	21.0	21.0
ϵ_{33}	830	830	830
ρ	7750	7725	7725
LOSS	———	———	5

Table B1 Table of mechanical and piezoelectric properties of 1MHz PZT-5A plate.

PROPERTY	NOMINAL	MEASURED	SIMULATION
Y_{11} .(10^{10})	12.6	———	12.9
Y_{13} .(10^{10})	6.5	———	6.0
Y_{33} .(10^{10})	14.7	15.0	15.0
h_{13} .(10^{8})	-7.3	———	-7.3
h_{33} .(10^{8})	21.5	21.5	21.5
ϵ_{33}	830	810	810
ρ	7750	7740	7740
LOSS	———	———	5

Table B2 Table of mechanical and piezoelectric properties of 2MHz PZT-5A plate.

PROPERTY	NOMINAL	SIMULATION
Y_{11} .(10^{10})	25.7	25.7
Y_{13} .(10^{10})	———	———
Y_{33} .(10^{10})	25.7	25.7
ρ	7400	7400
LOSS	———	3

Table B3 Table of mechanical properties of steel

PROPERTY	NOMINAL	SIMULATION
Y_{11} .(10^{10})	11.1	11.1
Y_{13} .(10^{10})	———	———
Y_{33} .(10^{10})	11.1	11.1
ρ	2800	2800
LOSS	———	7

Table B4 Table of mechanical properties of aluminium

PROPERTY	NOMINAL	SIMULATION
Y_{33} .(10^{10})	0.68	0.68
ρ	1100	1100
LOSS	———	6

Table B5 Table of mechanical properties of epoxy

PROPERTY	NOMINAL	SIMULATION
Y_{33} .(10^{10})	0.45	0.45
ρ	1200	1200
LOSS	———	8

Table B6 Table of mechanical properties of natural honey

PROPERTY	NOMINAL	SIMULATION
Y_{33} .(10^{10})	0.86	0.86
h_{33} .(10^{8})	16.5	16.5
ϵ_{33}	8	8
ρ	1780	1780
LOSS	———	———

Table B7 Table of mechanical and piezoelectric properties of PVDF

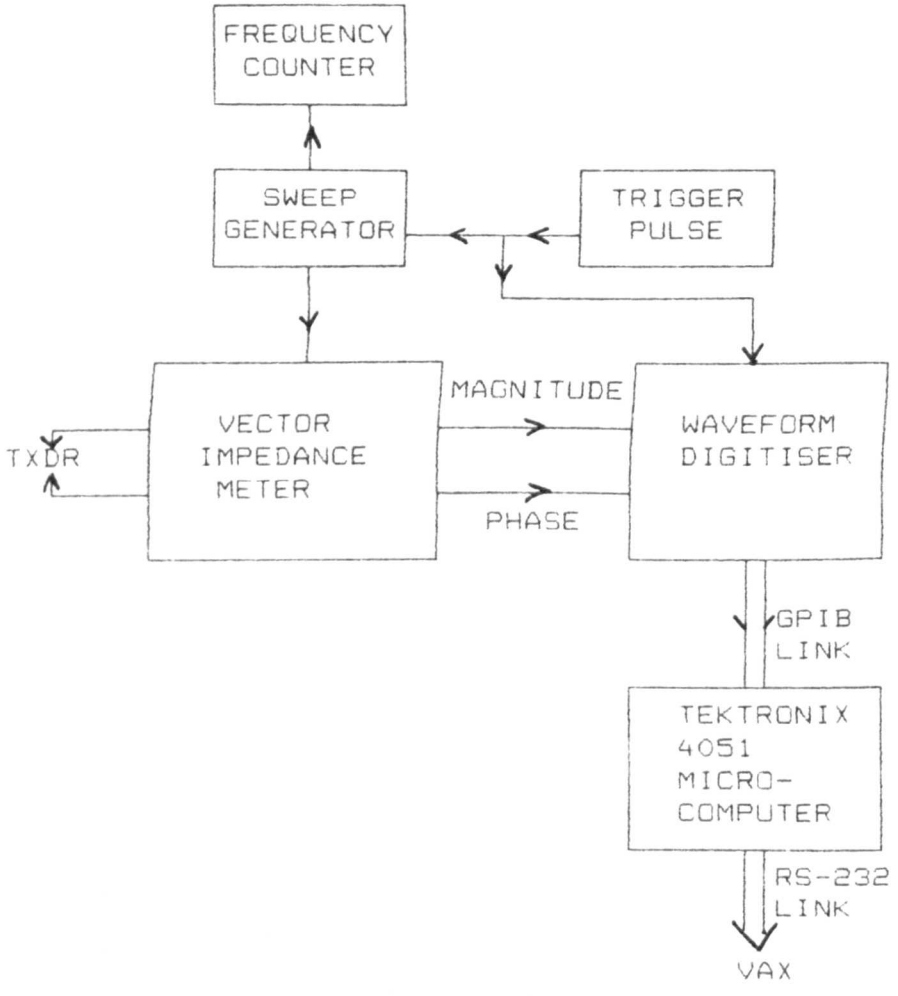

Figure B1 Experimental set-up for impedance measurements.

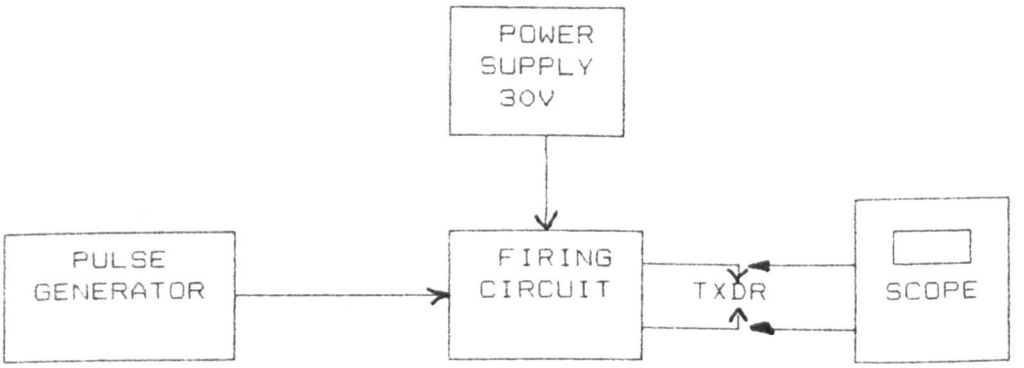

Figure B2 Experimental set-up for measurement of transmitter voltages.

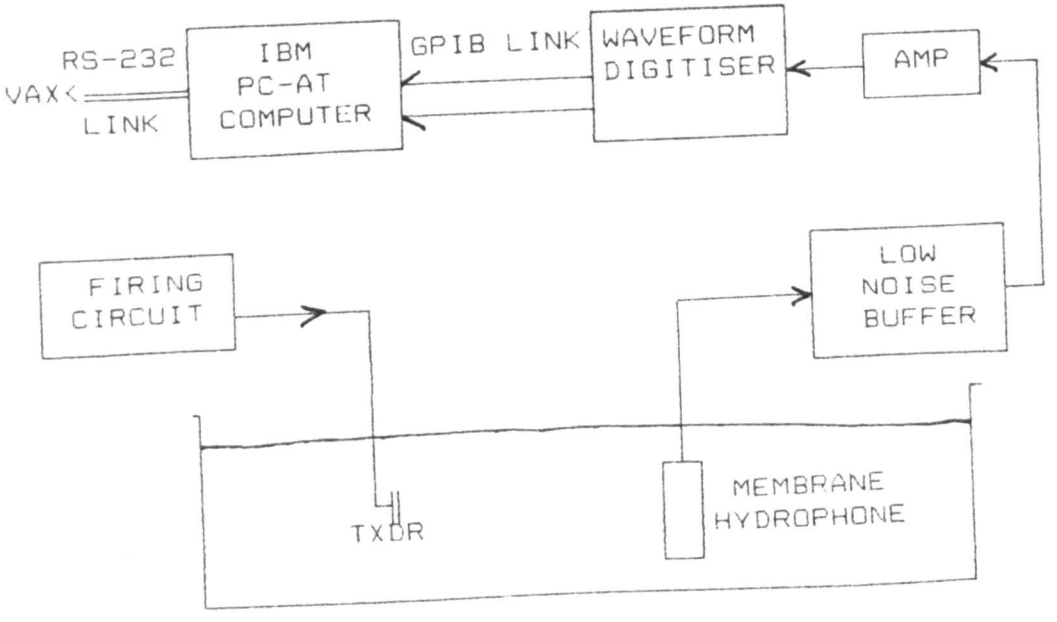

Figure B3 Experimental set-up for measurement of force profiles.

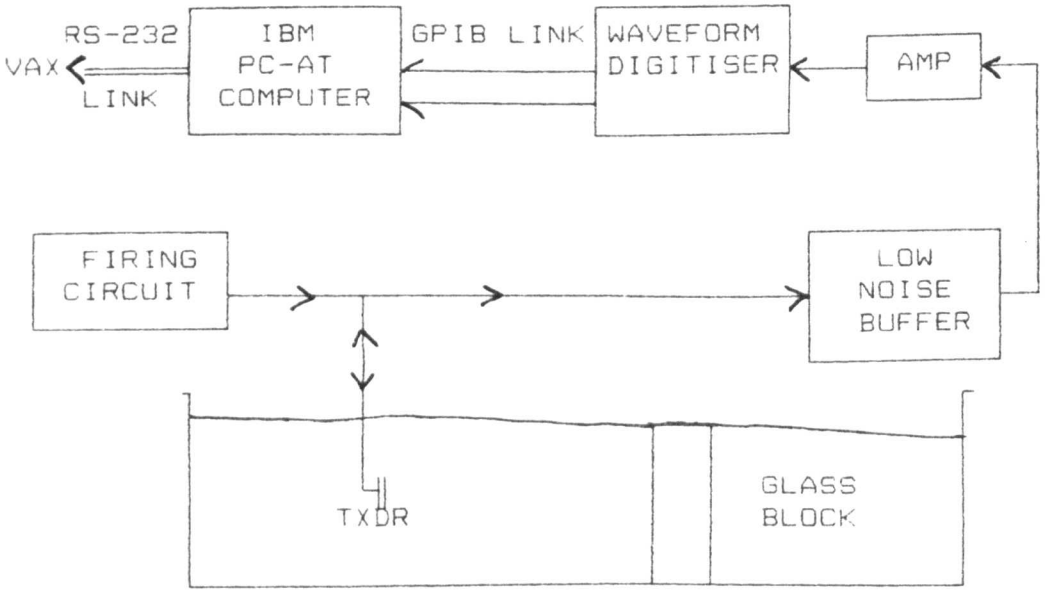

Figure B4 Experimental set-up for measurement of water tank pulse-echo responses.

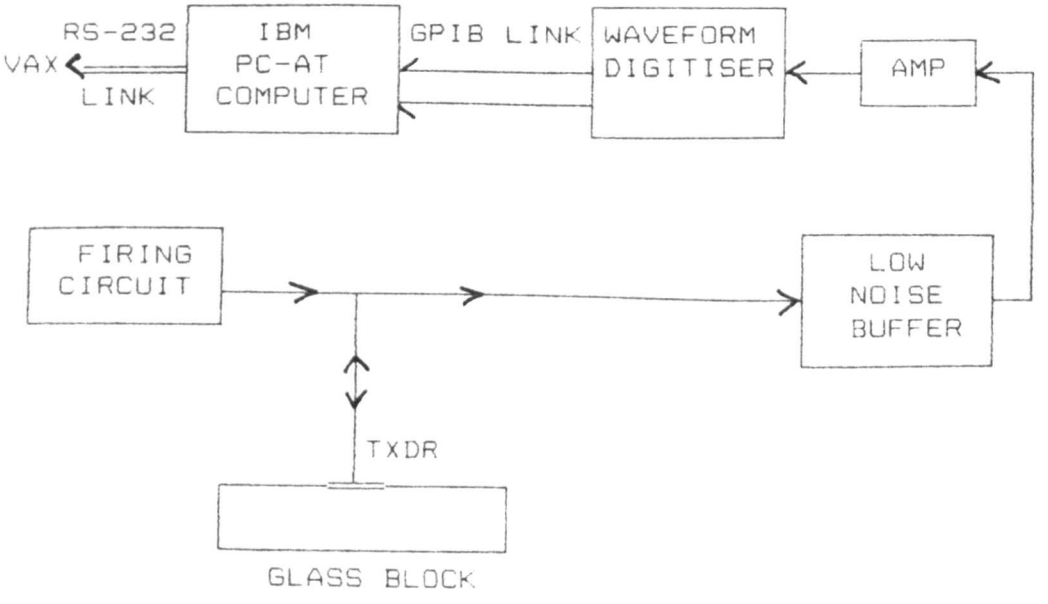

Figure B5 Experimental set-up for measurement of water tank pulse-echo responses.

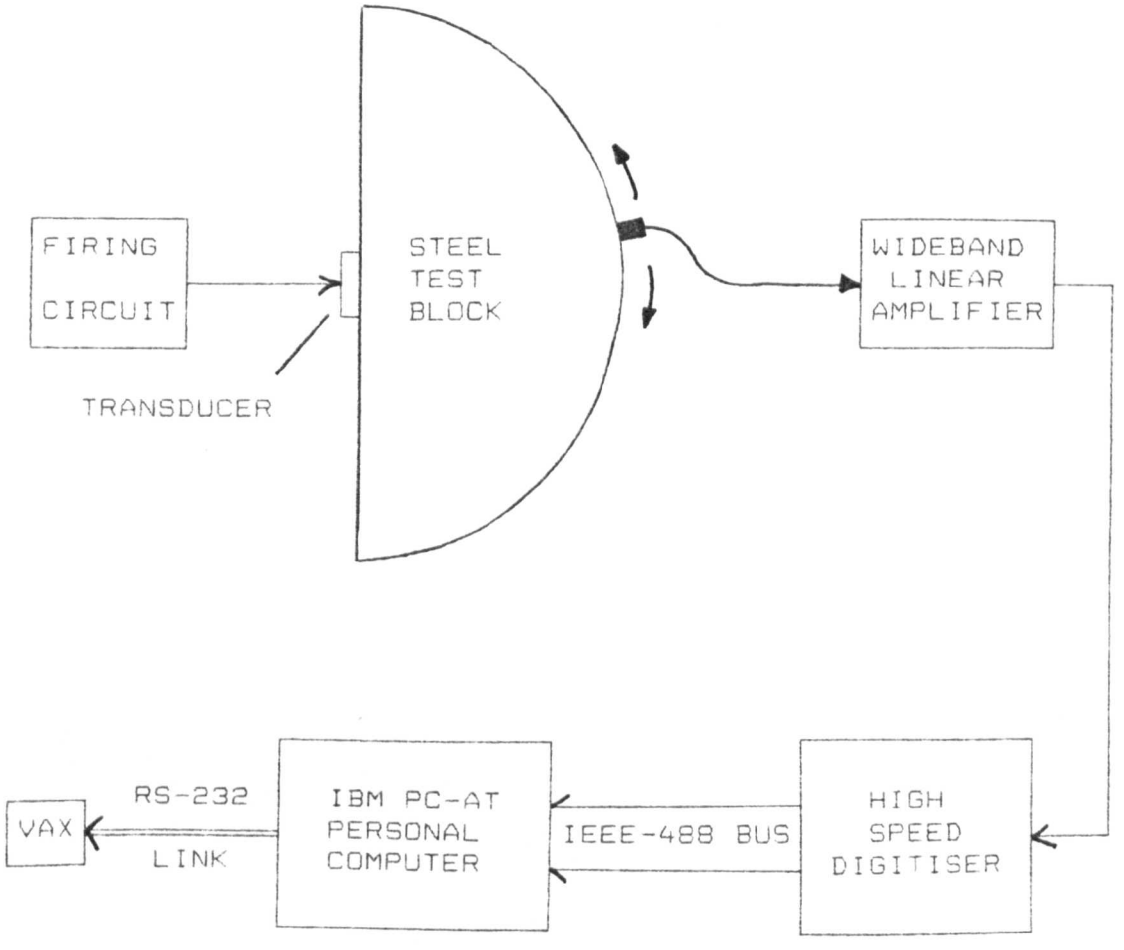

Figure B6 Experimental set-up for the evaluation of transducer directivity.

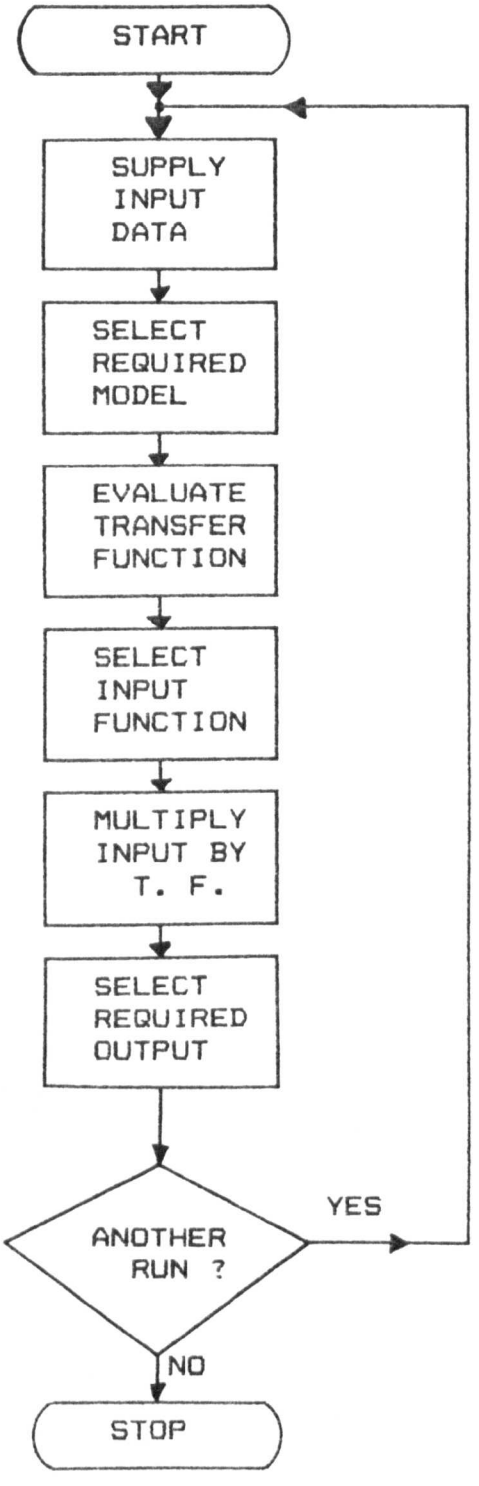

Figure C1 Flow chart describing the operation of the program SYSMOD.

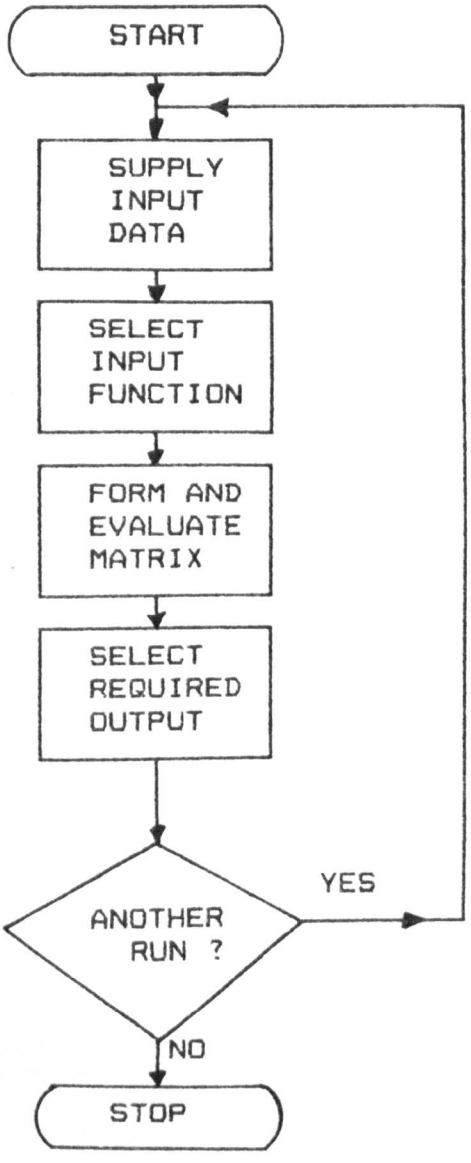

Figure C2 Flow chart describing the operation of the program TMOD.